Quantitative cardiac x-ray imaging

Andrew Graham Davies

Submitted in accordance with the requirements for the degree of Doctor of Philosophy

The University of Leeds

School of Medicine

18th February, 2020

Declaration

The candidate confirms that the work submitted is his own, except where work has formed part of jointly authored publications has been included. The contribution of the candidate and the other authors to this work has been explicitly indicated below. The candidate confirms that appropriate credit has been given within the thesis where reference has been made to the work of others.

The work in Chapter 2 of the thesis has appeared in:

Vijayan S., Barmby D.S., Pearson I.R., Davies A.G., Wheatcroft S.B. and Sivananthan, M. "Assessing Coronary Blood Flow Physiology in the Cardiac Catheterisation Laboratory" Current Cardiology Reviews 13(3):232-243, 2019.

I was responsible for reviewing, editing and providing input for the manuscript, specifically in the areas of X-ray imaging and physiological measurements. Dr Vijayan was responsible for creating the manuscript. The other authors provided feedback and review after the drafting of the manuscript.

The work in Chapter 3 of the thesis has appeared in:

Davies A.G., Gislason-Lee A.J., Cowen A.R., Kengyelics S.M., Lupton M., Moore J., Sivananthan U.M., "Does the use of additional beam filtration during cine acquisition reduce image quality and effective dose in cardiac interventional imaging?" Radiation Protection Densitometry 162(4):597-604, 2014.

I was responsible for the defining the research aims, the experimental design, data acquisition, analysis and writing the manuscript. Dr Gislason-Lee performed part of the analysis (specifically statistical modelling) and contributed to the manuscript preparation. Dr Cowen also contributed to the research aims, participated in the phantom data acquisition and reviewed the manuscript. Dr Kengyelics participated in the phantom data acquisition and image analysis for the phantom experiments. Mr Lupton and Ms Moore participated in the implementation of and data collection during the clinical study. Prof Sivananthan contributed to the research aims, the design of the clinical experiment, data acquisition in the clinical experiment and reviewed the manuscript.

Davies A.G., Kengyelics S.M, and Gislason-Lee A.J. "Image quality based x-ray dose control in cardiac imaging" In: Egiazarian K.O., Sgaian S.S. and Gotchev A.P. (Eds.), Image processing: Algorithms and systems XIII, volume 9399:81-88. International Society for Optics and Photonics, SPIE, 2015.

I set the research aims, designed the practical and computer simulation experiments, undertook the experimentation, analysed the results, and prepared the manuscript. Drs Kengyelics and Gislason-Lee assisted in the practical experiments, and reviewed and contributed to the manuscript.

Acknowledgements

I am extremely grateful to my friend and colleague of the last 20 years, Professor Mohan Sivananthan, who tragically died a few months before this thesis was completed. It was my collaboration with Mohan that led me to concentrate my research on cardiac imaging, and there is no doubt that the work presented in this thesis could not have been performed without his skill, academic abilities, enthusiasm, direction of the clinical team, and resources he was able to contribute.

I am very grateful for the understanding and support of my family, especially my wife, Sarah, and children Georgia, Anna and Abbey for the considerable amount of time I have spent working on this research into evenings and weekends rather than being with them.

I would like to thank my supervisors, in particular Dr Laura Treadgold, for her most valuable input, and endless encouragement. I am grateful too to Professor David Buckley for his helpful feedback, and also Dr John Kotre and Dr Steven Sourbron for their contributions. A number of my colleagues at the University, past and present, have been actively involved in this work, including Dr Arnold Cowen, Dr Stephen Kengyelics, Dr Amber Gislason-Lee and Dr Claire Keeble. My clinical collaborators, including Dr David Barmby, Dr Seth Vijayan, Ms Janet Moore, Mr Michael Lupton and Mr Chris Wilkinson, and the numerous radiographers, cardiac physiologists and other staff of the catheterisation laboratories at Leeds have input a lot of hard work, not infrequently at unsociable times. Seth, in particular, worked tirelessly on the clinical study under challenging circumstances. Without the assistance of Philips Healthcare for input into Chapters 3 and 4 and providing the data capture devices and implementing modifications used in the rest of the thesis, notably Dr Eric von Reth, Mr Tom Bruijns, Mr Kevin Drake and others, the changes required to the X-ray systems to enable this work could not have been achieved. Finally I would like to acknowledge my colleagues who freed me of many of my teaching responsibilities to allow this thesis to finally be completed—Mr Voyin Pantic, Dr Paul Baxter, Dr Ted Killan, and Dr Stephen Kengyelics. Finally, I am grateful to the patients and the medical professionals that volunteered to participate in this research.

Abstract

X-ray imaging plays a key role in the diagnosis and treatment of coronary heart disease. X-ray imaging is currently used to provide anatomical information regarding vessel lumen, identifying the stenotic lesions (narrowings of the artery) caused by coronary disease. However, appearance of a stenosis on X-ray imaging does not accurately predict the extent which it restricts the flow of blood in the vessel. Other physiological measurements are available in the catheterisation laboratory to supplement the X-ray imaging, but these do not fully describe the coronary haemodynamics. This thesis presents a method of using X-ray angiography to measure the absolute flow of blood in the coronary arteries. A method of calibrating the differential signal in an X-ray angiogram produced per unit volume of contrast agent is described. Using the calibration, a second injection of contrast agent, where all of the blood in one of the coronary arteries is replaced by contrast agent, allowed the flow of contrast agent, which was assumed to be the same as the flow of blood, to be calculated. Steps were taken to reduce the radiation dose delivered by the flow measurement imaging, and to overcome the motion of the heart within the computer analysis. Testing was performed in phantoms to validate the technique before a trial in humans. The phantom experiments indicated that the X-ray flow measurements were accurate and reproducible. The human trial indicated a moderate correlation between the X-ray flow and reference thermodilution flow measurements, although the lack of a dedicated infusion catheter may have affected the accuracy of the refernce measurements. The X-ray flow measurements were on average 25% lower than the reference. The results demonstrate that the X-ray measurement of flow can be integrated into the clinical routine in the catheterisation laboratory, although further clinical testing is required.

Contents

List of Figures

List of Tables

List of Abbreviations

ABC	automatic brightness control
ACS	acute coronary syndrome
ADC	automatic dose control
ALARA	as low as reasonably achievable
BMF	blood mimicking fluid
BMI	body mass index
bpm	beats per minute
CAD	coronary artery disease
CFD	computational fluid dynamic
CFR	coronary flow reserve
CHD	coronary heart disease
CMR	cardiac magnetic resonance imaging
CoV	coefficient of variation
CSV	comma separated values
CT	computed tomography
Cx	(left) circumflex artery
DAP	dose area product
DICOM	Digital Imaging and Communications in Medicine
DSA	digital subtraction angiography
EAK	entrance air kerma
ECG	electrocardiogram
ESD	entrance surface dose

FD	flat-panel detector
FFR	fractional flow reserve
FMD	flow moderated dilatation
fps	frames per second
GUI	graphical user interface
HMR	hyperemic myocardial resistance
HSR	hypereamic stenotic resistance
iFR	instantaneous wave free ratio
IMR	index of microvascular resistance
IVUS	intravascular ultrasound
Kerma	kinetic energy released in the medium
LAD	left anterior descending (coronary) artery
LAO	left anteroir oblique
LCA	left coronary artery
LUT	look up table
LVEF	left ventricular ejection fraction
mAs	X-ray tube current-pulse duration product in milli-Ampere-seconds
MBG	myocardial blush grade
MI	myocardial infarction
MRI	magnetic resonance imaging
MTF	modulation transfer function
MVO	microvascular obstruction
NHS	National Health Service
NSTEMI	non-ST-elevation myocardial infarction
OCT	optical coherence tomography
PA	posterior-anterior
PACS	picture archive and communication system

PCI	percutaneous coronary intervention
PET	positron emission tomography
PMMA	polymethyl methacrylate
QCA	quantitative coronary angiography
QFR	quantitative flow reserve
RAO	right anterior oblique
RCA	right coronary artery
RCFR	relative coronary flow reserve
ROI	region of interest
SID	source-to-image distance
SNR	signal-to-noise ratio
SOD	source-to-object distance
SPECT	single photon emission computed tomography
SPR	scatter-to-primary ratio
STEMI	ST-elevation myocardial infarction
TIC	time intensity curve
TIMI	thrombolysis in myocardiac infarction
TMBG	TIMI myocardial blush grade

Chapter 1

Introduction

Coronary artery disease (CAD) is the leading cause of death worldwide.[1] It accounted for 28% of deaths in the UK in 2014, and for and over 20 million in-patient episodes in the National Health Service (NHS) in 2012–13.[2] Myocardial infarction (MI) due to CAD has an event rate of 120 per 100,000 population in the UK in 2010.[3] Whilst the incidence and mortality rate for MI in the UK has been declining, partly due to improved diagnosis and treatment of CAD and MI, it remains a major cause of death and is a significant health burden.[3] In the United States in 2013, the situation was similar, and whilst mortality from coronary heart disease (CHD) is decreasing, its prevalence is increasing, and expected to further increase in the future.[4]

X-ray imaging is used in the diagnosis and treatment of CAD, using dedicated cardiac X-ray systems which are installed in dedicated rooms known as catheterisation laboratories. Exposure to the body by ionising radiation is harmful. It is important to ensure that for patients undergoing X-ray imaging, the benefits of the imaging outweigh the risks involved, and that the amount of ionising radiation is minimised. Blood vessels are not normally visible on X-ray images, as the X-ray attenuation properties of blood are very similar to those of the surrounding soft tissue. To visualise the cardiovascular system a technique called angiography is used, where a radio-opaque contrast agent is injected into the blood stream, creating a differential attenuation between the contrast agent and the surrounding tissue, permitting the passage of the contrast agent through a structure of interest to be observed in the X-ray image. An example image from a coronary angiogram is shown in Figure 1.1, where the right coronary artery has been injected with a contrast agent, and two severe constrictions, called

stenoses, in the vessel are revealed, along with diffuse narrowings in the mid-section of the artery which have been caused by CAD. Currently, X-ray imaging only provides anatomical information regarding the arterial lumen, and this is not a good predictor of how much the flow of blood is affected by the disease.[5] Having a complete assessment of how a stenosis is affecting the flow of blood down a coronary artery—and how other factors are affecting blood flow (such as resistance in the heart muscle itself)—allows for more tailored and effective treatments to be selected improving patient outcomes. For this reason, a range of other physiological measurements can be performed in the catheterisation laboratory, but to date, no combination of imaging or measurement provides a complete assessment of the coronary haemodynamics.

The focus of this research was to develop methods using X-ray angiography to provide quantitative information on the flow of blood through the coronary arteries; in other words, to quantify the blood flow along the artery in absolute units. This information would complement the anatomical information from the existing angiograms, and other physiological measurements that can be obtained in the catheterisation laboratory. It is hoped that this information ultimately would provide a more complete understanding of an individual's haemodynamics status, facilitating more personalised treatment.

The methods developed in this thesis combine changes to the acquisition protocols on an X-ray system, and the computer analysis of the signals provoked in the X-ray image by the contrast agent, with the aim of analysing the change in mass of contrast agent within the image sequence over time. As the mass of contrast agent can be related to its volume, measuring the change in mass permits the flow within a coronary artery to be calculated. A number of key challenges were overcome to translate such signal changes into measurements of blood flow. During coronary angiography the heart moves, and there is potentially other patient motion principally from respiratory motion. These movements alter the signal intensity in the image, and it is important that these alterations are not of sufficient magnitude to adversely affect too many cases. Secondly, the automated processing and control systems on a current cardiac X-ray system would cause the relationship between signal intensity and volume of contrast to change during an angiogram confounding the analysis. X-ray systems do not have calibrated values relating to a physical property for the pixel intensities in their images (such as Hounsfield Units on a computed tomography system which permit analysis such as urinary

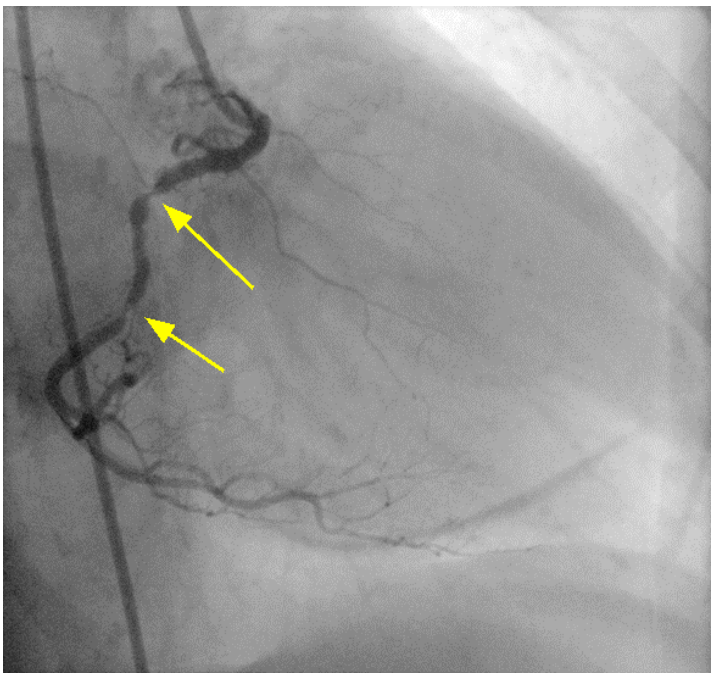

Figure 1.1: Example image from an angiogram of the right coronary artery. The contrast agent has filled the vessel lumen, and the uneven diameter is due to coronary artery disease. Two focal lesions are identified by yellow arrows, and there is diffuse disease between these lesions.

stone composition[6] or electron density for radiotherapy planning[7]). Furthermore, the two dimensional projection nature of the images means that the same volume of contrast agent in a blood vessel can provoke a different degree of change in signal intensity in an image depending upon the other objects in the beam as well as the location and orientation of the objects and vessel. A calibration relating pixel intensity change to mass of contrast agent on a per-patient basis was therefore developed. The technique must be straight forward to implement in the clinical environment, and minimise the risk of harm to the patient, for example by keeping the use of ionising radiation to a minimum. The computer analysis of the image sequences must be automated in so far as possible, so it can be ultimately integrated into a patient's procedure.

1.1 Aims

The aim of this research was to develop a quantitative X-ray imaging technique to measure the flow of blood in the coronary arteries of the human heart that can be easily implemented in clinical practice during invasive angiography, and to assess the accuracy and precision of

the flow measurements.

1.2 Overview of thesis

Following a review of X-ray coronary imaging and the other physiological measurements in the catheterisation laboratory, three studies are described which developed enabling techniques leading to an absolute flow measurement, viz. a means of acquiring the quantitative images at a lower X-ray dose than standard imaging, a means of analysing contrast agent flow in the moving heart by removing signals from the background anatomy, and combining these to measure relative flow between two angiograms. The relative flow method was then expanded to measure absolute flow in a coronary artery, with the new method then being tested first in phantoms, and then in humans. The thesis chapters are summarised below.

Chapter 2, Background briefly explores how the flow of blood is regulated in the normal heart, and how coronary artery disease affects this. An overview of the principles of X-ray angiography describes the issues of using a projection X-ray imaging system for the measurement of blood flow. A review of the physiological measurements available within the catheterisation laboratory, along with previous attempts at flow quantification with X-ray imaging, and their limitations, is provided.

Chapter 3, Reduction of radiation dose in coronary angiography describes an experiment designed to produce an means of producing angiograms at a lower X-ray dose to the patient. The lower radiation dose mode was designed to reduce the additional radiation patients would receive from the additional quantitative image sequences would be exposed to without compromising the quality of the images.

Chapter 4, Cardiac digital subtraction angiography investigates the use of a image subtraction technique aimed at removing the background anatomy from coronary angiograms. Removing the background anatomy from the image leaves just contrast agent, facilitating the analysis of the signals arising from the contrast agent. The cardiac motion and other patient motion can defeat such schemes due to misregistration artefacts, and the efficacy of algorithms aimed at minimising such artefacts was tested.

Chapter 5, Relative flow measurement using X-ray angiography describes work that

measures a relative flow—the change in flow following intervention by stenting—in a small patient study. The ability to measure relative flow between two angiograms was a stepping stone to absolute flow quantification.

Chapter 6, Absolute measurements of flow using X-ray imaging: Theory extends the relative flow method, describing the theory underpinning an absolute measurement of blood flow using angiography, using a method that can be employed into clinical practice.

Chapter 7, In vitro measurements of flow from X-ray angiography details testing of accuracy and precision of the absolute measure of blood flow using X-ray angiography in a series of phantom experiments.

Chapter 8, In vivo measurements of flow describes the additional procedural and analytical steps required to implement the absolute flow measurements in humans, and describes a preliminary study comparing the X-ray based flow measurements to reference flow measurements in humans.

Chapter 9, Summary, Discussion & Conclusions are presented and future work are discussed.

Chapter 2

Background

This chapter provides a brief overview of the factors affecting the flow of blood in the coronary arteries, and coronary heart disease. The principles of X-ray imaging and angiography of the heart are described, and the role of X-ray imaging in CAD is explored. An account of the invasive physiological measurements available within the catheterisation laboratory, and their limitations, is then presented. This is followed by an appraisal of the quantitative methods of describing coronary blood flow from angiography that have been previously developed. Finally these findings are used to make the case for the measurement of absolute blood flow within the catheterisation laboratory that can be successfully implemented in the clinical routine.

2.1 Coronary blood flow in the human heart

2.1.1 Coronary anatomy

The coronary arteries supply the heart muscle, the myocardium, with oxygenated blood. There are two arteries—the left coronary artery (LCA) and the right coronary artery (RCA), which originate from the aortic root. The arteries and their location are shown in Figure 2.1. These epicardial vessels are between 500 μm to 5 mm in diameter. Branching from the coronary arteries the pre-arterioles have a diameter of between 500–100 μm. Further distal are the arterioles, which have a diameter of less than 100 μm.

The left coronary artery branches after a short left main stem into the (left) circumflex artery (Cx) and left anterior descending (coronary) artery (LAD). The coronary arteries supply different regions of myocardium, with the LCA supplying the anterior and anteriolateral

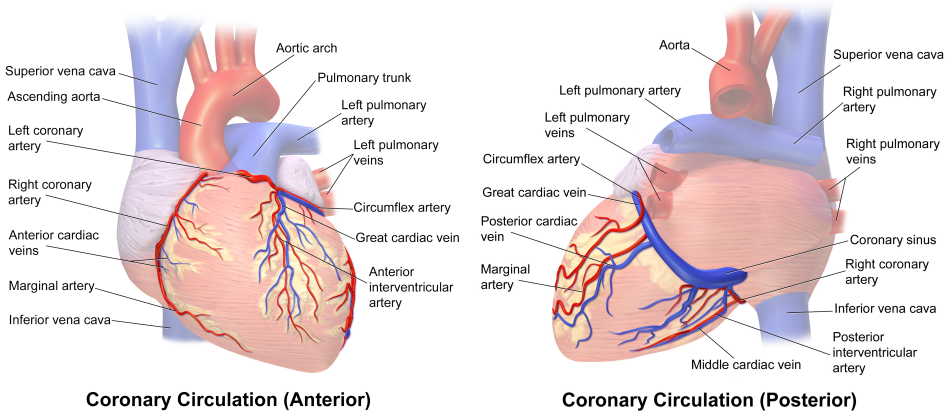

(a) Anterior view (b) Posterior view

Figure 2.1: Anatomy of the heart demonstrating the coronary arteries and veins, showing the a) anterior and b) posterior view. Created by Blausen Medical Communications, released under CC-BY license.[8]

regions (broadly corresponding to the left atrium and left ventricle) and the RCA supplying the posterior and inferior territories (broadly corresponding to the right atrium and right ventricle).

2.1.2 Control of coronary blood flow

The myocardium has the capacity to extract considerable amounts of oxygen from the blood (60%–80%), and therefore any increase in demand on the heart, which will result in an increased demand for oxygen by the myocardium, must be met with in an increase in coronary blood flow.[9] At perfusion pressures of between 40 and 150 mm Hg, the control of blood flow to the myocardium is governed by an autoregulation system. Under normal conditions the blood flow to the myocardium is regulated in line with the oxygen demand of the myocardium.[10] Curve A on Figure 2.2 shows how the flow of blood is maintained at a relatively constant level over the normal physiological range of aortic pressures. In the absence of disease, the epicardial arteries have very low resistance to blood flow, and therefore there is a negligible pressure drop along their length. The flow of blood is controlled by the interplay of two mechanisms in the prearterioles and arterioles. There is a measurable pressure drop across the pre-arterioles, and they function to maintain the pressure at the entrance of the arterioles within a narrow range. Overall, the resistance to blood flow is dominated by the arterioles. This is achieved via constriction in response to increased sheer wall stress.[11] The smaller arterioles respond to changes in oxygen demand, dilating in response to the release of metabolites

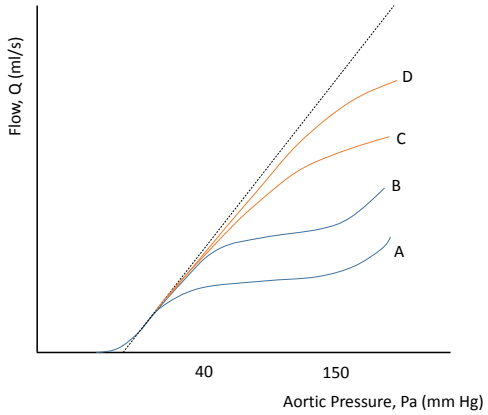

Figure 2.2: Autoregulation of blood flow in the coronary arteries. At rest, blood flow is kept reasonably constant over a large range of aortic pressures (A). An increase in oxygen demand in the myocardium will result in a raised level of flow (B). At maximal flow (hyperaemia, dotted line) flow is dependent upon the aortic pressure. Epicardial stenoses reduce flow (C & D).

in the myocardium during oxygen consumption.

An increased oxygen demand in the myocardium will initially result in a dilation of the smaller arterioles (25–45 μm) due to the release of metabolites such as adenosine.[12] The metabolites and myogenic actions also increase flow in the larger arterioles (50–80 μm in diameter). This increases myocardial blood flow and causes a reduction in the pressure at the inlet of the smaller arterioles. The prearterioloes and smaller arteries react to the drop in shear stress caused by the reduction in pressure, via endothelial-dependent dilation. The net effect is an overall drop in resistance and an increase in coronary blood flow (curve B, Figure 2.2).

At the point of maximal blood flow in the coronary arteries (hyperaemia), the resistance to flow in the prearterioles and arterioles is minimised, and in a normal heart the supply of blood will be sufficient to meet demand. In this case the flow of blood is dictated by the aortic pressure (dotted line, Figure 2.2). The maximal flow is reduced by either CAD causing a flow limiting stenosis, or increased microvascular resistance.[13] Curves D and C in figure 2.2 represent increasing epicardial stenosis, with the more severe stenosis producing a greater reduction in maximal flow. If there is a sufficient reduction in flow, this will lead to ischaemia in the myocardium.

2.1.3 Coronary artery disease

CAD develops due to the growth of atherosclerotic lesions (plaque) in one or more of the coronary arteries. As the plaque lesions increase in size, the arterial lumen is progressively reduced, which if severe enough, will restrict the blood flow within the artery, particularly during periods of high demand on the heart, for example during exercise. Multiple consecutive stenoses in an artery, or diffuse disease along a considerable length of artery, can be flow-limiting with lower levels of luminal loss. CAD leads to CHD (although the two terms are often used interchangeably), and can result in heart failure or myocardial ischaemia. The symptoms include angina pectoris—chest discomfort associated with myocardial ischaemia.[14]

An acute presentation of CAD, acute coronary syndrome (ACS), is caused by the rupture or fissuring of a atherosclorotic plaque, leading to thrombus developing around the rupture site, severely limiting blood flow to the myocardium in the affected vessel. ACS can be categorised as unstable angina (angina which is not triggered by a specific event, such as exercise) and MI. MI is further divided into two categories based upon the changes in the electrocardiogram (ECG), namely non-ST-elevation myocardial infarction (NSTEMI) and ST-elevation myocardial infarction (STEMI).[15] In recent years in the UK there has been a decline in mortality due to acute MI, in part due to reduced incidence and in part due to improved treatment. Despite this, MI remains a major cause of death, with mortality rates of 39.2 and 17.7 per 100 000 population for men and women respectively in the UK in 2010.[3]

2.2 X-ray imaging in coronary heart disease

Cardiac X-ray systems are installed in specialist X-ray rooms called catheterisation laboratories, and have a number of key differences to other types of X-ray system. Cardiac X-ray systems employ one or two imaging chains, i.e. have either one or two pairs of X-ray tube and image detector (referred to as monoplane and biplane systems respectively). A photograph of a monoplane catheterisation laboratory is shown in Figure 2.3. The X-ray tube and image receptor are attached to opposite ends of a C-arm, which can be rotated in both the lateral and cranio-caudal directions, allowing the X-ray beam to be rotated in two directions independently around the patient, who lies supine on a couch. This arrangement permits imaging to be performed from a wide range of angles to suit the current task, and the X-ray beam

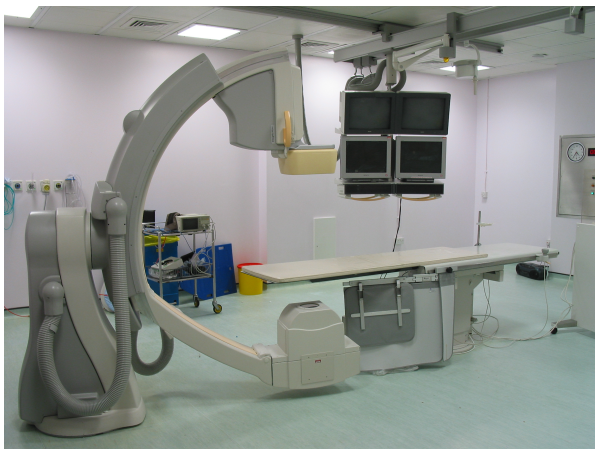

Figure 2.3: Cardiac catheterisation laboratory (Allura FD10, Philips Healthcare, The Netherlands) showing the floor mounted C-arm assembly with the X-ray detector at the top and X-ray tube assembly at the bottom, the patient couch and remote viewing monitors.

angulation is frequently changed during a procedure. The X-ray tube and generator have a high output (typically around 70 kW), and a dedicated solid-state cardiac X-ray detector which has a relatively small area (around a 25 cm diagonal size), suited to the imaging of the heart. This small detector size is advantageous when positioning the X-ray detector close to the patient.

Two modes of imaging are available, *fluoroscopy* and *digital cine acquisition*. Fluoroscopy uses a lower radiation dose and is used to position the patient and radiation beam, and to visualise interventional devices inside the patient such as catheters, wires, and stents. As a result of the lower radiation dose used in fluoroscopy (normally around a tenth of the acquisition dose rates),[16] fluoroscopy provides a lower quality image than the acquisition mode. Fluoroscopy images are generally not recorded. Digital acquisition provides a higher quality image, and is typically reserved for angiography with the images being stored as a record of the procedure. Both imaging modes employ pulsed acquisition, i.e. the X-ray beam is rapidly switched off and on, with the number of pulses per second either being controlled by the user or programmed into the settings of the X-ray system. The term pulses, frames or images to refer to individual X-ray exposures, are used interchangeably. Typically in cardiac imaging frame rates of 15 to 30 frames per second (fps) are used.

2.2.1 Angiography

Angiography—the process of visualising the arterial system—was first performed by Egas Moniz in the 1920s, who described the acquisition of cerebral angiograms via the injection of a contrast agent into the common carotid artery.[17] The development of catheterisation allowed both physiological measurements, such as intra-arterial pressure, and the injection of contrast agent directly within the artery of interest (so called selective angiography). The catheterisation of the human heart was first performed by Werner Forssmann (on himself) in 1929. Forssmann later demonstrated that the chambers of the heart could be visualised using injections of contrast into the chamber via a catheter in animal experiments.[18] The use of catheters to inject directly into the artery of interest greatly increases the concentration of contrast agent in the artery, compared to an injection at a more remote location (either further upstream in the arterial system or into the venous system), where the contrast will mix into the blood, becoming diluted at the site of interest. The amount of contrast required is therefore reduced, the timing of the imaging with respect to the injection simplified, and the quality of the images produced is greatly increased.

The first selective coronary angiogram was performed accidentally in 1958 by Mason Sones. Sones had been intending to inject the contrast agent into the aortic root, as it was believed that a direct injection of contrast into a coronary artery could be fatal. However, just prior to the contrast injection and unnoticed by Sones, the catheter had become engaged with the patient's right coronary artery resulting in the injection of contrast directly into the RCA. The ensuing asystole was corrected by asking the patient to cough.[19] Encouraged, Sones and colleagues proceeded to demonstrate the improved quality and relative safety of selective coronary angiography.[20] The angiographic technique was refined in the following years, notably with safer access to the femoral artery using the Seldinger technique,[21] and improved catheter designs by Judkins and Amplatz.[19]

Today, coronary angiograms are performed with selective catheterisation of the left or right coronary artery, with access from either the radial or femoral artery. Images are acquired at high frame rates (typically 15–30 frames per second), with the X-ray acquisition starting just prior to the commencement of the contrast injection. Imaging continues while the artery fills with contrast agent, and is normally terminated around two heart beats after the vessels are filled with contrast completely. As a result, the total duration of a typical coronary angiogram

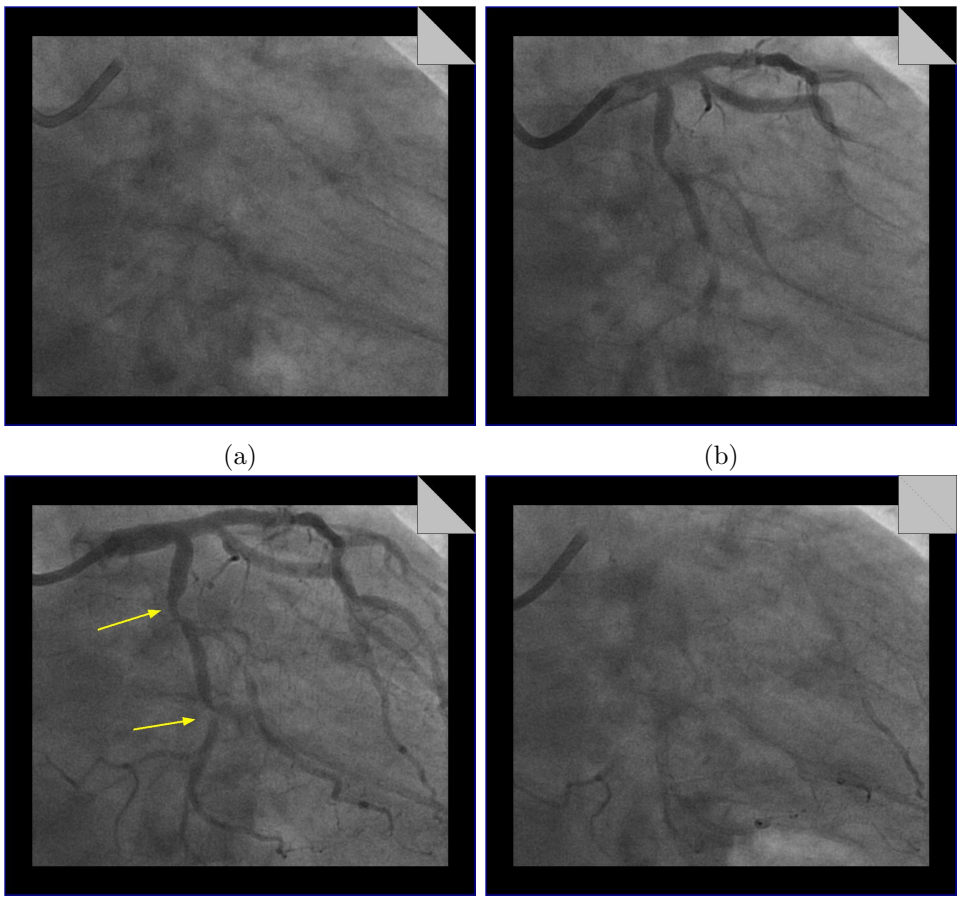

(a) (b)

(c) (d)

Figure 2.4: Images from a posterio-anterior caudal angiogram of the left coronary artery showing the transit of contrast agent through the vessel: a) immediately before contrast injection, b) the contrast agent has reach the mid artery segments, c) the entire arterial lumen is filled, and d) demonstrates venous outflow. Arrows on c show the location of two stenotic lesions in the circumflex artery.

is between six and 10 seconds. Longer sequences are sometimes acquired to visualise the contrast as it transits the myocardium and into the venous system. Imaging the moving heart requires not only a high frame rate, but also short X-ray pulse durations, typically between three and 12 ms to avoid motion blurring of the small arteries. Example images from an angiogram of a left coronary artery can be seen in Figure 2.4. The presence of CAD can be detected via the luminal loss caused by the atherosclerotic plaque. Two severe stenotic lesions can be seen in the circumflex artery in 2.4c. It is standard practice to take views of an artery from a number of projections, depending on the artery and segment of interest.[22]

2.2.2 Percutaneous coronary intervention

In addition to the diagnosis of CAD using angiography, X-ray imaging can also be used to treat the disease, in a process referred to as percutaneous coronary intervention (PCI). Low radiation dose X-ray imaging (fluoroscopy) permits the visualisation of interventional devices as they are manipulated within the coronary arteries. Angioplasty—the process of restoring the vessel lumen of a stenotic lesion—was first described by Dotter & Judkins in 1964,[23] but Gruntzig's invention in 1977 of a balloon which could be passed over a guide wire and expanded within an artery was a considerable advance.[24] The technique was prone to early onset restenosis. The development of the stent—an expandable semi rigid support structure commonly made of metal—reduced restenosis rates.[25] The first human use of a stent was in 1986 and since then, refined materials and stent coatings (including drug eluting stents), have improved outcomes, further reducing in-stent restenosis.[26]

During PCI, once a series of angiograms has been acquired and a suspect lesion or lesions identified, a guide wire is introduced via the guide catheter and advanced down the vessel to be treated so that it crosses the lesion, leaving its tip in a distal segment of the artery. The guide wire has a radio-opaque end to allow it to be clearly seen under fluoroscopy. Figure 2.5a shows the guide wire in position for the treatment of the stenoses shown in Figure 2.4. Often a balloon is introduced over the wire to the site of stenosis and angioplasty is performed before stenting. Figure 2.5b shows the balloon dilation on the proximal lesion. The two radio-opaque markers denoting the ends of the balloon can be clearly seen in the image, and these are visible even when the balloon is deflated, allowing it to be positioned accurately in the artery using fluoroscopy. Sometimes, however, this pre-stenting dilation is omitted and direct stenting is performed (i.e. without pre-ballooning). Stents are introduced over the guide wire, and as in the case with the balloon, radio-opaque markers on the extremities of the stent allow a stent to be accurately positioned at the lesion site prior to deployment. The placement of stents to both lesions in the example case is shown in Figure 2.6. Angiography is then performed to confirm the restoration of vessel lumen and to check that the stent is well apposed to the vessel wall (Figure 2.7).

The decision as to whether or not to stent a suspect lesion is important—stenting carries an inherent risk of complication, such as vessel rupture, dissection, sub-acute thrombosis and branch occlusion.[27] As a result, if intervention is performed unnecessarily, it can make the

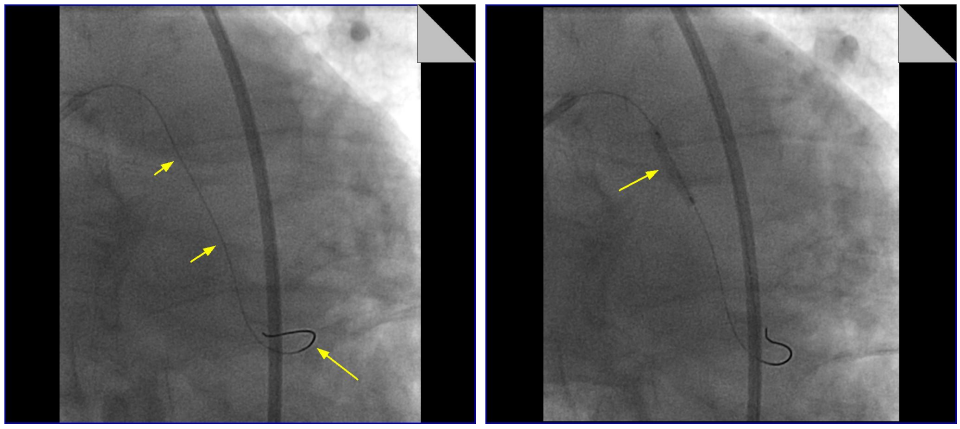

(a) (b)

Figure 2.5: Images taken during angioplasty, with arrows showing a the guide wire in situ in the circumflex artery, and b) balloon inflation being performed to the proximal stenotic lesion. The large horizontal tube in both frames is the guide catheter in the descending aorta.

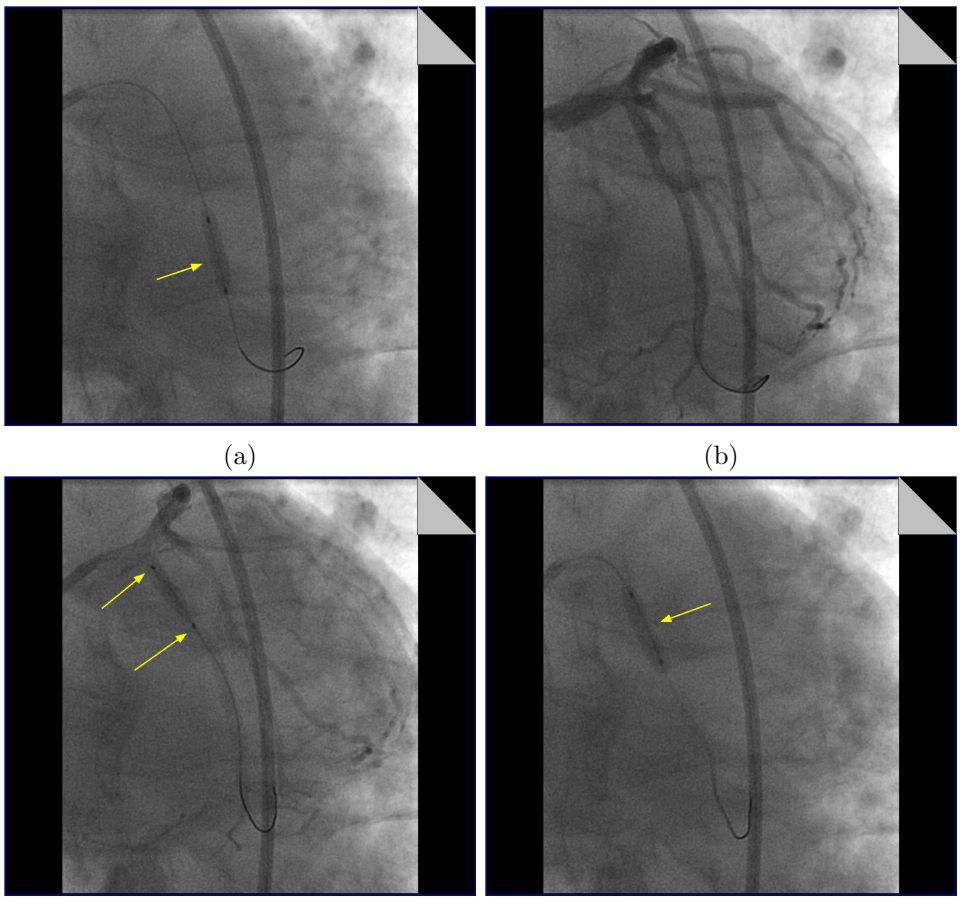

(a) (b)

(c) (d)

Figure 2.6: Images showing the stent placement: a) shows the deployment of the distal stent with the balloon indicated with an arrow, followed by b) an angiogram to confirm good deployment. Image c) shows the placement of the proximal stent using angiography with the radio-opaque markers indicated with arrows, and d) the stent deployment, again with the balloon position indicated by an arrow.

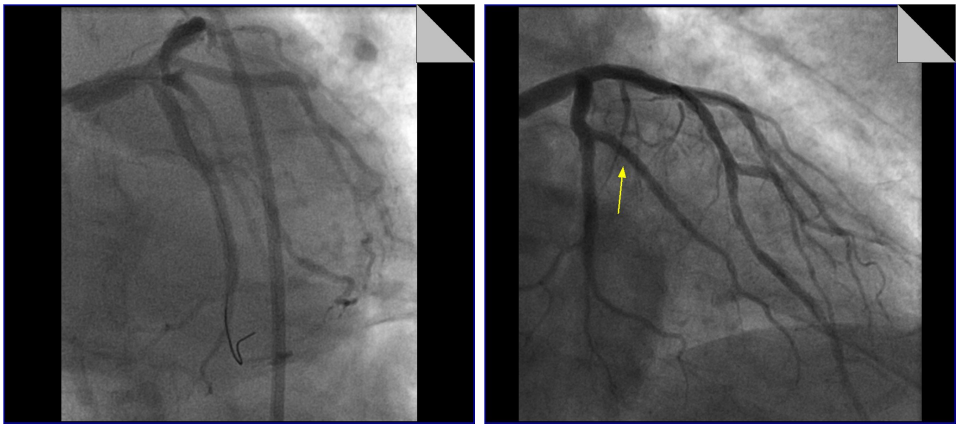

(a) (b)

Figure 2.7: Post intervention angiograms, showing the angiographic result a) after the stenting to the Cx and b) following further stenting in the obtuse marginal artery (site indicated by an arrow).

outcome for a patient worse than if no intervention were performed.

2.2.3 The role of X-ray imaging in the clinical setting

The methods employed in the diagnosis of CAD are varied according to a patient's underlying risk of having the disease. Risk factors for CAD include family history,[28] sex, smoking, diabetes, hyperlipidaemia, hypertension and age.[29,30] A wide range of imaging and non-imaging tests (such as biomarker assessment and exercise stress tests) are available to inform diagnosis. In cases with recent onset of chest pain, imaging options include stress echocardiography, magnetic resonance imaging (MRI) for wall motion analysis, and cardiac-computed tomography (CT).[31] These patients are likely to have a lower risk of CAD, and are therefore less likely to require PCI, and hence the preference for non-invasive testing. X-ray imaging plays an important role in the diagnosis and treatment of CAD in the high-risk and acute patient groups. More invasive treatments aim to provide revascularisation, i.e. the restoration of blood flow to the myocardium.[32,33] In cases of stable angina, whose symptoms are not sufficiently controlled by medical therapy, invasive angiography should be offered.[33] In unstable angina and NSTEMI, urgent invasive coronary angiography with follow on PCI, if appropriate, should be offered.[34] In acute coronary syndrome, specifically ST-elevation myocardial infarction, primary PCI is recommended where it can be delivered in a timely manner.[35] In the UK during 2016, there were 119 centres offering PCI, with a further 57 offering invasive angiography with 260,808 angiograms and 100,483 PCIs performed. The number of PCIs

rose quickly between 1995 and 2005, and whilst the rate of increase had reduced, it was still increasing; the rate of increase was 2.3% in 2016. The rate of PCI in the UK, at the time of writing, is approximately 1,500 per million population.[36]

In these patients with ACS, and in particular STEMI, the requirement for rapid restoration of myocardial blood supply precludes the use of many of the alternative imaging techniques, such as cardiac magnetic resonance imaging (CMR) or CT. Primary PCI has reduced mortality compared to fibrinolysis in STEMI patients, and outcomes are better when the time between first medical contact and treatment is minimised. There is also recent evidence supporting the use of primary PCI, even if it is delayed,[37] indicating that X-ray imaging will continue to have an important role in the treatment of STEMI. Even for patients with stable angina, PCI can lead to a reduction in symptoms compared to medical therapy, even if mortality is not reduced.[38]

Whilst mortality from MI is falling, an ageing population and improved health care outcomes, is increasing the number of patients with multi-morbidity,[39,40] resulting in more complex patient management. The strategy employed during intervention has an effect on patient outcome (for example with complete revascularisation resulting in better outcomes than treating the infarct related lesion only in STEMI[41]), and therefore, being able to refine treatment for patients based on their individual needs will further improve patient care.

2.2.4 Contrast agents for coronary angiography

For cardiac angiography, current contrast agents utilise iodine as a radio-opaque agent, producing a negative contrast (i.e. areas of the image with a lower signal intensity due to the increased X-ray attenuation of the contrast agent). In addition to providing high radiographic contrast, contrast agents should have minimal affect on the blood flow, have low incidence of side effects, low toxicity and high bio-compatibility (readily soluble, appropriate pH, iso-osmolar with blood and readily excreted).

Iodine in solution, such as sodium iodide, was used as an early X-ray imaging agent, but is toxic to humans. Current contrast agents ensure that the iodine remains covalently bound to a non-toxic molecule whilst within the body. Early versions of these contrast agents were ionic, and therefore more likely to interact with biological molecules.[42] In clinical practice, these have now been superseded by non-ionic compounds. The properties of the compounds used for

contrast agents varies. An example of a current non-ionic contrast agent, iohexol (trade name Omnipaque), is shown in Figure 2.8a. Iohexol has three iodine atoms attached to a single benzine ring. As a comparison, iodixanol (trade name Visipaque) has a structure with two linked iodinated rings (see Figure 2.8b), increasing the amount of iodine per molecule and thus reducing the osmolarity of the contrast agent, although this comes at the expense of an increase in viscosity. The physical properties of iohexol and iodixanol at concentrations recommended for coronary angiography are compared in Table 2.1. For reference the osmolarity of blood is 290 mOsmoles per kg water (so it can be seen that iodixanol is isomolar with blood).[43] The viscosity of blood depends upon haematocrit level, temperature and shear rate, and a viscosity in the range of 3.5 to 6 cP would be expected.[44]

Reactions and side effects from contrast agents include hypersensitivity reactions, contrast induced acute kidney injury, cardiovascular adverse reactions (arrhythmia, hypotension, shock and cardiac arrest), extravasation leading to tissue necrosis and/or compartment syndrome, and severe cutaneous reactions. Patients with certain other conditions including hyperparathyroidism, sickle cell disease and patients with phyrochromocytoma can have reactions relating to their disease. Many of the adverse reactions are relatively minor (such as nausea, headache, and dizziness) although a number are life threatening or fatal. The risks of serious complications are relatively low, with the number of reported deaths between 6.6 per million and 1 in 10,000.[45] There is some variation in the rates of adverse reaction depending on the specific agent used. For example, with iodixanol, adverse reactions occur in around 20% of patients.[46] Iodinated contrast agents are excreted via glomerular filtration, except in people with impaired kidney function, where faecal excretion also plays a minor role. The contrast agent is excreted unchanged.

The risk of injury to the kidneys, one of the more serious side effects, can be reduced by keeping the volume of contrast used during a case to a minimum. This is particularly important in children and in patients with impaired renal function, where the increased and prolonged exposure of the kidney to the contrast increases the risk of injury.[45] In adults, between 3 and 10 ml of contrast is typically injected per coronary angiogram, with the total patient dose not expected to exceed 200 ml.[46]

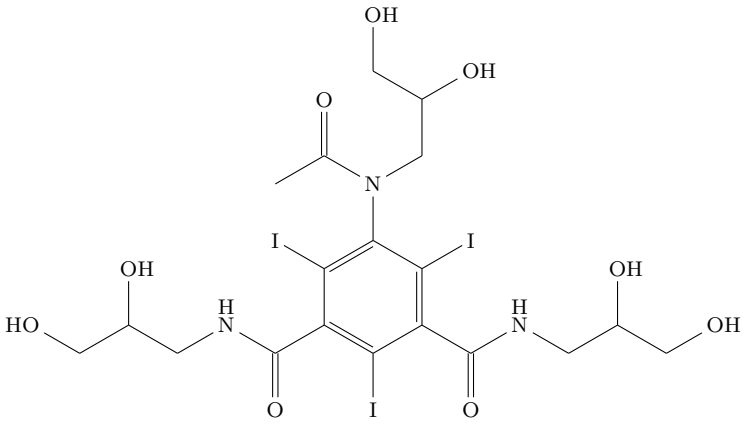

(a) Iohexol

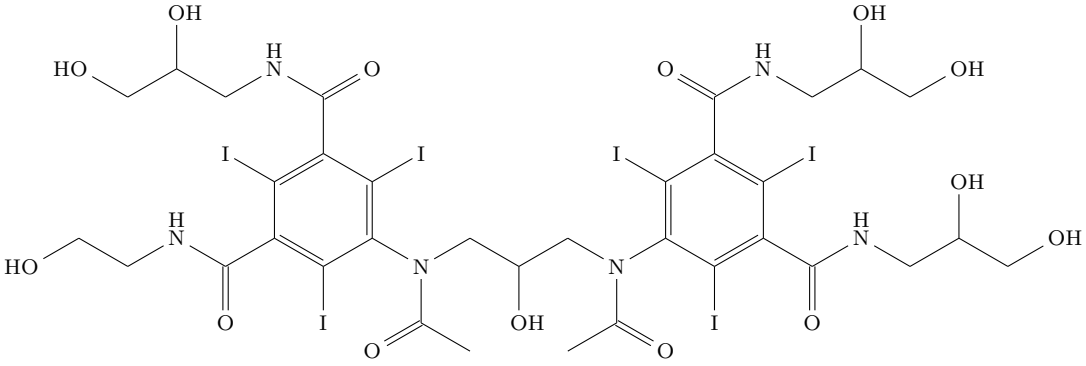

(b) Iodixanol

Figure 2.8: Chemical structures of two common contrast agents, iohexol and iodixanol (trade names Onmipaque and Visipaque respectively).

Contrast agent (concentration in mg I/ml)	Osmolarity (mOsmol/kg water)	Viscosity (cP)	
		20°C	37°C
Iohexol (300)	672	11.8	6.3
Iohexol (350)	844	20.4	10.4
Iodixanol (270)	290	12.7	6.3
Iodixanol (320)	290	26.6	11.8
Blood	290		3.5–6

Table 2.1: Physical properties of two common contrast agents, iohexol and iodixanol, with comparative figures for blood at body temperature.

2.2.5 Fundamentals of X-ray imaging

The X-ray attenuation by an object is classically described by the Lambert-Beer law. If N and N_0 are the number of X-ray photons per unit area with and without the object in the beam respectively, and a mono-energetic X-ray beam is assumed, and only primary radiation considered, then:

$$N = N_0 e^{-\mu t} \tag{2.1}$$

where μ is the linear attenuation coefficient of the material of which the object is comprised, and t is the thickness of material. The linear attenuation coefficient of a given material will vary with the material's composition and density, and in the case of a contrast agent, the attenuation it provides is highly influenced by the concentration of iodine. The density of a material can be accounted for by rewriting equation 2.1 as

$$N = N_0 \exp\left(-\frac{\mu}{\rho}x\right) \tag{2.2}$$

where ρ is the material's density and x the mass thickness, i.e. mass per unit area. μ/ρ is referred to as the mass attenuation coefficient.

Consider a pixel within an image, which has area A_0. Before contrast agent is injected into the field, an exposure is taken, and the pixel value has a value of S_m. If G is the relationship between the number of X-ray photons and the pixel signal intensity, and N_0' the number of photons incident upon the pixel, then

$$S_m = GN_0' \tag{2.3}$$

Contrast medium is injected into field of view, with m_c g of iodine accumulating above the pixel. A second identical exposure is taken. Assuming that the injection of contrast has a negligible effect on the mass of other material in the beam, and given that $x = m_c/A_0$, from 2.2, then the signal level in the contrast image, S_c is given by

$$S_c = GN_0' \exp\left(-\frac{\mu}{\rho}m_c/A_0\right) \tag{2.4}$$

In other words, there is a reduction in the pixel intensity depending upon the mass of iodine in the beam, and attenuation coefficient of iodine. Note that for this relationship to hold, complete replacement of blood is not necessary; if a vessel is only filled partially with contrast then the mass of contrast projected onto a given area will be commensurately less than if there were complete replacement of blood with contrast.

2.2.5.1 Planar projection imaging

The projection nature of an X-ray imaging system results in the same object producing different signals within an image, depending upon its orientation and position within the X-ray beam. Consider an object containing a uniform concentration of contrast agent within the body being imaged with a planar X-ray system. This is depicted in Figure 2.9a. The beam attenuation of the object will create an area of lower signal intensity (shadow) in the recorded image, and from equation 2.1 it can be seen that the differential signal between the object and the surrounding area is given by the linear attenuation of the contrast agent and the beam's path length in traversing the object. Altering the orientation of the object (Figure 2.9b) increases the beam's path length through the object, thereby increasing beam attenuation in the shadow region. The differential signal will be higher, but smaller, in the image (yet the sum of the differential signal values will be the same in both cases). Now consider the scenario where the object is moved in the vertical direction, as shown in Figure 2.9c. In this case the shadow is as intense as in (b) as the projected path lengths are (almost) the same, but the projected shadow will be larger in area than (b).

In addition to the object's orientation and location, the photon fluence on the detector for a given X-ray exposure is also affected by a number of other factors. Photon fluence reduces proportional to the square of the distance between the X-ray source and image receptor, and of course, to the X-ray beam intensity output from the X-ray tube.

2.2.5.2 X-ray attenuation and photon energy

The mass attenuation coefficient for a material depends upon its chemical composition, and is function of photon energy. Figure 2.10 shows the linear attenuation of both iodine based contrast agent (at concentrations of 370 mg I/ml and 150 mg I/ml) and soft tissue (comprised as per the International Commission on Radiation Units and Measurements report 44).[47] All

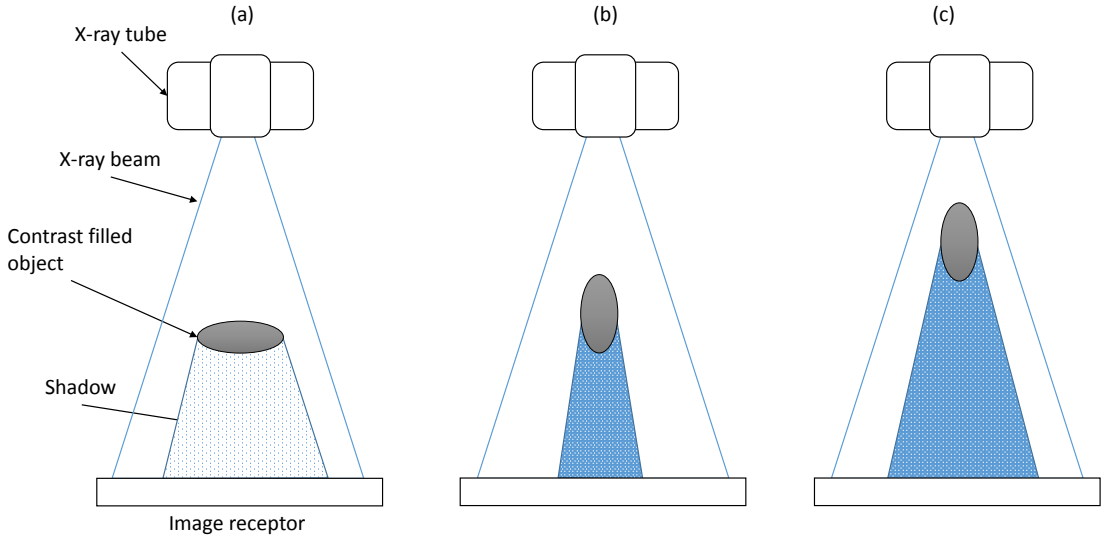

Figure 2.9: The same object will project a different attenuation profile depending upon its orientation (a vs b) or location (b vs c).

attenuation data for the graph were obtained from published tables of X-ray attenuation,[48] with the iodine attenuation scaled according to the required concentrations. The concentrations of contrast agent shown in figure 2.10 are the upper and lower concentrations currently used in clinical practice for angiography, with coronary angiography in adults typically using contrast agents with concentrations of 270–370 mg I/ml. It can be seen that for soft tissue, attenuation increases considerably at lower photon energies. For low photon energies (<20 keV) there is little chance of a photon penetrating more than a few millimetres of soft tissue, and as such is unlikely to contribute to the resultant image, but only to contribute to the radiation dose to the patient. Conversely, higher energy photons are more likely to penetrate a given thickness of soft tissue than lower energy photons, and this gives rise to the effect known as beam hardening.

X-ray tubes have a polyenergetic output, and the profile of the X-ray spectrum is dependent upon the potential difference between the anode and cathode within the X-ray tube, and the filtration in the tube exit port. The the spectrum is further modified by metal beam filters before it reaches the patient. Typically tube voltages in the range of 50–120 kV are used. Figure 2.11 shows a range of X-ray spectra commonly used in cardiac angiography, calculated from published tables of tube output spectra and material linear attenuation coefficients.[48]

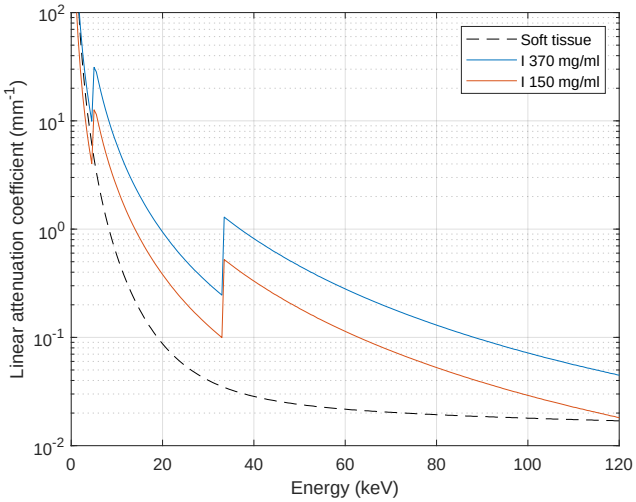

Figure 2.10: Linear attenuation of iodine based contrast agent at two concentrations and soft tissue as a function of photon energy.

All X-ray beams are filtered by the tube exit window, and in medical applications except mammography, further filtration of at least 2-3 mm of Al is also applied, and 2.5 mm of Al has been applied to each of the spectra in figure 2.11a. Additional beam filtration (metal filters used in the tube collimator assembly) have been widely used in fluoroscopy for some time, although they have only recently been introduced during angiography in an attempt to reduce patient skin dose.[49] It can be seen in figures 2.11b and 2.11c that whilst increasing the Cu filtration does indeed remove low energy photons, thus sparing patient skin dose, the combination of higher kV and thicker filter also results in a substantial number of photons above 80 keV and fewer in the 40–60 keV range.

2.2.5.3 Differential signal produced by contrast agent

The subject contrast of an object in an X-ray image is the difference in beam intensities in the shadow of the object in the image to that of an adjacent area relative to the local background. Assuming a linear relationship between X-ray dose and pixel intensity in the captured image, letting B and D be the mean pixel intensity in regions in the background and object's shadow, then the contrast, C, can be calculated as follows:

$$C = \frac{B - D}{B} \tag{2.5}$$

For a given object the subject contrast is increased by increasing the relative attenuation

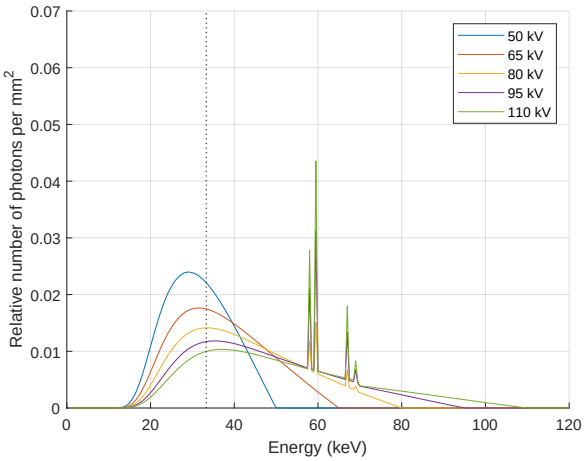

(a) No additional filtration

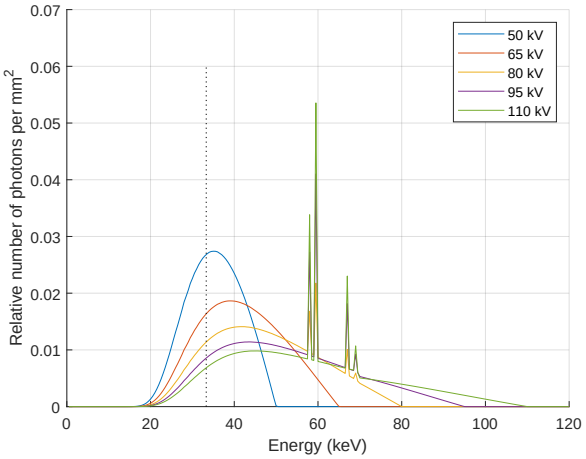

(b) 0.1 mm Cu filtration

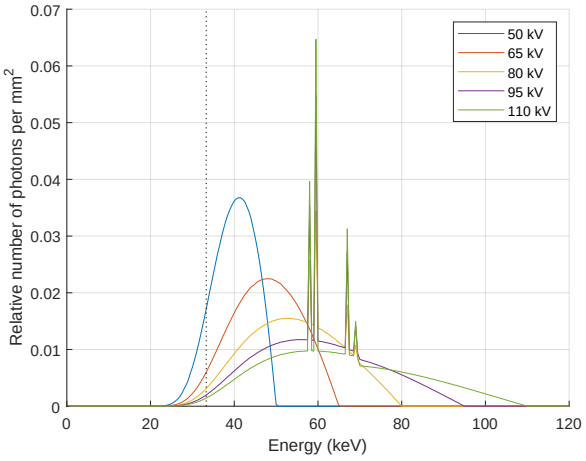

(c) 0.4 mm Cu filtration

Figure 2.11: Common X-ray energy spectra for cardiac angiography, showing a)–c) varying amounts of added beam spectral filtration. The K-absorption edge of iodine is shown by a dotted vertical line. All spectra are shown normalised to the total number of output X-ray photons per mm^2.

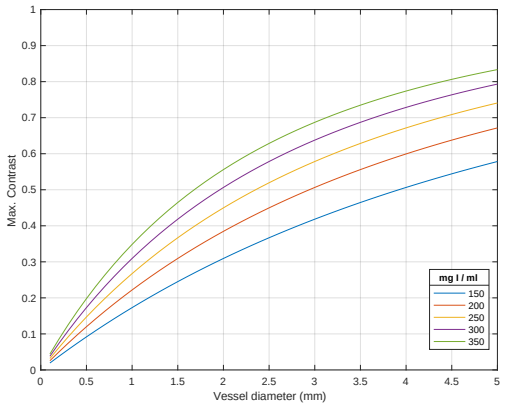

Figure 2.12: The effect of vessel diameter and contrast agent concentration on the contrast of a simulated coronary artery. The artery is simulated superimposed on a 200 mm PMMA phantom using an X-ray beam produced at 75 kVp, 0.1 mm Cu filtration.

of the object compared to the background. It can be seen from eq. 2.1 that the attenuation coefficient and the object's thickness determine the contrast. Figure 2.12 demonstrates the effect of varying vessel thickness and contrast agent concentration (and hence the attenuation coefficient) on the contrast of a simulated vessel. The vessel is simulated against a 200 mm uniform background, imaged at 75 kV with 0.1 mm Cu filtration. Only primary X-ray photons are included in the simulation.

Figure 2.10 shows that the attenuation of iodine has a discontinuity at 33.2 keV, caused by the K-absorption edge of iodine (where the energy of incident X-ray photons is sufficient to dislodge K-shell electrons via photoelectric absorption). The energy range from above the K-absorption edge through to approximately 80 keV offers the greatest differential attenuation between the contrast agent and soft tissue. By referring back to figure 2.11c, it can be seen that a choice of 50–60 kV with 0.4 mm Cu filtration produces many X-ray photons in the energy range where a high attenuation for contrast agent would be expected, but the beam would lack penetration, and for larger patients the skin dose would be too high even to achieve an adequate signal on the detector, even if the X-ray tube could produce the required output. Making the X-ray beam harder (by increasing the kV) will increase the penetration of the beam, but reduce the subject contrast of a vessel containing contrast agent. Figure 2.13a shows the effect of altering the kV and filtration on the contrast of a 3 mm contrast filled vessel against 200 mm polymethyl methacrylate (PMMA) background. It can be seen that the beam hardening effects of either increasing kV or filtration reduce the contrast of the

simulated vessel. Beam hardening effects also occur due to the background objects in the beam, and this is illustrated in Figure 2.13 which shows the effect of altering beam filtration and the underlying PMMA phantom thickness on contrast.

In a real X-ray acquisition, scattered radiation further degrades contrast. Assuming the number of scattered photons per unit area is uniform over an area surrounding an object of interest, if there are D and B primary photons per unit area in the region of the object and background respectively, then without scattered radiation the contrast of the object (C_p) is

$$C_p = \frac{B - D}{B} \tag{2.6}$$

Let S be the number of scattered photons per unit area, then the contrast in the presence of scatter becomes

$$C_s = \frac{(B + S) - (D + S)}{B + S} \tag{2.7}$$

$$C_s = \frac{B - D}{B + S} \tag{2.8}$$

Multiplying by D/D gives

$$C_s = \left(\frac{D}{D}\right) \frac{B - D}{B + S} = \left(\frac{B - D}{B}\right) \left(\frac{B}{B + S}\right) \tag{2.9}$$

Substituting C_p from Eq. 2.6,

$$C_s = C_p \left(\frac{B}{B + S}\right) = C_p / \frac{B + S}{B} \tag{2.10}$$

The final term is commonly rearranged as $1/(1 + S/B)$ and referred to as the scatter degradation factor.

A scatter-to-primary ratio (i.e. S/B) of approximately two would be expected in cardiac imaging, therefore reducing subject contrast by a factor of $1/3$.[50] Whilst anti-scatter grids and an air-gap of approximately 10 cm are commonly used in cardiac imaging (which will reduce the amount of scattered radiation reaching the X-ray detector), scatter remains a significant source of contrast loss.

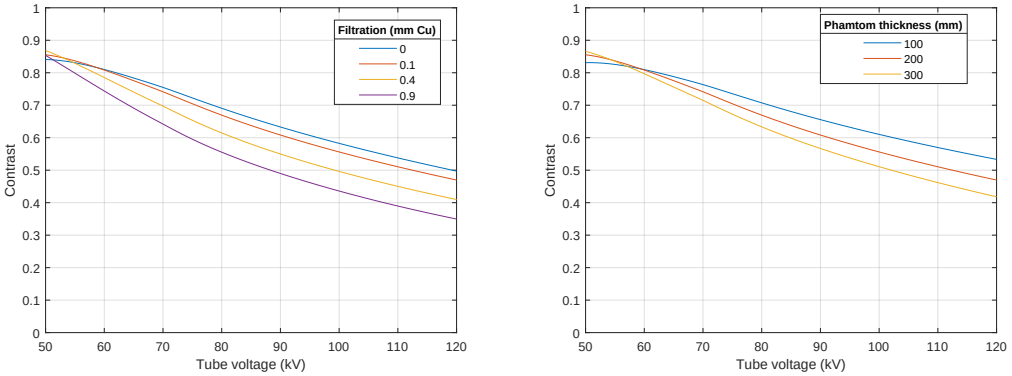

(a) Effect of beam filtration

(b) Effect of phantom thickness

Figure 2.13: Primary subject contrast for a 3 mm diameter contrast filled vessel. a) shows the effect of altering the beam filtration for a superimposed on a 200 mm thick PMMMA phantom. b) demonstrates the effect on contrast of phantom thickness (0.1 mm Cu filtration has been applied to the beam).

2.2.5.4 Automatic dose control

The radiographic factors used by a cardiac X-ray system are controlled by an automatic dose control (ADC). The ADC reacts to changes in the attenuating properties of objects in the X-ray beam. These changes can be due to different patient sizes, and changes in the tissue thickness within the X-ray beam as the C-arm is moved during a case. In response the ADC adjusts the radiographic factors to produce an adequate image quality at an acceptable radiation dose. The design and operation of ADCs varies between systems, particularly between manufacturers[16,51,52] and further modification to the parameters can be requested by end users post installation. These systems operate by normalising the X-ray dose reaching the image receptor. During an acquisition sequence for coronary angiography, an X-ray imaging system generates a series of images at a specified frame rate. Each image that is acquired is analysed, and the mean signal reaching the X-ray detector compared to a programmed level set by the manufacturer that would be achieved from a correctly exposed image. If the signal level from the current exposure is below the target value, X-ray output is increased for the next image acquisition, and conversely, if the achieved signal exceeds the set level, the X-ray output is reduced for the following image.

The radiographic factors selected by the ADC balance the quality of the image produced against the radiation dose given to the patient. Generally, a harder X-ray beam will reduce skin dose, but also reduce subject contrast. Increasing the operating dose level at the detector

will reduce the noise in the image at the expense of increased radiation dose. The wide latitude, programmable gain, and sophisticated post acquisition image processing in current digital imaging systems mean that there is considerable flexibility in selecting radiographic factors. The radiographic settings that best balance image quality and patient dose for cardiac imaging have been studied systematically in both adult[53] and paediatric imaging,[54,55] but the operation of the ADC must also ensure acceptable equipment lifespan and utilise a stable control system which may mean such schemes are not the most desirable.

The dynamic operation of the ADC does ensure that an X-ray system operates at an acceptable radiation dose and image quality, but the frame-by-frame updates of the radiographic output mean that there is variation in signal intensity and variation in contrast between objects in the image, both between different angiographic sequences and during a single sequence; the ADC reacts to the changing attenuation during the heart cycle, and in response to the injection of contrast agent. This variation in signal and contrast could compromise an image analysis method that quantifies contrast agent flow during an angiogram, or compares two different angiograms.

2.2.5.5 Image detection

The current generation of cardiac X-ray detectors utilise a CsI scintillator which converts energy from absorbed X-ray photons to visible light, and were introduced around 20 years ago.[56] The light photons are converted into charge using a photodiode, and the signal is amplified and digitised in a solid state pixel array of readout electronics. This design of equipment is efficient,[57] offering a significant advantage in terms of image quality to previous generation equipment.[16,58,59]

The characteristic response of an X-ray detector is not calibrated to any given reference, such as the conversion of intensity to Hounsfield Units in computed tomography. Often modern solid state detectors have a linear response to X-ray dose, but the captured image is manipulated by a series of computer processing algorithms, which results in the linear relationship between pixel intensity and exposure being lost. The result of these factors is that even though a modern X-ray imaging system is capable of producing consistent images when multiple images are taken of the same objects, it is not possible to predict from the image alone the physical properties of the objects that gave rise to the image.

2.2.6 Image processing in cardiac X-ray imaging

The image acquired from a current solid state cardiac X-ray imaging system is not presented as is to the clinical user. A series of image processing stages are applied as follows:

1. Offset (dark current correction). The X-ray detector acquires images even when the X-ray beam is off. These images are averaged to create the signal intensity of each pixel in the detector with no X-ray exposure. The recent offset correction image is then subtracted from any exposed image image.[60]

2. Gain correction. Each pixel in the X-ray image detector has a different characteristic response to X-ray exposure. This is due to variations in the scintillator layer, pixel photo-diodes, line amplifiers and line analogue to digital converters. This is corrected for by creating a gain correction during the routine service. A set of flat field exposures at the dose levels anticipated in clinical use are made for each of the operating modes. Each set is averaged, offset corrected and then used to calculate a gain correction map, which is applied as a multiplicative correction to newly acquired images.[60] Variations on this approach have been proposed to deal with operation across a wider exposure range where the detector response is not linear[61] and filtering of the gain images have been shown to improve image quality.[62]

3. Defect correction. A number of pixels on the detector do not function properly, producing pixel values outside acceptable ranges. These pixels are identified during routine servicing, and the values of these pixels is replaced using interpolation from surrounding pixels.[63]

4. Automatic gain control. This is a feed forward correction designed to prevent sudden variations in image brightness due to imperfect dose control (caused for example by the X-ray gantry being moved between exposures, leaving the dose control setting out-of-date). A region of the image in the centre is defined and the pixel intensities averaged, and a multiplicative factor applied to normalise this to a pre-defined value.

5. Look up table (LUT). A look up table is used to reduce the range of the pixel intensities. These are often a scaled logarithmic shaped function, and an example is shown in 2.14, which is incorporated into a common cardiac X-ray imaging system.

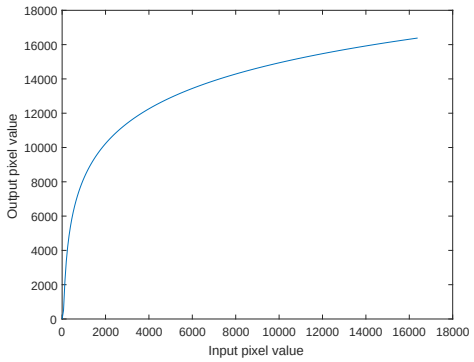

Figure 2.14: Logarithmic look up table applied to images on the Philips' FD10 cardiac system.

6. Image enhancement. The image is enhanced with sophisticated non-linear image processing intended to improve the appearance of the image. These algorithms aim to decrease noise and increase the conspicuity of features of interest. These algorithms vary between systems and are evolving, and have been shown to increase the perceived quality of the image.[64]

2.2.6.1 Digital subtraction angiography

A common form of processing applied to vascular angiograms is digital subtraction angiography (DSA). DSA images are created by using the log-subtraction of an image without contrast agent (the mask image) obtained prior to the contrast injection, from subsequent images.

A DSA image is created by the subtraction of the logarithms of the mask and contrast images, and therefore the difference in signal, ΔS, following the injection of contrast agent is from eq. 2.4,

$$\Delta S = k\left(\ln GN_0' \exp\left(-\frac{\mu}{\rho}m_c/A_0\right) - \ln GN_0'\right) \tag{2.11}$$

Simplifying gives

$$\Delta S = -k\frac{\mu}{\rho}m_c/A_0 \tag{2.12}$$

where k is a secondary gain applied in the image processing. In other words, the injection of contrast agent provokes a differential signal that is proportional to the mass of iodine within the body, and therefore concentration of contrast agent, even if the mass attenuation coefficient, organ location and organ size are unknown.

DSA images can contain artefacts where there is patient movement (causing misregistra-

tion between the contrast and the mask image) or where there is any variation in the radiographic settings. The use of DSA makes the subjective or computer analysis of the signal intensity due to contrast agent in the image straightforward, but DSA has not been adopted in cardiac imaging, not least due to the cardiac motion causing motion artefacts. Nonetheless, the ability to remove the underlying anatomy creating a DSA sequence in cardiac imaging would be most useful for the analysis of contrast agent flow.

2.2.7 Subjective assessment of X-ray angiograms

2.2.7.1 Stenotic severity

The severity of a stenosis demonstrated on angiography is often expressed as the percentage of the minimum luminal diameter compared to the luminal diameter of a region of non-diseased artery. Most often this is assessed subjectively, and expressed as a relative measure, referred to as percentage stenosis. The relative measure of stenotic severity is attractive in angiography where absolute distances and sizes of objects in the image are unknown due to variations in imaging geometry. Intervention is considered for stenoses of greater than 75% severity.[32] It has been known for some time that the functional severity of a stenosis correlates poorly to the visual interpretation of stenotic severity[5] and there is considerable variation between observers.[65,66] The decision of whether or not to perform angioplasty would ideally be made with the knowledge of the degree to which a stenotic lesion was inhibiting blood flow in the artery. If the lesion is not flow limiting, then intervention could be detrimental for the patient.[67]

In addition to the subjective interpretation, both cardiac X-ray systems and off-line analysis software, have quantitative coronary angiography (QCA) tools where stenotic severity can be assessed using semi-automatic computer analysis which supplements the visual inspection of an angiogram. QCA software often implements a spatial calibration of pixel sizes in the image, using an object of known size, normally the internal lumen of the catheter. This then permits the minimal luminal diameter to be measured in absolute units. The use of QCA is not widespread in clinical practice, having been superseded by both other invasive physiological measurements and more comprehensive image analytic techniques.

Even when QCA is employed, the single two dimensional projection from which it is formed gives limited information on the reduction in cross sectional area of an artery. Therefore

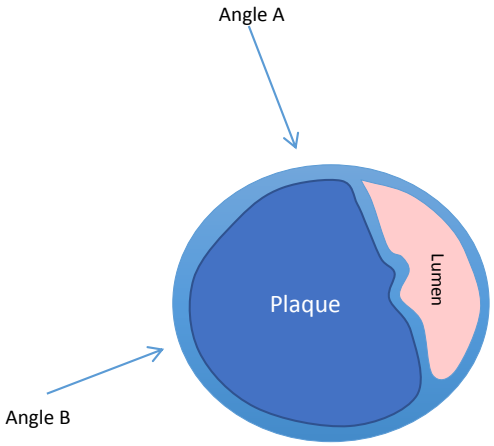

Figure 2.15: The projected width of a vessel's lumen depends on the beam angle when the lumen is not circularly symmetric. From Angle A the luminal loss would be evident, but from Angle B, the visible degree of stenosis would be much smaller.

stenotic severity is a poor predictor of the functional significance of a lesion, demonstrated by a poor correlation between FFR (the ratio of the flow in a diseased artery to the flow in the artery if it were normal; see Section 2.3.1.2) and stenotic severity.[68] Furthermore, the overlapping of objects in an image (a particular issue in the LCA due to its more complex structure than the RCA) can also obscure stenoses, or mask the severity. In large part, these issues are due to the two dimensional presentation of the arterial lumen, which can lead to an inaccurate representation of the loss of cross sectional luminal area in a stenotic lesion, especially when only one projection is considered. The visible degree of stenosis where a diseased vessel's lumen is not circularly symmetric in cross section, can be highly dependent upon the viewing angle, and this is illustrated in figure 2.15, which shows two projection angles, one where the luminal loss should be evident (Angle A), and one where it may not (Angle B).

2.2.7.2 Visual assessment of angiographic blush

The transit of contrast agent through the myocardium and into the venous system can be visualised on a angiogram of sufficient duration in most cases. This is referred to as the "myocardial blush" due to its characteristic darkening of large areas of the image. The

subjective assessment of the myocardial transit of contrast agent via angiography has been formalised into two grading systems, myocardial blush grade (MBG)[69] and TIMI myocardial blush grade (TMBG).[70] Whilst both are ordinal scales with possible values referred to by hte integers 0 to 3, MBG is based on the differential intensity of the myocardial blush, whereas TMBG has a greater emphasis on the temporal characteristics of the flow as well as the density. TMBG has been shown to be associated with ST-segment elevation resolution and left ventricular ejection fraction in patients with acute myocardial infarction.[71] In patients undergoing PCI with acute myocardial infarction, both TMBG and MBG have both been shown to be predictive of one year survival, with TMBG having the largest predictive value. In particular, patients with TMBG scores of 0 or 1 post-procedure fare particularly badly, with a 50% survival rate (although more modern management of these patients would likely yield a far lower mortality rate). Interestingly, lower post-procedure MBG scores of patients with grade 3 (normal) TMBG were also predictive of lower survival rates.[72] In patients with post-MI cardiogenic shock, only around one third of patients with TMBG grade 3 had grade 2/3 MBG, and patients with MBG scores of 0 or 1 were less than one third as likely to survive at 60 months, compared to those with grades 2 or 3.[73]

2.2.7.3 Angiographic assessment of epicardial flow velocity

Simple visual inspection of a coronary angiogram as it plays will reveal cases where flow velocity is clearly sluggish, such as no-reflow following PCI. However, more accurate and reproducible measures of velocity from angiograms may permit more accurate diagnosis and therefore more rapid treatment.[74] The thrombolysis in myocardiac infarction (TIMI) frame count is a long established subjective measure that assesses the time contrast takes to flow from first entering an artery to a distal landmark. The definition of the start of the injection is common to all three coronary arteries, i.e. frame 1 is the image where the contrast touches both borders of the lumen and moves forward. The distal landmark is different for each artery, viz. the first branch of the posterolateral artery for the RCA, the most distal branch of the obtuse marginal branch of the circumflex artery, and the most distal bifurcation of the LAD. The TIMI frame count is performed by calculating the number of images (frames) between the start and end points. The original work was performed assuming a frame rate of 30 fps, and if this is not used a correction factor of 30 fps must be applied. The frame

count for the RCA and Cx are then multiplied by 1.7 to correct for the different average lengths of the arteries to the LAD (creating a corrected TIMI frame count).[75] A normal range for TIMI frame count is between 14 and 28, with an average of 21 frames.[70] TIMI frame count has been shown to be reasonably reproducible, with a mean absolute difference of 4.7 frames (0.16 s) between two injections.[75] Longer TIMI frame counts are predictive of higher mortality and other adverse cardiac events following thrombolytic administration.[76] TIMI frame count has been shown to have a reasonable correlation with Doppler measured flow-velocity[77,78] (see section 2.3.1.1 for a further discussion on intra-coronary Doppler flow velocity measurement). TIMI frame count has been shown to predict survival at five years, but not 10 years, following acute MI.[79] It also predicts ventricular function and infarct zone wall motion following thrombolytic treatment[80,81], and has been shown to be higher in patients with Cardiac Syndrome X.[82] Interestingly TIMI frame count has been shown to be 40% higher than normal in non-culprit arteries patients with STEMI,[83] and in patients with lower than normal flow in the non-culprit artery, there was an improvement in non-culprit artery flow following PCI.[84] Lower flow in all three arteries is associated with poorer outcomes following STEMI.[70]

TIMI frame count has a number of advantages over TMBG: whilst still a subjective measure, it is a quantitative variable rather than ordinal, and the definition of contrast arrival at specific points in the arterial structure should be subject to less inter-observer variability, whereas the descriptions for blush grades could be affected by the observer's interpretation, or even the computer processing and display differences between X-ray systems. Unlike intra-coronary Doppler wires, the assessment of frame count does not require additional sensors to be used. Despite this, TIMI frame count has not been widely adopted. The use of a frame count, rather than directly expressing the time for contrast to traverse an artery in seconds (or perhaps as velocity using a standard value for the length of each artery) is unhelpful, especially given the varied frame rates used on modern X-ray equipment. Rather, the use of standard units such as seconds or cm/s might be helpful in interpretation (and comparison with Doppler in the case of velocity). Furthermore the fact that it is a subjective measurement has probably lowered its perceived accuracy. The biggest issues, however, are the inherent assumption about the artery size being the same in all patients; i.e. that the LAD is 1.7 times the length of both the circumflex and RCA, and the fact that velocity is not a measure of

flow, and the volume of the vessel is unknown.

2.3 Physiological assessment in the catheterisation laboratory

Recognising the inherent limits of the visual inspection of angiograms, a range of supplementary methods have been developed, specifically aimed for use within the catheterisation laboratory to improve the assessment of the patients haemodynamics and cardiac function. The principles physiological measures will be described, followed by how these are practically assessed within the catheterisation laboratory.

2.3.1 Concepts

2.3.1.1 Coronary flow reserve

Coronary flow reserve (CFR) is the ratio of the maximum flow in a coronary artery, i.e. flow under hyperaemic conditions (Q_H), to that at baseline (rest) conditions, Q_R.

$$\text{CFR} = \frac{Q_H}{Q_R} \tag{2.13}$$

2.3.1.2 Fractional flow reserve

Fractional flow reserve (FFR) is the ratio of hyperaemic flow in a diseased coronary artery (Q_S) to the flow in the same artery in the absence of disease (Q_N). In other words,

$$\text{FFR} = \frac{Q_S}{Q_N} \tag{2.14}$$

2.3.1.3 Resistance

The resistance of the coronary system is often considered as a combination of resistance of one or more stenotic lesions in the coronary arteries (*stenotic resistance*), and the resistance of the myocardium which they supply (*myocardial resistance*). These can be assessed by measuring a combination of intracoronary pressure and flow. The resistance of a stenosis can therefore be calculated by measuring the pressure in the artery just proximal to the lesion, and just distally to the lesion. The resistance is then the pressure drop divided by the flow. Similarly the myocardial resistance is the pressure drop across the myocardium divided by the arterial

flow. Whilst a simplified view of the coronary haemodynamics, this model can be useful in exploring the coronary system, and is explored in greater detail in section 2.3.3.2 on page 41.

2.3.2 Doppler flow velocity based measurements

2.3.2.1 Doppler based coronary flow reserve

Interest in the use of CFR as a means of testing the functional significance of a stenosis began in the mid 1970s,[85,86] and a decade later its use in practice was established.[87] CFR can be measured in the catheterisation laboratory using an intra-coronary Doppler wire, which can measure blood velocity within a selected coronary artery. By taking one measurement at rest, and a second after an intra-coronary injection or during an intravenous injection of a vasodilator such as adenosine, CFR can be calculated. CFR attempts to measure the ability of the coronary circulation to respond to increased demand, with a high CFR indicating that there is adequate capacity. A CFR value of four is considered normal, with a CFR of less than two considered to be indicative of ischeamia.[88] In addition to being used to guide intervention, CFR measured post intervention has also been shown to be predictive of short and long term prognosis, with patients with a CFR of >2.5 and a residual stenosis of <35% having lower rates of ischaemia, restenosis or further ischaemia.[89]

There are a number of difficulties in interpreting CFR in humans. Whilst there is good evidence that on a population basis CFR is a reasonable predictor of clinical outcome, on an individual level it is less so. Firstly, CFR relies on a vasodilator, most commonly adenosine,[90] to achieve hyperaemia. If the vasodilator does not cause full hyperaemia to be reached, the measurement will be inaccurate. CFR measurement relies on the basal state where the flow of blood in the myocardium is determined by the normal autoregulatory system. For any reasonable blood pressure, the autoregulation system will increase or decrease microvascular resistance to maintain a constant flow of blood through the myocardium. When hyperaemia is induced, however, the maximum blood flow becomes dependent upon both the condition of the heart, and also the current blood pressure. Reference to figure 2.2 demonstrates how different autoregulatory set points (curves A and B) and aortic pressure would affect CFR. Moreover, ratio of maximal coronary flow to baseline flow is also affected by blood pressure in the distal coronary artery, and the baseline flow is affected by the heart rate[91–93] and sex.[94]

There are also differences in regional CFR around the left ventricle, and as methods in

humans only assess global CFR, then these methods may be inadequate for an individual.[95] Baseline myocardial blood flow is also dependent on age (increasing with age) and sex (higher in females).[96] Moreover, hypereamic blood flow is lower for older patients (>55 years old), leading to lower CFR in older people.[97]

In addition to variations due to heart rate, flow-velocity measurements are also affected by the exact location of the Doppler sensor in the artery, for example, where velocity would be expected to be lower nearer to the arterial wall, and maximal in the centre of the artery.[98] Moreover, for the same flow, the velocity will be proportional upon the luminal cross-sectional area.

Relative coronary flow reserve (RCFR) has been proposed to try to account for the variation in CFR between patients, and to normalise for the current physiological state of the current patient (for instance due to differences in perfusion pressure and heart rate). It is defined as the ratio of the CFR measured in the target vessel to that in a normal vessel (i.e. one that does not demonstrate any disease), however this has not been shown to improve clinical decision making.[99] Moreover the measurement of RCFR requires a disease free artery, which may not be present, or the presence of diffuse disease may mean that a vessel with a normal angiographic appearance may not be disease free. It is also possible to measure CFR using non-invasive techniques, most notably positron emission tomography (PET), and studies using PET provide additional support that a lowered CFR is associated with higher levels of mortality and adverse events.[100]

The practical difficulties and range of factors described above, have limited the applicability of CFR in guiding intervention. The positioning of the sensor wire into a suitable location is often time consuming, meaning that Doppler assessment was not possible in around 10–15% of cases. This, along with the development of miniaturised intra-coronary pressure wire and the increasing evidence supporting the use of FFR, meant that by the mid 2000s, CFR had been replaced in practice by FFR.[101]

2.3.3 Intracoronary pressure-based measurements

2.3.3.1 Intracoronary pressure derived fractional flow reserve

Clearly there is no way to measure FFR directly as the flow in the disease free artery cannot be measured for comparison to the diseased vessel. In practice FFR is estimated using intra-

coronary pressure measurements. In the absence of any stenosis, letting P_A, P_D and P_V be the blood pressure in the aorta, distal coronary artery and coronary vein, then $P_A = P_D$ and therefore

$$Q_N = (P_A - P_V)/R_{min} \tag{2.15}$$

where R_{min} is the resistance in the myocardium at its minimum, i.e. during maximal flow. In the presence of a stenosis, P_D is reduced giving

$$Q_S = (P_D - P_V)/R_{min} \tag{2.16}$$

By measuring the aortic blood pressure with a transducer connected to the guide catheter, and using an intra-coronary pressure wire to measure the distal pressure, FFR can be calculated:

$$\text{FFR} = \frac{Q_S}{Q_N} = \frac{(P_D - P_V)/R_{min}}{(P_A - P_V)/R_{min}} \tag{2.17}$$

Assuming that R_{min} is constant, and P_V is close to zero, then

$$\text{FFR} \approx \frac{P_D}{P_A} \tag{2.18}$$

In the early work on FFR two definitions were proposed: FFR_{myo} following eq. 2.17 and FFR_{cor}, defined as

$$FFR_{cor} = \frac{P_d - P_w}{P_a - P_w} \tag{2.19}$$

where P_w is the coronary wedge pressure, in other words, the pressure in the distal artery, with the artery occluded at the stenosis site using an inflatable balloon. The distinction between the two measurements is that FFR_{cor} assesses the functional significance of the stenotic lesion, whereas FFR_{myo} assesses the myocardial bed fed by the artery, and accounts for the any collateral flow. The use of FFR in practice today, is that of FFR_{myo}, and is simply referred to as FFR.[102]

FFR is widely employed in clinical practice, and has effectively superseded CFR in providing functional assessment of stenoses in the catheterisation laboratory.[103] Minimal myocardial resistance, i.e. hyperaemia, is achieved using a pharmacological agent, commonly adenosine,

using an intravenous injection at rates of 140–170 μm/kg/min depending on the injection site.[104] Intracoronary injection of adenosine has also been used, as it can result in lower costs and fewer side effects, but lack of standard dosing, lack of a steady state and sub-optimal hyperaemia in some patients are issues with such infusions.[105] Contrast induced hyperaemia using a 10 ml injection of iodixanol has also been studied, but this produces sub-optimal hyperaemia compared to an intra-coronary adenosine bolus.[106] Whilst possibly reducing the short term unpleasant feelings for patients during an adenosine infusion, the lack of substantial validation, inadequate hyperaemia and concerns over increase nephrotoxicity associated with using contrast agent to introduce hyperaemia, probably contribute to the lack of adoption of this as a technique.

Early work by Pijls and colleagues[107] demonstrated that an FFR of less than 0.75 was highly predictive of ischaemia. Over time, the threshold considered to indicate that a lesion is flow limiting has been adjusted to 0.8, and FFR is now used to guide the decision as to whether to treat a lesion with PCI or medical therapy.[103,104] There is a considerable body of evidence that guiding intervention via FFR is beneficial for patient outcomes, from large multi-centre trials including:

- DEFER[108,109] demonstrated no disadvantage to not treating a stenosis with an FFR of 0.75 or more in patients with a single angiographically significant stenosis. After 15 years, the group of patients with an FFR of ≥ 0.75 had considerably fewer MIs when treated medically than when treated by stenting (although at the time only bare metal stents were available), with no observed difference in mortality between the groups;[110]

- FAME[111] demonstrated improved survival, lower rates of serious adverse outcome and lower rates of repeat revascularisation when guiding intervention using FFR in patients with multi-vessel disease.[67] Similar reductions in adverse events were seen in patients with stable angina, to those with unstable angina and NSTEMI;[112]

- FAME 2[113,114] Used broader inclusion criteria than the original FAME study, targeting all patients with stable angina, and also sought to compare the outcome of patients with an FFR of <0.8 randomised to receive optimal medical therapy or PCI plus medical therapy. The trial was stopped early due to an increased risk for patients in the medical treatment group. The conclusions also remained consistent with the original DEFER

trial, i.e. FFR guided angiography improved outcomes as patients with an FFR of > 0.8 had better outcomes, with medical therapy than intervention after two[114] and five years[115].

The benefit of FFR guided intervention is likely to be due to the relative risks to patients between medical therapy and revascularisation, depending on the functional significance of the stenosis. For high FFR value, the risks of PCI are greater than those of medical treatment, yet at lower levels of FFR, i.e. greater functional significance, higher events are seen in patients with medical treatment.[116]

In addition to guiding intervention, post intervention FFR has also been shown to be predictive of patient outcome, where patients with an FFR of 0.94 or higher had fewer post intervention cardiac events than those with a lower FFR.[117] Post-PCI measurement of FFR has shown that approximately one fifth of angiographically satisfactory lesions still had an FFR in the ischaemic range.[118]

For patients with STEMI, using FFR to guide complete revascularisation (i.e. treating all lesions with an FFR of <0.8 in addition to the culprit lesion) compared to treating only the culprit lesion, has been shown to reduce adverse events (mainly the requirement for further revascularisation).[119] The FAMOUS-NSTEMI study revealed that FFR guided intervention in patients with NSTEMI resulted in a greater number of patients being treated medically, with 8% lower rates of revascularisation. No difference in health outcomes between the angiographically guided and FFR guided intervention groups were found.[120] FFR has also been shown to predict the functional significance of a stenotic lesion post MI. Following MI, necrotic tissue may develop, leaving the diseased vessel supplying areas of viable myocardium and scar tissue. Under hyperaemic conditions, if the scar tissue has increased resistance compared to normal tissue as might be expected if the scar tissue cannot vasodilate, the pressure in the distal artery will be increased compared to the pre-infarct myocardium. FFR measurement would therefore be reduced, and it has been proposed that this is a beneficial effect for FFR assessment, as only the functional significance on the viable myocardium is being assessed.[121] This argument requires that the increased resistance in the myocardium can be attributable to necrotic tissue, and therefore early assessment following MI could be confounded by stunned myocardium or intra-myocardial oedema which may elevate resistance until they resolve. Similar cut-off values for detecting ischaemia in post-MI patients have

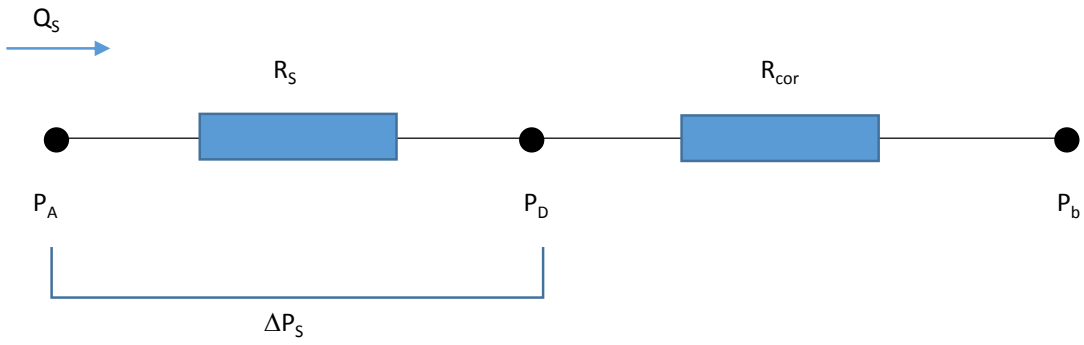

Figure 2.16: Model of coronary circulation, where R_S and R_{cor} are the resistance of the stenosis and myocardium respectively, Q_S is the coronary blood flow, and P_A, P_D and P_b are the pressures in the aorta, distal artery and myocardial outlet respectively. ΔP_S is the pressure drop across the stenosis.

been reported than in patients with no previous MI (0.78),[122] and microvascular resistance of viable myocardium post-MI has been shown to be the same as that in non-diseased areas,[123] supporting the use of FFR in chronic MI.

2.3.3.2 Limitations of invasive FFR

The pressure-only based invasive FFR measurement is an incomplete description of the coronary haemodynamics.[124–126] As such there are a number of areas where the assumption made in the measurement of FFR via intra-coronary pressure wire are not sound, such as that the outlet pressure is negligible and the myocardial resistance minimal. Siebes et al.[127] used a simple model of the coronary circulation, shown in figure 2.16. Whilst a greatly simplified model of the coronary circulation, the model is a useful vehicle to explore the assumptions made in invasive FFR measurements. Siebes et al. introduced P_b, the blood pressure at the outlet of the myocardium, noting it is normally a little higher than the venous pressure, P_V, and propose a definition of FFR as follows:

$$\text{FFR} = \frac{Q_S}{Q_N} = \frac{P_D - P_b}{P_A - P_b} \tag{2.20}$$

Applying the hydraulic analogy to Ohm's law to the model, and letting Q be either Q_N or Q_S, gives

$$P_D = QR_{cor} + P_b \tag{2.21}$$

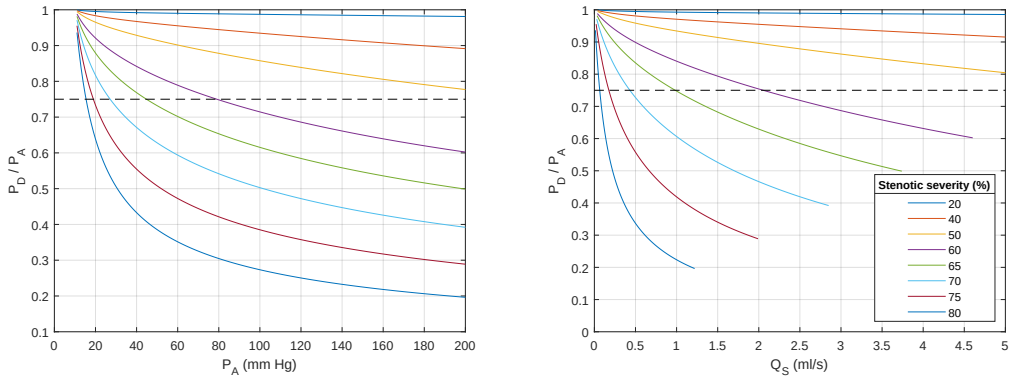

(a) (b)

Figure 2.17: Relationship between FFR to a) aortic pressure, and b) flow, for varying stenotic severity. The horizontal dashed lines represent an FFR of 0.75, usually taken as the critical value for indicating a flow limiting stenosis. P_A and P_D are the aortic and distal pressure respectively, and Q_S the flow in the diseased artery.

and

$$R_S = \frac{\Delta P_S}{Q} \tag{2.22}$$

Modelling the stenosis as a blunt-shaped rigid obstruction, the pressure gradient it produces was modelled as:

$$\Delta P_S = A_V Q + B Q^2 \tag{2.23}$$

where A_V and B are coefficients for pressure loss due to viscous losses and inertial pressure losses respectively. The values of A and B used in Siebes' model were derived from previous work.[128,129] Both of these coefficients are dependent upon the degree and shape of a stenosis. It can be seen from eq. 2.22 that R_S is dependent upon the flow through the artery. The net result of this is that the FFR is dependent both on the arterial flow and the aortic pressure. Using the coefficients from Siebes' model, but converting the flow units to ml/s for comparison with data presented in Chapters 7 and 8, Figure 2.17 shows the effect of aortic pressure and arterial flow on FFR. The figure shows that relatively modest changes to aortic pressure or arterial blood flow, both of which occur during the cardiac cycle and over time, could lead to a lesions measured FFR crossing the threshold of 0.75 usually considered the cut-off value, below which intervention is performed.

The model can also demonstrate that changes to the myocardial resistance, R_{cor}, or an elevation of the blood pressure at exit of the myocardium, P_d, will lead to discrepancies between pressure measured FFR and FFR defined as the ratio of flow in the presence of a

stenosis and without the stenosis. To do this, the model in figure 2.16 can be expressed as

$$Q = \frac{\Delta P}{R} = \frac{P_A - P_b}{R_S + R_{cor}} \tag{2.24}$$

Substituting for R_S from equations 2.22 and 2.23,

$$Q = \frac{P_A - P_b}{(A_V + BQ) + R_{cor}} \tag{2.25}$$

Rearranging into a quadratic form,

$$BQ^2 + (A_V + R_{cor})Q + (P_b - P_A) = 0 \tag{2.26}$$

allows the system to be easily solved for flow, Q, for given values of P_A, P_b, R_{cor}, selecting values of A_V and B for a specific degree of stenosis. Using this formulation of the model, the influence of the the outlet blood pressure and myocardial resistance were investigated, and shown in Figure 2.18. The figure demonstrates that assuming that the venous pressure is zero may cause the pressure derived FFR measurements to underestimate the severity of a stenosis, and that this effect is more pronounced at higher degrees of stenotic severity. Similarly, increases in myocardial resistance will depress the P_D/P_A value. This influence of myocardial resistance on FFR can be described with a formulation of FFR from the model:[127]

$$\begin{aligned} \text{FFR} &= \frac{Q_S}{Q_N} \\ &= \frac{P_A - P_b}{R_S + R_{corr}} \times \frac{R_{cor}}{P_A - P_b} \\ &= \frac{R_{cor}}{R_S + R_{cor}} \end{aligned} \tag{2.27}$$

Equation 2.27 demonstrates that the P_D/P_A will only drop below 0.75 when the stenotic resistance exceeds one third of the resistance of the myocardium. An elevated R_{cor} could then result in a flow limiting stenosis having an FFR in the normal range.

The model does not account for a number of features of human coronary circulation, any spatio-temporal variations in flow, pressure or resistance (not least the pulsatile flow driven by variation in the myocardial resistance as the heart contracts), collateral flow, the range of morphology of stenotic lesions, multiple lesions, branching vessels, compliance of the arteries,

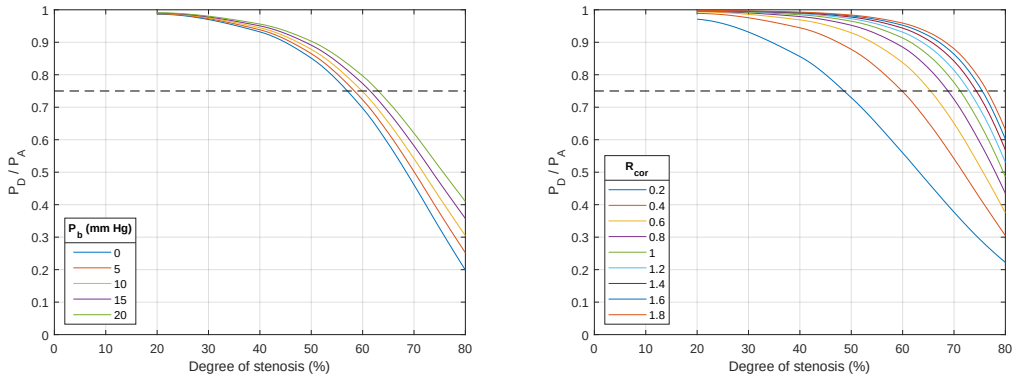

(a) (b)

Figure 2.18: The effect on the P_D/P_A of both a) the outlet blood pressure (P_b), and b) myocardial resistance (R_{cor}). The horizontal dashed line indicates a P_D/P_A value of 75%.

or indeed the physiologic and pathophysiologic processes involved in blood flow regulation to the myocardium. This means that translating the predictions directly into humans should be done with considerable caution. Nonetheless, the use of phenylephrine to increase the aortic blood pressure (by an average of 31 mm Hg) has been shown to reduce the FFR by an average of 0.05 in patients with hypotension ($P_A < 80$ mm Hg).[130] A similar drop in P_D/P_A is seen in figure 2.17a with a 60% stenosis and increase in P_A from 80 to 110 mm Hg. De Bruyne et al.[131] did not show the same dependence of FFR on aortic pressure, although the study induced a more modest reduction in P_A from 100 mm Hg to 79 mm Hg, using a vasodilator that increased the heart rate, which may have masked the effect.[127] Moreover, the minimum aortic pressure was higher in this study.[130]

In the absence of microvascular disease both CFR and FFR will reduce in the presence of increasing coronary stenosis. In its current definition, one can consider invasive FFR as an assessment of the artery. On the other hand, CFR can be considered as assessing both the arterial and microvascular system—increasing resistance of either the epicardial vessel or microcirculation will reduce the CFR. As has been demonstrated, an increase in myocardial resistance (R_{cor}), will increase the value of invasive FFR. In patients with stable angina and an intermediate degree of stenosis, discordance between FFR and CFR have been reported in just over 25% of cases. Slightly more of these cases were those with an abnormal FFR ($< 75\%$) and normal CFR (≥ 2.0), than those with a normal FFR and lower CFR.[99] Patients in the latter group had increase myocardial resistance, elevated baseline average peak blood flow-velocity, and an increased rate of hypertension compared to those with an abnormal FFR

and normal CFR.

Increased myocardial resistance could be due to a number of factors. One example could be in STEMI patients where the sudden onset of acute symptoms is due to plaque rupture and thrombotic debris occluding small arteries and the microvasculature. This will elevate P_D, resulting in a normal FFR even for a lesion which is flow limiting should the myocardium be returned to normal function. Patients with acute coronary syndrome could be more likely to have higher levels of microvascular resistance than those with stable angina, and the utility of guiding intervention based on FFR in this group has been studied,[68] but the data are poor—this was an observational study with no comparator group. Other patients with a higher possibility of microvascular obstruction are those with diabetes mellitus. Pre-intervention FFR measurements in patients for the same degree of stenotic severity have shown no difference for patients with and without diabetes.[132] However, post-intervention, despite having FFR values in the same range as patients without diabetes, patients with diabetes have been shown to have a lower CFR than those without diabetes.[133] This indicates that there may well be residual ischaemia in diabetic patients, attributable to increased microvascular resistance.

Myocardial bridging—where a coronary artery passes into the myocardium rather than being on its surface—can result in constriction of the artery as the heart contracts. This condition is reported in approximately one quarter of the population.[134] The varying resistance of the coronary artery leads to a loss in sensitivity of FFR in detecting ischaemia due to increase intracoronary systolic pressure; in such cases, calculation of FFR in diastole alone, and using dobutamine rather than adenosine to induce hyperaemia, should be used rather the the calculation of the FFR over the entire heart cycle using adenosine as a vasodilator.[135,136] Unfortunately, myocardial bridging is often not detectable using angiography alone.[134]

It is recognised in current European[32] and US[137] guidelines for PCI that the current cut-off value used for intervention when interpreting FFR is subject to some uncertainty for any given patient, and as such, is sometimes referred to as a "gray zone". In the DEFER study a cut off of 0.75 was used, but more recently 0.8 is generally used as threshold value, as a value of greater than 0.8 has been shown to exclude ischaemia in 90% of cases.[138] In reality, the value of FFR indicating ischaemia will vary from person to person. Even the largest outcome trials for FFR (DEFER, FAME and FAME 2) have relatively low patient numbers (91, 509 and 447 respectively). Moreover the inclusion parameters, especially for DEFER,

carefully selecting their patient cohort, mean that they must be interpreted appropriately when applying their findings to practice in the broader patient population. It has also been noted that these outcome studies did not record the right atrial pressure,[139] which was used in the validation studies for the threshold of ischaemia. This omission will have led to raised FFR values, thus affecting the cut-off.[140]

Long term follow up has demonstrated that in patients where revascularisation was deferred, those patients in the FFR range between 0.75 and 0.8 had no significant different in adverse events than those patients with an FFR of 0.8 to 0.85,[141] implying that FFR is not discriminatory between these groups. The decision as to whether or not to defer or intervene for these patients did not appear to affect the overall clinical outcome; deferred patients have been shown to have slightly higher target vessel revascularisation rates, but lower risk of periprocedural MI, again supporting the hypothesis that FFR is not able to discriminate patients that would benefit from intervention in this range.[142] Clearly the natural variation in repeated FFR measurements is partly the cause of the uncertainty,[143] yet on modern equipment the coefficient of variation of FFR has been shown to be only 3%,[144] implying that inter-patient variation (such as differences in myocardial resistance) are probably more important.

2.3.3.3 Contrast-fractional flow reserve

A variation of FFR, contrast-FFR uses the vasodilatory effect of contrast agent, rather than adenosine, to induce near hyperaemia, and proved superior to both resting P_d/P_a and instantaneous wave free ratio (iFR) in discriminating patients with an FFR of ≤ 0.8.[145]

2.3.3.4 Instantaneous wave free ratio

iFR is another pressure derived index of stenotic severity, but unlike FFR does not require the use of a vasodilator. iFR uses a ratio of P_D/P_A during one portion of the cardiac cycle (the so called 'wave free period'), with the premise that during this period the myocardial resistance at rest is correlated to the mean resistance of the myocardium during the full heart cycle under hyperaemia. The initial ADVISE trial demonstrated a good correlation between iFR and FFR.[146]

iFR has been criticised for lacking the theoretical underpinnings and laboratory testing of

FFR. The CLARIFY study, although having a relatively small sample (51 lesions), demonstrated good agreement between iFR and FFR and equal diagnostic agreement between both and hypereamic stenotic resistance (HSR).[147] Nonetheless, the use of iFR is an area of ongoing debate.[148] The VERIFY trial found weak correlations between iFR and FFR, and that iFR reduced under hyperaemia.[144] One of the reasons for the discrepancy between the original ADVISE trial and VERIFY could be attributable to the different algorithms used to determine the wave free period,[149] but this is not supported by modelling.[150] Furthermore, a more recent, larger, study involving 1,974 patients, found that both iFR and resting P_D/P_A averaged over the entire cardiac cycle, predicted an FFR of ≤ 0.8 with an accuracy of 80%.[151] The study demonstrated a very good linear fit between P_D/P_A and iFR, and this linear relationship has been independently confirmed.[152] This throws further doubt that the exact algorithm used for the calculation of iFR is critical. Systematic comparison of iFR and P_D/P_A at five different periods during diastole on the VERIFY2 data[153] has also failed to demonstrate any difference between the iFR and P_D/P_A from different timings within the diastolic period.[154]

More recently, the SWEDEHEART study compared the use of FFR and iFR in guiding PCI in patients with stable angina, unstable angina and non-ST elevation myocardial infarction. The cut-off values for FFR and iFR indicating deferral of intervention were 0.8 and 0.89 respectively, and had end points of death, non-fatal MI and unplanned revascularisation within 12 months. The trial concluded that iFR was non-inferior to FFR in guiding PCI. Another large trial (3,492 patients), DEFINE-FLAIR, of similar design, also reported non-inferiority for iFR guided PCI.[155] Further post-hoc analysis of the trial data reported that serious adverse events were lower in the iFR arm than the FFR arm where the target lesion was in the LAD, but not when the lesion was in another vessel.[156] Considering the general agreement of iFR and FFR in 80% of cases,[151] it is no surprise that given the broad inclusion criteria resulting in many such clear-cut cases, that SWEDEHEART and DEFINE-FLAIR demonstrated non-inferiority for iFR.

IFR, for the same reasons as invasive FFR, is an incomplete descriptions of the coronary haemodynamics. As discussed in section 2.3.3.2, unmeasured factors (notably myocardial resistance, venous pressure, and dependence on aortic pressure) are likely to alter an individual's threshold where a pressure derived index of ischaemia indicates a flow limiting stenosis

in that individual. In other words FFR is an inappropriate reference standard for comparison, as in many ways both measurements have the same flaws. Whist the relative merits of iFR and FFR, and the quality of the trials supporting them, are hotly contested in the letters pages of journals,[157] the limited nature of both measurements should be acknowledge and recognised in clinical decision making. For similar reasons, demonstrating better equivalence between iFR and CFR than between FFR and CFR[158] does not ultimately provide better insight for any specific patient when using iFR. On a practical basis, a hybrid approach has been proposed, with iFR being performed first and followed with FFR if the iFR value is in the "gray" zone,[159]. Such an approach will not progress clinical decision making beyond the limits of FFR. Ultimately, on average, iFR is a biased estimate of FFR, and the differences in individual values can be explained using the fundamental relationships between pressure and flow in the coronary arteries.[150]

2.3.4 Combined pressure and Doppler assessment of resistance

The development of miniturised intracoronary wires equipped with both Doppler velocity and pressure sensors permit simultaneous recording of flow-velocity and pressure, and therefore a more sophisticated investigation of the coronary haemodynamics than the use of flow-velocity or pressure alone.[160] With measurements of aortic and distal pressure, and a surrogate measurement of flow (i.e. flow velocity from the Doppler sensor), indexes of resistance of a stenotic and myocardial resistance have been developed.

HSR is defined as the ratio of stenotic pressure gradient to the flow-velocity, i.e.

$$\text{HSR} = \frac{P_A - P_D}{Q_v} \tag{2.28}$$

where Q_v is the hyperaemic average peak blood velocity.[161]

Hyperemic myocardial resistance (HMR) is defined as the ratio of mean distal arterial pressure to hyperaemic averaged peak blood velocity, i.e.

$$\text{HMR} = \frac{P_D}{Q_v} \tag{2.29}$$

In the absence of a stenotic lesion this will approximate to the ratio of mean aortic pressure to averaged peak blood velocity. Both HSR and HMR have units of mm Hg s cm^{-1}.

HMR has been shown to be predictive of adverse cardiac events following PCI for STEMI,[162] and HSR has been shown to be a more accurate indicator of ischaemia and reversible perfusion deficit than either FFR or CFR. A threshold of 0.8 mm Hg s cm^{-1} for HSR been proposed as cut-off for deferral of intervention.[163] Following MI, HMR has been shown to be predictive of peak creatine kinase level, and infarct size as measured using CMR (although CFR showed very similar levels of correlation).[164] Higher HMR values are associated with increased levels of remodelling of the left ventricle following anterior acute STEMI.[165]

The combined use of flow-velocity and pressure measurements undoubtedly give better description of the coronary haemodynamics than the use of pressure wire alone, but there are a number of limitations and draw backs. Firstly, there is currently only one manufacturer of a wire that can simultaneously record pressure and flow-velocity. The placement of an intra-coronary Doppler wire is also cumbersome in a number of cases, and the motion of the Doppler sensor within the artery during the cardiac cycle can introduce variation. The use of flow-velocity as an index of flow ignore differences in the vascular volume. In a relative flow index such as CFR, this term cancels out, but in an absolute measurement of either stenotic or myocardial resistance it does not. Additionally, the measurement of myocardial resistance also assumes that the outlet pressure is zero.

2.3.5 Thermodilution based techniques

Thermodilution can be used to assess the flow of blood in the coronary arteries using an injection of room temperature saline and an intracoronary temperature sensor equipped guide wire. The saline injection can either be given as a continuous infusion at a known rate (normally via a pump) or as a bolus injection (normally hand injected). The continuous infusion can be used to assess absolute flow, and the bolus injection can measure the mean transit time.

2.3.5.1 Bolus based techniques

CFR can be measured using a bolus injection of room temperature saline. As the vascular volume may reasonably be expected to remain constant between basal and hyperaemic conditions, the ratio of hyperaemic to basal flow will be the same as the ratio of hyperaemic to basal coronary mean transit times. To measure the mean transit time, a guide wire with a

thermistor near its tip is introduced into a distal arterial segment. By monitoring the temperature of the shaft of a guide wire the timing of an injection of room temperature saline can be detected, i.e. $t = 0$ is determined as the bolus is injected. The temperature of the distal tip of the wire then records the drop in temperature over time as the bolus of saline passes the wire. Mean transit time can then be calculated using standard tracer kinetic theory, letting $C(t)$ be the temperature difference provoked by the saline at time t (which is analogous to the concentration of saline),[166]

$$T_{mn} = \frac{\int_0^\infty tC(t)dt}{\int_0^\infty C(t)dt} \tag{2.30}$$

A moderate correlation between CFR measured using thermodilution and Doppler flow-velocity in humans has been demonstrated.[167]

A combination of thermodilution measured mean transit time and distal pressure has been proposed as an index of microvascular resistance. Given that[166]

$$Q = VT_{mn} \tag{2.31}$$

Index of microvascular resistance (IMR) assumes that coronary flow is proportional to $1/T_{mn}$ in the coronary arteries (where T_{mn} is the mean transit time), and is defined as the product of the distal coronary pressure and the hyperaemic mean transit time of blood down the artery of interest:

$$\text{IMR} = T_{mn}P_d \tag{2.32}$$

IMR has units of mm Hg s. A fair correlation of 0.54 between IMR and reference microvascular resistance has been demonstrated in swine.[168] IMR has been shown to have a lower coefficient of variation than Doppler measured CFR in humans.[92]

IMR has been shown to predict patient outcome in STEMI, predicting raised creatine kinase levels, and three month wall motion score, where other indicators including CFR, TMBG and S-T segment resolution time did not.[169] IMR is also associated with lower regional 18F-fluorodeoxyglucose uptake on PET at six months.[170] It has also been shown to be raised in patients with microvascular obstruction,[171] and a negative predictor of left ventricular ejection fraction (LVEF) and infarct volume (shortly after PCI and at a longer term follow

up of three to six months) post PCI for STEMI.[170,172,173] It should be noted that there was quite some variation between individuals—for example whilst the median IMR for patients with microvascular obstruction (MVO) were higher than those without (38 to 27 mm Hg s respectively), the interquartile ranges of IMR for the two groups was 29–55 and 18–36 mm Hg s respectively, and ranges were approximately 17–75 and 19–59 mm Hg s respectively. IMR has been shown to predict which patients are more likely to suffer periprocedural MI in stable patients undergoing PCI.[174] In addition to its predicive value in STEMI, IMR may have similar utility in other ACS,[175] and also in the more general PCI patient population.[176]

IMR's use of mean transit time as a surrogate for flow will introduce variability due to differences in vascular volumes both between arteries in the same patient, and between patients. Also in the presence of a significant epicardial stenosis, where collateral circulation is not negligible, $1/T_{mn}$ will underestimate the flow. In such cases a measurement of coronary wedge pressure may be necessary.[177] The three bolus injections of saline to calculate mean transit times is fairly straight forward from a practical point of view, and the predictive value of IMR is encouraging, however, replacing the mean transit time index of flow with a measurement of volumetric flow would be desirable.

2.3.5.2 Continuous infusion techniques

A continuous infusion of room temperature saline can be used to provide a measurement of flow in the coronary arteries using temperature sensing guide wires.[178] Letting Q_b be the flow of blood in a vessel where an indicator is injected at a rate of Q_i ml/s, and letting the temperature of blood, the injected infusate and the downstream temperature of the mixed blood and infusate be T_b, T_i and T, respectively then,

$$Q_b = 1.08\frac{T_b - T_i}{T_b - T}Q_i \tag{2.33}$$

The factor 1.08 is required to correct for the difference in specific heat capacity of saline and blood. If the temperatures are all recorded relative to the temperature of the blood, i.e. $T_b = 0$, then this becomes:

$$Q = 1.08\frac{T}{T_i}Qi \tag{2.34}$$

There are a number of requirements for this method to work, chiefly that there is full

mixing of the blood and infusate before any bifurcation and prior to the temperature sensor. Dedicated infusion catheters with side holes aimed at maximising the rapid mixing of blood and saline have been designed specifically for use with intracoronary thermodilution injections.[179] The injection of saline may affect the underlying flow rate in non-hyperaemic conditions as saline has an vasodilatory action. The injection rate of saline is important, with rates of injection below 0.5 ml/s underestimating flow in the physiologic range.[180] In cases where a 3 cm length of artery proximal to a stenosis with no side branches is present where the infusion catheter can be placed, the reproducibility of the technique is very good in animal models and humans.[178] In practice, this requires a small catheter to be advanced (2.8F in this case) into the artery of interest, and a suitable site for measurement to be found. This makes the procedure more complex to perform (and potentially increasing the risk of adverse incidents) compared to the bolus injection technique.

The use of continuous infusion thermodilution to measure microvascular resistance has been described and trialled in humans.[181] Repeated flow measurements reported in the study had a fairly large variation ($r^2 = 0.71$; coefficient of variation approximately 20%), which may be attributable to the incomplete mixing of saline and blood prior to the distal thermistor.

2.4 Angiographic measures and indices of blood flow

There are a large number of methods that have been described to measure flow via the analysis of X-ray images, and these include:

- Bolus tracking techniques measuring the velocity, or some other time related index such as mean transit time, of contrast agent bolus as it propagates down a vessel;
- Droplet tracking using insoluble contrast agent;
- Indicator dilution methods;
- Optical flow techniques; and
- First pass distribution analysis.

These are described in a review by Shpilfoygel et al.[182] The application of these methods into the measurement of flow in the coronary arteries is frequently hampered by the nature of

coronary arterial system. The coronary arteries are complex three dimension structures and there is considerable movement during the cardiac cycle of the arteries. In two dimensional angiograms vessels often overlap during part or all of the cardiac cycle, and overlay different amount of underlying tissue as the heart beats, confounding videodensitometric analysis of arterial segments. Moreover blood flow down the coronary arteries is both rapid and pulsatile making a number of the techniques named above inapplicable in these arteries. Coronary angiography is also performed at lower X-ray dose per frame than other forms of angiography, making the images noisier, again complicating analysis. The following review focusses on methods that have been described on the coronary arteries.

2.4.1 Early measurement of absolute flow with angiography

The absolute measurement of blood flow via angiography requires the calibration of the signal intensity to projected mass (or thickness) of contrast medium in the beam, and/or the calibration of the sizes of projected objects in the X-ray beam back into the object plane (such as converting vessel diameter from pixels to mm).

Early attempts to measure flow using X-ray angiography, undertaken in the 1960s, were hindered by the equipment of the time, making the recording and analysis of time varying signal intensities cumbersome. Despite this, Ritishauser et al.[183] described a method of measuring flow by analysing the flow of contrast in an artery and presented results from a phantom and the carotid artery from five dogs. Two recording locations A and B were used separated by a distance ΔS along the artery. Time-intensity plots were made simultaneously at both A and B, and the difference between the mean transit time of two sites A and B was calculated as follows:

$$\Delta\bar{t} = \frac{\int c_B(t)tdt}{\int c_B(t)dt} - \frac{\int c_A(t)tdt}{\int c_A(t)dt} \tag{2.35}$$

Flow, $\bar{Q}$, could then be calculated as follows:

$$\bar{Q} = \left(\frac{d}{2}\right)^2 \pi \frac{\Delta S}{\Delta\bar{t}} \tag{2.36}$$

where d is the measured vessel diameter as measured in the projected image. The calibration of the scale in the projected image was performed using an object of known dimension

(inserted inside the arterial lumen in the animal experiments). Calibration was performed using a phantom containing cylinders of differing concentrations of iodine. In further work, the group extended their experiments to investigate flow measurements in the coronary arteries in dog models[184] and in the right coronary artery in humans.[185] The experiments in dogs yielded excellent correlation between the reference measurements using a flow meter and the angiographic method. In the human experiments, flow was measured in the right coronary artery of 13 subjects with angiographically normal arteries, producing a mean flow of 1.45 ml/s although no reference measurements were taken. A very similar technique was employed by Smith et al.[186].

Whilst technically impressive, and producing very promising results, the practical application of these experiments were limited in part by the equipment of the day making the process both cumbersome and difficult. The hard X-ray beam would have resulted in a low subject contrast of iodine, compounded by the relatively low output of the X-ray tube and low efficiency of the image intensifier by today's standards. The variability in the film processing and projection system, and geometric distortions in the image intensifier would have also reduced the quality of the recorded time-intensity curves. This appears to have been a particular issue in the animal measurements rather than the phantom measurements from inspection of the time-intensity curves presented in the manuscript.[183] Despite these initially very promising results, to the author's knowledge, no further attempts were made to use X-ray angiography to measure coronary flow by the late 1980s. The requirement for a fairly long, straight section of artery required for the two measurements of arterial mean transit time, more common in grafts and the RCA, may have restricted further adoption.[187]

The advent of digital imaging and more sophisticated and widespread microprocessor based computing devices, along with improvements in X-ray tubes, generators and detectors, led to researchers revisiting the use of X-ray angiography to derive information intended to benefit patients in the catheterisation laboratory. Often these developments were influenced by the other invasive measurements available at the time, such as intracoronary flow-velocity and pressure measurement wires. It is noteworthy that the assessment of flow by combining velocity and vessel cross sectional area as per equation 2.36 are developed into some of the latest angiographic analysis software (see Section 2.4.7 on page 59).

2.4.2 Time-based angiographic indices

Many of the time based indices of flow have the advantage of not requiring a known relationship between DSA signal and iodine mass. Improvements in the imaging equipment, with better image quality, also meant that analysing lower intensity signal changes in the myocardium as well as the epicardial vessels also became possible. Early work focussed on deriving a video densitometric measurement of CFR and was based on indicator dilution theory, relating flow, Q, vascular volume, V_V and the mean transit time T_{mn} of blood through the myocardium:

$$Q = \frac{V_V}{T_{mn}} \tag{2.37}$$

The increasing interest in invasive CFR in clinical practice no doubt influenced attempts to quantify blood flow using angiography, with the attraction that it was a relative flow measurement (hyperaemic to baseline flow).

Vogel et al.[188] calculated contrast arrival time in the myocardium, presenting arrival time images with the intensity modulated by the overall maximum signal intensity. Good correlation in changes of flow was seen between thermodilution flow measurements (using downstream sampling in the coronary vein) and the ratios of angiographic appearance time, and stress to rest appearance time was also associated with stenotic severity.

Whilst the measurement of appearance time has the advantage of only requiring a relatively short angiographic sequence, it cannot be related directly to flow. In contrast, the mean transit time, T_{mn}, can be related to flow via the blood volume. Relative measurements of flow can then be made by comparing ratios of mean transit time, or by assuming that the volume of blood in the myocardium is constant, $1/T_{mn}$ can be used as an index of mean blood flow. Excellent correlation between flow and $1/T_{mn}$ has been shown in both animal models[189,190] and human subjects.[191–195] However, $1/T_{mn}$ does not necessarily correlate to improvement in left ventricular function,[194] although this may be dependent upon the patient population.

Correction for differences in vascular volume have also been attempted, using the peak signal intensity (D_{max}) as a surrogate for vascular volume. The index of flow is therefore D_{max}/T_{mn} and this has been shown to correlate with lowered creatine kinase levels, and to improved left ventricular ejection fraction.[196] However, peak intensity is not a good surrogate for vascular volume, and is itself inversely related to flow.[197]

2.4.3 Coronary flow reserve based methods

The first attempt to measure a relative ratio of blood flow under hyperaemia to that at rest, i.e. CFR, was performed by Foerster et al.[198] who created a video densitometer, and measured the transit of a known mass of contrast agent. If $V(t)$ is the signal on the video densitometer at time t, then the integrated area under the curve due to the passage of contrast agent is:

$$A = \int V dt = k_1 \int m dt \tag{2.38}$$

where m is the total mass of contrast agent in the vessel, and k_1 a constant describing the (unknown but presumed linear) relationship between signal intensity and mass of iodine. As the mass of contrast agent injected M and flow Q are related $A = (M/Q)k_2$, where k_2 is a second calibration factor similar to k_1. It follows, if two injections of mass M_1 and M_2 are performed, yielding areas A_1 and A_2, that the ratio of the flows would be

$$\frac{Q_2}{Q_1} = \frac{M_2 \times A_1}{M_1 \times A_2} \tag{2.39}$$

Having demonstrated that the technique could measure relative flow accurately in a dog,[199] a small human study was performed.[198] Two contrast measurements were performed eight seconds apart, under the assumption that the first contrast injection would have induced hyperaemia, thus obtaining rest and stress measurements of flow. From eq. 2.39, the ratio of the areas measured by the densitometer should therefore estimate CFR. Sadly no reference values were available, although the relative flow measure did decrease with stenotic severity.

By assuming that T_{mn} could be approximated to time of arrival of the contrast medium, and that the vascular volume does not change between rest and hyperaemia, CFR has been estimated by $T_{app,b}/T_{app,h}$[188] where $T_{app,h}$ and $T_{app,b}$ are the contrast arrival time at hyperaemia and rest respectively. This was found to be inaccurate, and corrections for changes in regional blood volume using peak contrast densities were introduced by Hodgson et al.[200], viz.

$$\mathrm{CFR}_{angio} = \frac{D_h/T_{app,h}}{D_b/T_{app,b}} \tag{2.40}$$

$$= \frac{D_h T_{app,b}}{D_b T_{app,h}} \tag{2.41}$$

where D_h and D_b are mean maximal contrast density at hyperaemia and rest respectively. This approach has demonstrated a reasonable correlation between Doppler measured CFR and CFR_{angio},[201–204] but as described in section 2.4.2, the vascular volume is neither constant or directly related to maximum density, and T_{mn} can be estimated from T_{app}, were not supported by theory or evidence. Other indexes derived from time intensity curves (i.e. variation in image intensity over time) were also investigated, such as the reciprocal of the time to peak density, $1/T_p$, and rate of washout of contrast, but these were not widely adopted due to practical difficulties, such as the requirement for a prolonged acquisition sequence.[205] The measurement of RCFR (the ratio of CFR in a diseased and healthy vessel) via angiography has also been described,[191] but as with RCFR in general has not been widely adopted.

The use of a relative index such as CFR_{angio} is advantageous as it removes the requirement to know the relationship between DSA pixel intensity and mass of contrast medium in the beam, providing the same imaging conditions are utilised in the two image acquisition sequences being compared. Without a known relationship between pixel intensity and iodine mass density based measures of perfusion, such as maximum density, D_{max} on the TIC[189,206,207] will be subject to error. Another source of inaccuracy in CFR and CFR_{angio} is due to collateral supply of blood to the myocardium[208].

2.4.4 Automated blush grading methods

The development of an automated image analysis based assessment of blush grades as an alternative to the subjective myocardial blush grades, has been described. The system, named QuBE (Quantitative Blush Evaluator),[209] has been released as open source software. There is evidence that the computer evaluation of blush grades could provide better prognostic value than subjective brush grade analysis alone,[210,211] and that measures from QuBE correlate with CMR assessment of myocardial dysfunction.[212,213] However, more recent work has shown a weak association between QuBE and MBG,[214] indicating that there can be considerable overlap between QuBE scores and MBG grade,[215] and showed even no significant association between QuBE grade and subjective MBG scores.[216] Many of the positive trials of QuBE have involved the software's authors, and presumably the algorithm development was performed on images from the imaging systems used in the trials. This may limit the software's success on other imaging equipment, especially as substantial differences in image processing is found

between different X-ray systems. The ability for the QuBE software to discriminate contrast from background structures in the presence of cardiac motion is critical, and yet improved methods of removing cardiac motion have not been found to improve QuBE's performance.[216] The lack of uniformly positive association between QuBE and MBG, the absence of outcome data, and the development of more comprehensive methods of computer assessment of invasive imaging have no doubt overtaken the rather simplistic automated evaluation of blush grades, and indeed the QuBE software has not been updated for four years at the time of writing.[217]

2.4.5 Three dimensional assessment of arterial lumen

As previously described, the full morphological assessment of an artery from a single projection is incomplete in terms of representing its complex three dimensional shape. Using two or more views from different projection angles taken during the same phase of the heart cycle can improve the shape analysis of a coronary vessel. The use of rotational angiography, where the C-arm gantry is rotated around the patient during an angiogram, can provide such images. Rotational angiography has been used with subjective appraisal of the images for some time, and whilst it has shown promise in reducing radiation dose and contrast agent use,[218] and provides similar visual interpretation to standard angiography,[219] however, its use is not widespread. Nonetheless, the use of rotational angiography to provide a means to create full or partial models of the coronary arteries using computer reconstruction algorithms has been in development over a considerable period of time,[220–222] and is an option for most cardiac X-ray systems today. Typically two images from the same point in the cardiac cycle yet separated by a reasonable angle of view, are selected from a rotational angiogram. A semi-automated algorithm is used to identify corresponding landmarks within the arterial structures in both images from which a 3D model is created. An example of images and a reconstruction from a rotation angiogram is presented in figure 2.19. These models typically provide measurements of artery segment lengths, cross sectional area, and can demonstrate which projection angles minimise foreshortening for a given arterial segment.[221,223,224] Increasing levels of automation, including full automation,[225] will make such models more readily integrated into clinical use by avoiding manual identification of corresponding landmarks in the selected image pairs. The reconstruction of a 3D model of the artery also permits three dimensional QCA to be performed. 3D QCA has been compared to both intravascular ultrasound (IVUS) and optical

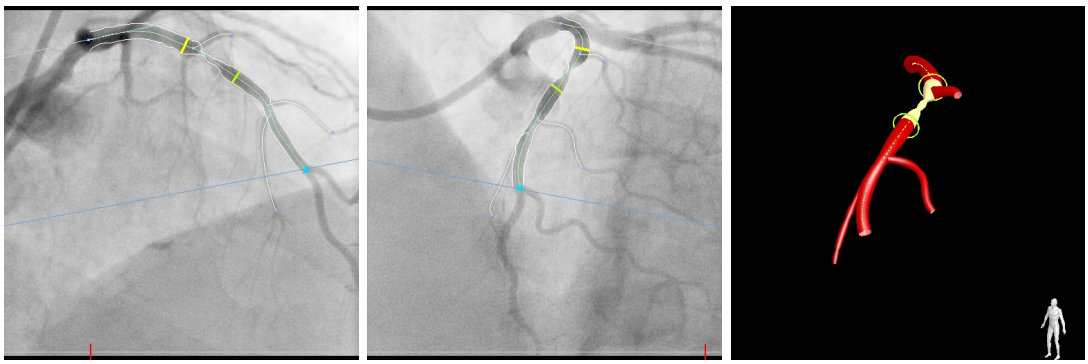

(a) (b) (c)

Figure 2.19: a) and b) are two images taken from a rotational angiographic sequence. The annotations on the image represent the semi-automated identification of matching segments in the image pair. Image c) is the reconstructed image.

coherence tomography (OCT), with both of these (and in particular IVUS) demonstrating larger luminal areas, especially in tortuous vessels (probably as the IVUS sensor is not aligned perpendicular to the vessel wall).[226] As might be expected, 3D QCA alone is limited in its correlation with FFR.[227]

2.4.6 Automated TIMI frame count

In addition to the visual inspection and QCA-like measurements from these reconstructed images, indexes of flow and FFR have also been developed. An automated TIMI frame count algorithm has been proposed by ten Brinke et al,[228] capable of using two standard angiograms taken at different angles to reconstruct the vessel tree whilst estimating the contrast transit velocity and therefore frame count, although the fully automated approach was not successful in reliably reconstructing the 3D vessel structure. This was likely due to the lack of precision in knowing the X-ray source and detector position with respect to the patient for both sequences, and also due to issues with automatically segmenting and identifying the arteries throughout the cardiac cycle in both sequence.

2.4.7 Angiographic assessment of FFR

Quantitative flow reserve (QFR),[229,230] now incorporated into a commercial software suite (Medis Suite XA, MEDIS Medical Imaging Systems B.V., Leiden, The Netherlands), uses a combination of blood flow-velocity measurements and geometric modelling of a vessel to calculate an estimate of FFR. QFR is a combination of 3D QCA and TIMI frame count.[231]

Unlike ten Brinke's approach, which used two standard angiograms, QFR separates the 3D reconstruction and frame counting into separate acquisitions, using a rotation angiogram for 3D information and a standard angiogram for contrast velocity measurement. Two images, at least 25 degrees apart from a rotational angiogram are chosen and used to create a 3D model of the artery. The model can then provide information on path lengths between arterial segments, and therefore be used with an automated TIMI frame count method on a standard angiogram, to calculate flow velocity.[232] Variations on the algorithm using fixed values of blood velocity, modelled hyperaemic velocity based on angiography without drug induced hyperaemia, and measures of velocity from angiography under drug induced hyperaemia have been compared, demonstrating that the both angiographic measurements (i.e. modelled from basal, and stress) were equally effective for predicting a stenosis with a pressure wire measured FFR of 0.8 or less.[233] The use of QFR without the use of pharmacologically induced hyperaemia have demonstrated QFR has good agreement with FFR,[234] and superior agreement with FFR to both QCA[235] and P_d/P_a.[236] The angle of difference between the views, whilst not important in circular lesions,[237] is likely to be important for the accurate modelling of non-circularly symmetric lesions. Vessel length measurements are however accurate when compared to IVUS.[238] The use of empirical parameters when converting the basal flow into the simulated hyperaemic flow are based on generalised findings from previous work,[233] containing a study population of 68 patients from a single centre study,[231] which may not suit a given individual or indeed patient population. In a similar developments to iFR, a hybrid approach has been tested, where QFR has been proposed as an initial test with cases in a zone of uncertainty progressing to have conventional FFR assessment.[239]

Another approach to the velocity and empirical model of QFR is to use the 3D model of an artery typically created via rotational angiography alongside computational fluid dynamic (CFD) modelling applied to the model. Reasonable agreement with a number of such models and invasive FFR have been reported.[240–244] In addition to the 3D model such methods must utilise a set of important boundary conditions and constraints—one of the main ones being the vascular resistance. These may be estimates taken from population studies (commonly used for myocardial resistance) or measurements performed alongside the imaging (such as aortic pressure). Whilst agreement between models and individual patients in tightly selected groups matching the population from which the estimates were taken (e.g. no MI, no acute

presentation within 60 days, no comorbidities) can be good when using a average population estimate, better results are likely if an individual measurement of microvascular resistance can be derived.[245,246] Indeed when considering a wider population, including acute and multi-vessel disease (but not STEMI), there were higher disagreement rates FFR(16%).[247] A meta analysis of the agreement between CFD models and invasive FFR showed generally good agreement, with a discordance in 12% of cases (n=1296), different computational approaches or software packages did not affect the agreement with FFR.[248]

Simplified models, aimed at eliminating the need for three dimensional data, use a one-dimensional arterial model to predict FFR, and have shown good agreement with three dimensional models, although the number of patients was limited (20), very few of the lesions studied appeared to have a predicted FFR of <0.85, and no account for correlations in the data (such as lesions coming from the same patient) was taken account of in the analysis.[249]

One of the issues in interpreting the findings of studies which include a large number of normal and severely abnormal patients, is that many of the patients have very severe or very limited disease, so there is likely to be good agreement with almost any measure of disease severity and FFR. Therefore the results of trials such as FAVOR II comparing QFR and FFR had only 32% of participants with intermediate stenosis (FFR between 0.75 and 0.85) should be interpreted with caution.[235] Larger studies, focussing on patients with intermediate disease, including long term outcome data are important.

The issue of boundary conditions for fluid dynamic models is an important one, and data from models of CT-FFR have demonstrated the largest sources of error are due to assumptions regarding the flow in the coronary circulation and resistance in the myocardium.[250] Indeed, the resistance of the micro-circulation is far more important than geometric variations in the models.[251] Using boundary conditions from normal, or highly selected, patient groups may limit the predictive value for a specific patient.[252]

It is also interesting to note the related work on FFR assessment using CT coronary angiography, which often uses computational fluid dynamic techniques to predict the flow limiting properties of a stenosis. Good agreement between CT-FFR and invasive FFR have been reported, with a recent meta-analysis indicating that a per vessel sensitivity and specificity of 0.85 and 0.82 respectively compared to invasive FFR.[253] However, the use of invasive FFR as a reference is flawed due to the limitations of pressure only assessment of FFR as

described in Section 2.3.3.2, and any fluid dynamic models will be limited by the assumptions in the boundary conditions in the same way as those derived from 3D data from rotational angiography from the catheterisation laboratory.

2.4.8 Mass-balance based absolute measures of flow from angiography

The measurement of absolute blood flow requires the calibration of pixel intensity to mass (or projected thickness) of contrast medium in the beam. The relationship between pixel intensity and iodine mass varies both between patients, but also within a patient for different imaging geometries.

2.4.8.1 Calibration schemes

A few such calibration schemes have been previously described. Firstly, a calibration image or sequence of images is acquired with a phantom containing objects of a known quantity of iodine or surrogate material, such as tin,[254] placed in the image frame. The signal intensity change for the known mass of iodine can then be measured, providing a constant calibration factor relating pixel intensity and mass of material. To measure the signal due to the iodine, the background anatomy must be removed, and this can be done in one of three ways. Most commonly, DSA is used (log subtraction of in image without the calibration phantom from one with it) to produce an image whose signal intensities relate only to the mass of iodine in the image field.[254,255] Secondly, energy subtraction can be used, where two or more images are acquired at different beam energies, and the differential attenuation of materials at the different beam energies can be used to isolate the material of interest.[256] Finally, computer analysis taking the mean signal levels around the calibration phantom to estimate the signal value if the phantom were not present can also be used.[257] Typically, calibration phantoms contain a number of details, each with a different mass of iodine. By summing the subtracted image pixels in the area of one of the details, the total signal caused by the known mass of iodine can be measured. This is normally averaged over all of the details, normalised to a set mass of iodine.

2.4.8.2 Flow measurement

Once a calibration is performed, an angiographic sequence containing the mass of contrast to be measured is acquired under identical imaging conditions. The calibration factor can then be used to infer the mass of contrast in the beam during the measurement sequence. For a contrast agent, with a known concentration of iodine, the mass can be converted into volume. By measuring the rate of change in this signal over time, flow can be measured. Consider an artery where contrast agent is injected, causing a complete replacement of blood at the arterial inlet with contrast medium. Two DSA images are acquired after the start of the injection, but before the contrast medium begins to exit via the venous outflow. The rate of accumulation of iodine mass into the system is therefore proportional to the flow of contrast agent into the artery. If the two images are acquired at times t_1 and t_2, flow can be calculated thus:

$$Q_S = \frac{c}{t_2 - t_1} \left(\sum_{x,y \in roi} dsa(x, y, t_2) - \sum_{x,y \in roi} dsa(x, y, t_1) \right) \tag{2.42}$$

where $dsa(x, y, t)$ gives the DSA pixel value at location (x,y) at time t, and c is a constant obtained from calibration relating pixel value to volume of contrast agent. It is also possible to measure arterial luminal volume by integrating only pixels within the epicardial vessels once these have filled with contrast and converting to volume using calibration. These techniques have been shown to provide accurate blood flow and vascular volume measurements in swine.[258–260]

It is important that the imaging conditions in both the calibration and measurement sequences are as near identical as practicable. Changes in radiographic factors, patient position, angulation or magnification will make the measurement inaccurate. The source to object distance for the organ of interest would ideally be the same as the source to test phantom distance, otherwise magnification differences will invalidate c as demonstrated in figure 2.9 on page 22.

2.4.8.3 FFR assessment from mass balance

The absolute measurement of blood flow alone is insufficient to measure FFR—it is also required to know the flow in the absence of a stenosis. There is evidence that the epicardial

luminal volume is related to the maximal flow in the normal vessel by the following relationship:[261,262]

$$Q_N = kV^{\frac{3}{4}} \tag{2.43}$$

Where Q_N is the maximal flow in an artery, V the arterial luminal volume, and k a scaling constant which will depend on the animal and organ under investigation. It is unknown if k varies between arteries within the human heart. With the estimation of Q_N the calculation of FFR is possible, and this has been demonstrated to be accurate in animal models.[263] It should be noted that the studies supporting this have been performed on swine, where it might be expected that arteries of the models were healthy. In cases of diffuse disease the arterial luminal volume may well be lower than than the native vessel, and therefore the normal hyperaemic flow in the artery would be underestimated (and the prediction of FFR therefore too high). There is also evidence that in addition to luminal volume, arterial branch length is also predictive of regional blood flow[261,263] and that this would not be subject to inaccuracies due to diffuse disease. Accurate measurements of length are not possible from a single angiogram, but could be provided by rotational angiography. It also remains to be demonstrated that this relationship is as reliable in humans.

The main issue with phantom-based calibration methods is, once again, due to the projection nature of the imaging system. When a patient is imaged, the heart must be framed appropriately, and to make the calibration, the phantom must be introduced to the scene. Placing the phantom on the detector would be the obvious location, but the patient's heart is some way towards the X-ray source and therefore magnified. As an object is moved towards the X-ray source its shadow is increased in size, but its intensity does not alter. Therefore, for a calibration phantom to work, the relative magnifications of the phantom and the heart must be known. With the phantom placed on the detector, its relative magnification compared to the heart is not likely to be known accurately. Molloi's methods involved placing the phantom on the exit surface of the animal, and using a fraction of the chest diameter to correct for the extra magnification of the heart.[263] Whilst this may be practicable in animal models, in humans this would limit the projection angles possible (for example any amount of lateral angulation would make the phantom placement impossible), and also presents a potential infection risk. Moreover, the magnification correction is only approximate. In the animal

experiments, the X-ray beam conditions were set manually whereas in human imaging this is impracticable, due to the considerable differences in patient body habitus, and differences in projected tissue thickness as beam angulation is altered. An ADC is used, and the normal operation of the ADC would alter the radiographic settings during a sequence to normalise the detector entrance dose as contrast is injected, effectively corrupting any TIC analysis.

2.5 The need for absolute flow assessment in the cardiac catheterisation laboratory

The use of invasive angiography for low risk cases is declining as alternatives such as CT, nuclear imaging and MRI become more readily available. As a result, acute presentations are become more important to the angiographic case load. In Sweden, acute presentations accounted for 70–80% of catheterisation laboratory cases, whereas 25 years earlier acute presentations accounted for only 20–30% of catheterisation laboratory cases.[264] In Ireland, 47% of PCIs were performed for acute cases in 2011.[265] Ideally, adequate information as to the best treatment for an individual patient will be available within the catheterisation laboratory, without sending the patient for further imaging. In the case of primary PCI, the time to revascularisation should be minimised as reducing the time between the onset of symptoms to revascularisation reduces mortality.[266] The need for rapid intervention precludes lengthy delays for other imaging, and it is unlikely that previous imaging, even if it exists for the patient, would be an adequate description of the current state of the patient's coronary circulation or myocardial state. Moreover, there are increasing rates of diabetes and multi-vessel disease, making the cases more complex.[264] It is important, therefore, that information on the haemodynamics of the heart can be rapidly assessed within the catheterisation laboratory.

Recently a tiered protocol of physiological assessment has been proposed, with a series of increasingly difficult or more invasive tests being used in a layered decision tree. In this way, the simpler tests are performed first and if sufficient evidence of ischaemia—or lack thereof—is found, a treatment plan is implemented.If not, the next test in the pathway performed. One example is the progression from angiography, iFR, and then FFR, first with contrast reactive hyperaemia, and finally adenosine induced hyperaemia.[145] Such schemes, whilst practically appealing, do not address the limitations of FFR. A similar approach using resting stenotic

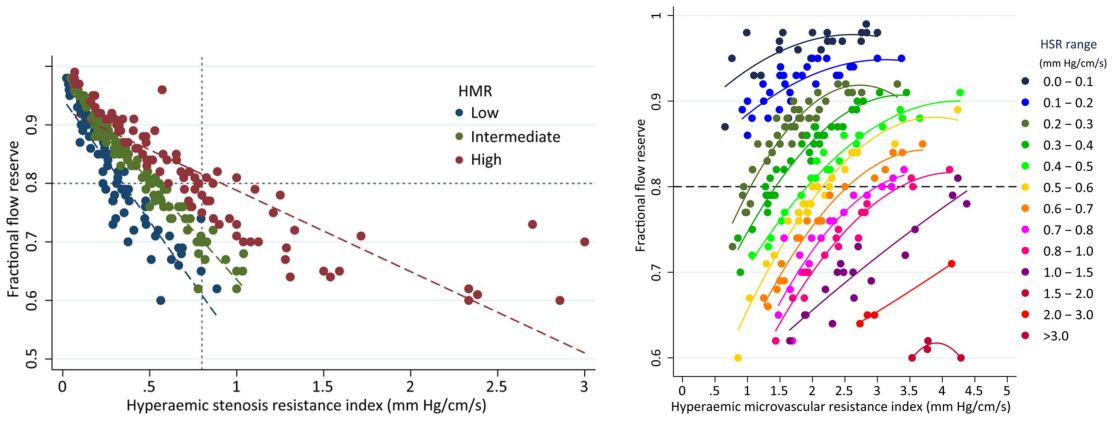

(a) (b)

Figure 2.20: Relationship between FFR and a) HMR and b) HSR for different values of myocardial and stenotic resistance respectively. Reproduced from van der Hoef et al.[270] with permission from BMJ Publishing Group Ltd.

pressure gradient then FFR has also be proposed.[267] FFR, assessed by pressure wire alone, lacks the theoretical foundation to be used as a reference as to the physiological significance of a stenotic a lesion.[126]

The existing physiological measurements available in the catheterisation laboratory, whilst all adding to the information from the anatomic information from the angiographic presentation of the arteries, are incomplete. Discordance between CFR and FFR occurs in approximately one third of cases.[268] The apparent discordance can be explained by considering that CFR is measured using only an index of flow (normally flow-velocity from Doppler ultrasound), and FFR via intracoronary pressure wire. The apparent discordance between CFR and FFR is explained by the consideration of both pressure and flow, rather than one or the other alone.[88,269] Figure 2.20a shows the effect of myocardial resistance on FFR. Patients with a low myocardial resistance but high stenotic resistance could have a "normal" CFR, but abnormal FFR (blue dots in the diagram), yet increased myocardial resistance leads some patients with a relatively high stenotic resistance (and therefore low CFR) to have a "normal" FFR (red dots). Figure 2.20b demonstrates that for a given stenotic resistance (for example the light green cases in the HSR range between 0.4–0.5 mm Hg s/cm), the FFR varies from 0.7 to 0.9 depending on the microvascular resistance. In other words, the apparent discordance between CFR and FFR can be readily explained by measurement of the resistances of both the stenosis and myocardium.[270]

Current indices of coronary flow available in the catheterisation laboratory, i.e. flow-

velocity from intracoronary Doppler and mean transit time from bolus thermodilution injection, also have their own limitations, not least in that they do no account for the vascular volume. Continuous infusion thermodilution can, in theory, provide absolute flow, but requires a dedicated infusion catheter, and cannot be used where bifurcations are close to the site of infusion as adequate mixing of the room temperature saline and blood cannot be guaranteed. Nonetheless, the use of these measures of flow, when combined with intracoronary pressure measurements, have enabled the assessment of stentotic and myocardial resistance. The predictive values of microvascular resistance from either IMR or HMR in assessing myocardial obstruction, infarct size, and ventricular remodelling are demonstrating that a move away from FFR alone could give more information, either relating to the patient's future prognosis or to guide further treatment. Interestingly, CFR often performs as well, or almost as well, as the myocardial resistance measure, but in the absence of an epicardial stenosis this is to be expected. The combination of high myocardial resistance with lowered CFR (indicating residual epicardial obstruction) has been shown to considerably outperform any of a range of single metrics in predicting MVO post-MI.[171] Developing such multi-faceted assessment (requiring pressure and flow indexes) is likely to be more useful than refining simpler indices such as FFR or iFR alone—increasingly it is being shown there is little to discriminate these indices.[271]

Previous attempts to measure flow, or indexes of flow, from angiography have not been widely adopted, and absolute measurement of flow is difficult due to the projection nature of the imaging system and the lack of calibration of the energy absorbed by the X-ray detector and signal intensity. Previous descriptions of a mass-balance based approach to overcome these limitations, whilst promising, require dedicated phantoms filled with contrast to calibrate the signal intensity to iodine mass. In phantoms and animal models this works well, but in human imaging placing the phantom on the patient during a case, and correcting for the change in magnification from the phantom to the heart, would introduce errors and would likely be impracticable. Nonetheless, the combination of both pressure wire and angiographic flow measurement have been used to estimate stenotic and myocardial resistance has been demonstrated in swine.[272]

An angiographic protocol for assessing absolute blood flow, which is straight forward to use in clinical practice (thus overcoming the practical limitation of requiring external calibration

phantoms), could therefore supplement intracoronary pressure wire assessment, providing resistance measurements for a stenotic lesion and the myocardium. Based on absolute flow, these would be an improvement on the current HSR and HMR measurements that rely on Doppler flow-velocity, or IMR that uses mean transit time, as these methods rely on imperfect surrogates for flow in their calculation. Accurate measurement of stenotic and myocardial resistance should lead to a more complete assessment of the coronary haemodynamics and therefore enable better decisions to be made as to the treatment options for individual patients.

Chapter 3

Reduction of radiation dose in coronary angiography

3.1 Introduction

Any additional X-ray imaging, such as that required by quantitative flow assessment, will increase the radiation dose to the patient. The X-ray acquisitions required for the measurement will have to made in additional to imaging performed during the standard procedure, or even if they can be used as an enhancement of one of the standard sequences, the duration of the acquisition may be increased. Given the harmful effects of ionising radiation on the body it is essential that any additional radiation required for the measurement of flow is minimised.

Even before any increase in radiation dose, the radiation exposure in PCI is amongst the higher levels of radiation exposure in medical imaging, and unlike other areas of X-ray imaging where dose levels have considerably reduced over time, between 1997 and 2007 the average radiation dose for angiography was the same as those recorded thirty years earlier, with effective dose ranges between 5.5 and 14 mSv for PCI, although there is considerable variation between studies.[273] In Leeds, comparing the two systems used throughout this thesis, dose area product (DAP) for PCI were reported as 2292 and 6338 cGy cm^2, clearly indicating that the age and specification of the system is an important factor.[49] Damage to the patient's skin at the point of beam entry is a particular concern in cardiac imaging, as dose levels can exceed the threshold required to cause both transient erythema and even deep wounds to the skin.[274,275] The skin is most at risk due to the exponential attenuation of X-rays leading to

the overwhelming majority of energy deposited within the patient from an X-ray exposure at in the 10-150 keV energy range, being in the soft tissue where the beam enters the patient. There is also the potential for longer term stochastic harm which could lead to radio-induced cancers, which is a particular concern in paediatric cases,[276] although CAD patients are older.

There are a number of ways that radiation dose to the patient can be reduced, some of which relate to the operation of the system (including field size selection, projection angles, X-ray detector positioning, and the duration of imaging), other relate to the patient's body habitus, and others are inherent to the dose control algorithms and settings in the system's ADC (such as target detector dose rate, frame rate, and beam energy). It is clearly not possible to alter the size of the patient, and it is also likely that quantitative imaging sequences would be acquired follow a prescriptive protocol, meaning that any reduction in dose for such sequences would then be derived from alterations to the system's ADC settings. The use of an X-ray beam whose energy is optimised to the task in hand (patient thickness and a specific mass area of iodine), has been shown to increase the image quality per unit of radiation dose in cardiac imaging.[53,55] This is achieved using a combination of spectral beam filters (a filter placed in between the tube exit and patient, normally in the collimator assembly), and tube potential difference (kV). A harder beam is more penetrating, and therefore results in a lower entrance-skin-dose for a given patient than a softer beam for the same detector dose. The harder beam, however, will reduce the subject contrast in the image and therefore the image quality can be reduced. The selection of the kV is performed by the ADC, and whilst there may be a number of pre-programmed options, defined by the equipment manufacturer, that can be selected (normally by a service engineer),[277] the arbitrary selection or modification of the kV-mA relationship by the end user is not available on current cardiac X-ray systems.

The selection of spectral beam filters, is normally programmable, and the filter selection has been shown to be effective in fluoroscopy[278–280] and in other areas of interventional radiology.[281] Mostly these filters are constructed of aluminium and copper, although K-edge filters (i.e. ones containing a k-absorption edge in the diagnostic X-ray energy range, such as samarium, tantalum, gadolinium and tin) have been investigated, but not found to be more effective than copper.[55,282–284] At the time of this experiment, the use of copper beam filtration was routine practice in cardiac fluoroscopy although practice varied between manufacturers,[285] but was not routinely used in acquisition imaging.[286]

3.2 Aims

The aim of this work was to describe the operation of the dose control system of the cardiac X-ray systems that were to be used in the study and to investigate if the radiation dose to patients could be reduced by introducing an additional X-ray beam filter in the acquisition mode, without undue reduction in the quality of the images that were produced.

3.3 Materials and methods

One of the cardiac catheterisation laboratories in Leeds—an Allura Xper FD10 (Philips Healthcare, Best, The Netherlands)—was modified to create a new low-dose operating mode selectable for coronary angiography. The mode was identical to the default operating mode, except that a 0.1 mm Cu plus 1 mm Al spectral beam filter was used in the acquisition mode. The default mode used no additional beam filter. The 1 mm of Al absorbs the secondary radiation emitted by the added Cu filter. The total filtration of the X-ray tube (without the added filter) was 2.7 mm Al. Both imaging modes used a frame rate of 15 fps and retained the same target detector dose. Two experiments were performed—a phantom study comparing entrance surface dose (ESD), and a clinical study comparing the image quality.

3.3.1 Phantom study

Measurements of ESD were performed using an extension of the method of Martin et al,[287] which were the standard protocol recommended by the Institute of Physics and Engineering in Medicine at the time. A PMMA phantom was used to simulate a patient, and Martin et al. proposed three phantoms—one of 20 cm PMMA thickness, one 30 cm PMMA thickness and one with 30 cm PMMA and 3 mm lead to induce the maximum output. For these purposes phantom thickness was varied between 10 and 30 cm using stack of PMMA blocks. Blocks of size $30 \times 30 \times 2.5$ cm and $30 \times 30 \times 1$ cm were stacked on the couch in combinations such as to achieve the desired phantom thickness. The experimental configuration is shown in Figure 3.1. The phantom was placed on the couch supported by two 5 cm thick wooden spacers to allow for an ionisation chamber to be placed at the entrance surface of the phantom. The C-arm was positioned vertically, with the X-ray tube under the couch. The couch height was adjusted to be 90 cm about the floor, resulting in the entrance surface of the phantom

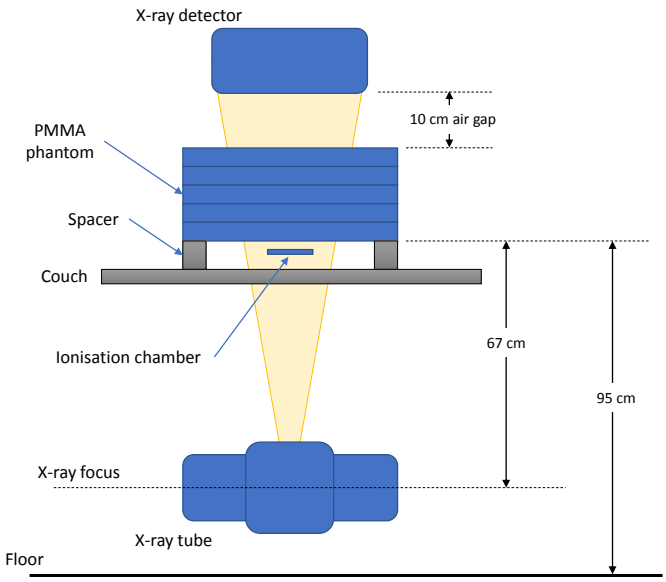

Figure 3.1: Configuration of the PMMA dose phantom.

being 95 cm above the floor.

An ionisation chambers was used positioned at the entrance surface of the phantom to measure the ESD including the scattered radiation from the phantom. The 20X6-6 ionisation chamber connected to a 2026C dose meter (Radcal Corp, Monrovia CA, USA) was used for phantom ESD measurements. The chamber and meter were calibrated using a service approved by the dose meter's manufacturer. All imaging was performed in the 20 cm field of view using both the standard and low-dose acquisition modes. Sufficient time for the automated dose control system to reach a set point was allowed before recording the dose rates. The X-ray anti-scatter grid was left in position in front of the detector as is standard in clinical use. The PMMA stack was initially made 10 cm high, and the X-ray detector assembly placed 10 cm from the exit of the phantom, and the dose rate measurement in both acquisition modes was performed. PMMA blocks were added increasing the thickness of the phantom 0.5 cm at a time, and the dose rate measurements repeated until the phantom thickness of 30 cm was achieved. As each block was added, the detector was repositioned to maintain the 10 cm distance between the phantom exit and the detector. For each measurement, the tube potential difference (kV), tube current (mA) and pulse duration (ms) at which the ADC settled were also recorded.

In addition to the dose measurements, the contrast loss due to the harder beam when the

reduced dose filtered X-ray beam was assessed. The experiment was performed on the phantom at 20 cm and 30 cm thicknesses of PMMA. A 0.3 mm thick tin detail, approximately 1 cm^2 in size, was placed at the entrance to the phantom to simulate the presence of iodine-based contrast agent (iodine and tin have very similar X-ray absorption characteristics). Using the 20 cm field of view, twenty-five images taken from acquisition sequences after the automatic dose control had stabilised were captured using a dedicated image capture device provided by the X-ray equipment manufacturer. The device attached parasitically onto the system's image chain, extracting data after correction for gain, offset and defect pixel correction (see Section 2.2.6 on page 29), but prior to any image enhancement with is normally applied prior to image display. Images were recorded prior to image enhancement processing that is normally applied to clinical images. The contrast of the tin detail was measured with respect to a neighbouring area of the image of similar size to the detail following the method of Gislason et al.[54]

3.3.2 Patient study

This study was approved by the local research ethics committee. Forty-eight patients from those undergoing PCI scheduled in the modified catheterisation laboratory were recruited into this study. Each patient gave informed written consent prior to participation. Each procedure was begun as normal using the standard X-ray operating mode for angiography. Radiation dose was measured using DAP–the product of the X-ray beam area and dose at a given distance from the X-ray source. As both X-ray beam area and radiation dose vary with the square of the distance to the X-ray source, with beam area rising dose decreasing, DAP is not independent of distance from the X-ray source. After at least four angiograms were performed, the DAP accrued from acquisition imaging was recorded, and the modified acquisition mode selected for the remaining procedure. The total DAP for the procedure for acquisition mode and fluoroscopy was recorded. The total number of images acquired in both angiographic modes was also recorded, and then used to calculate an average DAP rate for both acquisition modes.

Twelve months after the completion of the cases, four consultant cardiologists, four radiographers, and four clinical scientists (all working in cardiology) separately compared a selection of the standard dose and reduced dose images acquired in a double blind study. A

TG17 medical grade monitor (Philips Healthcare, Best, The Netherlands) was used to view all image sequences. All viewing was performed in a dedicated viewing room, which had dimmed ambient lighting and no light sources shining directly onto the monitor. All of the observers completed the viewing of the image sets in a single session without a break.

Observers viewed the images in pairs comprised of one sequence from the standard dose and one from the reduced dose set. The images in each pair were from the same patient, one pair per patient, with matching target artery, projection angle, and geometric set up (for example the same field of view). Thirty-five pairs of images were created, as in three patients no suitable matching image sequences were found. The images were displayed simultaneously, side-by-side on the monitor using software written in MATLAB. The sequences were made to have the same duration by truncating the longer sequence, and were played synchronously in a repeating loop. The left-right placement of the standard dose and reduced dose sequence was randomised by the display software for each sequence, and the order of sequences was also varied randomly for each observer. The MATLAB software allowed the user to select which of the left or right image sequence was perceived to have the higher quality, and the software wrote the response, along with the identifying codes for the image sequences into a log file for subsequent analysis. A single tailed sign test was used to test if the observers more often preferred the standard dose images, with a significance level of 5%. A binomial logistic regression model was also created to determine the influence of individual observers, clinical roles and the combination of observer and clinical role on the subjective image preference. The model was crated in SPSS v16.0 (SPSS, Chicago, USA).

For each patient, the patient's height, weight and chest diameter in the posterior-anterior (PA) axis were measured and recorded, and the body mass index (BMI) was calculated. For each procedure, the number of stents placed, the fluoroscopy time and overall procedural DAP were also recorded.

3.4 Results

3.4.1 Phantom study

The dose measurements with the phantom are shown in Figure 3.2. On average, across the range of phantom thicknesses studied, the filtered beam used in the low-dose acquisition mode

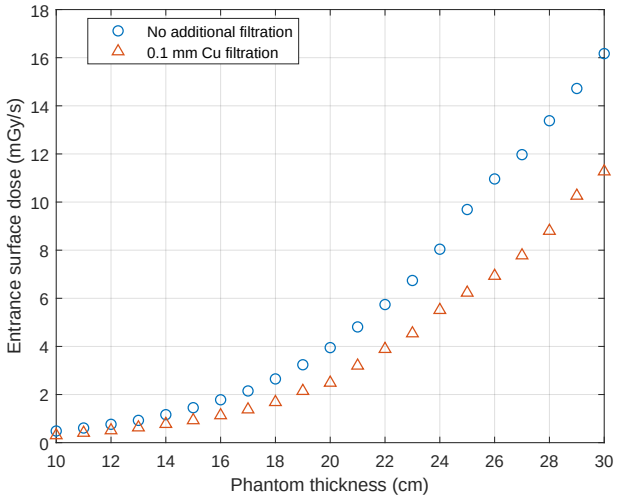

Figure 3.2: Phantom entrance surface dose for the standard acquisition mode (no added filter) to the low-dose mode (the additional Cu filtration) as a function of phantom thickness.

produced a reduced phantom ESD of 34% compared to the standard acquisition mode. There was a small increase in tube potential difference when the filter was used, shown in Figure 3.3, which varied from 0 to 5 kV, increasing with phantom thickness.

An examination of the kV-mA relationship, produced by plotting all of the kV against the mA values for each experimental configuration and shown in Figure 3.4, revealed the anti-isowatt ADC design[285] of the Philips' system. This design of ADC, in response to increasing phantom thickness, initially increases both the kV and mA proportionally (hence the initial slope of the kV-mA curve is a straight line), before a power limit is reached. After this point, further increases in phantom thickness produce an increase in kV, but with a reduction in mA to maintain a constant power output. From Figure 3.4 a power limit just under 72 kW is evident, which was achieved at approximately 77 kV. This inflection point can also be observed in Figure 3.3, where above phantom thickness of 24 cm, the kV began to rise more quickly as phantom thickness was increased.

The contrast of the tin detail was reduced by 0.02 for both phantom thicknesses, a relative difference of 3% and 5% for the 20 cm and 30 cm thick phantom respectively. Given the relatively large area of the tin detail and background regions used in the calculation of contrast, quantum noise had little influence on the calculated, and standard deviation of frame by frame contrast measurement was 0.0014, giving a standard error in the measurement of 2.86×10^{-4}.

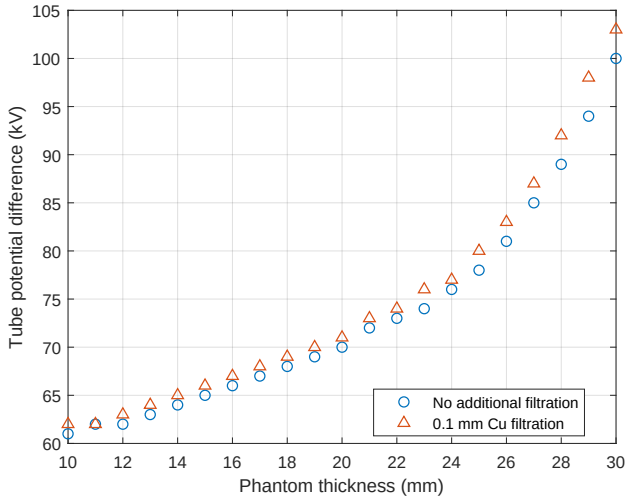

Figure 3.3: Tube potential difference for the standard acquisition mode (no added filter) to the low-dose mode (the additional Cu filtration) as a function of phantom thickness.

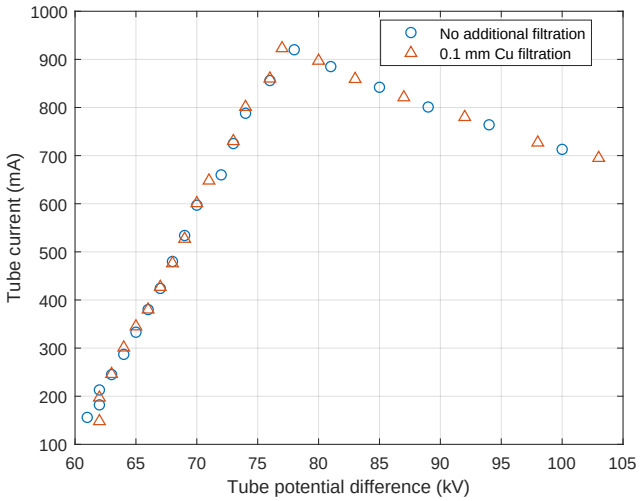

Figure 3.4: kV-mA operating curve for the dose control system, showing an anti-isowatt design with a power limit of 72 kW.

Phantom thickness (cm)	Standard mode	Low dose mode
20	0.65	0.63
30	0.41	0.39

Table 3.1: Contrast measurements of the tin detail in the phantom experiment.

Number of patients	48
Patient height (m)	1.69 ±0.08
Patient weight (kg)	83.9 ±16.4
Body mass index (kg m^{-2})	29.2 ±4.8
PA chest diameter (cm)	24.9 ±2.5
Mean number of stents per procedure [range]	1.6 ±0.9 [0, 5]
Median fluoroscopy time (min) [Q1 Q3]	11.0 [7, 14.9]
Median number of frames acquired [Q1 Q3]	948 [623, 1235]
Median procedural DAP (cGy cm^2) [Q1 Q3]	3805 [2245, 5138]

Table 3.2: Patient and procedure details (mean ±1 standard deviation unless otherwise stated); first and third quartiles [Q1 Q3] are shown where the median us presented.

3.4.2 Patient study

The patient and procedure characteristics are summarised in Table 3.2.

For the patient study the average DAP rates reduced by 43%, from 41.4 μGy s^{-1} to 23.8 μGy s^{-1}, when the filter mode was selected. Pooled observer scores analysed using a sign test showed no preference for the standard dose images (p=0.2). The regression model found no relationship between individual observer, clinical role or a combination of observer and clinical role was predictive of the preference score.

3.5 Discussion

There was a large ESD rate reduction when the addition copper filter was used both in the phantom and patient experiments. In the phantom experiments only one set of measurements were acquired, and therefore the variability associated with measurements of dose, kV and mA were not explicitly measured. For dose measurements, the major sources of variability would most likely be due to inaccuracy in the dose meter, in the positioning of the ionisation chamber, and in the measurement of distances in particular between the X-ray source and ionisation chamber. The dose meter used was calibrated by a national calibration centre, and the manufacturer specified an accuracy of 5% in the measurements. As all of the phantom measurements were acquired in one session where the equipment was positioned in the same location for the standard and low-dose measurements. As such any inaccuracy in the ionisation chamber position and distance measurements would introduce the same relative error between in the standard and low-dose measurements. Variation in the radiographic output by the X-ray system, as seen in the frame-by-frame differences in the contrast measurements were

minimal.

The difference in dose rates between the standard dose and low-dose modes using the Cu filter was larger in the patient experiment, and this difference may be due to the difference in composition between the human body compared to the phantom and the much greater variety in practice clinically. In particular the effect of field size choice may also have been a factor; different rates of use of the three available field sizes between the filtered and standard dose modes in the study may have occurred and as these magnification modes im. The reduction in ESD observed in this study is likely to be mirrored by a reduction in effective dose as the two are closely related in cardiac X-ray imaging.[288]

There was a very small increase in the tube voltage when the additional filtration was used (1 kV across most of the phantom thicknesses tested), which together with the beam hardening effect of the filter itself would be expected to reduce the contrast of the image compared to when no filter was used. Indeed a small reduction in contrast (3%) was noted with the tin detail on the 20 cm phantom. There was no evidence that this reduction in contrast was noticeable by the clinical observers.

The filtration proposed in this study was relatively thin at only 0.1 mm Cu, whereas in fluoroscopy, even at the time of the study, filtration of up to 0.9 mm Cu was fairly common. Increasing Cu filtration would place more attenuating material into the X-ray beam, hardening the beam further, both through the attenuation of the filter itself, but also as a result of the commensurate increase in kV given the anti-isowatt kV-mA response of the X-ray system's ADC. The result of this increased X-ray output would be a greater load on the X-ray tube, and larger loss in contrast than that observed in this experiment. The amount of dose reduction would be greater, however.

The effect on image quality of the filter in this study was only due to the loss in the contrast due to the beam hardening. The noise within the image, which is dictated by the photon fluence on the detector, should be approximately constant as the detector dose was kept constant between the filtered and standard dose modes. A greater dose reduction could be achieved if the detector target dose were also reduced, but this would also increase the noise within the image. The decision to retain the same detector dose between the two modes was deliberate and intended to keep a near parity between the two modes, permitting images acquired in the low-dose mode to be used in place of standard mode angiograms during a

patient's procedure, where they are interpreted by a clinical observer.

As well as being applicable to minimising the radiation dose in quantitative imaging, the findings can be generalised into the standard cardiac angiography. As the clinical observers could not detect a decrease in the image quality it may be assumed that the use of the 0.1 mm Cu spectral filtration can also be safely applied to general cardiac angiography, thereby substantially reducing the radiation dose for patients undergoing diagnostic and interventional procedures. This study was supported by the X-ray equipment manufacturer, and it is interesting to note that the systems introduced following this study have indeed featured spectral filtration in acquisition mode.[289,290]

3.6 Conclusion

A patient entrance surface dose was reduced by approximately 40% by introducing an additional 0.1 mm Cu spectral beam filter, with a negligible loss in image quality, which was undetectable by clinical users. As a result, the quantitative image protocols developed in the remainder of this thesis would utilise the lower dose operating mode. The wider implication were that the use of copper filtration in acquisition mode for standard coronary angiography would also be desirable, and would produce a substantial reduction in the dose delivered to patients.

Chapter 4

Cardiac digital subtraction angiography

4.1 Introduction

Most vascular procedures using X-ray imaging employ a technique called digital subtraction angiography (DSA). DSA removes background anatomy from an angiographic image sequence, allowing just the injected contrast agent to be viewed against a flat background. A series of images are acquired, with the injection of contrast agent initiated after the start of the X-ray acquisition. This creates a sequence with one or more images without contrast agent and a set of those with contrast. One of the contrast free images, referred to as a mask image, is selected and log-subtracted from subsequent images (see Section 2.2.6.1 on page 30 for further explanation). In an ideal situation, this creates a set of images where pixels within a region containing contrast agent have a negative value, and those without have a value of zero. DSA therefore facilitates the quantitative analysis of contrast agent in an image as the DSA signal intensity should reflect the mass-area of contrast agent,[291] and indeed the use of DSA as a vehicle for quantitative X-ray image has been recognised since DSA was introduced,[292] and has also been used as a processing step in quantitative cardiac imaging.[191,201,204,293,294]

Any movement of the patient causes mis-registration between the mask and contrast images, and produces artefacts in the subtraction images. In most areas of angiographic imaging such artefacts can be avoided if the patient remains still. In cardiac angiography, there is almost continuous movement of the heart. Whilst supine on the couch the patient is unlikely to

move, breathing, however, causes substantial motion in the image. As the patient breathes, the position of the heart and diaphragm alter in the image, and there is movement of the ribs and soft tissues surrounding the heart. For these reasons DSA has not been adopted in cardiac imaging.

Two solutions have been proposed to remove motion misregistration from coronary angiograms. Cardiac motion could be removed using a phase-matched selection of the mask image. By acquiring at least one full heart beats worth of images prior to the contrast injection, a set of possible mask images are obtained throughout the cardiac cycle, and therefore for each contrast image, selecting the mask image at the closest matching point in the cardiac cycle would minimise cardiac motion related artefacts. This approach has been used in previous work measuring flow from coronary angiography in animal models.[260,295,296] The frame rate used will have an effect on how closely matched in terms of the cardiac phase that the mask and contrast images could be. At standard frames rates of 15 fps used in the coronary angiography, there could be up to 33 ms difference between the mask and contrast image.

For the correction of breathing related artefacts, warping of the mask image, such that it is deformed to match the contrast image, has also been attempted.[297–301]

Further complications to the implementation of DSA on a cardiac X-ray system are the dose control mechanisms employed in the cine acquisition mode, and the image processing that is applied to the image sequences. The automatic dose control system employed in a DSA system is different to that used in cardiac angiography. Initially on both systems, estimates for the correct acquisition mode radiographic factors are made from the most recent fluoroscopic sequences. In cardiac angiography, once an acquisition sequence is initiated, the dose control operates using a feed forward control system—the signal level in the most recently acquired image is compared to a programmed target level, and the selected radiographic factors are updated with the intention of bringing the signal level in the next image closer to the programmed target level. In this way, the radiographic factors can alter on an image to image basis. This is not desirable for the acquisition of DSA sequences—if the mask image and subsequent images have different radiographic factors this will cause artefacts in the subtracted sequence, such as variations in the background intensity. For DSA dose control, at the start of the sequence a test shot is acquired using the parameters derived from the last fluoroscopy sequence. The resultant signal level is compared to the pre-programmed target

level. If the difference between the target and achieved dose is small enough, the acquisition sequence is then continued with the radiographic factors fixed for the rest of the sequence. If not, the radiographic parameters are adjusted, another test shot taken and the sequence continues if the test shot yields a signal level sufficiently close to the target value. This process is continued until either the radiographic factors are found that produce an acceptable dose to the detector, or the maximum permissible number of test shots is exceeded and the acquisition is terminated.

The main image processing stages in a cardiac imaging system are described in Section 2.2.6 on page 29. The feed forward automatic gain control (which normalises the pixel values to a set level) is used in cardiac imaging to prevent variation in the background pixel intensity when the automated dose control has not reached its set point (for example, darker or brighter images following a movement of the C-arm without the use of X-rays making the current radiographic settings inappropriate for the current projection). This processing also reacts to breathing, contrast injection, or indeed anything else that alters the image content and would therefore cause a mismatch in the pixel intensities between the mask and contrast image, which in turn would lead to an unacceptable subtraction image.

Working with the X-ray equipment manufacturer, alterations were made to implement a cardiac DSA system in one of the catheterisation laboratories in Leeds, comprising changes to the dose control settings, image processing and an in-room computer that could produce DSA sequences using a software provided by the equipment manufacturer. The additional spectral filter, which was shown to reduce patient dose in the previous chapter, was also employed in the DSA mode. The subtraction software was also provided as standalone software so that it could be applied to images at a later stage. The software implemented both a cardiac phase match subtraction with a system of warping the mask image to compensate for breathing motion artefact. This provided an opportunity to assess how effectively cardiac DSA could be implemented at the low frame rates used in modern coronary angiography, and whether the phase matched subtraction is improved by a means of correcting breathing related artefact.

4.1.1 Aims

The aims of the investigation presented in this chapter were as follows:

1. To devise a modification to the automatic dose control system which provided a stable

dose output for DSA imaging, whilst reacting to the large differences in projection used in cardiac imaging,

2. To test if a phase matched cardiac subtraction scheme with an automated image warping scheme for motion correction could be successful, gauged by producing an acceptable quality result in a sufficiently high fraction of cases, operating at the 15 fps used in standard cardiac angiography,

3. To investigate if breathing motion is successfully removed in using the image warping mask correction.

Secondary aims were to investigate whether the duration of image sequences were important (with the hypothesis that patients' ability to breath hold may decrease as the time they are required to do so is increased); to determine if the cardiac-DSA was also useful for the subjective presentation of cardiac angiograms, i.e. if human readers found the images easier to gauge the vessel lumen of the artery, or the myocardial blush (the darkening seen as contrast agent flows into the myocardium). Finally, the effect of the subtraction algorithm on the interpretation of subjective measures of blood flow (TMBG) was also assessed.

4.2 Materials and Methods

With the aid of the manufacturer two of the cardiac catheterisation laboratories in the General Infirmary at Leeds were modified to implement changes required for cardiac imaging. One of the systems featured the in-room DSA system provided by the manufcturer, and the other had equivalent changes to its acquisition protocols and a data capture device fitted to enable the recording of images prior to the normal image processing enhancement algorithms, allowing DSA sequences to be created off-line. Both catheterisation laboratories contained Allura FD10 X-ray systems (Philips Healthcare, Best, The Netherlands) was adapted to create a specific DSA imaging mode that could be selected by the radiographer at the table side control (allowing DSA to be selected for part of a procedure). The mode had a number of changes compared to the standard acquisition mode:

- A 0.1 mm Cu beam filter in acquisition to lower ESD rates.

- The feed forward automatic gain control commonly used in cardiac imaging (which normalises the mean signal intensity in an acquired image to a set level) was disabled and a fixed linear detector response was applied.

- The image receptor radiation dose rate was set to be constant when smaller fields of view were selected.

- The radiographic factors lock after the first five frames of an acquisition sequence, providing constant dose per frame throughout the remainder of the sequence.

- Bypass of the standard image enhancement algorithms and automatic gain control, so that these were not applied to images. Instead only offset, gain and defect correction were performed, and a linear response between pixel intensity and incident dose was selected on the detector with a fixed gain. A LUT was applied that had a logarithmic shape, scaled linearly to give the same range of possible output values as input values (2^{16}).

- Acquisition sequence start was synchronised to the next ECG R wave after foot pedal activation.

- Automated power injector coupling synchronised to the R wave following the acquisition start.

4.2.1 Subtraction algorithm

The subtraction algorithm used in this study was provided by the X-ray equipment manufacturer, Philips Healthcare. The subtraction software performed two main tasks—identification of the most suitable mask image for each contrast image using a cardiac phase matching algorithm (to remove cardiac motion related artefact from the subtraction sequences), and automated motion correction to remove residual motion artefacts (principally from breathing).[302] Firstly the software detected the contrast arrival in the scene, thereby allowing the identification of a set of mask images—i.e. each image before the contrast arrives, yielding a set of mask images each at different phases of the cardiac cycle. To calculate the subtracted image from a given contrast image, the set of available mask images was compared to the contrast image to find the closest match (i.e. the one most closely matching the cardiac phase).

The mask image matching each contrast image was recorded in a log file by the subtraction software. Once the corresponding mask was identified for a given contras image, movement correction was implemented using an analysis and warping of the mask image to match the contrast image in an attempt to account for other types of motion. A comparison between the subtraction algorithm used in this study to a standard subtraction using a single specified image frame as a mask image can be seen in Figure 4.1, where motion artefacts from the cardiac motion can be seen in the single mask sequence.

4.2.2 Clinical protocol

Ethical approval was sought and given by the local research ethics committee for this study. Patients were largely imaged as per the standard clinical protocol, but a small number of images sequences could be acquired using the DSA system. Patients undergoing elective PCI were enrolled onto the study. Acquisitions were performed using standard angiographic projections, replacing one or more of a patient's standard sequences with a DSA sequence. For each acquisition, contrast injection was delayed by at least one and a half times the duration of the patient's cardiac cycle, allowing at least one full heart beat of mask images with fixed radiographic factors before the contrast arrival. Prior to the DSA sequence acquisition patients were advised that they would be required to breath hold at inspiration, and the instruction to "hold your breath" was repeated continually during the sequence acquisition. The duration of the sequences was as per standard clinical practice, plus time for the mask images, therefore around 7 s duration was expected for a standard angiogram, and around 12 s was expected for one where the myocardial blush was to be imaged.

Up to four subtraction angiograms were acquired for each patient which were as follows: pre-intervention rest, pre-intervention stress, post intervention rest and post intervention stress. Hyperaemia was induced by an intraveneous injection of adenosine. Pre-intervention images were acquired in all patients. If pressure wire assessment was indicated during the case, stress imaging was also performed. If intervention was performed, the pre-intervention subtraction imaging was repeated. All images were transferred from the hospital to the University for the purposes of this study allowing both subtracted and unsubtracted sequences to be viewed.

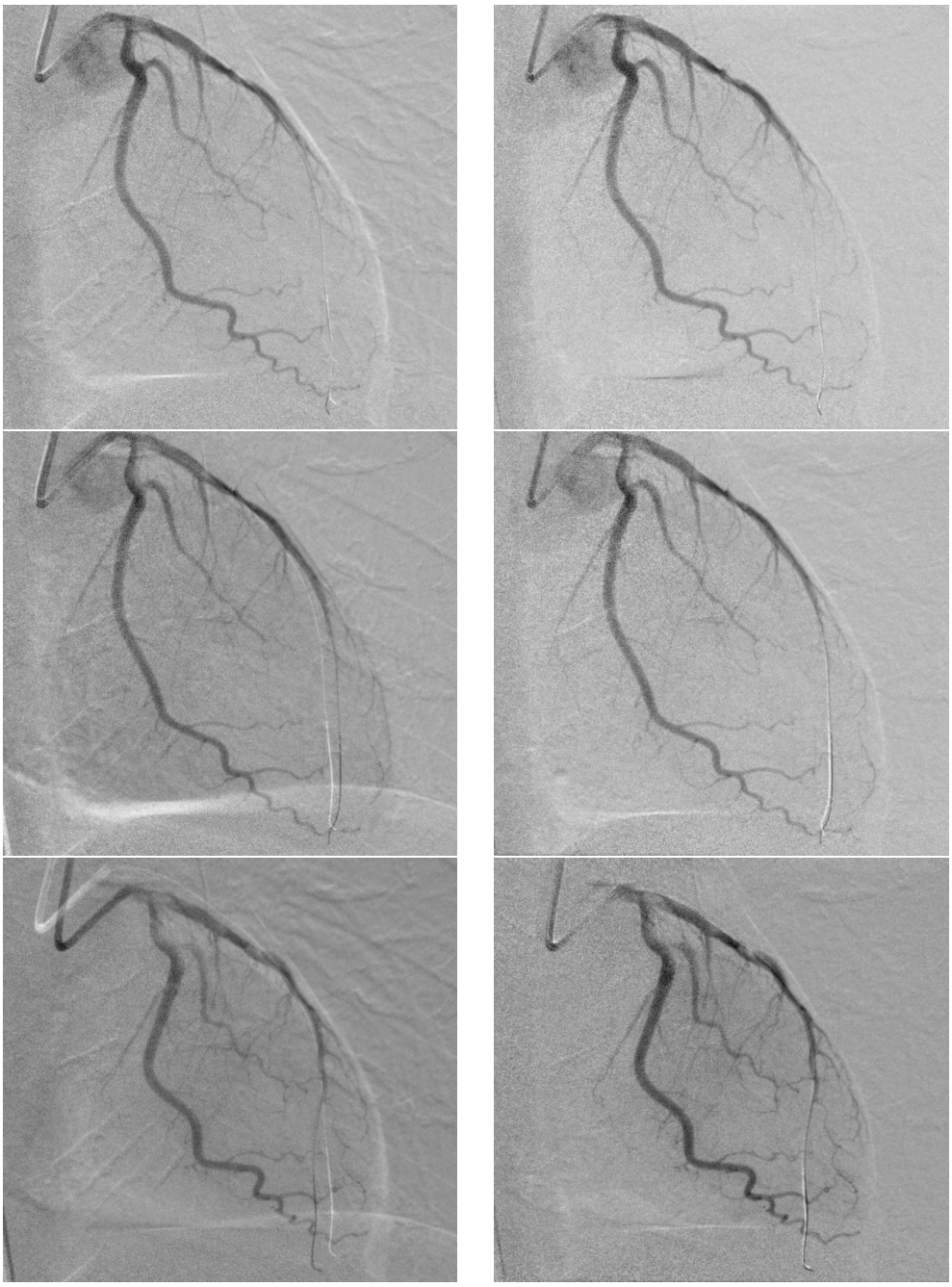

Figure 4.1: Selected frames at three points in the cardiac cycle from subtractions created using a single mask (left hand images) compared to the subtraction algorithm used in this study (right hand images). Cardiac motion artefacts are removed due to the matching of the mask and contrast images such that they are selected from the same part of the cardiac cycle.

4.2.3 Subtraction success rate

149 image sequences from 47 patients were acquired. DSA sequences were calculated offline using the dedicated software provided by Philips Healthcare. The acceptability of the DSA result was assessed by classifying images on an ordinal scale:

1. Negligible visible motion artefacts present;
2. Minor motion artefact that does not impinge on the visual appraisal of the coronary arteries or myocardial perfusion;
3. Major motion artefact that adversely affects the visibility of the coronary arteries or myocardial blush, but their assessment is still possible;
4. Considerable motion artefact making the image unacceptable for the appraisal of the coronary arteries or myocardial blush.

Every subtracted image sequence was appraised on the scale once per second—the first image was assessed, and the sequence advanced by one second and reappraised. This was repeated until the end of the sequence was reached. The scores at each second interval were pooled, and the percentage of the sequences falling into each category was calculated at every time point.

4.2.4 Efficacy of movement correction

The ability of the subtraction algorithm to correct for breathing motion was tested by selecting 15 image sequences. A non-movement corrected subtraction sequence was created using only the cardiac phase matching of the mask and contrast image. The log file from the subtraction software detailing which mask image was used for each contrast image. Software was written in MATLAB to read this file and the original image sequence, creating a phase matched only corrected subtraction sequence by performing a log subtraction of each contrast image using the previously identified matching mask image. In this way, two subtraction sequences were available—one using the full subtraction software, and one with the movement correction section omitted using the MATLAB functions. The 15 sequences were assessed by showing matching pairs of images from the two subtraction routines side by side. Every tenth frame (i.e. every 0.75 s) from each pair of sequences was displayed side by side, with the left–right

order randomised on each occasion. One observer scored the pair of images on a five point ordinal scale referring to the motion assessment in section 4.2.3 on page 87:

-2. Left image better than right image and would be rated in a more favourable category in the movement assessment.

-1. Left image better, but would fall into the same movement category as the right image.

0. No difference in the quality of the left and right images.

1. Right image better, but would fall into the same movement category as the left image.

2. Right image better than left image and would be rated in a more favourable category in the movement assessment.

The observer preference, frame number, which image was displayed on the left side, and the sequence number was recorded in a log file for subsequent analysis.

4.2.5 Subjective image preference

Thirty-five image sequences were selected at random to be included in an assessment of image quality. Eight observers were recruited from the catheterisation laboratory staff at the General Infirmary at Leeds. Six observers were interventional cardiologists with 25, 5, 31, 20, 14 and 5 years' experience and two dedicated catheter lab radiographers, one with 10 years' experience and the other with over 20 years' experience. For each observer the image sequences were shown in a random order, with observers scoring as many sequences as permitted by their time available, with a minimum of 12 sequences required. For each sequence the standard image was viewed first, followed by the subtracted image. No computer enhancement was performed on either the DSA or the unsubtracted image. Observers scored each image for two criteria: firstly the quality of the presentation of the coronary artery lumen, and secondly for the visibility of the myocardial blush. The image sequences were scored on a five point ordinal scale where 1=very poor, 2=poor, 3=acceptable, 4=good, and 5=excellent. All viewing was performed in a dedicated viewing room in the cardiology department, with dimmed ambient lighting. A medical grade RadiForce RX340 monitor (Eizo Corporation, Ishikawa, Japan) was used for all sequences. The monitor was attached to a personal computer and the ImageJ software version 1.47 software[303] was used to display the images. All sequences were converted

Grade	Description
0	Dye fails to enter the microvasculature
1	Dye slowly enters but fails to exit the microvasculature
2	Delayed entry and exit of dye from the microvasculature
3	Normal entry and exit of dye from the microvasculature

Table 4.1: Overview of the TMBG system (adapted from[70]).

to the tagged image file format, and playback was at 15 frames per second. The images were scaled to fill the 33 cm × 44 cm monitor (whilst maintaining the original aspect ratio). Observers sat approximately one metre away from the screen.

4.2.6 Effect on visual blush grade and stenosis severity

Six of the observers (the cardiologists) also scored each image sequence according to the TMBG four point scale summarised in Table 4.1. (A description of angiographic blush grades is given in Section 2.2.7.2, on page 32.) The same observers also were asked to report the maximum percentage stenosis visible of the most significant lesion present in the image.

4.2.7 Statistical analysis

All analyses were completed using the statistical software R (R Foundation for Statistical Computing, Vienna, Austria) and MATLAB. Cumulative link mixed models allowing for paired data with clustering were used to investigate differences between standard and DSA image sequences assessed using the 1 to 5 categorical scale for visualisation of the epicardial coronary arteries and myocardial blush, and using the 0 to 3 TMPG. Linear mixed effects models[304] allowing for paired data with clustering were used to investigate differences between standard and DSA image sequences assessed using the continuous percentage scale for stenosis severity. Pairing was used because the same image sequences were presented in both their standard and DSA form. Each observer rated several sequences, therefore the observations could not be classed as independent, hence clustering was incorporated into the analysis. Each cluster represented a single observer due to expected intra-observer similarities in image grading.

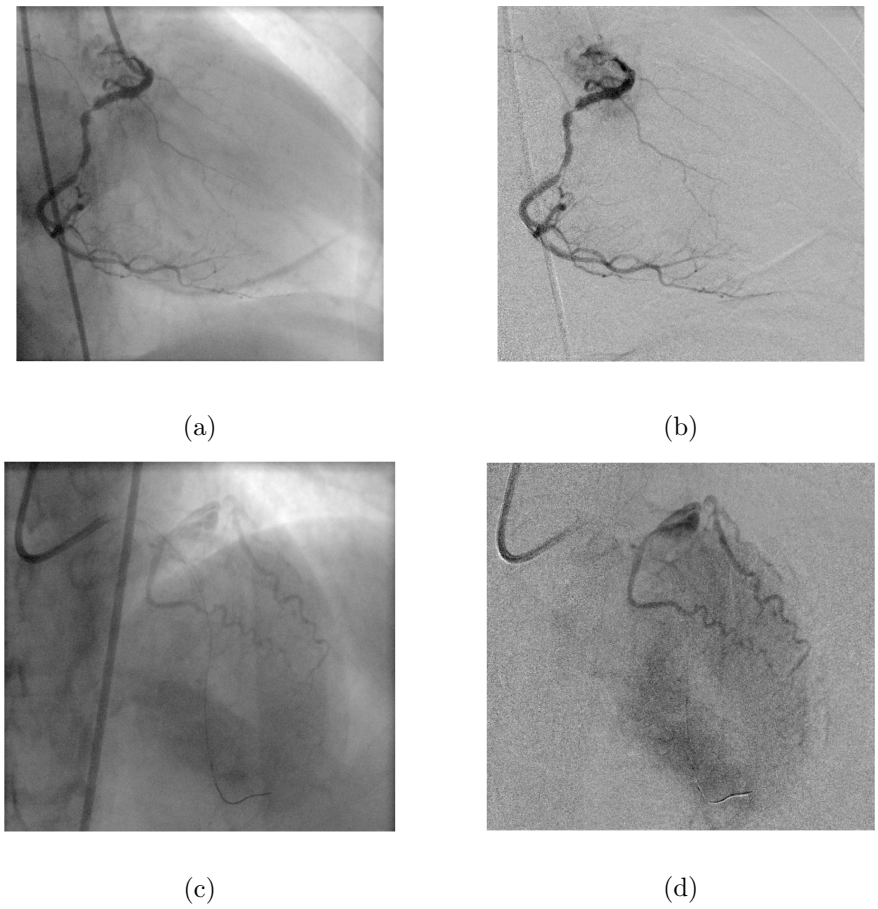

(a) (b)

(c) (d)

Figure 4.2: Comparisons of unsubtracted and subtracted versions of the same image in the coronary phase (a & b) showing a severe proximal stenosis to the LAD and myocardial phase (c & d) showing reperfusion of the myocardium supplied by the circumflex artery following intervention. The unsubtracted images are in the left column (images a & c), and the subtracted images are shown to the right (images b & d).

4.3 Results

Example comparison frames showing unsubtracted and subtracted versions of the same image are shown in Figure 4.2.

The mean duration of the subtraction acquisitions was 10.8 s, with the mean duration of the calculated subtraction sequence being 9.3 s. The number of sequences that were available at each second assessment point is given in Figure 4.3. Over 50% of sequences were 9 s or longer in duration, but beyond 10 s there are relatively few examples (e.g. 35 at 11 s, and 7 at 14 s).

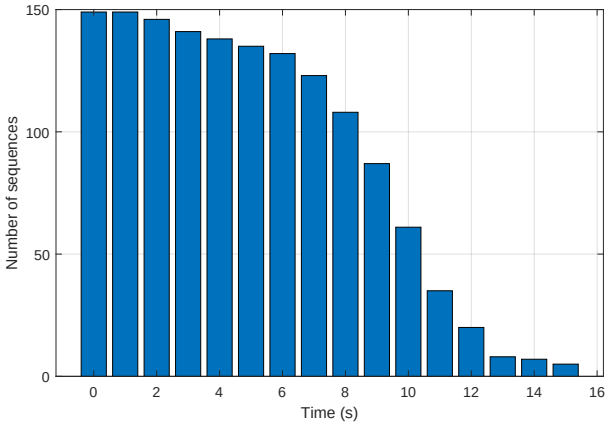

Figure 4.3: Number of sequences at each assessment time point.

4.3.1 Subtraction success rate

The number of images sequences assessed for motion artefacts as a function of time is shown in Figure 4.5. Overall, the phase matched subtraction performed well in removing cardiac motion related artefacts, and the main cause of misregistration artefact seen in the images was due to breathing motion. It was common for patients to be able to breath hold well for short periods of time, meaning that early in the subtracted sequences the majority had few motion artefacts—the percentage of cases with negligible or minor artefacts at the beginning of the subtracted sequence was 96%. The longer the sequence in duration, fewer patients could adequately breath hold introducing motion artefacts, with 74%, 58% and 41% of sequences having negligible or minor motion artefacts at 3, 5 and 10 s respectively. Example images being scored in the different categories are shown in Figure 4.4. These are shown in pairs showing the worsening of the motion artefacts as sequences progressed.

The percentage of each case being assessed as belonging to each of the ordinal acceptability categories is shown in Figure 4.5, which shows an increasing level of motion artefacts as the sequences become longer in duration. At the start of the sequences, 75.8% of sequences showed negligible motion artefacts, yet by 5 s this was reduced to only 5.2% of sequences. At 4 s, just under 90% of cases were still of acceptable quality, although 27.5% contained significant motion artefacts.

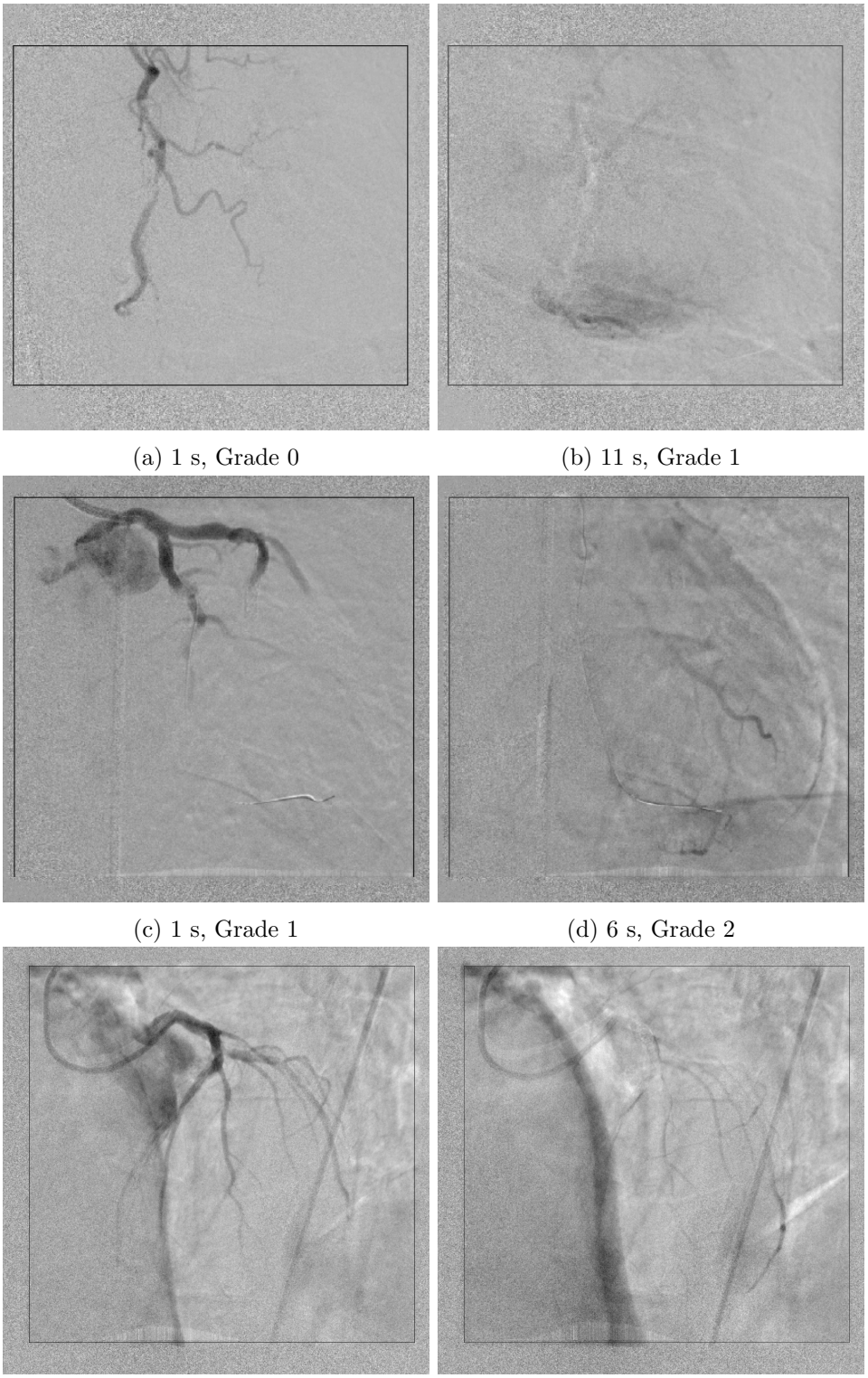

(a) 1 s, Grade 0

(b) 11 s, Grade 1

(c) 1 s, Grade 1

(d) 6 s, Grade 2

(e) 2 s, Grade 2

(f) 4 s, Grade 3

Figure 4.4: Pairs of images (a-b, b-c and c-d) from three DSA sequences, with the right hand image taken from a later point in the acquisition sequence to the left image. Beneath each frame, the time within the sequence when it was taken is shown, along with the quality grade (bigger score indicates worse quality). In each pair of images, misregistration artefacts worsen as the sequences progress over time.

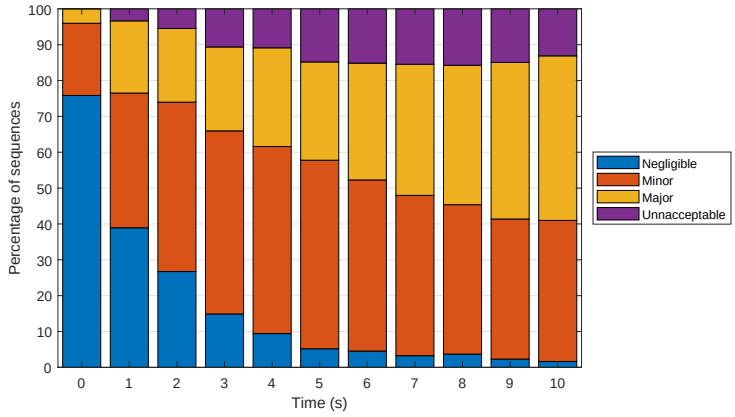

Figure 4.5: The percentage of sequences assessed as being in each movement category as a function of time.

4.3.2 Efficacy of the motion correction

In the paired image comparisons, in 55 images the cardiac phase matched only image was preferred, in 48 cases the motion corrected image was preferred, and in the remaining 130 comparisons no difference in the quality was found. Looking at the fifteen sequences, the modal score for each sequence (i.e. the mode of the scores for each 10 frame observation) indicated a preference for the cardiac phase matched only sequences in two cases, a preference for the motion corrected image in two cases, and no preference in the remaining 11 cases. Example images from the comparison are shown in Figure 4.6. Only one image frame in the 233 compared would have been rated in a different motion category from its comparator (i.e. only one score of -2 or 2 was found).

4.3.3 Subjective image preference

Comparing the subjective image preference scores, the statistical model showed a significant preference for the unsubtracted sequences when viewing the coronary arteries ($p = 3.92 \times 10^{-5}$). This preference was reversed when assessing the mycardial blush, where there was a significant preference for subtracted images ($p = 6.47 \times 10^{-16}$). Histograms of the quality score distributions for both the coronary artery and myocardial blush scores are shown in Figure 4.7.

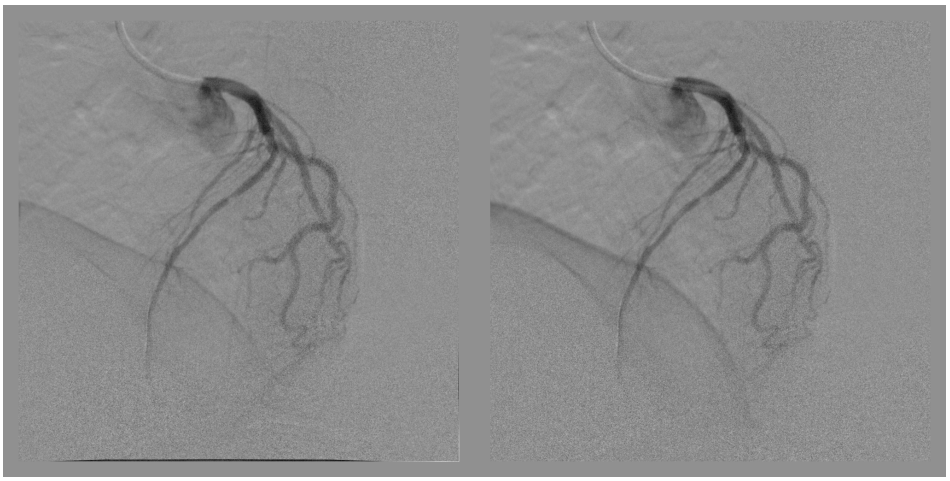

(a) Movement corrected image on the left

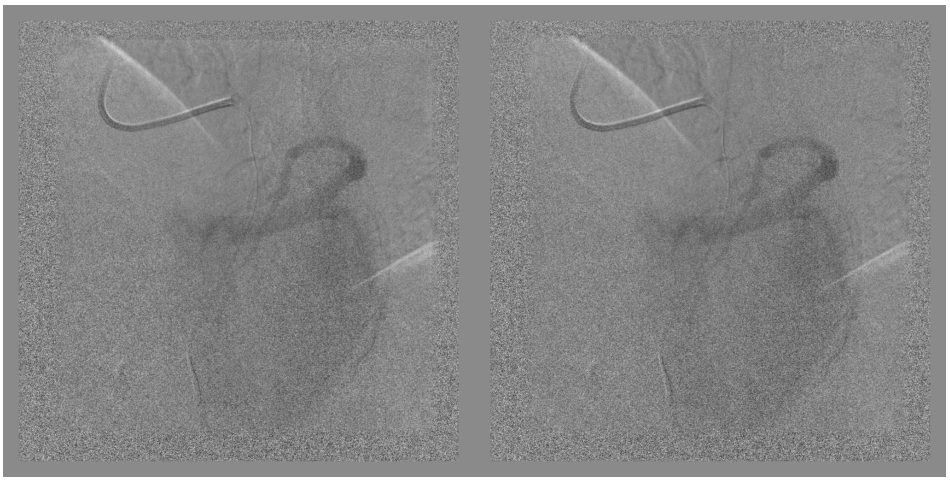

(b) Movement corrected image on the left

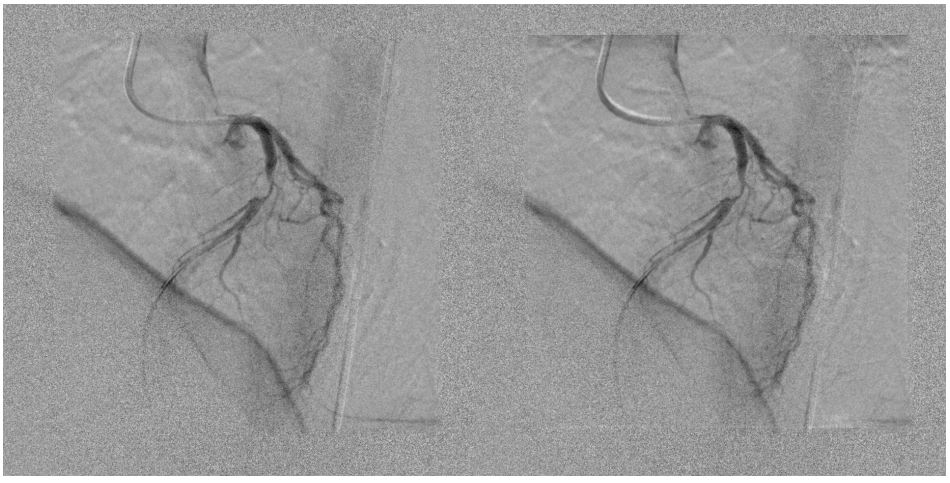

(c) Movement corrected image on the right

Figure 4.6: Pairs of images comparing motion corrected to non motion corrected subtraction algorithms. The motion corrected image was preferred in a), no preference was given for b), and the non-corrected image was preferred in c).

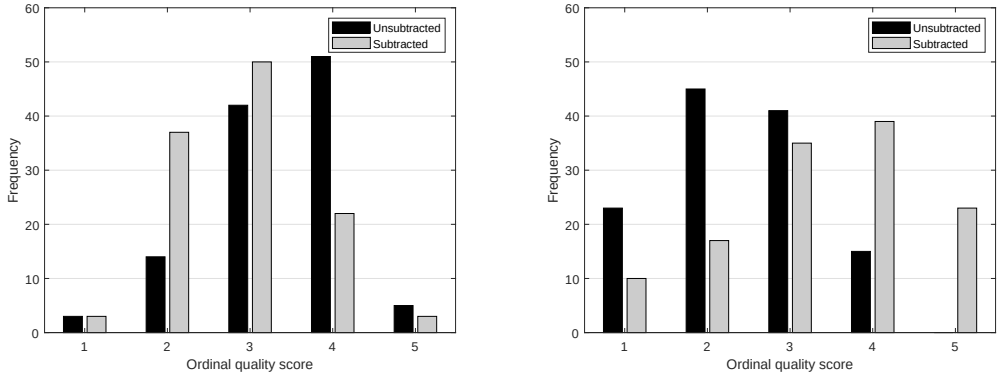

(a) Coronary arteries (b) Myocardial blush

Figure 4.7: Histograms showing the distribution of image quality scores for a) the coronary arteries, and b) myocardial blush.

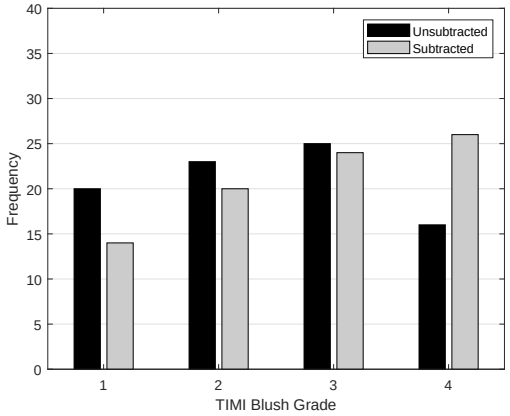

Figure 4.8: Distribution of the TMBG grade scores for the unsubtracted and subtracted sequences.

4.3.4 Effect on visual blush grade and stenosis severity

No significant difference was found in the stenotic severity scores ($p = 0.77$) between the unsubtracted and subtracted images, nor was there any significant difference in the TMBG scores. A histogram of the TMBG scores is shown in Figure 4.8.

4.4 Discussion

The sequences acquired using the subtraction mode demonstrated consistent signal levels and noise content indicating that the dose control had stabilised at a suitable set point, despite only being active for a short period. No undue variations in background signal intensity or contrast of the signals from the contrast agent in the scene was observed. The frequency

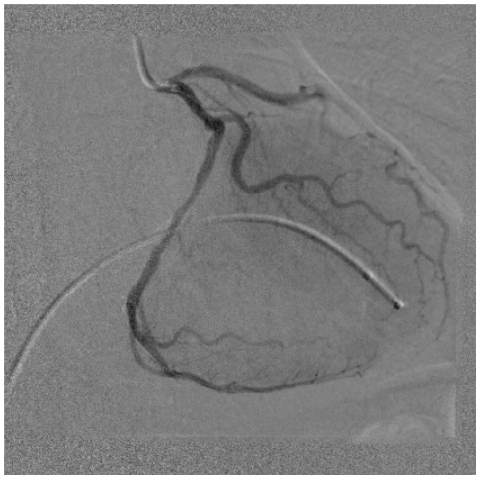

Figure 4.9: Subtraction image showing good registration of bone and soft tissue, with only a minor bright area at the top right of the image on the heart border, probably due to an imperfect match in cardiac phase between the mask and contrast image. There is also misregistration artefact of a pacing lead.

and severity of misregistration artefacts increased as the duration of the image sequence increased. Artefacts relating to cardiac motion were well controlled, indicating that the phase matched subtraction algorithm was viable despite the relatively low acquisition frame rate. Figure Figure 4.9 shows an example subtracted image with a minor bright area in the top right of the heart margin, which was most likely due to a mismatch in the phase of the mask and contrast images.

Larger artefacts were due to breathing related motion, and the algorithm supplied by the equipment manufacturer was far less successful in correcting for motion due to breathing. The comparison of the motion corrected images against the phase matched only images demonstrated no overall preference for either sequence when the motion correction was employed. This is likely due to the fact that cardiac motion is well corrected for by the cardiac phase matching of the mask and contrast image, yet motion due to breathing was not well corrected by the motion correction algorithm. In other words, the complex overlapping of structures of the chest during respiration cannot be compensated in the final two dimensional projection image with the image warping used by the algorithm in this study. In addition to misregistration of anatomy, misregistration of catheters and other interventional devices such as pacing leads also occurred and such an artefact is also visible in Figure 4.9.

A number of techniques have been proposed for coronary subtraction images without temporal subtraction. These techniques analyse images in an angiographic sequences containing

contrast agent and attempt to create a mask image to perform the subtraction. The mask images are an estimate of the signal intensity in the image if the iodine were not present. A number of approaches have been proposed to create such images, ranging from averaging local areas by taking the median, interpolation, detection of inflowing contrast into an artery,[305] motion layer analysis,[300,306,307] local motion correction[298] and using image in-painting methods.[257] These methods have focussed on the production of subtraction images of the coronary arteries alone, and are not likely to produce acceptable results for non-arterial phases of contrast transit, and as such would be unsuitable for the quantitative analysis of signal intensities. Methods such as those described by Yamamoto et al.,[308] where a mask is created from the image a recent images within a sequence would not operate well on the myocardial blush; the slower transit of contrast through the myocardium would result in this signal being incorporated into the mask image, and therefore such algorithms are not likely to give the same improvement in blush visibility as found in this study. It is also the case that the majority of descriptions of the algorithms do not include a comprehensive evaluation of image quality.[300,307] Energy based subtraction has also been proposed and used in the analysis of blood flow, but has not been implemented on a clinical X-ray system.[309]

In terms of the preference scores, observers preferred the unsubtracted images for viewing the coronary phase of contrast transit, yet the subtracted image for the myocardial phase. The coronary arteries are of high contrast, and therefore stand out well against the other anatomy on the unsubtracted image, limiting any advantages in the subtraction. The lack of additional conspicuity of the artery, and familiarity with the unsubtracted images may have been responsible for the preference for the unsubtracted images. When assessing the myocardial blush, the contrast agent is dispersed over a larger area in the image, and therefore produces a much lower differential signal to the coronary arteries. In this case subtraction has an advantage, as the removal of the underlying anatomy can make such signals easier to appreciate, and despite mis-registration artefacts in most sequences by the time the contrast is entering the myocardium, observers preferred these sequences. The subtracted images will be noisier than the unsubtracted images, as in this study the unsubtracted image shown to the observers came from the same acquisition sequence as the subtracted image. In most vascular applications the image detector target dose is increased in subtraction imaging to reduce this effect, but these results suggest that cardiac DSA can be implemented without an

increase in radiation dose to the patient.

The study has a number of limitations. The assessment of the degree of misregistration artefacts was performed on a subjective scale, and therefore a direct relationship to the degree of influence on a quantitative analysis of pixel intensities in the sequence cannot be made. Moreover, these subjective assessments were performed once by a signle observer, so no assessment of inter or intra observer variability has been made. An analysis of the misregistration artefacts alone would have been impossible using the sequences that were acquired, which contained both the intensity changes due to misregistration, but also those from the injection of contrast agent. The subjective approach did therefore allow the observer to visually compare the degree of motion misregistration to the signal intensity provoked by the contrast agent. The number of observers completing all of the image comparisons was also limited, but in the preference study the use of the modelling in the analysis made account of the different image sets viewed by some of the observers.

4.5 Conclusions

Cardiac DSA can be successfully implemented in clinical practice at standard frames rates of 15 fps. Motion artefacts due to cardiac motion can be corrected for by using multiple mask images acquired throughout at least one heart beat before the contrast injection begins. Motion artefacts due to breathing, however, were not successfully removed, even with the use of a complex motion correction algorithm. Breathing motion artefacts are the main reason for decreased image quality in cardiac subtraction imaging, but nonetheless, for a five second sequence, over 90% of sequences were found to be of acceptable quality. It is essential that the clinical team are attentive to clearly communicating to the patient the need to breath hold during the sequence acquisition. The unsubtracted images of the coronary arteries were preferred by the clinical observers in this study compared to the subtracted images, and there was no difference in scoring of stenotic severity. Given this, there is no compelling case for the introduction of subtraction imaging for routine coronary angiography. The situation is different if the myocardial blush is to be assessed, where despite increase levels of motion artefact compared to those earlier in the sequence, there was a significant preference for the subtracted images. The use of subtraction imaging is therefore recommended, and viable, for

the subjective assessment of myocardial perfusion using X-ray angiography. In cases where motion artefacts are large enough in magnitude making the subtracted image unacceptable (approximately 17% of cases), the subtraction can be turned off, and the unsubtracted image viewed instead. The implications for quantitative assessment of the sequences are that any imaging should be kept as short as possible in duration; cardiac motion can be corrected using a phase match algorithm, but breathing artefacts cannot be corrected, and become worse the longer the sequence continues.

As well as the ability to overcome the cardiac motion to produce images only containing the contrast agent, the protocols used for the DSA acquisition also required stable radiographic output and disabling of the automatic gain and image enhancement algorithms. Fixing the radiographic factors after a short number of frames allows the stable radiographic output after establishing a safe and appropriate level of X-ray output for the current angiographic projection; the patient would not receive a dose higher than that required to produce an acceptable image, nor would the dose be too low so as to produce images of sub-standard quality. With the fixed radiographic output and disabled image processing, the image sequences retained a consistent characteristic response of pixel intensity to dose incident upon the X-ray detector. As a result, the response to changes in contrast agent is stable between images in a sequence. Moreover, if two sequences are taken of exactly the same scene, the dose control should settle at the same output, and therefore the two sequences are comparable. This feature allows contrast volume change in two sequences to be compared, creating a relative flow measurement, and such a relative flow measurement is investigated in the following chapter.

Chapter 5

Relative flow measurement using X-ray angiography

5.1 Introduction

The success of the phased matched subtraction imaging described in the previous chapter suggested that the technique could be used to facilitate the analysis of contrast agent transit through the coronary arteries and myocardium, providing that the patient was able to breath hold adequately during the acquisition sequence. The changes made to the dose control schemes meant that once the first few sequences had been acquired, the X-ray output was constant, which was necessary to produce a good quality subtraction result. It would also permit the relative change in contrast agent volume to be calculated during a single sequence.

The purpose of the work described in this chapter was to explore the combined analysis of two sequences from the same patient to create a relative measure of flow, in this case to assess the improvement in blood flow following intervention. This is a stepping stone to the absolute measurement of blood flow, which is explored in later chapters. The X-ray derived relative flow measurements are compared to intracoronary pressure measurements as a reference.

5.1.1 Theory

5.1.1.1 X-ray measurement

Consider a ROI drawn around a section of the myocardium supplied by the artery of interest as show in Figure 5.1. The average of the pixel values in the ROI containing M pixels at time

t be S_t:

$$S_t = \frac{1}{M} \sum_{x,y \in roi} dsa(x, y, t) \tag{5.1}$$

where $dsa(x, y, t)$ is the pixel value of a pixel at location (x, y) in the image at time t. From equation 2.12, if $m_{(x,y,t)}$ is the mass of iodine above the pixel at location (x, y) at time t, then

$$S_t = -\frac{k\mu}{M\rho} \sum_{x,y \in roi} m_{(x,y,t)}/A_0 \tag{5.2}$$

Where μ/ρ is the mass attenuation and $m_{(x,y,t)}/A_0$ is the mass thickness of contrast agent (see Section 2.2.5 on page 20, and k a gain applied in the image processing).

If the mass attenuation coefficient, k, M and A_0 are constant, which is the case if the imaging geometry and radiographic factors are constant, it can be seen that the DSA pixel intensity is proportional to the mass of iodine above the ROI. In other words,

$$S_t = Km_r \tag{5.3}$$

where K is a constant relating mass to signal intensity, and m_r the mass of iodine above the ROI.

At the start of the contrast injection in the region, contrast will be flowing into the coronary arteries and myocardium, but will not yet have reached the venous outflow. During this time contrast is accumulating in the region in proportion to the rate of contrast injection into the feeding artery. If all of the blood in the arterial inlet is replaced by contrast, then the rate of accumulation of contrast in the region of interest is proportional to the arterial blood flow. All analysis is performed in the early phases of the contrast injection where there is only contrast accumulation in the ROI. Consider two times t_1 and t_2 during the inflow period, then the mass of contrast medium in the ROI will increase as follows:

$$m_{t_2} - m_{t_1} = fcQ(t_2 - t_1) \tag{5.4}$$

where c is the concentration of contrast agent injected, f the fraction of the myocardial volume in the ROI, and Q the blood flow.

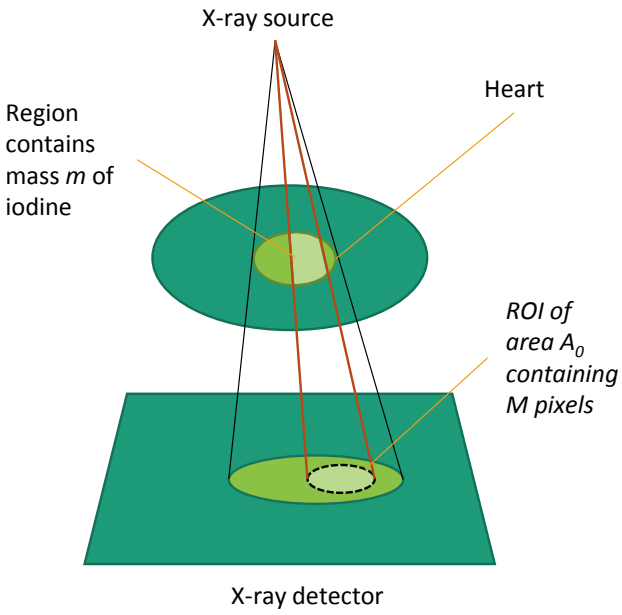

Figure 5.1: Region of interest drawn over the heart covering the myocardium of the vessel of interest.

Substituting equation 5.3 into equation 5.4 gives

$$\frac{1}{K}(S_{t_2} - S_{t_1}) = cQf(t_2 - t_1) \tag{5.5}$$

Rearranging this gives

$$Q = \frac{(S_{t_2} - S_{t_1})}{Kcf(t_2 - t_1)} \tag{5.6}$$

Picking single time points for t_1 and t_2 could lead to errors if in one of the images there was patient movement. If the signal intensities S_T are calculated for a range of values of t where contrast is accumulating in the ROI, a TIC is generated, and it follows that

$$Q = CG \tag{5.7}$$

where G is the gradient of the TIC, and C is a constant ($C = 1/Kcf$).

If two sequences are acquired before and after intervention, then it can be seen from eq. 5.7 that the ratio of the gradient of the post- and pre- intervention TIC is equivalent to the ratio of the post and pre intervention flow, i.e. it is a measure of the increase in flow following intervention. In other words, if G_{pre} is the TIC gradient pre-intervention and G_{post}

the gradient post-intervention then,

$$\frac{1}{C}G_{post}/\frac{1}{C}G_{pre} = G_{post}/G_{pre} = Q_{post}/Q_{pre} \tag{5.8}$$

5.1.1.2 Reference Measurement

If the FFR is measured both before (FFR_{pre}) and following intervention (FFR_{post}) then from eq. 2.14,

$$\frac{FFR_{post}}{FFR_{pre}} = \frac{Q_{post,S}/Q_{post,N}}{Q_{pre,S}/Q_{pre,N}} \tag{5.9}$$

where Q represent blood flow, "pre" and "post" refer to pre- and post- intervention, and N and S refer to flow in the normal and stenotic artery respectively. Given that the flow in the "normal" artery would be independent of any intervention $Q_{pre,N} = Q_{post,N}$ and therefore

$$\frac{FFR_{post}}{FFR_{pre}} = \frac{Q_{post,S}}{Q_{pre,S}} \tag{5.10}$$

In other words, the ratio of the FFR post to pre intervention will measure the improvement in blood flow, and can therefore be used as a reference to the X-ray angiographic measure. Accepting the assumptions inherent to pressure derived FFR as discussed in section 2.3.3.2 on page 41 the ratio of flow following intervention to that before can be measured as the ratio of the post-intervention FFR to pre-intervention FFR.

5.2 Materials and Methods

Patients for this analysis were a subset of those from the cardiac DSA study described in the previous chapter, who had intracoronary pressure wire assessment both before and following intervention. Longer DSA sequences were acquired (continuing until contrast could be seen entering the venous system). For all image acquisitions, the same procedures as described in Section 4.2 on page 83 was used. In total thirteen patients were included. The ECG trace was recorded in synchronisation with the image data.

The angiograms and FFR measurements were performed during pharmacologically induced hyperaemia using intravenous injection of adenosine at 140 mg/kg/min, started two minutes prior to measurements. The pre and post intervention angiograms were acquired

using the same projection and, in so far as practicable, the same framing of the heart. For the left coronary artery the lateral or right anterior oblique (RAO)-caudal angulation was used, and for the right coronary artery straight RAO projection was used. The 25 cm field of view was selected and the frame rate set to 15 fps. Prior to each of the angiograms the catheter was flushed with contrast to ensure that contrast was present to the tip of the catheter. The entire heart was positioned within the frame and patients were instructed to hold their breath at inspiration during the angiographic acquisition. Angiograms were terminated when the venous outflow of contrast became visible. FFR was measured pre and post intervention via intra-coronary sensor (ComboWire, Volcano Corp, San Diego, California) during the same period of induced hyperaemia as the angiogram sequences.

Following the procedure, both the image data and ECG trace were transferred from the catheterisation laboratory to the University for analysis using software written in MATLAB (Mathworks Inc, Natick, California). Prior to analysis the first five frames of all sequences, where the X-ray dose control was still active, were discarded. Software was written that could create phase matched sequences at a given point in the R-R interval, taking the image sequence, synchronised ECG and specified fraction of the cardiac phase. The output was a sequence of images and time points containing one image per heart beat closest to the specified point of the cardiac cycle. The software's graphical user interface (GUI) is shown in Figure 5.2.

For analysis purposes sequences were created at a specified end-diastole when the heart is relatively motionless (0.8 of the R-R interval). Figure 5.2 shows the creation of such as sequence. Two ROIs were selected on each image sequence: one in the myocardium, and one in an area of the image adjacent to the heart. The user could adjust the position of the ROI in the individual image frames if required (to compensate for patient breathing for example). For each frame in the phase match images the median pixel value in each ROI was calculated. The median of the ROIs from the first frame was subtracted from each subsequent frame. For each frame the inverse of the relative change in the background ROI value was applied as multiplicative correction for any offset in the image background, for example due to respiratory motion. Following the background correction, a TIC for the main ROI was created by subtracting the value of the first frame ROI. A gamma-variate function fitted to the TIC[310] and the gradient of the curve at half peak were calculated. Statistical analysis was

Figure 5.2: Sequence creator software showing the image sequence with a graph of the ECG plotted above. The software has automatically identified the R-waves in the ECG and these are highlighted on the ECG plot with red crosses). In this case the synchronised sequence is being created at 0.8 of the R-R interval, and these times are indicated on the ECG plot with the red vertical lines. The current time-point of the frame being displayed is indicated by a black vertical line on the ECG plot.

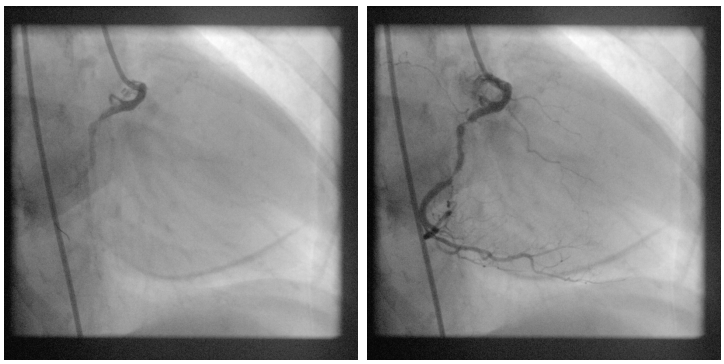

(a) Frame 2 (b) Frame 4

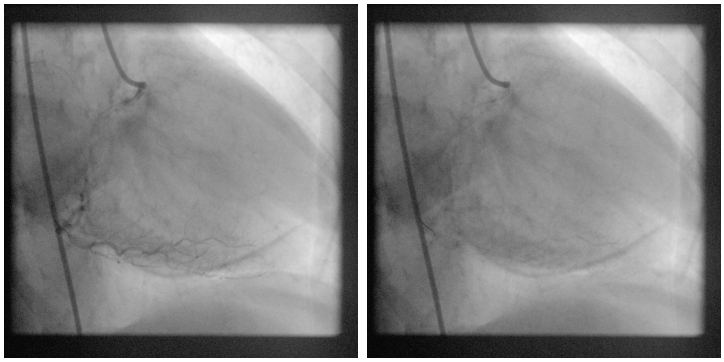

(c) Frame 6 (d) Frame 8

Figure 5.3: Frames from a frame matched sequence created with sequence creation software.

performed using linear regression and Bland-Altman analysis. The software's GUI is shown in Figure 5.4.

5.3 Results

Four patients were excluded from the study; one patient could not maintain an adequate breath hold during angiography, in one case no intervention was performed, and in two cases there was a failure of the contrast injection protocol—on one occasion the pump failed to trigger due to the R-wave not being recognised by the automated triggering system on the ECG, and in the second case the catheter was not flushed with contrast prior to the acquisition sequence, leading to insufficient contrast injection.

The increase in blood flow following intervention measured from the angiograms correlated strongly with that predicted by the post/pre ratio of FFR ($r^2 = 0.97$, $p < 0.01$). These results are shown in the scatter plot and Bland-Altman plots in Figure 5.5.

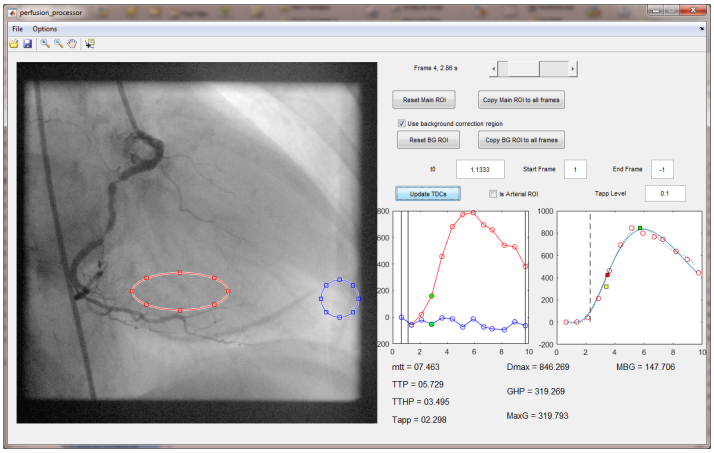

Figure 5.4: Analytic software GUI showing the main and background ROIs and computed results.

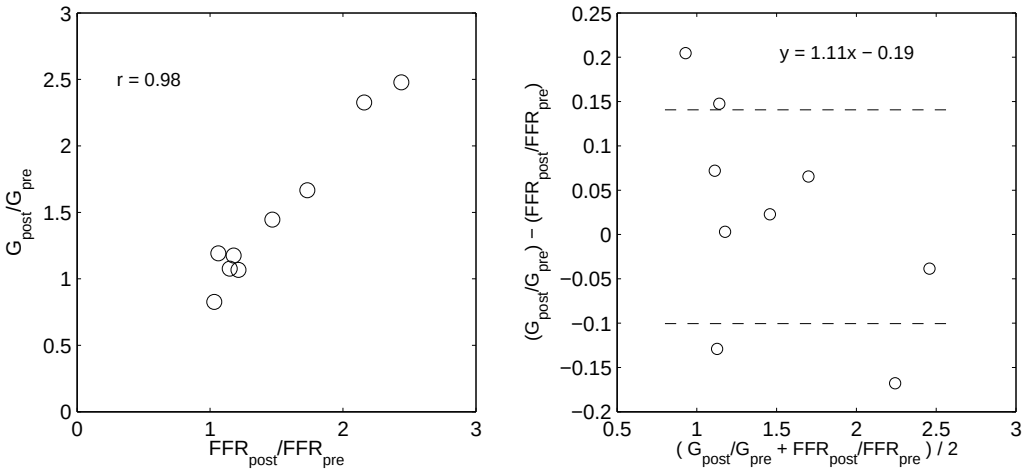

(a) Scatter plot

(b) Bland-Altman plot

Figure 5.5: Ratio of post/pre intervention FRR and gradient at half peak shown as (a) scatter plot and (b) Bland-Altman plot.

5.4 Discussion

Key to the success of this method were the modifications to the X-ray system to produce angiograms that were acquired without variation in radiographic factors throughout the image sequence acquisition, and that the feed forward automatic gain control and standard image enhancement algorithms in the image processing system were disabled. In a standard X-ray system the automatic dose control and will continually react to the amount of contrast medium within the image and the cardiac motion of the heart, adjusting the radiographic output to maintain a constant dose the image detector. This causes the relationship between pixel intensity and contrast medium mass in the image to vary both within a single sequence and between sequences. Furthermore the bypass of the normal image enhancement algorithms, and the automatic gain control (which seeks to maintain a constant signal level in the image output stream) are also necessary. These modifications do not require additional hardware, and could in theory be implemented on many similar X-ray systems. The combination of the ADC and automatic gain control combine to produce a stable pixel intensity in the central region of the image. Therefore if the change in pixel intensities is to be monitored over the central region of the image (which contains almost all of the heart in most cases during an acquisition, the expected drop in pixel intensity as the contrast is injected due to the additional X-ray beam attenuation it produces is not seen. This can be seen in Figure 5.6b which shows the sum of pixel intensities in a large circular ROI placed in the centre plotted throughout two image sequences. The first sequence (blue line) was acquired in the standard right coronary acquisition mode, and the TIC is almost flat due to the actions of the dose control and automatic gain. Conversely a comparable sequence taken from a patient imaged in the modified mode used in the DSA mode in Chapter 4 and the measurement sequences in this chapter, shows a substantial decrease in pixel intensity as the contrast agent is injected and flows into the image. Even in cases where a small ROI is drawn in the myocardium, such as that shown in Figure 5.6b as used in this chapter, where the myocardial blush is visible in the angiogram, the analysis of the TIC shows a reduced response to the contrast agent in the standard sequence compared to the modified sequence (shown in Figure 5.6d). The images shown in Figures 5.6a and 5.6b are from the sequence captured in the standard and modified acquisition modes respectively.

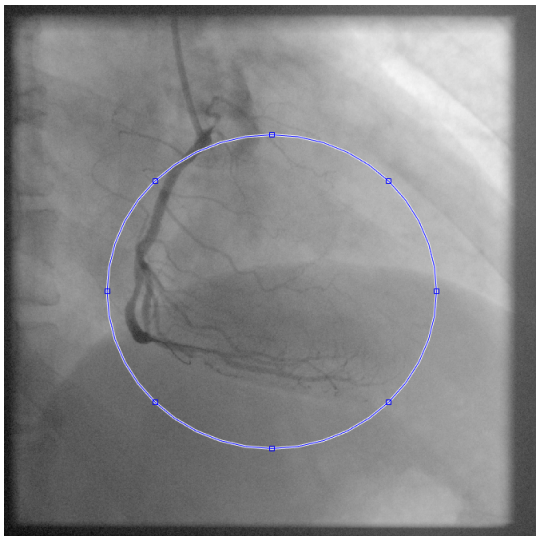

(a) Large ROI location

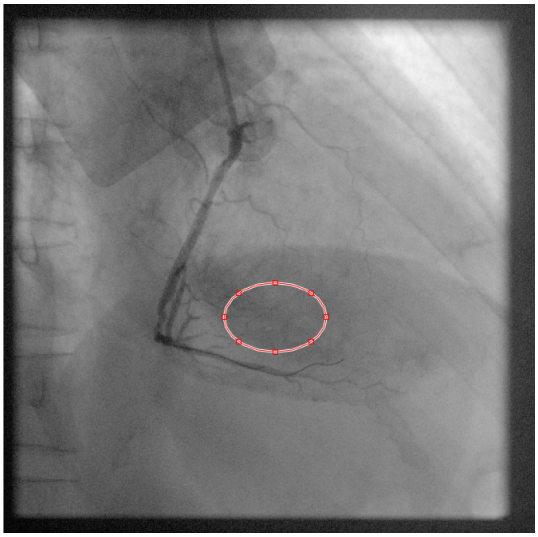

(b) Small ROI location

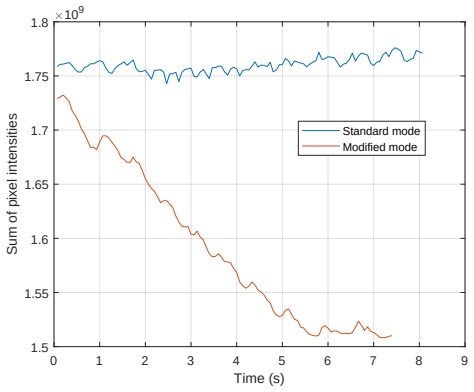

(c) Large ROI TICs

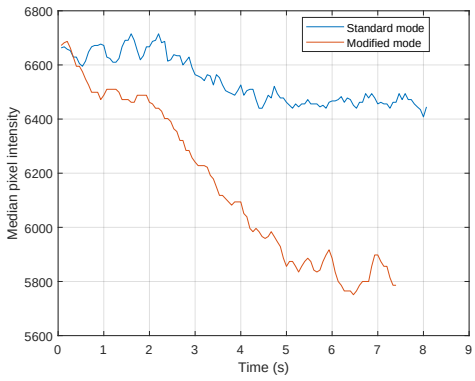

(d) Small ROI TICs

Figure 5.6: Comparison of time intensity curves (TICs) in images acquired (a) large and (b) small regions of interest in the standard and modified acquisition modes. The modified mode fixes the automatic dose control and disables the automatic gain control, the effect of which is to normalise the mean pixel value in the centre of the image. This can be see in (c) where the is little variation in the pixel values despite the injection of contrast in the standard mode, but the appropriate reduction in pixel values due to the addition attenuation of the contrast agent is seen in the modified mode. Even in smaller regions, where the blush can be seen visually, there is a reduced response in the quantitative analysis (d).

The dose control was allowed to operate for five frames at the start of each sequence to ensure that a reasonable X-ray output was used for the current projection, patient position and image geometry. The setting of an appropriate level is important—if the dose output is too low, the image will be noisy and may not be of sufficient quality for analysis, and the dose output is too high the patient will be exposed to unnecessary amounts of ionising radiation. It is important that the exact imaging geometry was reproduced for the pre- and post- intervention sequences, otherwise the dose control would settle to a different set point in each sequence, leading to an inaccurate measurement of relative flow. These results indicate that this was achieved.

Previous studies measuring relative flow from angiography have concentrated on measurements of CFR, the ratio of blood flow at rest and during stress[200–204] or relative coronary flow reserve (the ratio of CFR between a normal and diseased vessel).[191] Here, improvement in flow following intervention was assessed. Clearly this measurement would not have any role when deciding upon whether or not to stent a lesion, but rather in the assessment of the efficacy of intervention in improving blood flow, but there is no reason that the method could not be performed at rest and under hyperaemia to measure CFR.

There were a number of limitations and difficulties in this study. The ECG triggered pump injection of contrast, whilst capable of reproducible and accurate injections, was a change to normal clinical practice, and failed to work in one case where the R wave triggering failed to detect a suitable trigger point in the single ECG lead being fed to the triggering system. The two requirements for the injection are that it be delayed for one or more heart beats following the start of imaging, and that all blood should be replaced at the arterial input, and it is possible that this could be done with a hand injection, or power injector programmed with a fixed delay greater than one heart beat.

This study considered only a small number of patients (9 patients). In five patients small improvements in FFR were noted following intervention, although the overall range of increase in flow was approximately 1–2.5 times, and this may have elevate the correlation coefficient. Moreover the study did not include any test-retest element in its design to assess the precision of either repeated invasive FFR or X-ray relative blood flow measurements. Doing so would have been very difficult. Removing and reintroducing the invasive pressure wire would introduce potentially serious complications such as arterial dissection, and repeated

injections of adenosine to induce hyperaemia would have been a burden for the patient.

The use of the software tools in this study was time consuming. The first of the two—the phase matched sequence creator—could be automated (and indeed the DSA software described in Section 4.2.1 on page 84 implemented such a scheme), although the single ECG channel input was noisy and proved unreliable. The physical connection beteen the physiological monitoring equipment in the cath lab, and the X-ray system itself which permitted the synchronised recording of the image data with a time match ECG signal, was a plug that connected under the couch in the room that was prone to being knocked out of place or damaged. The use of image based metrics to assess a frame's point within the cardiac cycle could overcome the limitations with the use of the ECG signal.

The use of the relatively small ROIs which contain only a fraction of the myocardium could be a source of error for a number of reasons. Firstly, the ROI size and location are determined subjectively. This is time consuming and prone to inter and intra operator variations in location, although this variation was not assessed in this study. Furthermore their exact location would be subject to the variation in flow in different regions of the myocardium.[311]

This analysis was based on ROIs in the myocardium, as opposed to using regions within the artery as used by early angiographic measures of flow.[185,186] These were chosen as the frame rate for the acquisitions was much lower than the earlier studies (15 fps compared to 50+ fps). Whilst this did enable the standard frame rates of modern cardiac angiography to be used, the longer sequences required to analyse the transit of contrast through the myocardium are more prone to breathing artefacts. It should be noted, however, that the sequences for this measurement, were much shorter than those assessing myocardial mean transit times using angiography,[189] as the washout phase does not have to be described.

5.5 Conclusions

Alterations to the X-ray system's dose control, image processing and data capture, were necessary to produce images used for the measurements sequences produced images that had pixel values that were proportional to the X-ray dose incident upon the detector. This proportionality was stable over time during a single acquisition sequence and between sequences as long as the imaging geometry and patient position were consistent. Without that consis-

tent, proportional relationship between dose and image pixel value, it would not be possible to gauge the change in mass or volume of contrast agent within an image sequence, and a relative measurement of flow would not have been possible. A relative index of blood flow measured from analysis was implemented using a cardiac phase matched subtraction scheme, retrospectively selecting a single frame per cardiac cycle. By comparing the ratio of this index post-intervention to pre-intervention, a measurement of the increase in blood flow to the myocardium was obtained. The technique has been compared to an index of relative flow using intra-coronary pressure measurements, and the two indexes were found to have a very strong correlation and low discrepancy, although the number of patients was small.

This work suggests that given the stable high quality images produced by modern X-ray imaging equipment and the modified acquisition settings used, with the implementation of a suitable calibration of pixel intensity to iodine mass, these methods could be developed to measure absolute flow. The next chapter in the thesis describes the background theory on how such a calibration can be achieved by comparing two angiograms using similar methods to the analysis in this chapter.

Chapter 6

Absolute measurements of flow using X-ray imaging: Theory

6.1 Introduction

The previous chapter developed a method of measuring relative flow intended to quantify change in the flow before and after intervention (or potentially at rest and hyperaemia to measure CFR). Careful control of the X-ray system's automatic dose control and image processing resulted in a method that was sensitive to the relative change in flow between two runs on the same patient. If the radiographic output of an X-ray sytem vary over time, or image processing which aims to improve the displayed quality of an image is applied, then the relationship between dose incident upon the X-ray detector and pixel intensity varies over time, which precludes assessment of mass of contrast agent in an image by signal intensity inherent in the flow measurement method. In this chapter the relative flow measurement method is extended to incorporate a calibration of signal intensity to contrast agent volume, permitting the estimation of absolute flow of blood in a vessel.

Using planar X-ray imaging to measure the absolute flow of contrast agent in a vessel is difficult for several reasons. A number of these were discussed in detail in the previous chapter, and are:

- The pixel values of an X-ray system are neither calibrated to absolute scale nor is the pixel's relationship to X-ray dose linear.

- The use of computer processing can undo the proportionality between pixel intensity and dose in a manner which cannot be recovered. The algorithms, usually employed to improve the appearance of an image, are often sophisticated and non-linear.

- The use of an automatic dose control system, different patient body habitus and X-ray projection geometry will result in alterations in X-ray beam energy, meaning that the differential signal due to the injection of contrast agent can vary both for different acquisition from the same patient and between patients.

- The planer nature of X-ray imaging removes depth information so the volume of structures in an image is extremely difficult or impossible to calculate.

It is possible to address the first two of these points by calibration and configuration of the equipment with help from the manufacturer. The last is a fundamental characteristic of the projection nature of the imaging system.

This chapter describes a method for imaging absolute blood flow in a coronary artery using X-ray imaging by exploiting the predictable relationship of signal intensity to mass of contrast agent, and also proposes how stenotic and myocardial resistance could be inferred using an intra-coronary pressure wire.

6.2 Principle

Consider Figure 6.1 which represents the object representing the heart, being imaging by a diverging X-ray beam onto an X-ray detector. The main body is omitted from the diagram, and only the heart and X-ray detector are shown. The heart has a cross section area of A_0 mm^2 and is located a distance, known as the source-to-object distance (SOD), from the X-ray source. The distance between the X-ray source and the X-ray detector is known as the source-to-image distance (SID). Initially the image scene contains no contrast agent (Figure 6.1a), but after some time t, a mass of m_t iodine is present in the heart from the injection of contrast agent.

A DSA image can be created by the log subtraction of the first contrast free image (the mask), from the image at time t containing contrast. The projected area of the heart's shadow will be $A_0(SID/SOD)^2$. If we consider a ROI drawn around the entire heart (see Figure 6.1b),

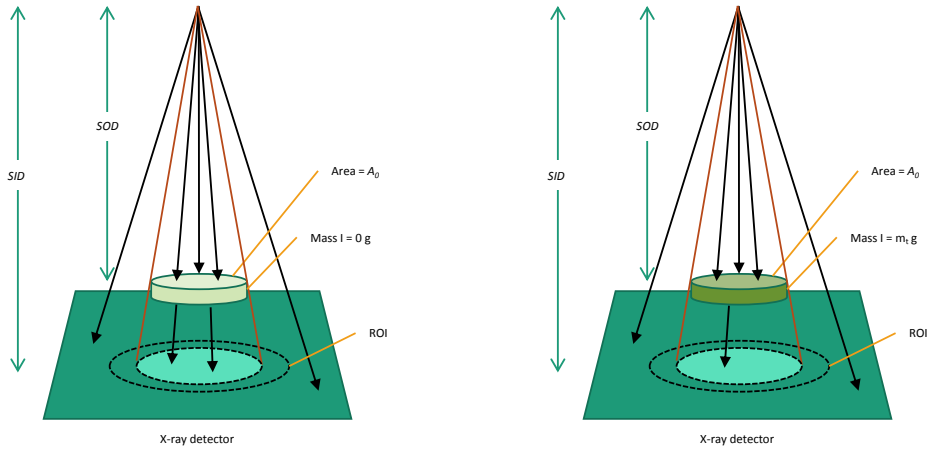

(a) (b)

Figure 6.1: The attenuation of an X-ray beam by an object of volume V with surface area A_0, a) before contrast injection, and b) after contrast injection.

every pixel in the ROI outside of the heart will have a value of zero, and those within the heart will have a negative value depending on the mass thickness of iodine. Let N be the number of pixels per square millimetre on the detector, From Eq. 2.12 on page 30, assuming the object filled with contrast is small compared to the mass of the patient in the X-ray beam, and so the injection of contrast medium causes negligible change in the mass of the other materials in the ROI, the sum of the pixel intensities at time t, S_t, within the ROI will be given by,

$$S_t = -kNA_0 \left(\frac{SID}{SOD}\right)^2 \frac{\mu}{\rho} m_t / A_0 \tag{6.1}$$

$$S_t = -kN \left(\frac{SID}{SOD}\right)^2 \frac{\mu}{\rho} m_t \tag{6.2}$$

If by time t contrast agent has not yet reached the venous system, the volume V_t ml of contrast agent injected is given by the total mass of iodine in the heart, m_t divided by the iodine concentration of the contrast agent, c, and therefore

$$S_t = -kN \left(\frac{SID}{SOD}\right)^2 \frac{\mu}{\rho} V_t c \tag{6.3}$$

If during an acquisition the imaging geometry and radiographic factors are fixed, then the mass attenuation, $(\mu/\rho$, and SID/SOD are constant. k is a fixed factor in the computer

processing creating the DSA image, and N is fixed, then

$$S_t = CV_t \tag{6.4}$$

where $C = -kNc\,(SID/SOD)^2\,\mu/\rho$, and is a constant relating total pixel intensity change to volume of contrast agent.

Considering two time points t_1 and t_2, after the start of the contrast injection, during which contrast is injected into the heart at Q ml/s. Again assuming none of the contrast agent has not yet reached the venous outflow,

$$Q = \frac{\Delta V}{\Delta t} = \frac{V_2 - V_1}{t_2 - t_1} \tag{6.5}$$

From Eq. 6.4, $V_t = S_t/C$ therefore

$$Q = \frac{S_{t_2} - S_{t_1}}{C(t_2 - t_1)} = \frac{g}{C} \tag{6.6}$$

where $g = (S_{t_2} - S_{t_1})/(t_2 - t_1)$. In other words, the flow is proportional to the gradient of the TIC within the ROI.

This relationship can therefore be exploited to measure the blood flow in a coronary artery. If an injection sequence is made where the rate of contrast injection is known (Q_c), and much lower than the native arterial blood flow (Q_m), then all of the contrast agent will flow down the coronary artery. Analysis of the image sequence will provide the gradient of the time intensity curve shortly after the injection starts (g_c). If a second injection of contrast is performed, with all of the blood in the inlet artery replaced by contrast agent, contrast will be flowing into the organ at an unknown rate Q_m. This yields a second time-intensity curve with gradient, g_m. We can now calculate Q_m using Eq. 6.6 as follows:

$$\frac{g_m}{g_c} = \frac{CQ_m}{CQ_c} \tag{6.7}$$

$$Q_m = Q_c \frac{g_m}{g_c} \tag{6.8}$$

The flow in the artery can therefore be derived by the known rate of contrast injection in the calibration sequence, Q_c and analysis of the time-intensity curves in the calibration and

measurement sequences.

6.2.1 Comparison to previous work

As discussed in Section 2.4 calibration schemes have been used before in angiographic blood flow measurements, but previous techniques have relied on an external phantom containing a known material for calibration purposes, for example a known amount of iodine, placed on the surface of the patient.[255,258,259] This presents a number of practical problems. In an interventional setting, where maintenance of the sterile area of the patient is important, the calibration phantom must be sterile and the iodine must remain stable and within the phantom (e.g. not leaking). Such requirements would probably favour a single use phantom. Placing the phantom on the patient whilst imaging at oblique views (i.e. highly angled X-ray beam) would be very difficult. An adhesive phantom might be necessary, but would be difficult to attach to the sterile surgical drapes over the patient and X-ray equipment. Another problem with the use of an external phantom is the fact that the phantom and heart are at different distances from the X-ray source. Figure 2.9 on page 22 shows that the distance of an object from the source will determine the size (but not intensity) of its shadow projected onto the X-ray receptor. Equation 6.3 shows that the sum of projected pixel values in the DSA image is proportional to the the square of the ratio of SID to SOD. Therefore if the calibration phantoms is placed on the entrance or exit surface of the patient, a correction must be made for the different magnification of the calibration phantom and the heart. Following from our theory above, an organ of cross section A_0, at a distance, d_1 from the X-ray source, will project a shadow of area A,

$$A = A_0 \left(\frac{d_1}{SID} \right)^2 \tag{6.9}$$

where SID is the source-to-image distance (distance from the X-ray source to the image receptor). The calibration would have to account for the fact that the distance to the phantom (d_2) would require correction by a factor $(d_1/d_2)^2$. This correction was employed by Molloi for his work,[263] and would be reasonable to implement on animal models, and humans where the distances involved could be reasonably predicted. This would limit the projection angles that could be used, as an estimate for the location of the heart to the phantom could be possible

for projections such as straight PA, but not for highly angled oblique projections. However, the human coronary tree, and in particular the left coronary artery, is not well visualised in many projection such as PA as the circumflex and left anterior descending arteries and their associated myocardial beds overlap in the projection image. Other oblique or lateral views would make such distance correction very difficult to achieve accurately.

In the scheme presented here the calibration phantom is replaced with an injection of contrast at a known rate. There are downsides to the use of a calibration requiring an intracoronary bolus of contrast. Firstly, the patient would receive a larger amount of contrast which can increase the possibility of an adverse reaction to the contrast agent, and secondly the calibration sequence acquisition would probably be longer than if a phantom were used as image must take place during the contrast injection for some seconds. The calibration sequence requires a known rate of contrast injection, and in practical terms this means using a power injector. The volume of additional contrast agent would be low compared to that used in the overall procedure. The contrast injection for the calibration has to be at a rate that provokes a high enough signal change to be easily detectable, so a low rate should be sufficient. Given arterial flows in the range of 1.6–2.35 ml/s,[178] a contrast injection rate of 0.5–1 ml/s should be acceptable. Furthermore the duration of injection must be low as the principle requires analysis before any of the contrast agent has reached the venous system. A four second injection would give around three heart beats to allow some averaging of the results over some heart beats, resulting in the calibration injection overall bolus being 4 ml, which is not significant. The relatively short acquisition time also means that the additional radiation would not be excessive. The use of a power injector is common in the X-ray cardiac catheterisation laboratory, for left ventriculograms. They are therefore readily available and staff are familiar in their use. They are not commonly used for intracoronary injections however, and care must be taken to ensure that the maximum driving pressure is not capable of damaging the artery. Pumps have a programmable maximal driving pressure that can be set, which can be used to reduce the chances of damage to the artery.

The calibration is based on an injection at a known rate rather than an injection of a known bolus—this is an important feature, as the injection of a known bolus into a coronary artery is very difficult. Contrast agent is more dense than blood, which will lead the contrast agent to naturally flow out of the catheter tip over time (along with the inevitable mixing

with blood at the distal end of the catheter). These factors make the leading edge of any contrast injection be a mixture of blood and contrast agent, and the trailing edge not be a sharp stopping of contrast injection but a gradual tailing off of injection. Therefore, even if an injection syringe is weighed before an after injection to determine the mass of contrast ejected from the syringe (or a specific bolus of injection programmed into a pump injector), the mass of contrast actually leaving the catheter tip into the vessel will be different. Whilst the use of known volume contrast injections have been demonstrated to measure relative flow,[199] the technique has not been widely adopted. It has been proposed that the volume of contrast entering a coronary artery can be assessed using the arterial input function,[293] but this involves accurate vessel tracking and higher image acquisition rates. Vessel tracking is complicated by the overlapping arterial tree, particularly in the LCA, and the use of high frame rates increases the patient's radiation dose.

6.3 Measurement of resistance

Currently the microvascular and stenotic resistance can be assessed in the catheterisation laboratory using intracoronary combined Doppler flow-velocity and pressure wires as HMR and HSR (these are discussed in Section 2.3.4 on page 48). Additionally myocardial resistance can be measured using IMR (see Section 2.3.5.1 on page 49), which uses coronary mean transit time as a surrogate for flow. The use of flow-velocity or mean transit time instead of flow is not ideal (as both for instance do not account for differences in vascular volumes both between vessels or between patients). An angiographic measurement of flow could be used, and combined with intracoronary pressure measurements.

The total resistance to blood flow, Q, down a coronary artery could be made from flow a pressure averaged over the cardiac cycle:

$$R = \frac{P_a - Pv}{Q} \tag{6.10}$$

Where P_a is the aortic blood pressure, and P_v is the venous blood pressure. Whilst P_v is not often measured in practice, it will be low (typically 5 mmHg), especially when compared to the arterial pressure. Intra-coronary pressure wires are commonly used in the measurement of FFR, and could also be used to provide individual resistances for both a stenotic lesion

and the myocardium (R_S and R_M respectively), by measuring the pressure in the coronary artery distal to a stenotic lesion (P_d), giving

$$R_S = \frac{P_a - P_d}{Q} \tag{6.11}$$

$$R_M = \frac{P_d}{Q} \tag{6.12}$$

Again, for R_M it is assumed that P_v is negligible.

6.4 Challenges to the clinical implementation

There are a number of simplifications made in the flow measurement methods presented in this chapter, that will have to be overcome in human imaging. Firstly the heart is not stationary, and therefore measurement of the gradients of the time intensity curves is complicated by the cardiac motion affecting the attenuation of tissues in the ROI. In systole the heart is contracted to its minimum volume, and therefore there it is likely that more tissue will be present in the ROI than in diastole, even if the ROI is made large enough to cover the entire heart in diastole. This variation in tissue mass in the ROI will introduce a variation in signal intensity in an image. Phase matched DSA could be used to overcome this, as was done in the previous chapter, but only if there is no other motion, notably due to breathing. In practical terms, however, unlike the long acquisition mean transit time based angiographic flow measurements that have previously been proposed, the sequences required for these measurements should be relatively short (≈ 6 s).

Secondly, the idealised scatter-free, monochromatic X-ray beam required for the derivation of Eq. 6.8 are not realistic. Scatter will mean that the signal in the ROI also has an additive component, which is not attenuated by the contrast agent, invalidating equation 2.1. Adding a signal GS, arising from S scattered photons per unit area into Eq. 6.14 from page 120, gives

$$\Delta S = k\left(\ln\left[GN_0' \exp\left(-\frac{\mu}{\rho}m_c/A_0\right) + GS\right] - \ln(GN_0' + GS)\right) \tag{6.13}$$

Therefore

$$\Delta S = k\left(\ln\frac{N_0' \exp\left(-\frac{\mu}{\rho}m_c/A_0\right) + S}{(N_0' + S)}\right) \tag{6.14}$$

This results in a non-linear relationship between the mass thickness of contrast and the resultant attenuation. The simple linear relationship between contrast agent volume and log-subtracted signal intensity shown in Eq. 6.4 is therefore not correct, and the relationship is a non-linear function of primary photon fluence, scattered photon fluence and volume of contrast agent. The greater the deviation in the relationship between volume and intensity from linearity, the more inaccurate measurement of flow would become. Moreover the polychromatic X-ray beam also means the relationship between mass thickness of material and attenuation is not linear, with the relationship varying depending upon the beam energy spectra (determined by the kV and spectral filtration), and patient thickness.

The effects of scatter and beam energy on the non-linear relationship between contrast volume and signal intensity in the log-subtracted image were explored using a computer model of conditions typical in cardiac X-ray imaging. X-ray tube output as a function of beam energy and material attenuation coefficients were obtained from published sources,[48] and software was written in MATLAB to model the relative intensity of an iodine filled vessel against a PMMA background. Base line conditions for the model were an X-ray beam an energy profile resulting from a 75 kV exposure with 2.5 mm inherent Al filtration and 0.1 mm added Cu spectral beam filtration. This beam exposed a 200 mm thick PMMA phantom with a simulated vessel filled with contrast agent with an iodine concentration of 300 mg I/ml. The diameter of the vessel was varied from 0 (i.e. no vessel) to 5 mm, and the ratio of the minimum beam intensity behind the vessel to the scene with no vessel—the relative beam intensity, or 1 minus the attenuation—was calculated. A scatter free, monochromatic, X-ray beam would produce a linear relationship between vessel thickness and relative attenuation when plotted on linear-log axes, with the gradient of the line being the linear attenuation coefficient. In turn the model were recalculated whist independently varying the scatter-to-primary ratio (SPR) from 0 to 2, kV from 60 to 120 kV, beam filtration from 0 to 0.9 mm Cu, and phantom thickness from 100 to 300 mm of PMMA.

The impact of scatter on the relative signal intensity can be see in Figure 6.2. In this case a 50 keV mono-energetic beam was used so that the effect of scatter and beam energy can be separated. It can be seen that in the absence of scatter (as described by Equations 6.1 to 6.8), the logarithm of relative intensity (and therefore log-subtraction) is linearly proportional to the volume of contrast agent as described by Eq. 6.4. As the scatter to primary ratio is

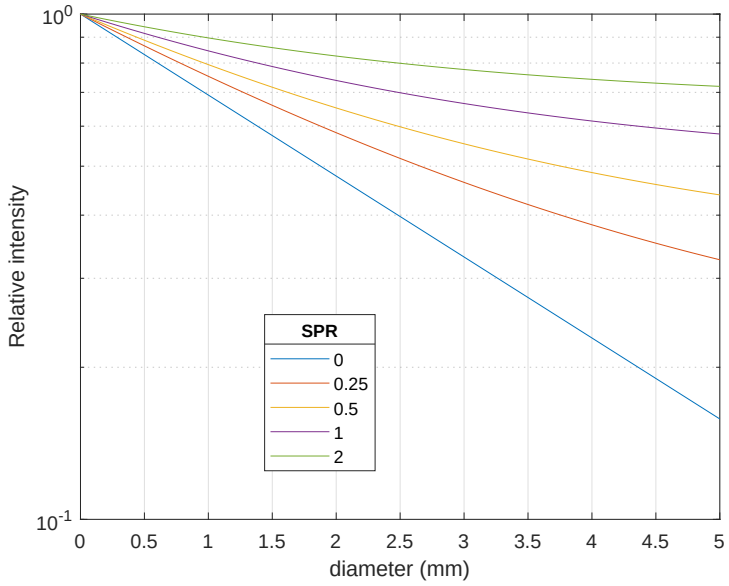

Figure 6.2: Non-linear relationship between volume of contrast agent (modelled by vessels of different diameter) and relative signal intensity introduced by scattered radiation. Modelling using a 50 keV mono-energetic beam, demonstrates a linear relationship between log-relative signal intensity for primary radiation only (SPR=0), and the non-linearity and contrast loss introduced by increasing scatter.

increased there is both a non-linear relationship between the log-subtracted signal, and also an overall reduction in subtracted signal intensity as scatter increases.

The effects of beam energy are shown in Figure 6.3. The figure demonstrates that changes in thickness for higher diameter vessels (increased mass thickness) provoke lower changes in attenuation than for smaller vessels. This effect is more pronounced when the beam is softer (lower kV, lower Cu filtration or lower phantom thickness).

Nonetheless over reasonably large ranges the relationship between mass of iodine and attenuation does approximate to be linear under the conditions studied. In cardiac imaging, the irradiated field is relatively small, and it is standard practice to use an anti-scatter grid, meaning that scatter to primary ratios are lower than in many other areas of radiography. Nonetheless, depending on the precise conditions used, these non-linearities could lead to inaccuracies in the X-ray based flow measures.

The accuracy of the calibration requires that the calibration injection is performed at a known rate, that for the measurement sequence has complete replacement of blood with contrast agent, and that the measurement injection does not affect the flow of blood. For the calibration sequence no black-flow of contrast into the aorta should occur (i.e. the entire

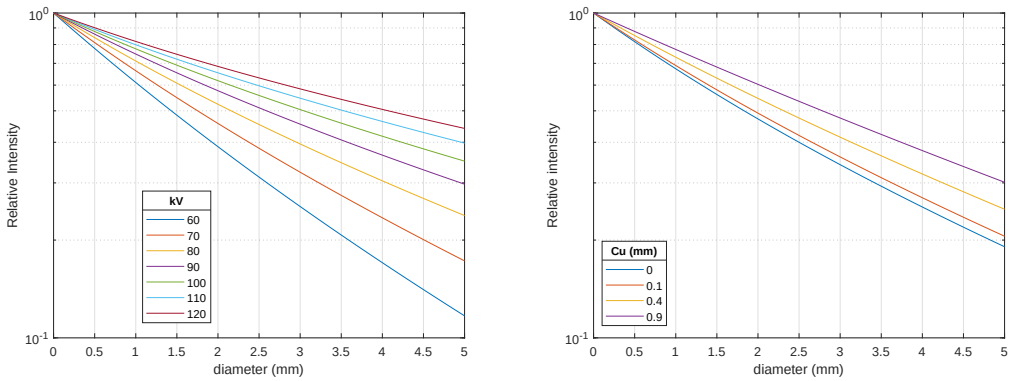

(a) kV

(b) Beam spectral filtration

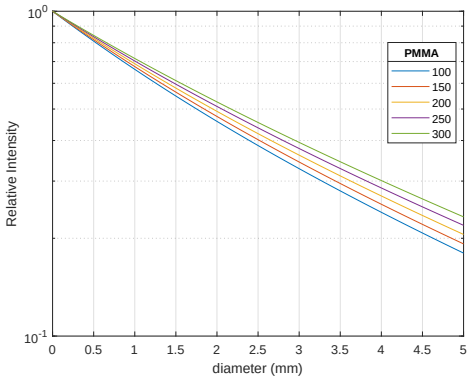

(c) Phantom thickness

Figure 6.3: Results from modelling the effects of the X-ray beam's energy spectra as altered by b) kV and c) beam filtration, and patient thickness on introducing a non-linear relationship between object thickness and attenuation. A contrast filled vessel of varying size is modelled with a beam of 75 kV, 0.1 mm Cu filtration, 200 mm PMMA equivalent phantom and a scatter to primary ratio (SPR) of 0, and the relative intensity (1-attenuation) is plotted with each of the model's variables being altered with the other base line conditions remaining constant.

contrast bolus is delivered down the coronary artery). For the measurement sequence if the injection rate is not high enough there will be incomplete replacement of blood. Furthermore the native flow might be altered by being increased due to an increase in pressure in the proximal artery due to the injection, or prompt a reactive hyperaemia. Alternatively there could be reduced flow due to the higher viscosity of contrast agent compared to blood.

6.5 Conclusions

The proposed measurement scheme has a number of appealing properties. The additional contrast administered and radiation doses are likely to be small due to the short acquisition sequences, as the analysis is performed on the early stages of contrast flow through the heart. Moreover the short acquisition sequences will minimise the motion artefacts. when performing the calibration, the use of an injection at a known rate into the heart overcomes limitations of requiring to know the exact volume of contrast injected, and the calibration being performed within the heart as opposed to an external calibration phantom removes the uncertainties inherent in correcting for different magnifications between the calibration and measurement conditions. Furthermore, the exact location or size of the ROI used in the analysis will not affect the sum of the pixel intensities, providing the whole heart is encompassed by the ROI and mis-registration artefacts are kept to an acceptable level. The large, simple, ROI should reduce the time required to perform the analysis and minimise inter- and intra-operator variability.

There remain a number of simplifications that have been made in methods, compared to practical X-ray imaging. Scatter and beam energy related non-linearities may introduce inaccuracies, and the injection of the contrast itself particularly during the measurement sequence may affect the underlying flow in the vessel during the injection. It was therefore decided to test the methods in phantoms, to verify that these simplifications do not results in flow measurements that are too inaccurate, before proceeding to test the method in humans.

Chapter 7

In vitro measurements of flow from X-ray angiography

7.1 Introduction

The aim of the investigations presented in this chapter was to determine whether accurate and reproducible measurements of flow using the methods described in Chapter 6 could be obtained in phantoms using the X-ray catheterisation laboratories in Leeds.

Two phantoms were devised for this purpose. The first phantom contained a single inlet, single outlet, fixed volume reservoir, representing a coronary artery flowing into a region of myocardium. Contrast could be injected at known flow rates directly into the reservoir, and hence this phantom is referred to as the direct injection phantom. The design allowed an appreciable delay from the contrast arriving in the reservoir before it began to flow out of the outlet. This phantom design provided a means of performing a proof of concept and reproducibility for the theory presented in the previous chapter, i.e. that using a calibration sequence to assess the rate of change of signal intensity from a known inflow of contrast, an estimate could be made for the inflow of contrast in a second contrast injection where the inflow is unknown. The phantom was not representative of coronary flow due to its direct power injection design, but was subject to many of the potential issues that would be encountered in human imaging, such as the system dose control, signal non-linearity due to the polychromatic X-ray beam, and the potential effect of scatter on measurements.

The second phantom employed a much more sophisticated model of the coronary circu-

lation. In this phantom, the simulated coronary artery branched off an larger vessel, which simulated the aorta. The coronary branch flowed into a similar reservoir to the direct injection phantom. Unlike the direct injection phantom, where the rate of contrast flow into the reservoir was determined by the volume of contrast injected, in the second phantom, flow down the simulated coronary artery was determined by the pressure in a simulated aorta and downstream resistances in a simulated coronary branch, in a similar way that the coronary flow is driven in humans. The simulated aortic pressure could be varied, and the variable resistances simulating a coronary stenosis and myocardial resistance could be introduced. Contrast injection was via a catheter engaged with the ostium of the simulated coronary artery, so the contrast flow into the simulated artery was a combination of the injection rate and native arterial flow. This phantom allowed the calibration and measurement injections to be tested in far more realistic conditions investigating for instance whether complete replacement of blood with contrast during the measurement sequence was achievable, whether the arterial flow was affected by the contrast injections and whether the type of contrast agent affected the measurements.

The following experiments and their respective objectives were performed with the two phantoms:

- Direct injection phantom: proof of concept. Does the use of a calibration sequence where contrast is injected at a known rate permit the measurement of blood flow in a sequence where the contrast injection rate is unknown?

- Direct injection phantom: An assessment of the flow measurement accuracy and reproducibility.

- Coronary circulation design validation: does the coronary flow in the phantom behave in the expected way when the pressures and resistances are varied systematically?

- Coronary circulation phantom: does the contrast injection affect the flow down the artery, and does the choice of contrast agent affect the accuracy or reproducibility of flow measurements?

7.2 Direct injection phantom

7.2.1 Phantom design

A single inlet, single outlet phantom was designed to mimic a coronary artery feeding a region of myocardium with a single venous outlet. An early design used a plastic tube inlet into an open bath chamber with a drain near the top. This approach was discarded, as contrast accumulated in the bottom of the chamber (as it more dense than water) and did not drain easily down the outlet. As such it was difficult to clear the phantom of contrast. Moreover, the volume of liquid in the chamber was not constant during injections. The open bath was replaced by a glass jar with a lid (Marmite Original 250 g, Unilever Ltd, London). Two holes were drilled into the jar lid for each of the inlet and outlet hose, whilst ensuring water tight fit of the hoses and lid. The inlet hose terminated close to the lid of the jar (i.e. near the top of the jar), and the outlet hose terminated in contact with the bottom of the jar. The jar was filled with liquid and with the lid closed an injection of water or contrast into the inlet would expel an equal volume of liquid from the outlet, keeping the liquid volume in the jar constant. A sponge was attached to the end of the inlet hose inside the jar. The sponge caused injected contrast agent to diffuse through the sponge's structure, and prevented the contrast from simply falling to the bottom of the jar, therefore delaying the transit of contrast from the inlet to the outlet. Several sponge types were tested; too dense sponges retained contrast for too long a time, yet too open sponges failed to delay the contrast sufficiently. A common cleaning sponge was finally selected, which delayed the contrast for approximately two seconds before contrast could be seen beginning to flow to the bottom of the jar. The inlet hose was connected via a Y-connector to both a power injector (Angiomat Illumena, Liebel Flarsheim Inc., Cincinnati, OH, USA) for injection of contrast medium. The power injector was the pump used in clinical practice, and therefore a calibrated medical device maintained and serviced by the supplier. A clean warm water source was pumped via microprocessor controlled pump. The clean water pump was turned on after a contrast injection to flush all contrast from the phantom before a subsequent contrast injections. The outlet hose's position at he bottom of the chamber allowed contrast in the chamber to be flushed quickly and prevented the contrast accumulation seen in the original phantom design. Liquid from the outlet hose was discarded. The configuration is shown in Figure 7.1.

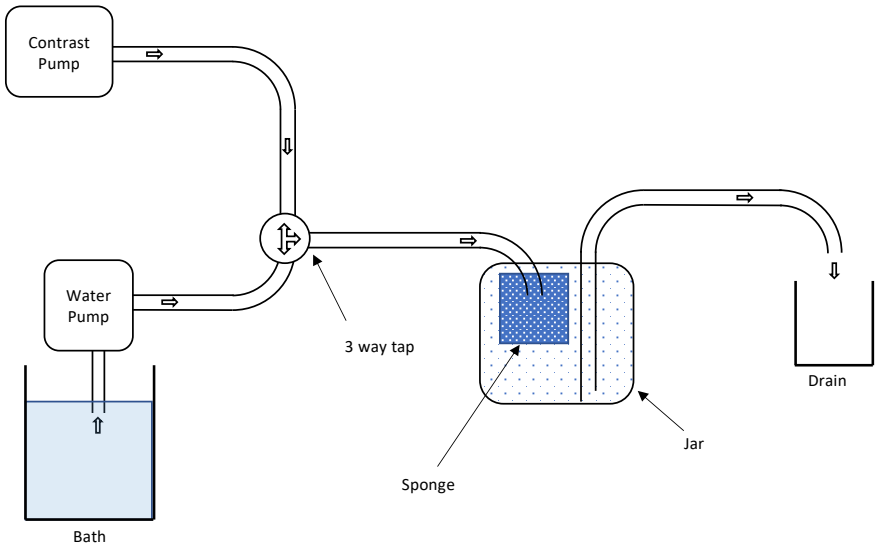

Figure 7.1: Configuration of the direct injection phantom.

The chamber and all hoses were filled with body temperature water, and all air bubbles cleared from the system. Imaging was performed during which contrast was injected at a known rates. During the acquisition the tube to the clean water inlet was clamped, preventing contrast from flowing into the clean water inlet reservoir. Following each injection sequence the clean water inlet was unclamped, and the clean water pump turned on until the all visible signs of contrast medium in the jar on fluoroscopy were cleared.

7.2.2 Imaging

Two experiments were performed using the direct injection phantom. The first was a proof of concept experiment, and the second a test of reproducibility. Two catheterisation laboratories were used for the experiments, one containing an Allura Xper FD10 and the other an Allura Clarity FD10 (Philips Healthcare, The Netherlands). Visipaque 320 (GE Healthcare, UK) was used as the contrast medium, and was pre-warmed to 37 degrees prior to injection. All images were acquired at 15 frames per second.

7.2.2.1 Proof of concept

The X-ray gantry was placed in the lateral position, and the mixing chamber placed on the couch in a larger tub to catch any spilt liquid. The SID was set to 121 cm, and the source-to-chamber distance was 93 cm. Six PMMA blocks of dimensions 10x10x2.5 cm were

placed between the tube and the jar, adding 15 cm of PMMA attenuation to simulate a patient's soft tissue. The entrance to the PMMA blocks was 59 cm from the X-ray source. Baseline radiographic settings were determined by acquiring an initial image sequence using the automatic dose control with the test phantoms framed in the image, and thereafter all acquisitions were performed using fixed radiographic settings based on those used by the automatic dose control (viz. 75 kV, 800 mA, 6 ms with 0.1 mm copper beam filtration). After the factors were determined the automatic dose control was disabled and the same settings used for every acquisition sequence.

Sequences were acquired at 15 fps using contrast injection rates of 0.5, 1,1.5, 2, 3 and 4 ml/s. The contrast injector was programmed to commence injection two seconds after the start of the X-ray imaging sequence and terminate the injection four seconds later. X-ray acquisition was continued for at least 11 seconds. Image capture was performed by dedicated hardware provided by the equipment manufacturer, which permitted the capture of images without the image enhancement and other image manipulations that are made to clinical images. The captured images were recorded on a dedicated computer placed in the equipment rooms of the catheterisation laboratories. The device recorded images prior to the normal image processing algorithms applied to clinical images, using a proprietary file format. Images were transferred from the capture computer to the University for analysis using custom software written in MATLAB R2013b (Mathworks Inc, Nattick, MA, USA). Twelve frames starting at 1 s into the sequence were averaged and the average of these frames subtracted from all of the frames in the sequence, effectively removing all background objects from the image. A region of interest was drawn around the jar, and the sum of pixel intensities within the region was calculated for all frames in a sequence forming a TIC. The gradient of the TIC between frames 60 and 90 was calculated by curve fitting a first order polynomial. The 1 ml/s sequence was selected as the calibration sequence and a calculation of flow was made as per Eq. 6.6 on page 116.

7.2.2.2 Reproducibility

On a different occasion the phantom was reassembled with only minor changes from that above. Firstly the X-ray beam was configured in a vertical position facilitating easier access and placement of the beam filters. The X-ray dose control was not overridden for this ex-

periment, but rather the dose control scheme used for the cardiac DSA system was used, i.e. the dose control operated for the first five frames of an acquisition sequence, than then the factors were locked for the remainder of the sequence. Three sequences were obtained with contrast of 1, 2, 3, 4 and 5 ml/s, producing 15 sequences. The contrast injection was initiated approximately two seconds after the X-ray acquisition, and continued for four seconds. Image capture and analysis was completed using similar methods to the proof of concept experiment.

The coefficient of variation was calculated for the gradient of the TIC for each injection rate. Three measures of flow were calculated for each of the injection rates of 1.5 ml/s or greater, using different combinations of calibration sequences taken from the 1 ml/s sequences and one from the measurement sequences; for example if the three 1 ml/s sequences were A, B and C, and the three 4 ml/s sequences D, E and F, then the (calibration-measurement) image pairs used to calculate flow for the 4 ml/s injection were A-D, B-E, and C-F. To obtain flow measurements the the injection rate of 1 ml/s, three combinations of the 1 ml/s sequences were combined as calibration-measurement as follows: 1-2, 2-3, and 3-1.

7.2.3 Results

7.2.3.1 Proof of concept

Three frames from the 3 ml/s injection sequence are shown in Figure 7.2, taken from near the start of the acquisition, and in the middle and near the end of the injection sequence. The time intensity curves from the background subtracted images and their linear curve fits from each of the acquired sequences are shown in Figure 7.3. The linear portions during contrast accumulation can be clearly seen.

The calculated rates of flow from the X-ray measurements are shown in Figure 7.4. For the flow measurements the average coefficient of variation between all flow rates was 4.3%

7.2.4 Discussion

The results from the direct injection phantom indicated that the X-ray flow measurements were reasonably accurate, with a mean difference between the X-ray measurements and actual flow of 0.05 ml/s, and a root mean squared error of 0.17 ml. The absolute difference between the X-ray measurement and actual flow increased with the flow, and the maximum absolute difference was 0.43 ml/s with an actual flow of 5 ml/s (9%). The measurements

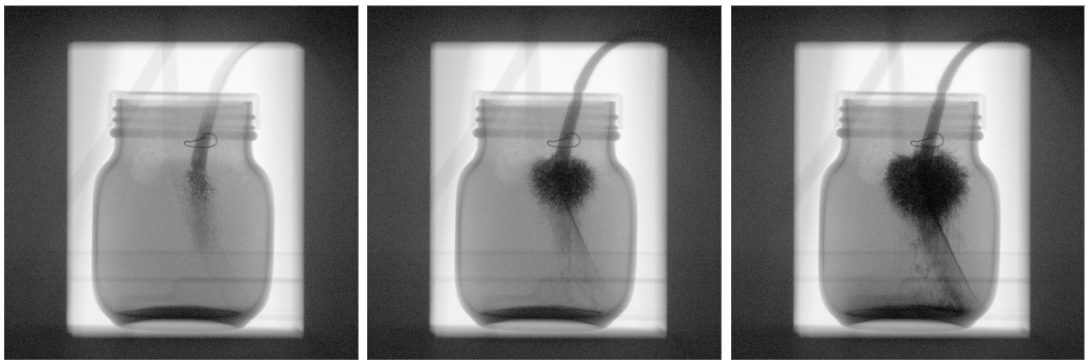

(a) frame 25 (b) frame 55 (c) frame 90

Figure 7.2: Frames from the 3 ml/s direct injection phantom sequence a) as the injection was commencing, b) in the middle of the contrast injection and c) towards the end of the injection. The jar can be seen, along with the contrast accumulation in the sponge during the injection.

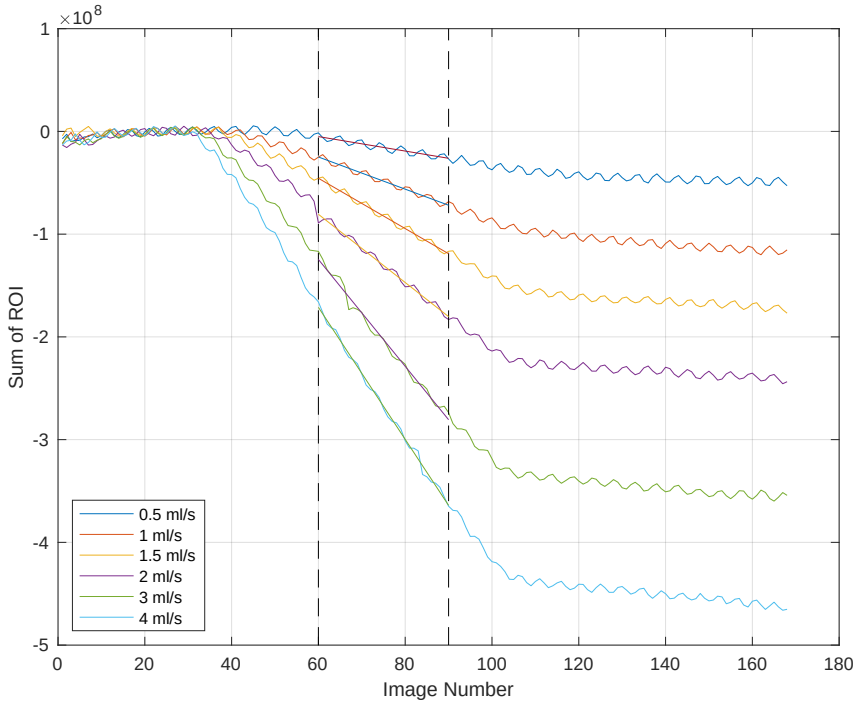

Figure 7.3: Time intensity curves for each of the acquisition sequences, and fitted curves to calculate gradient.

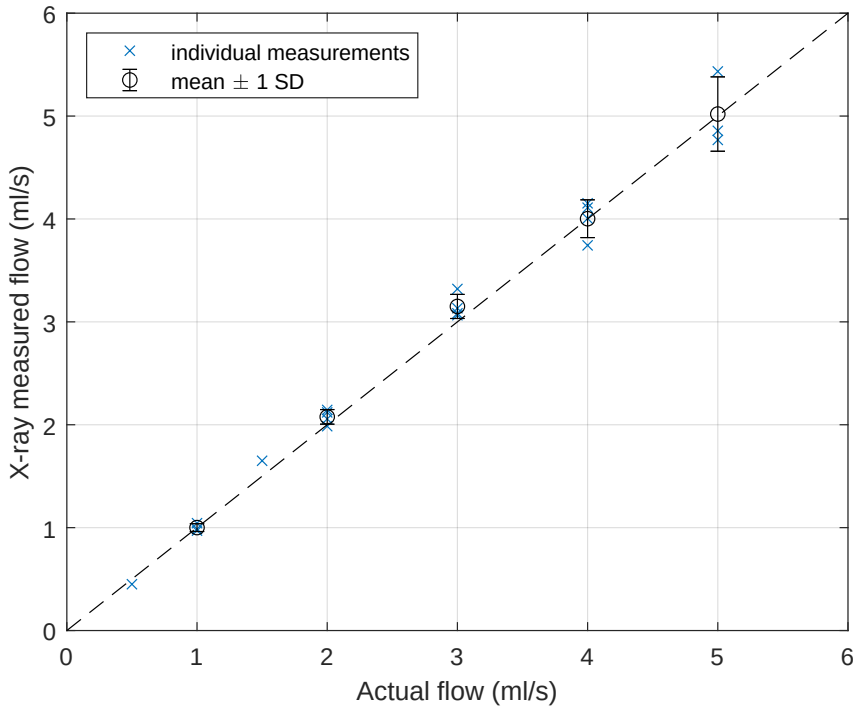

Figure 7.4: Scatter plot of actual vs X-ray measured flow from both the initial and reproducibility experiments using the direct injection phantom.

were also reproducible, with a mean coefficient of variation of 4.2%. These results indicated that, given that with a polyenergetic X-ray beam typical of that used in cardiac imaging, and in the presence of scattering materials, that acceptable levels of accuracy and precision could be achieved in the phantom. The next stage of the experiment, using the more sophisticated coronary circulation phantom, would investigate if the measured flow is affected by the contrast injection itself, and if the choice of contrast agent is an important factor.

7.3 Coronary circulation phantom

The second phantom model was constructed with far closer resemblance to the human vascular system. The design of the phantom is shown in Figure 7.5. All of the tubing in the phantom was silicon walled. The circuit comprised the following segments (each segment is shown in a circular marker in Figure 7.5):

Segment A: The ascending aorta model. Joining this section is a branch allowing a catheter to be introduced through a seal. The second branch is the coronary artery model (segment C), and the main exit of this segment becomes segment B.

Segment B: The descending aorta model. This has an adjustable screw clamp (R1 in the diagram) allowing the silicone tubing to be compressed, creating resistance to flow and therefore increasing the pressure in segments A and B. This clamp could therefore be used to alter the pressure in the aortic segment of the model (P_a). This segment drains either back into the heated tank (creating a recirculating circuit), or into a drain bucket, whose contents were disposed of so that contrast flowing through this section would not recirculate in the phantom.

Segment C: The coronary artery model. The tip of the catheter was engaged with the start of this segment (as would be the case in human PCI). An second adjustable clamp (R2) was placed in this segment which allowed the tube to be compressed simulating a stenotic lesion in the epicardial vessel. When used the intracoronary pressure wire was advanced beyond clamp R2 to measure (P_d).

Segment D: A 250 ml glass jar reservoir (the same as used in the previous experiment) was used to model the microvasculature.

Segment E: The venous outflow model. A third adjustable clamp (R3) could be used on this segment to simulate microvascular resistance. An inline flow meter (GTF2BHS, CT Platon SAS, Cedex, France) was present after the clamp. In the same way as segment B, this segment of the phantom could either be set to recirculate its outlet into the main heated water bath or divert its output into a drain bucket from which it was discarded.

A mixture of 40% glycerol and 60% water was prepared and used as a blood mimicking fluid (BMF) as in previous studies.[312] Two pumps were available for use: a pump with a pulsatile flow (GP8825, Whale Industrial, Bangor) and a combined pump and heater (GD120, Grant Scientific, Shepreth, Cambridgeshire). These where submerged in the reservoir or attached to the top of the tank containing the BMF as appropriate. For the second pump, the heater was thermostatically controlled, and set to heat the liquid in the bath to 37 °C. The glycerol-water mixture was stirred regularly to ensure good mixing of the water and glycerol.

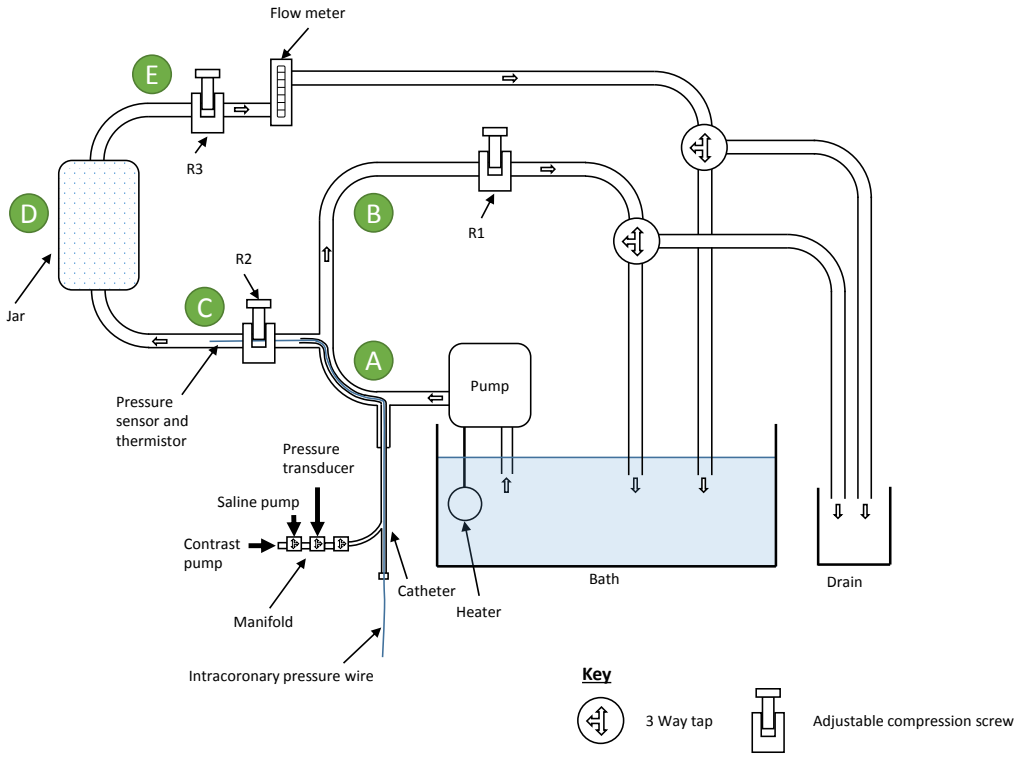

Figure 7.5: Configuration of the fluid flow in the experiment.

7.3.0.1 Reservoir jar

The purpose of the jar was the same as in the previous experiment, i.e. to provide a suitable volume of liquid and a long enough transit time to allow for a period of contract accumulation in the early stages of the acquisition sequences which could be fitted into the imaging field. Improvements were made to the design of the reservoir jar following the work with the direct flow phantom. Experience with the first phantom had revealed that whilst the sponge was an acceptable solution, securing it in place was fiddly, it could take some time to completely clear of contrast, and was perishable. Whilst the sponge used was cheap, it was also unlikely to be particularly consistent between batches.

Initially, the jar was replaced by a coil of silicone tubing, wound such that its entire content was visible in the image field. Whilst attractive from a simplicity point of view, as the volume of liquid in the loop could be easily adjusted by altering the length of the coiled tubing. In practice, however, the increased length of tubing was problematic as it increased the resistance to flow compared to the jar. This was especially problematic during contrast

Figure 7.6: Glass jar in position with the C-arm in a lateral position. The beam filtration attached to the tube exit is just visible.

injections (due to the increased viscosity of the contrast agent compared to water or BMF). During high rates of contrast injection the pulsatile pump was unable to maintain adequate flow, with the pump running ineffectively, and drawing air into the circuit.

The jar was therefore reintroduced, but filled with plastic beads rather than the sponge. Plastic beads are an attractive method of diffusing the contrast agent throughout the jar, as they have a very similar X-ray attenuation to water and BMF, are readily available in fairly reproducible sizes, and are inexpensive. Additionally the beads allowed the phantom to be easily cleaned and dried, and their use resulted in the phantom not containing any perishable parts. Smaller beads were found to increase the contrast's transit time, but if the beads were too small they could be drawn into the main circuit via the jar's outlet tube. Too larger beads lead to too rapid contrast agent transit and too low a liquid volume in the jar. Following some trials with different beads, using beads with a hole through their centre (designed for threading the beads over a string) produced good results. This meant that the beads could be selected with sufficient outer diameter that they were large enough so that they could not be drawn into the outlet, but the hollow centres created a larger number of paths for the transit of contrast, and resulted in a larger liquid volume in the jar, thus increasing the transit time. The beads used had an outer diameter of 8.4 mm, a length of 6.1 mm and internal diameter of 4.4 mm. Once connected the jar was positioned in the imaging field with the C-arm in the lateral position. The source to object distance was adjusted so that the jar filled most of the imaging field. The arrangement is shown in figure 7.6.

Connections

The catheter allowed a number of devices to be connected to the system. A three way manifold was attached to a pressure transducer which measured pressure within the catheter. Hence with the catheter engaged at start of segment (C), the pressure sensor is measuring the simulated aortic pressure (P_a). Two power injectors were also connected to the manifold, one for warmed contrast agent, and one for room temperature saline. The catheter could also be used to introduce smaller catheters, such as a thermodilution catheter (RayFlow, Hexacath, Rueil-Malmaison, France), and a intracoronary guide wire with pressure and temperature sensors (PressureWire Certus, St. Jude Medical, St. Paul, Minnesota, USA). With the tip of the intracoronary pressure wire advanced beyond the simulated stenotic lesion, the pressure sensor at its tip records the simulated distal pressure (P_d).

The outlet of segment C had an inline flow meter attached. The meter was calibrated for water, and therefore not accurate when using the BMF. As a result, the outlet from this section could also drain into a graduated cylinder, where the time taken for a given volume of fluid to drain could be measured and used to calculate flow.

7.3.0.2 Phantom design testing

A number of tests were performed to confirm that the phantom behaved as a suitable model for the human coronary circulation. With the pump running it is possible to adjust the three clamps (R1–R3 in in Figure 7.5) to achieve the desired flow rates and pressures within the phantom. Using the pulsatile pump, R1 was adjusted to provide pressure similar to that in a human aorta, and R2 and R3 were adjusted to simulate the following situations:

i. no stenosis or myocardial obstruction (R2 & R3 minimum)

ii. stenotic lesion only (high R2, minimum R3)

iii. stenotic lesion and myocardial obstruction (high R2 & R3)

iv. myocardial obstruction only and no stenosis (high R3, minimum R2)

Recordings were made of the pressure waveforms, calculated FFR and coronary flow for each configuration.

A series of experiments were conducted to confirm that flow within the coronary segment of the phantom altered was as would be expected in response to variations in the three clamps. A number of experiments using the pulsatile pump were performed, with the four conditions listed above while pressure was simultaneously recorded using an intracoronary pressure wire (to measure P_d) and via a transducer attached to the catheter (P_a). However during this testing phase, the pulsatile pump was seen to run at a reduced output, either gradually over time, or suddenly. It was therefore replaced with the steady state GD120 pump. Using this pump the simulated aortic pressure, distal pressure and output flow were measured as resistance R1 (to control the aortic pressure) R2 (stenotic lesion) were varied. Although there was an inline flow meter in the coronary outlet segment of the phantom, it was not used as the primary source of flow measurement as it was calibrated for use with water and not the BMF used in the phantom experiments. Instead, the outflow from the simulated coronary artery segment was measured using both the flow meter and by measuring the time taken for 30 ml of liquid to accumulate in a graduated measuring cylinder using a stopwatch. In all cases, time measurements were repeated three times and the mean taken to calculate flow.

Initially, R2 and R3 were set to their minimum values, simulating no added myocardial or stenotic resistance, and R1 was varied to alter the simulated aortic pressure from 90 to 125 mm Hg. Measures of P_a, P_d and outflow were taken. The simulated aortic pressure was reset to 100 mm Hg, and then progressively R2 was altered to simulate increasing stenotic resistance with P_d values between 100 mm Hg (no stenosis) to 41 mm Hg (severe stenosis). Again, measures of P_a, P_d and outflow were taken, and the relationship between stenotic resistance ($(P_a - P_d)/Q$) and flow described.

X-ray blood flow measurements

The coronary flow phantom was set up in a cardiac catheterisation laboratory (Allura Clarity FD10, Philips Healthcare, The Netherlands). The combined pump & heater unit was used, with R1 adjusted to provide P_a of 125 mm Hg and R2 and R3 set to minimum. The output flow from the coronary branch was measured using the graduated cylinder, as before. The reading on the inline flow meter was noted, and referred to during the experiment to ensure that the flow conditions had not changed. The controls on the manifold were set to allow the flow from the contrast pump into the catheter. Contrast agent injections for each of two

types of contrast agent- iodixanol (Visipaque 320, GE Healthcare, Amersham) and iohexol (Omnipaque 140, GE Healthcare, Oslo, Norway) were performed at a range of rates: 0.5, 1, 2, 3 & 4 ml/s. Prior to each injection, the contrast pump was advanced by hand until contrast was visible at the tip of the catheter. All imaging was performed with the jar centred in the X-ray beam with the C-arm gantry in the lateral position. 25 mm of Al filtration was added to the X-ray collimator output window. The main pump was started, and a short while later, after the flow had stabilised, X-ray image acquisition at 15 frames per second was initiated. The radiographic dose was set by the automatic dose control, which was programmed to lock the factors for each sequence after five frames. After approximately two seconds the contrast injection was initiated, and this continued for four seconds. No delay or rate rise and a maximum pressure of 200 mm Hg were programmed into the contrast pump. X-ray image acquisition was continued for several seconds after the cessation of the contrast injection. The main pump was left running after the image acquisition to flush contrast from the tubes and jar. During contrast injection and washout the outlet pipes were configured to flow into the drain bucket, so no contrast was recirculated in the system. Fluoroscopy was used to confirm the complete washout of contrast agent before the pump was stopped and the system prepared for the next injection. Each of the injection rates was performed three times. Images were recorded on a dedicated image capture PC that could record the image sequences prior to the image enhancements normally applied by the manufacturer.

The images were transferred from the capture computer to the University for analysis. All analysis was performed with the software developed for human use. This software is described in detail in chapter 8, but the calculations performed to measure flow, i.e. the ratio of the measurement and calibration curves' gradients, were the same as in the previous phantom work. The rising gradient of the TIC was calculated for each sequence, and standard deviation calculated. The 1 ml/s sequences was selected as the calibration sequence, and the flow of each of the other rates was calculated. To calculate flow for the at 1 ml/s, different 1 ml/s sequences were combined as the calibration and measurement sequences. Three such measurements were taken for each rate.

Stenotic Lesion	Myocardial obstruction	Pa [max/min, mean] (mmHg)	Pd [max/min, mean] (mmHg)	P_d/P_a	Flow (ml/s)
n	n	80/45, 58	72/39, 50	0.89	2.67
y	n	85/47, 59	45/20, 30	0.51	1.57
y	y	87/48, 61	77/42, 54	0.88	0.60
n	y	87/48, 61	84/44, 57	0.95	0.65

Table 7.1: Coronary circulation phantom pressure and flow measurements as different resistances are introduced with the clamps.

Contrast agents

Finally the phantom experiments aimed to assess the effect of the contrast agent choice on the X-ray based flow measurement. If the contrast agent injection affects the flow of blood in the coronary artery this will introduce error into the flow measurements. Two contrast agents were selected: iodixanol 320 mg I/ml and iohexol 140 mg I/ml. Iodixanol 320 mg I/ml was the standard contrast agent in clinical use at the time of the study. The lower concentration iohexol has a lower viscosity, but with the downside of using the lower iodine concentration contrast is the reduced attenuation and therefore lower differential signal intensity compared to the background.

7.3.1 Results

7.3.1.1 Phantom design testing

Using the pulsatile pump the four resistance configurations were compared, viz. no stenotic or myocardial resistance, stenotic resistance only, both stenotic and myocardial resistances, and myocardial resistance only. Pressure traces from the experiment are plotted in Figure 7.7. Example pressure measurements are recorded in Table 7.1, which also includes a calculation of P_d/P_a (analogous to pressure measured FFR) and measured coronary output flow. The phantom behaved as expected, for instance with P_d/P_a decreasing as a stenosis is simulated, but then increasing once an increase in myocardial resistance is simulated along with stenotic lesion. In other words the increased resistance downstream from the stenotic lesion, resulted in a "normal" FFR, yet there was very low flow. When the stenotic lesion was removed, the P_d/P_a increased further to 0.95, and the flow improved slightly to 0.65 ml/s, but again the reduced flow could not be detected by the measurement of P_d/P_a alone.

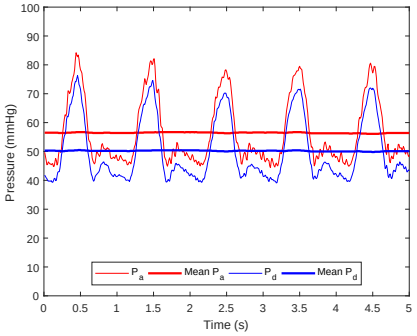

(a) No obstruction

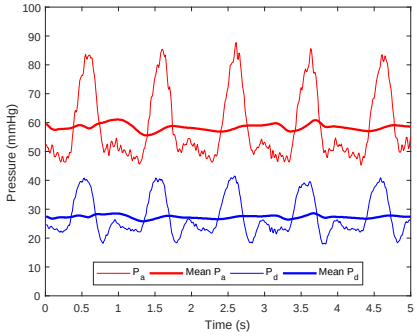

(b) Stenotic lesion

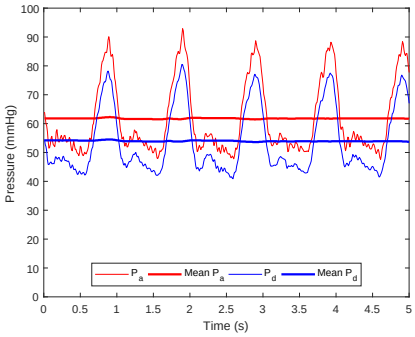

(c) Stenotic and myocardial obstruction

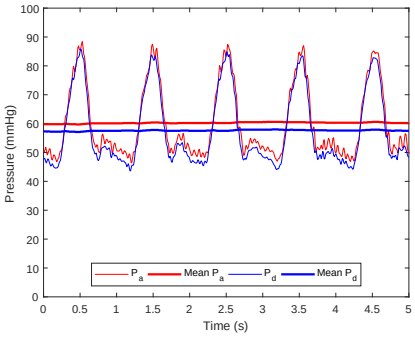

(d) Myocardial obstruction only

Figure 7.7: The effect on pressure in a phantom simulating obstruction to blood flow in the artery (b), artery and myocardium (c) and myocardium only (d). All three of conditions b)–d) result in greatly reduced coronary flow, but only b) is detectable using pressure measured FFR. The mean P_a and P_d plots are the pressure averaged over a simulated heart cycle.

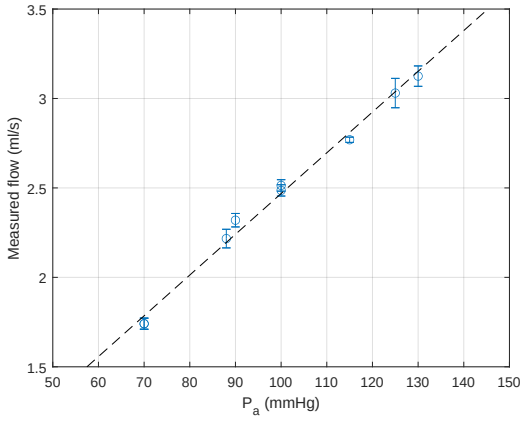

Figure 7.8: Output coronary segment flow as the simulated aortic pressure is varied. This demonstrates a linear relationship between aotric pressure and flow when no coronary resistances are introduced. Error bars indicate ± one standard deviation.

Considering the measurement of flow using a stopwatch for the accumulation of 30 ml of liquid in the graduated cylinder, the mean coefficient of variation for the time measurements was 1.81% indicating good reproducibility of the output flow measurements. The relationship between the flow meter reading and outlet flow measured using the time for 30 ml of liquid to accumulate in a measuring cylinder was found to be strongly correlated ($r = 0.98$) and related by $t_{30} = 0.803m - 0.803$ where t_{30} is the time based measurement, and m is the meter reading.

With no additional simulated stenotic or myocardial resistance (so $P_d/P_a = 1$), the coronary segment flow measured at the outlet as a function of the aortic pressure are shown in Figure 7.8, and demonstrated a linear relationship between simulated aortic pressure and coronary flow as expected in the absence of a stenotic lesion.

With the pressure set to 100 mm Hg in the simulated aortic segment of the phantom, clamp R2 was tightened simulating a stenotic lesion. As this was done, the pressure gradient across the clamp would increase, and P_d/P_a would decrease, and Figure 7.9a shows that flow also decreased as expected. Figure 7.9b shows the same data plotted as stenotic resistance ($(P_a - P_d)/Q$) as a function of flow.

7.3.1.2 X-ray blood flow measurements

With R2 and R3 both set to minimum (i.e. no simulated stenotic or myocardial resistance), R1 was adjusted until a flow of approximately 3 ml/s was achieved in the coronary artery

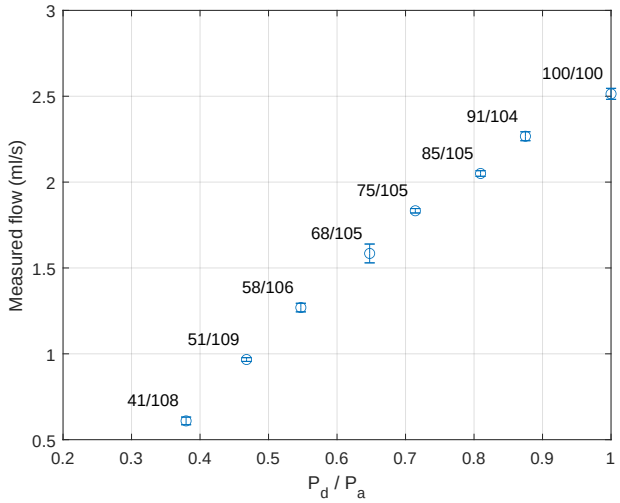

(a) Pressure ratio

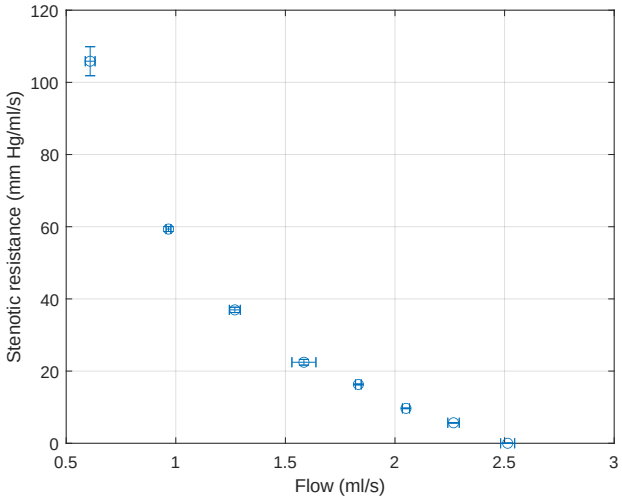

(b) Resistance

Figure 7.9: The effect on flow as clamp R2 is tightened on the circulation phantom, simulating a stenotic lesion of increasing severity, showing a) flow decreases with reduced Pd/Pa, and b) Increased stenotic resistance. The labels by the points in a) indicate P_d/P_a, and error bars indicate ± one standard deviation.

branch of the phantom. This was achieved with a P_a, of 135 mm Hg, which was close to the value achieved in the previous experiment. The time taken for 30 ml of BMF to flow out of the coronary model branch was measured as 9.91, 10.17 and 10.24 s, giving a flow of 2.97 ml/s.

One image file was not available for analysis in the iohexol 3 ml/s set, probably due to a misidentification error in the file transfer. The mean coefficient of variation in time intensity curve gradient was 1.6% and 2.2% for iohexol and iodixanol respectively. For equivalent conditions the use of 320 mg I/ml iodixanol produced on average 1.8 times the signal change of the 140 mg I/ml iohexol.

The measured flow values for iodixanol and iohexol are shown in Figure 7.10. For contrast injection rates well below the 2.97 ml/s flow down the coronary artery segment, it would be expected that all of the contrast agent would flow down the artery, and the measured flow would be equivalent to the contrast injection rate in the measurement sequence; that is indeed what is observed. For injection rates approaching and above the underlying coronary flow, some of the injected contrast would be expected to flow back into the simulated aorta, and then never enter the coronary segment, instead being expelled out the segment B (descending aorta model) of the phantom. Assuming that the contrast injection did not increase the underlying flow down the arterial segment, then as the injection rate were increased through beyond the native flow then it would be expected that the measured flow would approach and eventually be equal to the native flow, and this behaviour was observed. The maximum measured flow with a 4 ml/s injection rate was 3.01 and 2.83 ml/s for iohexol and iodixanol respectively; in other words the higher strength more viscous contrast agent underestimated flow by 0.17 ml/s (5.7%). The mean coefficient of variation was 1.7% and 4.8% for the iohexol and iodixanol contrast agent respectively.

7.4 Discussion

Reasonably accurate measurements of flow were obtained during this in vitro study using both the direct injection and coronary circulation phantoms; for the direct injection phantom the average root mean squared error was 4.4%, and for the coronary circulation phantom it was 1.9% and 8% depending on the contrast agent used. In terms of precision, for the direct

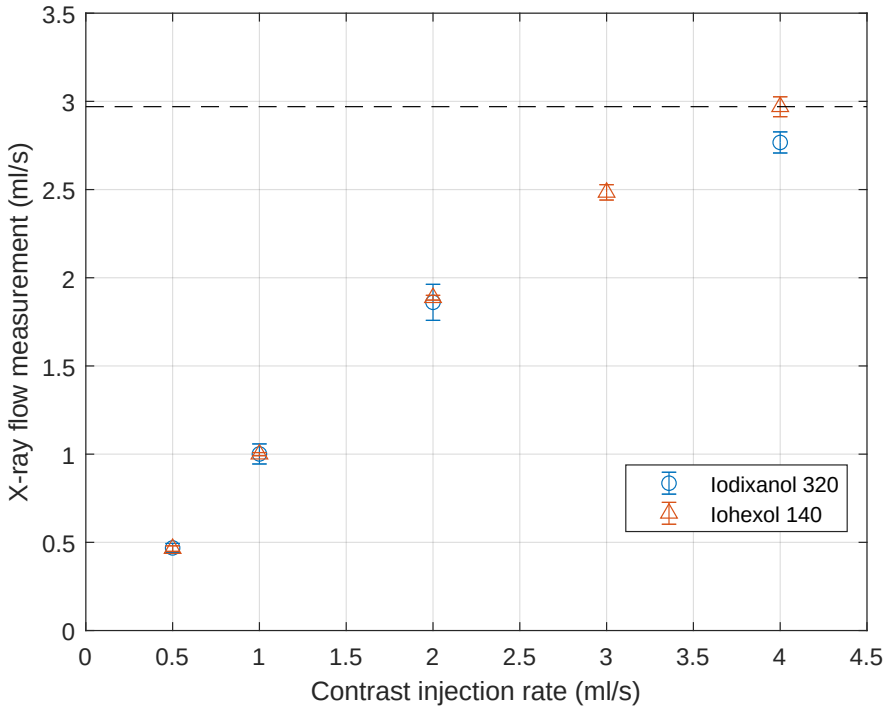

Figure 7.10: Contrast injection rate and measured flow in coronary circulation phantom using both iodixanol and iohexol contrast agent. Error bars indicate ± one stanadard deviation. The native artery flow of 2.97 ml/s is shown by the dashed line.

phantom coefficient of variation for flow measurements was 4.3% and for the coronary circulation phantom 1.5% and 2.2% for iohexol and iodixanol respectively. The flow measurements were therefore reasonably accurate and precise in the phantom experiments. It is likely that a number of factors would have influenced both the accuracy and precision of the X-ray based measurements. Incomplete wash out of contrast between acquisition sequences would lead to a lowering of the gradient as this contrast is ejected from the phantom early in the injection sequence. The sponge/beads not delaying contrast transit as much as required would have resulted in the contrast reaching the outlet at the bottom of the container rapidly due to its higher density than water, again lowering the TIC's gradient. Contrast agent transit on the inlet and outlet pipes which impinge on the image, could affect the TIC, as could variations in dose control settings between sequences, say due to small movements in the jar. The non-linear relationship between iodine mass thickness and signal intensity, which is assumed in the methods, is not exactly true, due to the poly-energetic beam and scattered radiation. Some of these factors were unique to the phantom experiment (transit time in the jar, and external tube positions for example), but others would also be found in human imaging. These include

movement in the exact position of objects in the beam and non-linearity of the contrast agent mass to signal intensity. The magnitude of these may be very different in human imaging; for example the scatter-to-primary ratio was probably low in the phantom compared to clinical cases as the main attenuators were placed at the tube exit window, leaving a large air gap to the detector, and breathing could introduce considerable movement in the image and variations in the overlapping anatomy, rather than the simpler translations of the phantom elements observed in these experiments.

Compared to previous work, Molloi et al.[259] found a standard deviation for differences between X-ray and ultrasound measured flow to be 0.05 ml/s, but the flow rates were much lower in these animal experiments (0–1 ml/s). The mean difference between the angiographic and reference measures was very close to zero. In later work, using an automated analysis system, the group demonstrated a mean difference of 0.1 ml/s between X-ray and ultrasound measurements with a standard deviation of 0.06 ml/s, although again the flow rates were lower than used in these experiments, and variations at different flow rates were simply combined in the analysis, despite the variation clearly being related to the absolute flow.[260] In phantom measurements Goszczynska & Rewicki demonstrated an accuracy of 20% using a similar calibration to the Molloi method.[313] Overall, the precision of the phantom work here is comparable to the animal work of Molloi's work and better than that of Goszczynska & Rewicki.

From a practical point of view, the methods described in this chapter should fit well into a clinical work flow. A power contrast injector is required for the calibration sequence, although these are widely available. These phantom experiments indicated that a calibration of injection of 1 ml/s provided a good signal level, and produced accurate results. This flow rate can be accommodated by the major coronary arteries, even in the presence of all but the most serious of disease. Although not presented, a calibration of lower rates (say 0.5 ml/s) would not have significantly altered the results. For the patient, the measurement sequence could replace one of the standard angiograms performed. The measurement of flow would require some additional radiation and contrast medium dose to the patient, but the amounts would be a small fraction of the total of quantity used in the routine procedure.

The two contrast media tested produced very similar result, albeit with the more viscous contrast agent slightly underestimating the flow in the circulation phantom. The benefit of

using the contrast agent with a higher iodine concentration, is the higher signal per unit volume of contrast agent injected. In these phantom experiments, where there is no movement during the acquisition sequence and a large region of interest almost eliminating the variation due to quantum noise, this advantage would not be seen, but in human imaging, misregistration artefacts due to movement will cause variations in the TIC, and therefore making the intensity changes due to the contrast agent larger in magnitude would be beneficial. There was slightly higher variation in the flow measurements made with the higher iodine concentration contrast agent (as can be seen by comparing Tables **??** and **??**). In clinical practice, it would not be advisable to use two different types of contrast agent during a procedure, as this would increase the risk of adverse reactions. The use of two different concentrations of the same contrast agent would be possible, but Visipaque (the iodixanol product used in the hospital in Leeds) is not available below 270 mg I/ml.

There did not appear to be an increase in arterial flow due to the injection of the contrast agent. At no point in Figure 7.10 do the measures of flow exceed the injection rate for injection rates of less than the arterial flow, nor do the injections of contrast at 4 ml/s cause measured flow values to exceed the native flow of just under 3 ml/s. For this to happen the excess contrast agent must flow back into the simulated aorta, and be washed out of that segment of the phantom. This was confirmed by imaging the bifurcation of the simulated coronary artery from the aorta in the circulation phantom during a contrast injection at a greater rate than the arterial segment flow whilst using the pulsatile pump. Images from the sequence are shown in Figure 7.11. Figure 7.11a shows the very beginning of the contrast injection. The simulated aorta is running from the top-left to the bottom-left of the image, with the coronary segment branch east. As the injection progresses, contrast begins to fill the space upstream from the catheter tip, and between strokes of the pump accumulates around the injection site (Figure 7.11b). As the simulated aortic flow increases during the pump stroke, this contrast is carried downstream along the aortic segment (Figure 7.11c).

Whilst the phantom experiments were informative, in demonstrating the accuracy and reproducibility of the X-ray flow measurements, they are limited by the range of experimental conditions examined. It would have been preferable for a greater range of coronary segment flows to have been tested using a combination of aortic pressures, stenotic resistances and myocardial resistances. However, time available within the catheterisation laboratory was

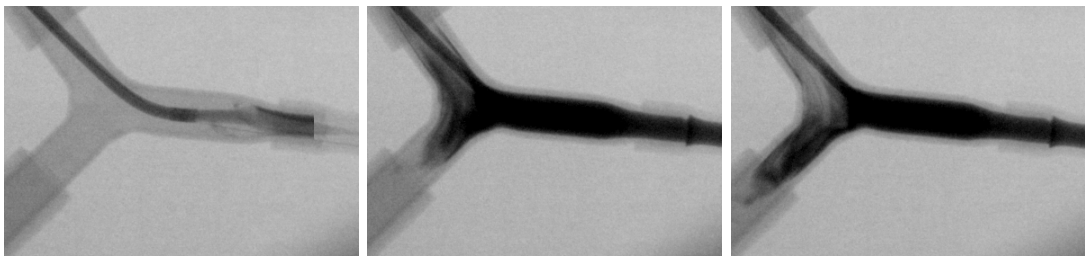

(a) Frame 16 (b) Frame 50 (c) Frame 66

Figure 7.11: Frames from the coronary circulation phantom showing the catheter engaged with the coronary artery segment. During a contrast injection at a higher rate than the flow down the arterial segment, contrast can be see flowing back into the aortic segment of the artery.

limited to weekend use when the laboratories were not used on the on-call rota. The time taken to set up the experimental equipment, and then to dismantle and clean the catheterisation laboratory after use, was considerable and the requirement to completely assemble the phantoms for use, and return the laboratory in a state for clinical use after each day limited the amount that could be performed on any given occasion. The failure of the image capture device in one of the two laboratories further limited the experimental time available. Three people were required to operate the X-ray equipment and perform the measurements safely, again creating logistical problems performing these experiments. Finally the bath, flow meters and steady state pump were loaned to us by the University of Bradford, and there was a limit to the equipment availability.

7.5 Conclusions

The X-ray measurements proved reasonably accurate and reproducible in phantom experiments, and the injection protocols required would not be overly onerous for use within the catheterisation laboratory in human use. The use of rate of signal change, calibrated with a known injection rate was shown to be a viable alternative to calibration phantoms containing known quantities of iodine, rather than the injection of known bolus of iodine, as used in previous work, should overcome the problems implementing those fixed volume calibrations in human use. Finally, the settings on a modern clinical cardiac X-ray system were successfully modified to facilitate the quantitative assessment of absolute flow from angiography. These advances indicated that the technique could be viable in human imaging, and indeed the following chapter describes a preliminary study of the X-ray flow measurement in humans.

Chapter 8

In vivo measurements of flow

8.1 Introduction

The phantom experiments described in the previous chapter indicated that, with a suitable clinical protocol, X-ray angiography could be used to measure coronary blood flow and therefore an experiment was designed to test the method in humans. The translation into humans required that a number of potential complications were overcome that were not addressed or relevant in the phantom experiments. Clearly the heart is not static like the phantoms, and there is substantial movement of the heart during the cardiac cycle, which will result in variation in any time-intensity curve measured in an ROI. The earlier DSA work described in Chapter 4 indicated that a phase matched subtraction scheme could be used to overcome cardiac motion, and the relative flow experiment in Chapter 5 demonstrated that using retrospective selection of images at one point in the cardiac cycle was a viable means of achieving this. Coronary angiograms are also subject to other patient motion, most noticeably from breathing. The DSA work also indicated that minimising the duration of the injections of contrast agent (and therefore acquisition sequence) should reduce the number of cases lost due to breathing-related misregistration artefacts.

The human coronary arteries are considerably more complex in form than the phantoms described in Chapter 7 used test the X-ray measurement technique, and their structure can be challenging to image on a planar projection imaging system. There is also variation in coronary anatomy between people. In some people collateral arteries are developed in response to coronary heart disease. There are also normal anatomical variants, for example with the

posterior descending artery branching from either the right or left coronary arteries (referred to as right-dominant and left-dominant respectively). The two main arteries are selectively engaged during cardiac catheterisation, and therefore both are not normally visible on a single angiogram. This means that any measure of flow to the myocardium using X-ray angiography would have to assess the territories supplied by each of the two main coronary arteries individually. In the LCA it is desirable to be able to assess the Cx and LAD separately, however, the anatomy of the Cx and LAD are such that both arteries, and their myocardial territories, are often superimposed on common angiographic projections used on the left coronary system. Furthermore, the ascending and descending aorta could also carry contrast agent within the image field and therefore, ideally, these would not overlap with the heart itself in the projections used for flow measurement.

The following preparatory stages were therefore required prior to a human study:

- develop a clinical measurement protocol including angiographic projections and pump protocols,
- develop analysis software to measure flow on the image sequences that was resilient to the cardiac motion,
- select and utilise a reference measurement of blood flow.

Thereafter a study comparing blood flow from X-ray derived measurements to reference measurements in humans was performed.

8.2 Preparatory work

8.2.1 Selection of angiographic views

Diagnostic views of the coronary arteries are taken in a range of projections. Up to seven views with different combinations of left anteroir oblique (LAO)–RAO and cranial–caudal angulation for the LCA, and for the RCA three views are typically used,[219] although practice varies between institutions. Each view is intended to demonstrate different segments of the coronary arteries, whilst minimising foreshortening and overlapping vessels.[224] For the measurement of flow, however, different objectives were required, and issues such as minimising foreshortening of particular vessel segments are not required. The heart must fit within the entire image

frame throughout the heart beat. To reduce radiation dose, highly attenuating areas of the body (such as the spine or liver) would not be placed near the centre of the field, and the projection angle would ideally result in a relative low tissue thickness in the beam (i.e. not be too steep). This would also permit the use of lower kV, thus improving contrast. For the left system, the Cx and LAD and their perfusion territories would be projected into different areas of the image. Ideally overlap with the aorta would be minimised.

Previous angiographic sequences were reviewed by the project's clinical collaborators, and the following views were selected. For the left coronary artery: left lateral, or LAO (45–60°)-cranial (20°), and for the right coronary artery straight RAO (around 30°) or LAO(45–60°) with cranial angulation as required. Example images in these projections are shown in Figure 8.1. For the left system, the left lateral position (8.1b) does achieve the required objectives, but is not commonly used in clinical practice as there are a number of drawbacks to its use. The left lateral projection places the X-ray source close to the interventionalist, increasing staff dose. It requires a large amount of clear space around the patient which, given the use of two power injectors during this experiment, could be difficult to achieve. The heart is magnified in the image such that it may not fit in the image frame for larger patients. Finally, lateral projections can be difficult to achieve in patients with radial access due to the position of the patient's arm. For this reason the RAO-caudal projection (8.1a) was selected as an alternative, but there is not as good a separation of the Cx and LAD. The descending aorta can overlap the Cx which may result in contrast flowing back into the aorta during the measurement sequence entering the ROI used for analysis. This projection also suffers from the steep projection angle, with the diaphragm being high in the image field, and the spine encroaching some way into the image on the right hand side, and the descending aorta potentially overlapping with the Cx territory.

For all sequences the heart was framed to keep the entire heart within the imaging field, no magnification was employed (i.e. the largest field of view, 25 cm was used), the collimators were moved so they were just visible in the image frame, and the brass filters were completely withdrawn from the image field.

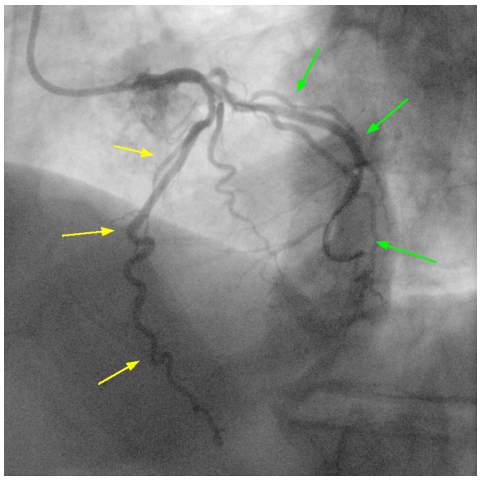

(a) LCA, LAO Cranial

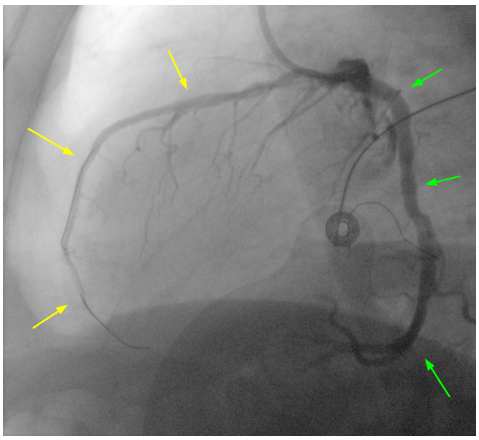

(b) LCA, left lateral

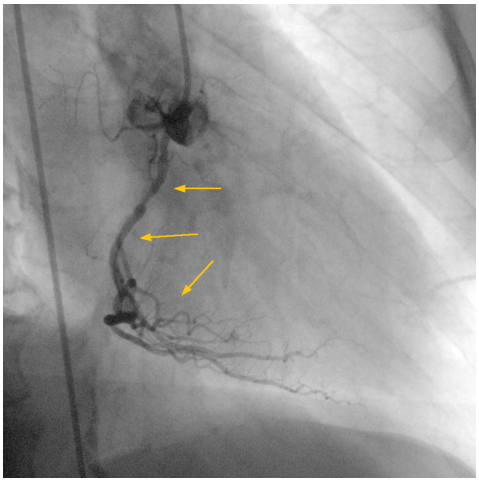

(c) RCA, straight RAO

Figure 8.1: Frames from angiograms taken in the projections used in the clinical study. The left coronary artery was imaged either in (a) LAO-Cranial or (b) left lateral, and in the images the left anterior descending and circumflex arteries are highlighted with yellow and green arrows respectively. In (c), taken with a straight RAO projection, the right coronary artery is highlighted by the orange arrows.

8.2.2 Pump protocols and angiographic timings

The duration of the contrast agent injection was selected to balance a number of competing requirements. From a contrast dose (and radiation dose) point of view, a shorter injection with a lower overall contrast volume would have been preferable. However, during the initial part of the injection, the contrast at the distal tip of the catheter would likely contain a mixture of blood and contrast, as contrast tends to leak out of the catheter over time. Therefore the initial part of the injection must be disregarded, as in the calibration sequence the mixture of blood and contrast would result in an unknown inflow of contrast agent, and in the measurement sequence complete replacement of blood with contrast would not occur. On the other hand, an absolute minimum of one heart beat with contrast inflow was required, and having a number of heart beats would allow some averaging of results over time. It was decided to use a fixed duration of injection rather than varying the injection duration based on an individual patient's heart rate, with the expectation that a simple table of injection rate and bolus volume would minimise the chance of error when programming the power injector.

Following discussion with the clinical collaborators, a four second injection duration was selected. This allowed two full heart beats even at a low heart rate of 40 beats per minute (bpm), and more at higher heart rates. For the calibration sequences, an injection at a rate of 1 ml/s was chosen, balancing the fact that all of the contrast agent must flow down the artery, against providing sufficient signal levels to be reliably quantified in an image sequence containing signal variations from cardiac and other motion. A lower injection rate (0.5 ml/s) was also available for use if a particularly low coronary flow was suspected. The maximum driving pressure of the pump was set to 200 psi, with no rate rise. Where possible, the pump was triggered to start automatically shortly after the beginning of the X-ray acquisition, with an inject delay programmed to at least 1.5 cardiac cycle durations for the current patient (so the pump would commence injection 1.5 s after the start of the X-ray acquisition for a patient with a heart beat of 60 bpm). In cases where the pump could not automatically be synchronised with the start of the X-ray exposure, that is when the necessary combination of pump model, connector lead, lead adaptor and catheterisation laboratory were not available during a given clinical session (not all combinations of equipment available in the catheterisation laboratories provided links between the electronic connections required to achieve automated coupling with the X-ray acquisition), the pump was triggered manually, ensuring a sufficient

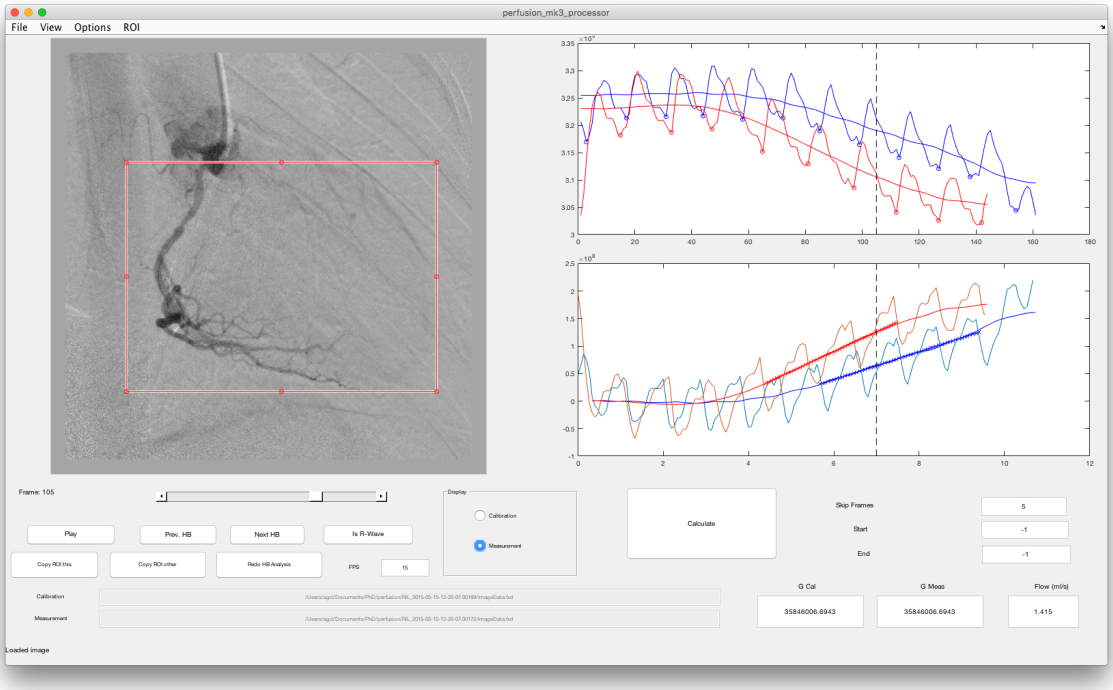

Figure 8.2: Full graphical user interface of the analysis tool showing a completed measurement.

delay allowing at least one cardiac cycle of images before commencing the injection.

For the measurement sequence, the injection rate was varied according to the overall size of the current artery and was 3–5 ml/s at the discretion of the clinical operator. In all cases, the resulting angiogram was reviewed and checked to ensure that continuous back flow of contrast into the aorta was present, indicating that the injection rate exceeded the native arterial flow.

8.2.3 Image analysis software application

A single application was created in MATLAB for analysing the sequences that combined and built upon the tools used in the relative flow experiment described in Chapter 5. The previous applications were time consuming to use, and in this phase of the project the analysis application was intended to be easy to use (suitable for unsupervised use by the clinical collaborators), and fast to produce results. As inputs, the software took either the raw (unprocessed) images from the data capture device fitted to the X-ray systems, or Digital Imaging and Communications in Medicine (DICOM) files transferred from the picture archive and communication system (PACS) system. The software's interface is shown in Figure 8.2.

The work-flow when using the analysis application was as follows.

1. Load the calibration image sequence into the application.
2. Draw a region of interest covering the whole heart.
3. Alter any of the parameters for the analysis software as required, and initiate the sequence analysis.
4. Load the measurement image sequence.
5. Copy the ROI used on the calibration sequence onto the measurement image and adjust as necessary.
6. Run the analysis using the same parameters, with the software reporting the measured flow.
7. Repeat from step four with any other measurement sequences from the same patient.

The application allowed the user to play the loaded image sequences as movies at the frame rate as acquired, or to manually step through image frames. Images can be displayed either as unsubtracted or subtracted image sequences. To create the DSA sequence a single mask image was automatically selected near the start of the sequence and subtracted from all images in the sequence. The subtracted sequences were useful for assessing patient movement, to visualise low concentrations of contrast—such is in the myocardium—or to visualise contrast in the aorta. This simplified subtraction scheme was only used for image display purposes. Reference markers could be shown as an overlay marking a fixed position in the image, allowing the position of objects in the image sequence (such as the catheter, arteries or the diaphragm) to be tracked over time. The ROIs, analysis settings and image sequence details in the current analysis session could be saved to disk and reloaded at a later date.

8.2.3.1 Drawing regions of interest

The perfusion analyser tool allowed the user to select a number of ROI shapes—rectangular, elliptical, or a generalised polygon. The rectangular shape was easiest to draw, whereas the ellipse could better match the shape of the heart in some cases without containing other features such as the aortic root. The most complex shape, the polygon was most time consuming

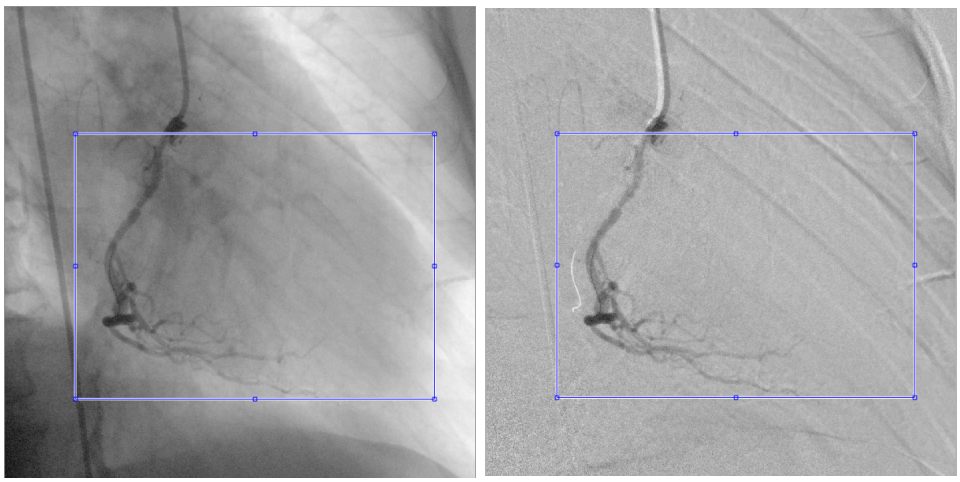

(a) (b)

Figure 8.3: Drawing a rectangular ROI in the MATLAB analyser tool, displaying the a) conventional unsubtracted presentation and b) digital subtraction view.

to draw, but allowed for any number of vertices to be added to the shape, permitting a great deal of flexibility in the ROI shape. Initial ROI locations, covering approximately the centre third of the image, were created by the software. The user was then able to interactively alter the shape and position of the ROI. The ROI type and shape could be saved to a file on disk, and re-loaded allowing the same ROI to be used with different analysis settings. Buttons were created on the GUI allowing the ROI to be copied from one sequence to the other, for example after loading the measurement sequence, meaning that the ROI from the calibration analysis could be applied with one click. The software allowed the user to specify that the ROI was either in a fixed location for the entire sequence (the default), or could be moved or reshaped on an image-by-image basis. Whilst drawing the ROI the user was free to manually alter the image shown or have the software automatically play the sequence at the captured frame rate. Example ROIs are demonstrated in Figure 8.3, which shows a rectangular ROI over both an unsubtracted and subtracted image display. The rectangular ROI may be resized in one or two dimensions by dragging the mouse at one edge or in a corner respectively, and repositioned by clicking and dragging within the ROI.

8.2.3.2 Sequence analysis

Once the ROI was drawn, the analysis on the displayed image sequence could be analysed. The goal of the analysis for each sequence was to calculate the gradient of the TIC within ROI during the period where contrast was flowing into the coronary artery. In the calibration

sequence this would permit the signal intensity per unit volume of contrast agent to be calculated (as the injection rate of contrast agent is known). On the measurement sequence dividing the TIC gradient by the intensity per ml of contrast obtained from the calibration would yield the flow in the measurement sequence.

The analysis was automated by the software as far as possible, and in most cases no additional user input was required. The main steps in the analysis were as follows. Each step is described in more detail in the following sections.

1. Select and identify the image frames from a sequence to be considered in the analysis.
2. Extract the pixels within the ROI within each selected frame.
3. Calculate some summary metric on the pixel values in each frame, thus producing a raw TIC.
4. (optionally) Smooth the resultant curve to remove cardiac cycle variation.
5. Invert the curve so as to have a positive relationship between pixel value and contrast volume.
6. Curve fit to the points in the time period in the first few seconds of the contrast injection.
7. Obtain the gradient.

Step 1: frame selection

The analysis could be performed on either selected frames or the whole sequence. Selecting individual frames would allow for only images in matched phases of the cardiac cycle to be included, removing the issues relating to heart beat motion in the sequence. This approach was taken in the relative flow experiment in Chapter 5, and the initial plan had been to replicate this in this section of the study. In the relative flow experiment, the ECG was recorded synchronised with the image acquisition and extracted from the DICOM image files, but unfortunately ECG data were not available from the DICOM files from one of the two catheterisation laboratories used in this study, and was only intermittently recorded in the other laboratory due to a connecting cable between the physiological monitoring equipment and the X-ray system often becoming dislodged.

An alternative image analysis based system of identifying cardiac phase was explored. The sum of the pixels in the ROI was calculated for every imaging in a sequence, and the resultant TIC searched for local minima or maxima using MATLAB's findpeaks function, corresponding to approximations of end systole and end diastole respectively. The rationale was that during systole the contracted heart would be denser than in diastole, creating greater X-ray attenuation, resulting in a lower pixel signal intensity. Small deviation from the local average, and peaks too close together were excluded.

Unfortunately, there were a number of issues with the image based approach. Firstly, the automated detection of peaks in the TIC worked well on many sequences, but not always. In particular, during the contrast injection the automated detection could be confused. Manual correction of the cardiac phase detection was then implemented in the application, allowing the user to remove, insert or correct a detected peak, but this could be time consuming for the user. Even once the peaks in the TIC were identified it was noted that there were differences in the absolute signal intensities of extremes of the TIC per cardiac cycle. Figure 8.4a shows the sum of pixel intensities for a ROI drawn around the heart during a sequence where the automated power injector failed to trigger, i.e. there was no contrast injection. The first few frames of the sequence show a rapid decrease in signal intensity as the automatic dose control settles, and thereafter the variation in signal intensity due to the cardiac cycle is clearly visible. Between 1.5 and 3 s there is a gradual decrease in signal intensity due to shallow breathing. In Figure 8.4a square and circle markers indicate the automatically detected end diastole and end systole marks, and in this example the phase detection has worked as intended. The figure shows that there is a variation in the absolute value of the maxima and minima between heart beats, even outside the section where breathing was observed. The shape of the TIC also varied between heart beats, for example the peak at 3.4 s and minimum at 4.8 s show fluctuations near the extremities, leading to uncertainty in the exact phase of the cardiac cycle being identified. Indeed, the automated analysis was found not to clearly identify images from a consistent part of the cardiac cycle, even when the peaks and troughs of the TIC were correctly identified. Moreover, Figure 8.4b shows the difference between the maximum signal and minimum signal per heart beat relative to the range in heart beat one. It can be seen that as well as the absolute values of the maxima and minima varying, the difference between them also varies. For the relatively short injections used in this study, there may be very few

heart beats available for analysis and the variation in these single frame measures could affect the gradient of the TIC. In summary, the image intensity detection of cardiac phase was time consuming for the user and inaccurate in selecting frames from the same cardiac phase, and as a result an alternative approach was required.

Fourier analysis of the TIC has been proposed[314] where the variation due to cardiac phase is eliminated by removing signal contributions at the frequency of the heart beat (for example using a band stop filter with a stop band at 1 Hz for a heart beat of 60 bpm). This was disregarded as an irregular heart beat or ectopic beat would not be dealt with appropriately. An alternative approach was therefore implemented, where all frames where included in the analysis, and the variation in the TIC removed using low pass filtering. The filter is described in step 4.

Steps 2 and 3: extraction of pixels and TIC calculation

The ROIs are recorded in the analysis application as a series of vertices for the polygonal shape, or as a bottom left vertex, width and height for the rectangular and elliptical shapes. All of the ROI shapes were recorded in normalised units with respect to the image size. For example, a rectangle with position (0.5, 0) and size (0.5, 0.5) occupies the bottom right quarter of an image. To identify pixels within an ROI, a binary mask of the applicable ROI was created at the same resolution as the image sequence. Pixels lying under areas of the mask with a value of 1 were retained for analysis and the rest discarded. A calculation was made on these pixels, and the user could select to calculate the sum, mean or median value of the retained pixels, with the sum of intensities being the default.

Step 4: low pass filter

A low pass filter was applied to the TIC in cases where all frames were selected for analysis (i.e. when the one frame per cardiac cycle scheme was not used). The low pass filter was a Gaussian filter with default standard deviation of 15 frames width (1 s). The standard deviation of the filter could be adjusted by the user. The aim of the low pass filter was to smooth the cardiac cycle related variation from the TIC without overly affecting changes in intensity due to contrast agent arrival. An example showing filtered TICs from a calibration and measurement sequence is shown in Figure 8.5. In the figure, the original TICs are shown,

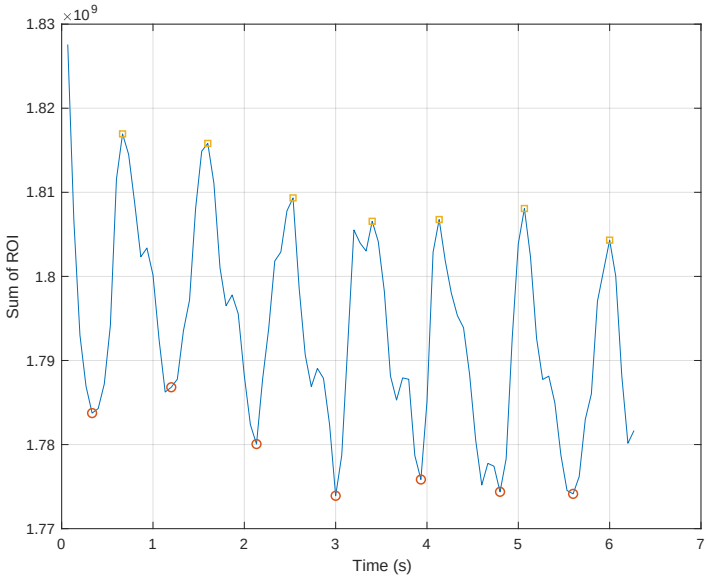

(a) Automated detection.

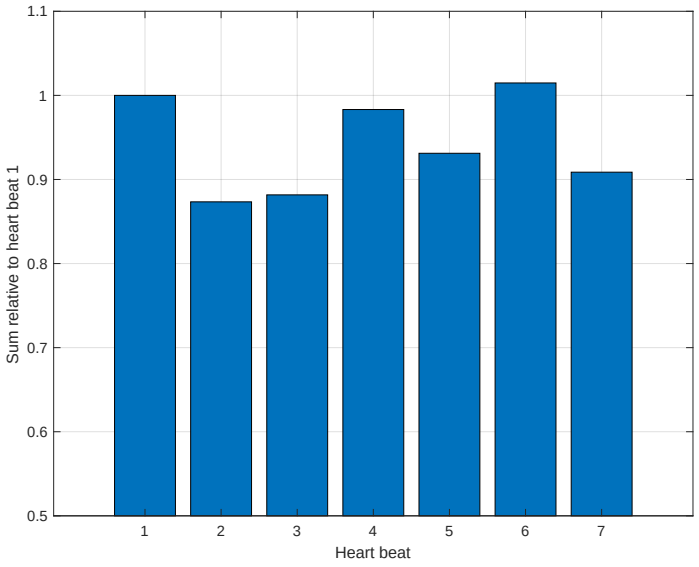

(b) Relative difference between maximum and minimum.

Figure 8.4: Time intensity curve from a sequence where no contrast agent was injected. Automated phase detection is shown in a) where the end systole markers are identified with circles, and end diastole with squares. The patient has not held their breath fully between 1.5 and 3 s, leading to the decrease in signal intensity. During the other heart beats differences in the absolute values of the maximum and minimum intensity values can be seen, and also differences in the difference between the maximum and minimum values as shown in b).

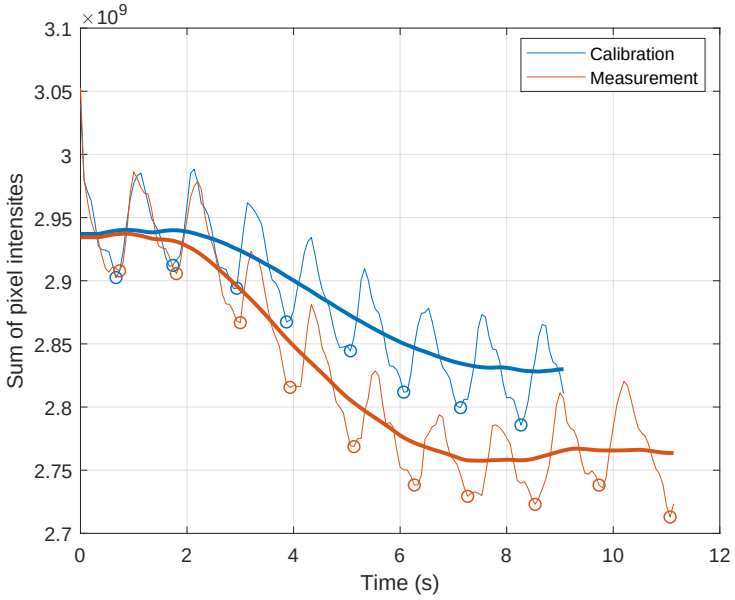

Figure 8.5: Time intensity curves from a calibration and measurement sequence produced by the analysis application. The raw TICs are shown with the auto-detected cardiac cycle markers shown as circles. Some inconsistency in the auto-detected markers is evident in the measurement sequence. The smoothed TICs are shown as the thicker lines.

along with the filtered curves, indicated by the thicker line width. The figure also shows the auto-detected cardiac phase markers, which demonstrate some inconsistency in the phase identification in both curves, but especially on the measurement sequence.

Step 5: TIC correction

Following this calculation, the curve is inverted (so the arrival of contrast provokes a positive response in intensity value), and an offset applied to set the mean calculated value prior to the contrast arrival to be 0. Figure 8.6 demonstrates the corrected TICs calculated from Figure 8.5.

Step 6: Curve fit

The next step of the curve analysis involved a curve fit, which was a linear fit between 25% and 75% maximum intensity. Figure 8.6 shows a linear fit with the cross markers overlaid on the corrected TICs. The start and end images of the curve fit were automatically calculated, although these frames could be overridden by the user (for instance if the automatic analysis was incorrect due to motion artefacts.) The gradient of the linear fit was then calculated.

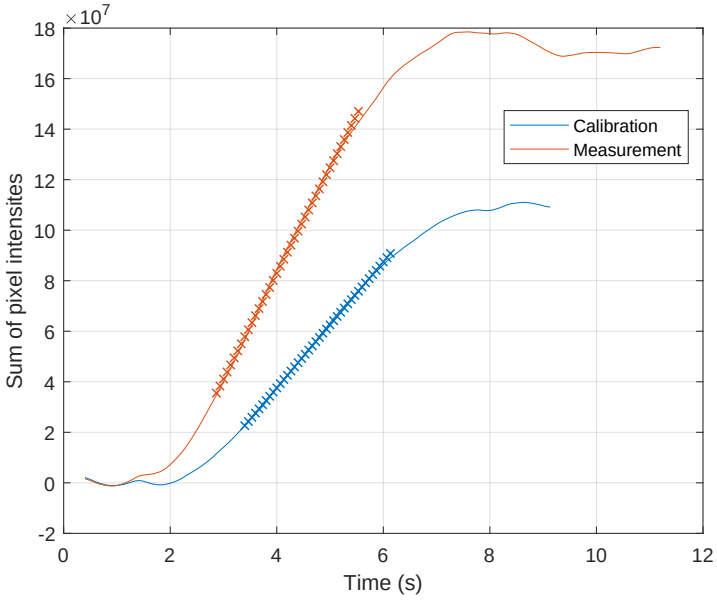

Figure 8.6: Inverted and offset time intensity curves. A linear fit to the contrast accumulation is shown with crosses on both curves.

Step 7: Flow calculation

Loading the measurement sequence into the analysis tool and repeating the calculations with the same parameters produces a second gradient value. As the calibration injection rate was 1 ml/s then the flow is the ratio of the gradients of the measurement and calculation sequences. Referring back to Figure 8.2 shows the full analysis tool's graphical user interface, with the graphs showing the calibration and measurement sequences in blue and red respectively. In this case the measured flow was 1.4 ml/s. The aorta can be seen in the left hand side of the DSA image as contrast flows back from the injection site into the aortic root.

8.2.4 Reference flow measurements

Two reference measurements of flow were taken in this study, one based on a continuous infusion of room temperature saline, and an image based metric using the vessel size and time taken for the contrast to transit the length of the coronary artery of interest.

8.2.4.1 Thermodilution flow measurement

Thermodilution was used for the reference measurement of flow following the method of Aarnoudse et al.[178] This involved the injection of room temperature saline into the coronary

arteries, and the temperature was measured using a thermistor sensor integrated into a guide wire.

To perform the measurements a steady state saline injection was achieved using a power injector. The pump injection was manually triggered and programmed with no rate rise and a maximum driving pressure of 200 mmHg. Two measurements of temperature were taken—one inside the catheter at its exit (measuring the temperature of the saline as it enters the bloodstream, T_i), and one taken in the distal artery, T_d. If T_b is the temperature of the blood before the start of the injection, then:

$$Q_b = 1.08 \times Q_i \frac{T_b - T_i}{T_b - T_d} \tag{8.1}$$

Where Q_b and Q_i are the rate of flow of the blood and indicator (saline) respectively. The correction factor of 1.08 is to correct for the relative heat capacity difference between saline and blood.[178] If T_b is set to zero by calibrating the zero of the temperature sensor in the artery, then eq. 8.2 becomes:

$$Q_b = 1.08 \times Q_i \frac{T_i}{T_d} \tag{8.2}$$

Temperature measurements were made and recorded using a Radi Analyser head unit (Radi Medical Systems, Uppsala, Sweden), and RadiWire combination pressure/temperature wire. The Radi Analyser was set to CFR mode. Prior to a saline injection, the thermistor was zeroed (making $T_b = 0$), the Radi unit was set to record, and the pump injection initiated. The recording and injection were stopped once a steady temperature was observed. The infusate temperature was measured as the guide wire was being introduced, and distal temperature measurements were taken as per the clinical protocol, which is described later in this chapter.

Recordings from the Radi Analyser unit were transferred to a laptop computer using dedicated software provided by the manufacturer (RadiView v2.2, Radi Medical Systems, Uppsala, Sweden). The Radi software could be used to inspect instantaneous temperature measurements at a given time using an interactive cursor, but contained no method of calculating an average temperature between two time points, nor a convenient method of correcting for cases where the temperature of blood is not set to 0 (due to drift in the offset or user error by not zeroing the temperature sensor appropriately).

To overcome this, the data were exported from the RadiView software into a comma sep-

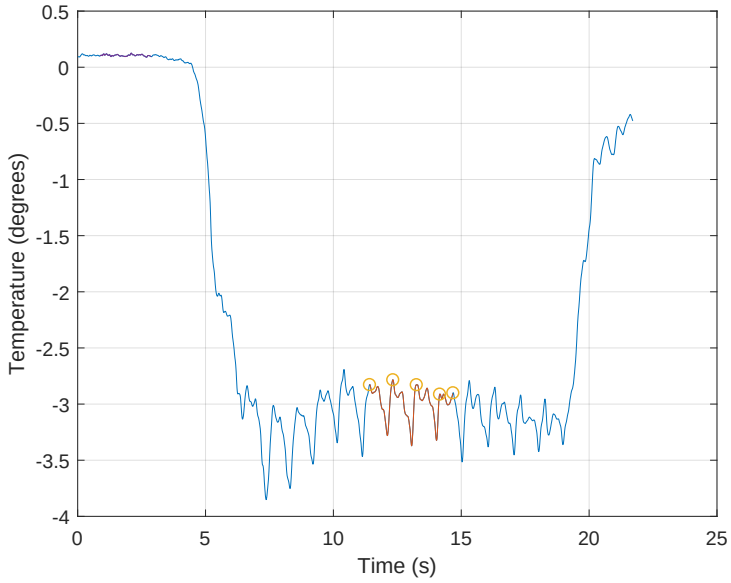

Figure 8.7: Example from the analysis of temperature recordings from the Radi system. The offset measurement is shown in purple between 0.87 and 2.87 s, during which the average temperature was 0.11 degrees. The three averaged heart beats are shown in orange between 11.41 and 14.67 s, where the average temperature was -2.99 degrees. The corrected temperature reading was therefore -2.88 degrees.

arated values (CSV) file. Software was written in MATLAB to read the CSV files, extracting time, aortic pressure, distal pressure and temperature readings. It was found that the temperature recorded varies as the saline is injected throughout the cardiac cycle as would be expected with a pulsatile flow. A graphical user interface was designed showing the temperature trace, allowing the user to click on the trace, and three whole cardiac cycles centered at the time where the user clicked were automatically selected by the software and the average temperature over this period was calculated. The cardiac cycles were identified using the MALTAB findpeaks function to identify local minima. An additional time point was identified just before the contrast injection and a baseline temperature (T_b) was taken, correcting for temperature drift on the sensor or user error where the recording had been made without zeroing the temperature sensor in the artery. An example of the analysis of a distal temperature recording from the Radi data is shown in Figure 8.7.

8.2.4.2 Frame count based flow index

The flow of liquid down a tube can be calculated by taking the product of the cross sectional area of the tube and the velocity of the liquid as it moves down the tube. This approach

was adapted for the coronary angiograms, using πr^2 as an index of the arterial cross sectional area, where r is the radius of the vessel measured from a single angiographic sequence, and the inverse of the corrected TIMI frame count as an index of velocity. That is the index of flow is $\pi r^2/C$ where C is the corrected TIMI frame count. This measurement was performed separately on the LAD and Cx in cases where the LCA was being considered.

The vessel radius measurements were taken by loading the image sequences into the ImageJ software,[303] and identifying a frame where a clear view of the proximal vessel was present. The line selection tool was used to draw a cross section orthogonal to the vessel direction, and the number of pixels between the points where the cross section dropped to 50% of its original intensity (judged subjectively) was calculated, obtaining a measurement of the vessel diameter in pixels. This processes was repeated on the catheter, yielding a catheter diameter in pixels. The catheters used in the study were 6F in size, i.e. had an external diameter of 2 mm, and therefore if d_a and d_c are the measured diameters of the artery and catheter in pixels respectively, the arterial radius could be calculated as follows:

$$r = d_a/2 \times (2/d_c) = d_a/d_c \tag{8.3}$$

TIMI frame count was determined using standard start and end frame landmarks.[75] The start frame was defined when a column of nearly full or fully concentrated contrasted agent extended across the entire width of the origin of the artery, with contrast touching both borders of the origin of the artery and antegrade motion of contrast apparent. The end frame was the frame number when contrast reaches a distal landmark, defined per artery as follows. For the LAD, the distal bifurcation of the LAD (i.e., the "whale's tail"). For the Cx, the distal bifurcation of the segment with the longest total distance that includes the culprit lesion, and for the and in the RCA, the first branch of the posterolateral artery. Where the artery of interest was not the Cx, the most distal bifurcation of the most distal marginal artery was used in the Cx.

8.3 Clinical study

This study was approved by the local research ethics committee. Patients were recruited from those undergoing angiography proceeding to PCI at the General Infirmary at Leeds. Two

pump injectors were utilised, one with room temperature saline (with the heater disabled), and one with body temperature contrast (with the heater operating as normal). For the contrast pump a short extension was used, as it was found that the higher flow rates required could not be achieved with the longer extension (presumably due to viscous losses in the extension connector).

8.3.1 Patient selection

Patients undergoing angiography with a view to continuing to PCI or pressure wire assessment for single vessel coronary disease were considered for enrolment. Exclusion criteria were: patient less than 18 years old; patient pregnant or breast feeding; body mass greater than 100 kg; body mass index of greater than 30 kg/m^2; left main stem stenosis; significant respiratory impairment precluding adequate breath hold; atrial fibrillation; previous myocardial infarction PCI or coronary bypass grafting; impaired renal function (estimated glomerular filtration rate less than 30 $ml/min/1.73m^2$); previous known adverse reaction to iodine based contrast agent; more than two previous or planned imaging involving high levels of ionising radiation within six months of recruitment; patients found to have no visible CAD, or minimal luminal narrowings of less than 30% after the initial angiograms; or any other condition considered by the investigators likely to compromise patient safety or successful completion of the study protocol. Patients were sent the study information sheet the day before their procedure, and gave written informed consent on the day of their procedure.

8.3.2 Acquisition protocol

The patients underwent standard peri-procedural and procedural preparation. 6F catheters were used, with radial access performed where possible. Diagnostic angiography was performed on both arteries. If the patient were found to have a suitable stenotic lesion meeting the inclusion criteria (i.e. stenting or pressure wire assessment were indicated), then the study protocol was commenced. The full set of measurements would include both X-ray and reference thermodilution measured flow pre- and post- intervention, both at rest and stress. FFR was also measured pre- and post- intervention where possible. The order of events was planned as follows.

1. Radial or femoral access obtained.

2. Diagnostic catheter engaged and initial angiograms acquired. If no suitable target artery was identified, or significant multi-vessel disease present, the patient was withdrawn from the study.

3. Appropriate interventional catheter engaged.

4. Measure the temperature of the saline infusate by:

   (a) introducing the Radi guide wire to the tip of the catheter,

   (b) zero the temperature sensor (set $T_b = 0$), and

   (c) perform a saline infusate temperature measurement (T_i) using an infusion of room temperature saline at 1 ml/s.

5. Cross the lesion with the guide wire.

6. Perform rest distal temperature measurement (T_d), again using an infusion of room temperature saline at 1 ml/s.

7. Perform rest X-ray calibration sequence (1 ml/s contrast injection).

8. Perform rest X-ray measurement sequence (3–5 ml/s).

9. Begin adenosine injection to induce hyperaemia.

10. Perform stress X-ray measurement sequence (3–5 ml/s).

11. Perform stress distal temperature measurement.

12. Record FFR from pressure measurements.

13. Stop adenosine injection.

14. If intervention not indicated, the study is complete. If intervention is indicated angioplasty and stenting are performed as appropriate, and the study protocol continues.

15. Perform post intervention rest distal temperature measurement.

16. Perform post-intervention resting X-ray measurement sequence (3–5 ml/s).

17. Begin adenosine injection to induce hyperaemia.

18. Perform post intervention stress X-ray measurement sequence (3–5 ml/s).

19. Perform post intervention stress distal temperature measurement.

20. Record post intervention FFR.

21. Stop adenosine injection.

22. Complete the case as per normal clinical procedure.

At the operator's discretion elements of the protocol were not performed if he or she felt it inappropriate for the current patient; for example, the pre-intervention stress measurements may not have been performed on patients with very severe lesions whose resting ratio of distal to aortic pressure was considerably less than 0.8. For each patient the X-ray calibration sequence was performed only once, and used with all of the measurement sequences. Similarly, one measurement of the temperature of the room temperature saline was performed and used with all of the other distal temperature measurements.

All of the study related angiograms were performed using the same projection and positioning as far as possible, making reference to the angulation recorded on the X-ray system's run log, and using a reference image for positioning on a second monitor. X-ray parameters were as described in Section 4.2; briefly, the large image field (25 cm) was selected, the beam collimators were introduced at least 0.5 cm in both directions, and further in if the heart did not fill the entire frame, the brass wedge filters were removed from the beam and a dedicated flow acquisition mode was selected. The mode used additional 0.1 mm Cu filtration compared to the standard coronary angiography programmes, and locked the automatic dose control after five frames.

Prior to commencing the X-ray acquisition sequences, the patient was asked to practice holding their breath on command. Prior to an acquisition patients were instructed to take a number of full breaths with the last couple imaged under fluoroscopy to ensure good positioning of the heart in the frame during breath-hold (the heart moves up and down in the image frame with breathing). As the initial exposure factors for an exposure sequence are calculated from dose information obtained in the last fluoroscopy sequence, the use of fluoroscopy with the correct patient positioning and breath phase ensured that the starting point for the automatic dose control in the acquisition was reasonably close to the required set point for the

angiographic sequence, allowing the dose control to stabalise within its five frame limit. Once the breath hold was initiated, acquisition commenced at 15 fps, and the patient reminded to "Hold your breath" periodically during the acquisition, and "Breathe normally" immediately afterwards. All contrast injections were delivered for four seconds with the overall bolus calculated according to the desired injection rate. Prior to contrast injection, the pump was wound forward by hand until contrast was visible at the catheter tip. No rate rise and a maximum driving pressure of 200 mm Hg was selected. The acquisition sequence was terminated some seconds after the contrast injection ceased, or if venous contrast flow became visible.

Following each acquisition sequence, the images were reviewed on one of the in-room monitors, and repeated if they contained an obvious deficiency, for example too much breathing motion, catheter disengagement during the injection, and for the measurement sequence, lack of clear back-flow, indicating that the injection rate was lower than the native flow of the artery. Repeated failures of the patient to comply with the breath hold instruction would result in the flow measurements being abandoned.

8.3.3 Recording of the X-ray data

All images were recorded using a data capture devices provided by the X-ray equipment manufacturer, and were transferred via encrypted hard disk to the University as described in a similar way as used previously in Chapters 5 and 7. The capture devices recorded images prior to any image processing other than gain, offset, defect and a logarithmic look-up-table being applied. The images were recorded at their full spatial resolution (960×960 pixels), and bit-depth (14-bits). The capture devices were located in the X-ray equipment room (containing the X-ray generator, and control computers), and it was therefore impractical to start and stop these during a case, so the data capture systems were started before the case began and stopped at the end of the case. The capture software recorded every image taken on the system whilst it was operational, including fluoroscopy and acquisition sequences. These captured data recorded the images with only a time stamp for identification, and no patient demographic or other identifiable information was included. Approximately 80 Gb of data were recorded and transferred for each case. In most cases, anonymised DICOM images were also transferred to the hospital PACS system, and later extracted and copied to compact disc for transfer to the University. The DICOM images contained additional information including

the radiographic factors, projection angles, source to image distance. Dedicated software was written in MATLAB to decode and read images from the proprietary file format used by the capture devices. Following transfer to the University, the captured image sequences were reviewed to identify the study specific angiograms. This process was made faster by noting the number of images in the study sequences during the case, and using a MATLAB function to scan every captured image sequence in the current case, and report the number of frames in each, allowing potential matches to be quickly identified.

8.3.4 Analysis

Measurements of the three different indices of flow were performed blinded to any of the other results, and a considerable amount of time was left between measurements to minimise the chance of case memory affecting the analysis. A rectangular ROI was used in all cases. All frames in the sequence were included in the analysis, and the low pass filter with the default 1 s standard deviation duration was used. The linear curve fit was selected, with automated start and stop frames for the fit determined at the 25% and 75% intensity of the TIC. These were overwritten manually to avoid sections of the sequence where there was breathing, or where the automated identification of the start and end frames were inappropriate.

8.3.4.1 X-ray measurement success rate

During the analysis of the X-ray sequences, each sequence was assessed to ensure it did not contain features that would render it unsuitable to successfully perform the X-ray flow calculation. Reasons for insufficiency of the image sequences were as follows.

1. Failure of the data capture device either corrupting the image sequence, or not recording the sequence at all.

2. Incorrect framing of the heart (either the entire heart was not contained within the field, or the framing of the measurement sequence was different to the measurement sequence).

3. Inadequate engagement of the catheter with the artery, or the catheter becomes disengaged during the injection.

4. Breathing related artefact making noticeable affect on the time intensity curve.

An X-ray flow measurement could therefore be taken if both the calibration and measurement sequence were deemed to be of acceptable quality. The fraction of cases where this possible out of the total available was calculated both as an overall total and as a function of time. In the latter case, cases were analysed in groups of ten consecutive cases to determine if the clinical team got better at the procedure over time.

8.3.4.2 Comparison with reference flow measurements

Linear regression and Bland-Altman analysis were used to compare the X-ray measures of flow with thermodilution flow measurements and the frame count based flow index. Cases performed with the on the left and right coronary arteries, were analysed separately.

8.3.4.3 Observer variability assessment

Intra-observer variation in the X-ray measurements was assessed by the author performing the analysis twice. Inter-observer variation was investigated by having the cases involving the RCA analysed by a second observer (a consultant cardiologist). The inter and intra observer difference was calculated using a mean absolute difference between observations, and their standard deviations.

8.3.5 Saline infusion for thermodilution

A specially designed thermodilution infusion catheter was intended to have been used for all cases. These catheters are designed such that their tip has a series of holes for the saline to escape, ensuring rapid mixing with blood. Unfortunately, when the study commenced, despite the clinical team's expectation following discussion with catheter manufacturers, no such catheter was commercially available. With no other method of measuring absolute flow in the human coronary artery, the initial group of patients (patients 1–12) were performed with the saline infusion via a standard 6F catheter with the temperature sensor positioned distal to a stenosis. The expectation was that mixing of blood and saline would occur anyway upstream to the temperature sensor, especially as the presence of CAD would make laminar flow along the artery unlikely. These initial patient data were then analysed, finding that thermodilution measures taken in the first 12 patients were found to be unreliable in the left system.

Number	Stage
44	Pre intervention, rest
37	Pre intervention, stress
10	Post intervention, rest
6	Post intervention, stress

Table 8.1: Number of patients where measurements were attempted at each of the four measurement stages.

The study proceeded recruiting (patients 13–36) with a thermodilution reference only available in patients whose artery of interest was the RCA. The final patients (37–45) made use of a dedicated thermodilution catheter (RayFlow, Hexacath, Paris, France) which had become commercially available in the UK. The rate of saline infusion for cases where no specific infusion catheter was used was 1 ml/s, and was 0.3 ml/s for all cases where the RayFlow catheter was used.

8.4 Results

Forty-five patients were conditionally enrolled into the study. One patient (number 1) was withdrawn during the case at the decision of the interventionalist. The number of patients having measurements attempted at the four measurement stages is summarised in Table 8.1. In seven patient pre intervention stress measurements were not taken. In the first three cases the stress measurement was not performed as the clinical team wanted to ensure that their proficiency with the research protocol was sufficient to ensure that the stress measurements could reliably be performed without an excessive period of pharmacologically induced stress for the patient. The measurement was not performed in subsequent cases due to the lesion being judged so significant the measurement was inadvisable (n=2), insufficient adenosine being available during the procedure (n=1), or requirement to finish the case quickly due to the catheterisation laboratory being required for a primary PCI (n=1). In total 11 out of 44 patients proceeded to have intervention (angioplasty and stenting). Following intervention, rest measurements were not acquired in one case (due to error), and five stress measurements were not acquired. A summary of the all of the X-ray measurement runs acquired on a patient by patient basis is provided in Table 8.2.

Table 8.2: X-ray image acquisitions. All failures were due to breathing unless noted by (f) – framing error, (c) – insufficient catheter engagement, (r) error in Radi Wire data, or (d) – data capture error. Post intervention fields marked n/a are cases where intervention was not performed.

ID	Artery	Performed					Acceptable					Notes
		Calibration	Pre-Intervention		Post-intervention		Calibration	Pre-intervention		Post-intervention		
			rest	stress	rest	stress		rest	stress	rest	stress	
Phase 1 - Initial patients												
1	RCA											withdrawn
2	LCA	Y	Y	N	n/a	n/a	N	N				
3	RCA	Y	Y	N	Y	N	N	N	Y	N		(1)
4	RCA	Y	Y	N	n/a	n/a	N	N				
5	RCA	Y	Y	Y	n/a	n/a	Y	Y	Y			
6	RCA	Y	Y	N	n/a	n/a	Y	Y				
7	LCA	Y	Y	Y	n/a	n/a	N	N	N			
8	LCA	Y	Y	Y	n/a	n/a	Y	Y	Y			
8	RCA	Y	Y	Y	n/a	n/a	Y	Y	Y			
9	LCA	Y	Y	N	Y	N	Y	Y		Y		
10	LCA	Y	Y	Y	n/a	n/a	N	Y	N			
11	LCA	Y	Y	Y	n/a	n/a	N	Y	Y			
12	LCA	Y	Y	Y	n/a	n/a	Y	Y	N			

ID	Artery	Performed					Acceptable					Notes
		Calibration	Pre-Intervention		Post-intervention		Calibration	Pre-intervention		Post-intervention		
			rest	stress	rest	stress		rest	stress	rest	stress	
Phase 2 - Thermodilution reference on RCA only												
13	RCA	Y	Y	Y	n/a	n/a	Y	Y	Y			
14	RCA	Y	Y	Y	N	Y	Y	Y	Y		Y	
15	RCA	Y	Y	Y	n/a	n/a	N	N	N			
16	RCA	Y	Y	Y	Y	Y	N	Y	N	Y	N	
17	RCA	Y	Y	Y	n/a	n/a	N	Y	Y			
18	RCA	Y	Y	Y	n/a	n/a	Y	Y	N (f & r)			
19	LCA	Y	Y	Y	n/a	n/a	Y	Y	Y			
20	LCA	Y	Y	N	Y	Y	Y	Y		N	Y	(2)
21	LCA	Y	Y	N	n/a	n/a	N (d)	N (d)	N (d)			
22	LCA	Y	Y	Y	Y	N	Y	Y	Y	Y		
23	RCA	Y	Y	Y	n/a	n/a	Y	Y	Y			
24	LCA	Y	Y	Y	n/a	n/a	Y	N (c)	Y			
25	LCA	Y	Y	Y	n/a	n/a	Y	Y	Y			
26	LCA	Y	Y	Y	Y	Y	Y	Y	N	Y	Y	
27	RCA	Y	Y	Y	Y	Y	Y	Y	Y	Y	N	

ID	Artery	Performed					Acceptable					Notes
		Calibration	Pre-Intervention		Post-intervention		Calibration	Pre-intervention		Post-intervention		
			rest	stress	rest	stress		rest	stress	rest	stress	
28	RCA	Y	Y	Y	n/a	n/a	Y	Y	Y			
29	RCA	Y	Y	N	Y	Y	N	Y		Y	Y	(2) (3)
30	LCA	Y	Y	Y	n/a	n/a	Y	Y	Y			
31	LCA	Y	Y	Y	n/a	n/a	Y	Y	Y			
32	LCA	Y	Y	Y	n/a	n/a	Y	N	N			
33	RCA	Y	Y	Y	n/a	n/a	Y	Y	Y			
34	RCA	Y	Y	Y	n/a	n/a	Y	Y	Y			
35	RCA	Y	Y	Y	Y	N	N	N	N	N		(4)
36	RCA	Y	Y	Y	Y	N	Y	Y	Y	Y		
Phase 3 - RayFlow catheter used for thermodilution reference												
37	LCA (lad)	Y	Y	Y	n/a	n/a	Y	Y	Y			
38	RCA	Y	Y	Y	n/a	n/a	Y	Y	Y			
39	LCA	Y	Y	Y	n/a	n/a	Y	Y	Y			
40	LCA	Y	Y	Y	n/a	n/a	Y	Y	Y			
41	RCA	Y	Y	Y	n/a	n/a	Y	Y	Y			
42	LCA	Y	Y	Y	n/a	n/a	N	N	N			

ID	Artery	Performed					Acceptable					Notes
		Calibration	Pre-Intervention		Post-intervention		Calibration	Pre-intervention		Post-intervention		
			rest	stress	rest	stress		rest	stress	rest	stress	
43	LCA	Y	Y	Y	n/a	n/a	Y	Y	N			
44	RCA	Y	Y	Y	n/a	n/a	Y	Y	Y			
45	LCA (lad)	Y	Y	N	Y	Y	Y (5)	N		N	Y	(2) (6)

(1) - Thermodilution recording failed.

(2) - Pre intervention stress sequence not performed as the lesion was very severe.

(3) - Pre intervention lesion too severe to allow 1 ml/s flow in calibration sequence.

(4) - Post intervention stress not performed as all previous runs contained breathing.

(5) - Sequence repeated post intervention due to breathing in pre intervention calibration.

(6) - Data capture device failure - missing frames in recorded sequences.

8.4.1 X-ray measurement success rate

Table 8.2 shows which of the X-ray acquisitions were found to be of acceptable quality during post-procedure analysis. The overall success rate of acquiring usable X-ray sequences (i.e. ones with the correct X-ray system settings, framing, timing, and where the patient was sufficiently compliant with the breath hold) was 106/146 (72.6%). The rate of successful acquisitions improved as the clinical team became more practised with the procedure. Figure 8.8 shows that for the first ten patients, only approximately 57% of sequences were acceptable, whereas from patient 21 onwards, around 80% of sequences were acceptable. In all but four cases the reason for a sequence being deemed unacceptable was due to lack of compliance by patients in holding their breath, resulting in artefacts in the image sequence.

Considering the data on a per measurement basis, i.e. both an acceptable calibration and measurement sequence must be present, the overall success rate was 62.5%, slightly lower than the success rate on a per sequence basis. This was to be expected as if no acceptable calibration sequence is available for a patient, no absolute flow measurement can be taken on any measurement sequence from that patient. Figure 8.8 also shows data split into each consecutive ten patients, indicating that again the performance improved after the initial cases, with the success rate from patient 21 onwards being 74.4%.

8.4.2 Comparison with reference measurements

8.4.2.1 Thermodilution

Analysis of the first 12 patients, where no dedicated thermodilution infusion catheter was used, gave cause to believe that the thermodilution measurements were unreliable in the LCA, where five out of 12 measurements exceeded 7 ml/s (four measurements were greater than 9 ml/s), greater than might be expected in the left system. The range of the measurements in the Cx was 2.33–20.27 ml/s). Conversely in the RCA the range of flow values from thermodilution was 2.15–4.06 ml/s. It was therefore decided to discard the thermodilution measurement in the Cx and LAD until a suitable infusion catheter was sourced.

Considering the cases where measurements were performed in the RCA over the whole patient cohort, a moderate correlation (r=0.47, p=0.0076) was found between the thermodilution flow measurements and the X-ray based flow measurements. Figure 8.9a shows a scatter

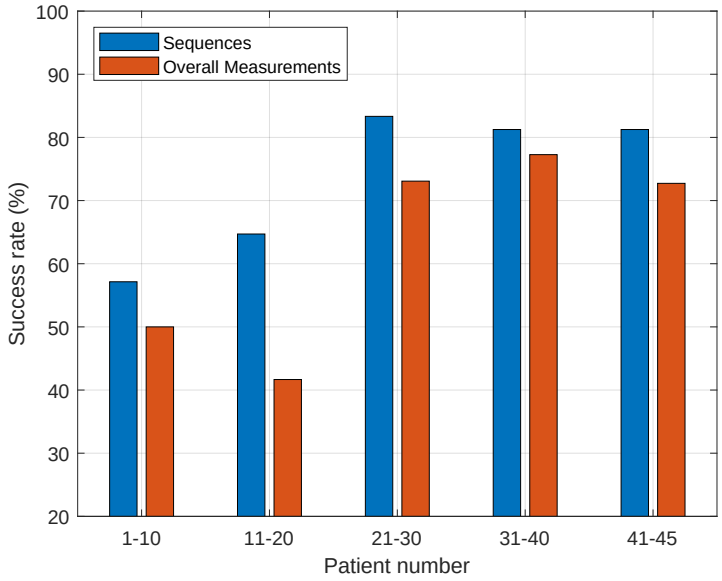

Figure 8.8: Success rate of acquiring usable X-ray measurement sequences (either calibration or measurement sequences) and performing measurements (requiring both an acceptable calibration and measurement sequence) throughout the patient cohort. It can be seen that success rates improved in the latter periods of the study.

plot of the thermodilution and X-ray derived measurements. Bland-Altman analysis (shown in in Figure 8.9b) demonstrated an that the X-ray flow measurements were lower than the thermodilution reference, with a mean difference of 25.6% (0.55 ml/s).

Considering the left coronary arteries, Figure 8.10 shows a scatter plot of the thermodilution and X-ray derived flow measurements the LAD (all of the cases performed in the left system were performed on the LAD). The first 12 patients have been discounted (as the thermodilution measurements were deemed to be unreliable), so only cases where an infusion catheter was used are shown. There was no appreciable correlation between the measurements (r=0.08, p=0.877).

8.4.2.2 Vessel size and frame count derived reference

Scatter plots of the relationships between the X-ray and thermodilution measurements to the frame count derived flow index are shown in Figure 8.11. Overall there was a moderate correlation between the X-ray derived flow measure compared to the vessel size-frame count derived index (r=0.49). The correlation between the thermodilution based flow measurements to the vessel size-frame count index was 0.38; however, inspection of Figure 8.11b reveals a slight different relationship between the relationship in left and right systems with correlation

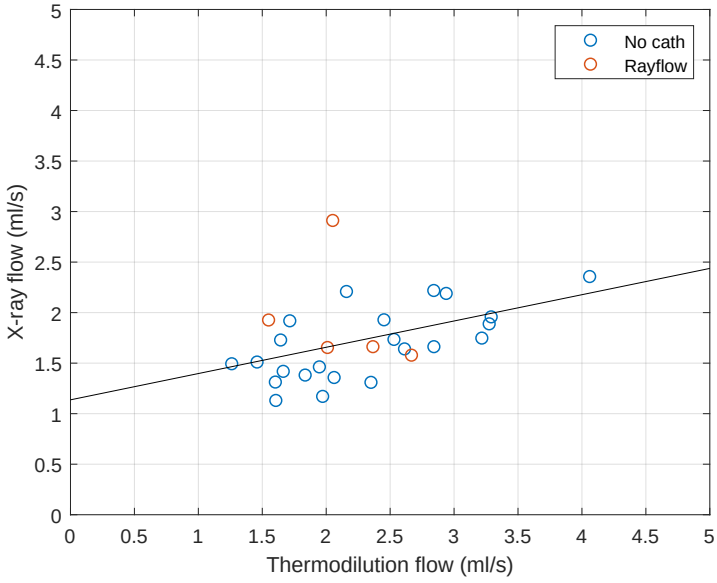

(a)

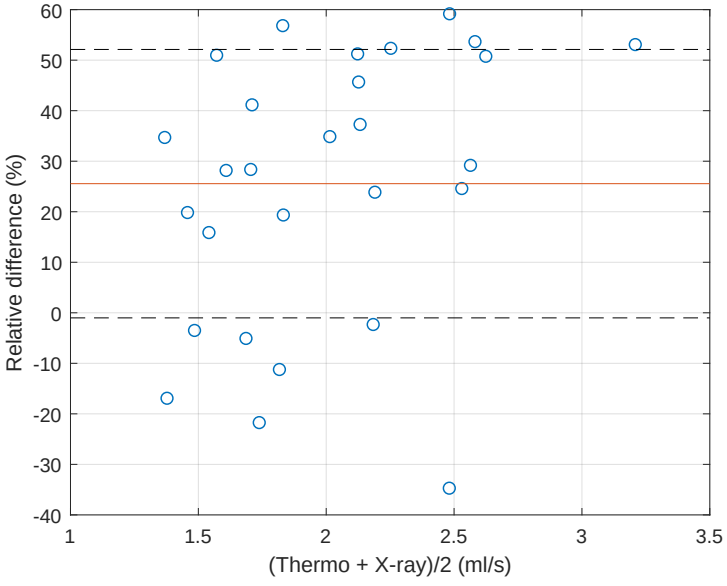

(b)

Figure 8.9: Scatter plot (a) showing thermodilution against X-ray derived flow measurements for the right coronary artery. There is a modest correlation (r=0.477) and the line of best fit is shown as the solid black line. A Bland-Altman plot (b) shows the mean difference between the thermodilution and X-ray measurements was 25.6%. Dashed lines indicate mean ± one standard deviation.

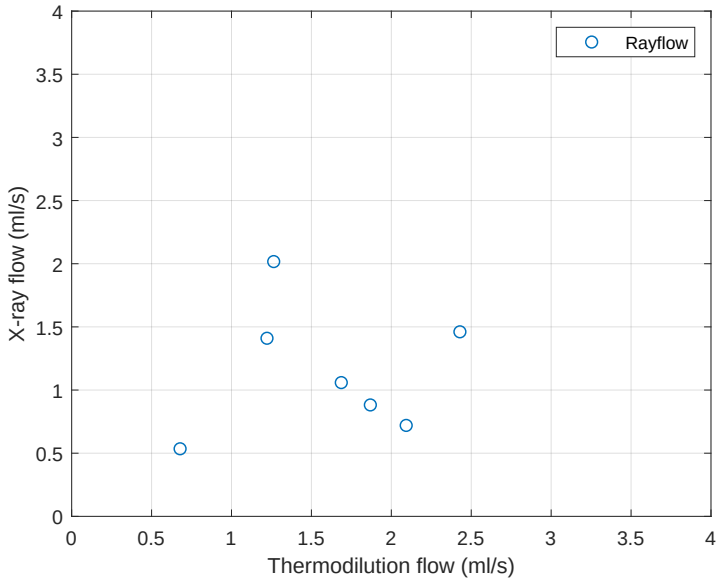

Figure 8.10: Scatter plot showing thermodilution against X-ray derived flow measurements for the left coronary artery where the RayFlow was used, showing no appreciable correlation, although there are very few cases to consider.

coefficients of 0.45 and 0.16 for the RCA and LAD respectively.

8.4.3 Inter and intra observer variability

There was no systematic difference between repeated observations by the same observer when analysing an entire left or right coronary artery (mean difference=0.04 ml/s), nor when the Cx or LAD were considered individually (mean difference=0.04 ml/s). There was a higher amount of variation when the LAD and Cx were considered individually compared to when the left system was considered as a whole (standard deviation=0.19 and 0.27 ml/s) respectively. Considering inter-observer difference, a mean difference of -0.15 ml/s was found (standard deviation=0.17 ml/s). These differences are shown in Bland-Altman plots in Figure 8.12.

8.5 Discussion

8.5.1 Practical implementation and success rate

The practical implementation of the X-ray based blood flow measurements was relatively straight forward to implement in clinical practice. No adverse reactions were found to either the X-ray or thermodilution measurement protocols. The most cumbersome aspect is

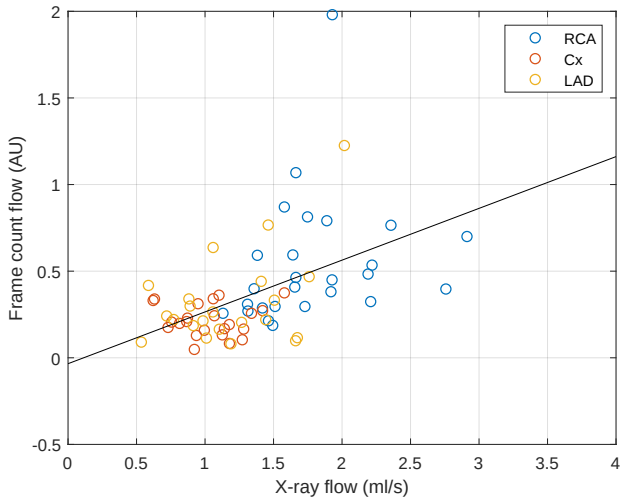

(a)

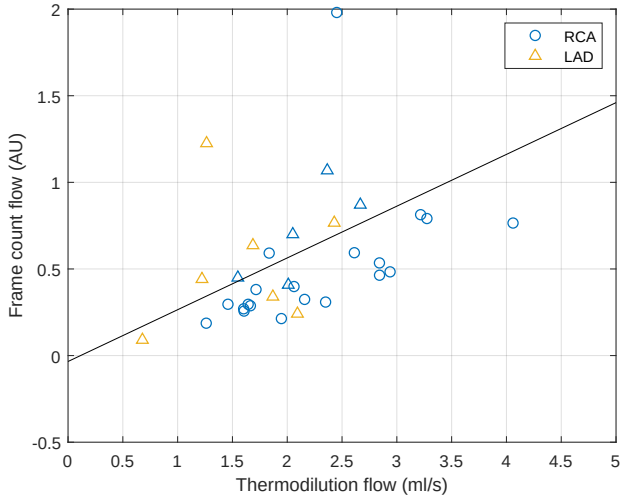

(b)

Figure 8.11: Scatter plots of (a) X-ray and (b) thermodilution derived flow measurements against the vessel size-frame count flow index. Marker colour indicates the artery as shown by the figure legends, and the marker shape indicates the infusion catheter used for the thermodilution measurement (round: no infusion catheter; triangle: RayFlow). The solid black line in both plots shows the line of best fit.

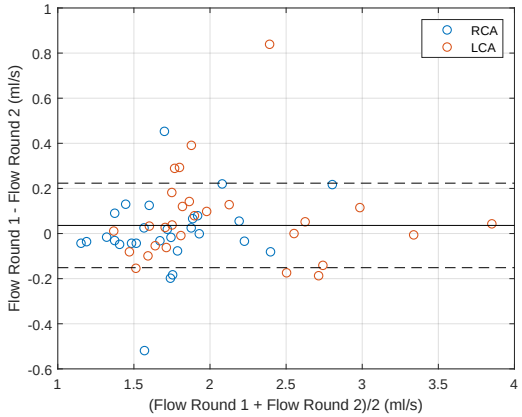

(a) Intraobserver, whole artery.

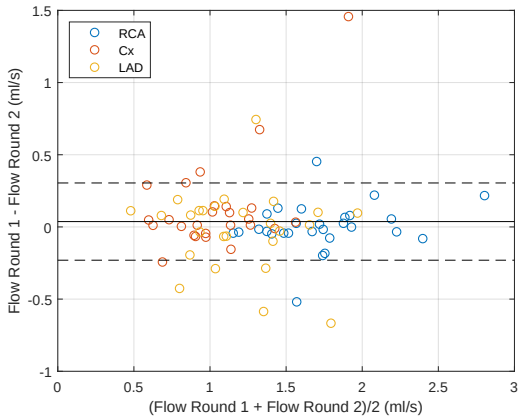

(b) Intraobserver, individual artery

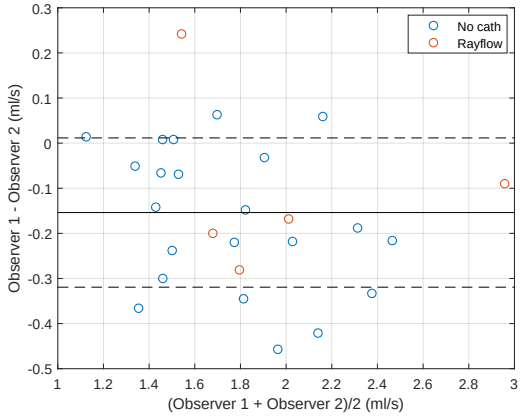

(c) Interobserver, RCA

Figure 8.12: Repeated measures by the same observer showing the intra-observer variation on a) the whole left and right artery and b) separate analysis of the right coronary artery, circumflex and left anterior descending arteries. c) shows a Bland-Altman plot of inter-observer difference on the right coronary artery cases from two observers. Black dotted lines are plus and minus one standard deviation.

the use of the power injector, but these are used routinely in the catheterisation laboratory for left ventriculograms, and therefore the clinical staff are comfortable in their use. The maximum pressure and flow rates set on the pump were designed to prevent damage to the artery. Previously coronary angiography has been performed using a power injector with an infusion rate of 3–6 ml/s and maximum pressure of 150 psi (albeit with a lager catheter),[315] and 3 ml/s at 300 psi maximum pressure,[316] without undue complications. More recently, there has been increased use of intracoronary optical coherence tomography, where the safe use of power contrast injection with infusion rates of 4 ml/s with a maximum pressure of up to 408 psi has been reported.[317] The timing of the contrast injection must be delayed following the initiation of the X-ray image acquisition to allow for a sufficient number of mask images to be acquired, and this is different to the practice when acquiring ventriculograms, where the contrast injection is started simultaneously with the X-ray acquisition. Therefore if the start of the contrast injection is triggered by the radiographer (as is standard practice for ventriculography), there is the danger that the injection is started prematurely by mistake. We found that the most reliable solution was to use a pump coupled such that the pump is triggered automatically after the start of the X-ray acquisition, with an inject delay programmed into the pump based on the patient's heart rate to allow for the mask images to be acquired. This automated triggering was not supported on all of the pumps available in the department, and at times manual triggering was required. Appropriate training and good communication during the case were essential to ensure successful injection timing.

Following each X-ray acquisition sequence, careful review was required to ensure that it was of adequate quality, paying particular attention to the breath hold, catheter engagement, contrast flow, framing and angulation. This was particularly important for the calibration sequence, as a single calibration sequence was used for every measurement sequence for a given patient. Therefore, if the calibration sequence was flawed, no calculation of flow could be made for that patient. As the patient breathes, the heart alters its position in the image field, and we found that use of fluoroscopy for a few seconds while the patient breathes and performs practice breath holds permitted the position of the heart in the breath hold to be accurately predicted, improving the image framing. The use of the reference image display to show a previous calibration or measurement sequence was useful in ensuring matching angulation and table positioning. When reviewing the image the use of subtraction imaging

would have been helpful, as this would have highlighted both contrast agent flow issues (e.g. insufficient injection during the measurement sequence, or contrast back flow during the calibration sequence) and breathing-motion artefacts, but unfortunately this was not possible during these sequences, as the DSA system used in Chapter 4 had been removed.

After some practice, approximately eight out of 10 sequences were judged to be of sufficient quality for use in the flow calculations. The main reason for an unacceptable image sequence was the presence of breathing related motion artefact where the patient was not able to sufficiently breath hold during the acquisition. Whilst improved communication with the patient by the interventionalist and practice breath holds prior to the sequence acquisitions no doubt increased the success rate, there were a number of cases where the patient could not comply sufficiently with the breath hold. Whilst patients can feel uncomfortable when the adenosine vasodilator is used to achieve hyperaemia, we did not find that they were much less likely to be able to breath-hold during hyperaemia; overall at rest 73% of sequences were successfully acquired, compared to 67% under hyperaemia. It is interesting to note that in the earliest work using regional analysis of DSA images from angiography from Vogel et al.,[188] a similar reject rate (19%) was reported due to image misregistration. Whilst it may be possible to further increase the success rate with more careful review of the in-room angiograms, it is not likely that the success rate will be considerably improved due to patients being unable to comply with the breath hold.

Compared to the reference thermodilution method, the clinical staff found the X-ray measurements faster to perform. The continuous infusion of saline requires a power injector in the same way as the X-ray method. Thermodilution also requires the use of a guide wire equipped with a thermistor, whereas the X-ray method does not require any additional instrumentation of the patient. Furthermore, the use of an infusion catheter also adds cost and time to the procedure, particularly in the left system where the Cx or LAD must be selectively engaged.

In terms of the time taken to perform the analysis, in most cases the analysis software's automated features operated successfully, meaning that users were only required to load the image sequences and draw the ROI on the calibration and measurement sequences. In such cases the analysis could be performed in approximately one minute. This speed of analysis is important if the flow measurements are to be integrated into clinical practice. Other clinical tools using X-ray images in the catheterisation laboratory, such as stent enhancement software

or three dimensional model creation tools, require similar or greater time to process a case.

8.5.2 Agreement between the flow measurements

There was a moderate correlation between the X-ray based flow measurements to both reference measurements (and therefore between the reference measurements) in the RCA. In the left system, there were too few cases to draw meaningful results for the thermodilution reference. Considering the vessel size-frame count based reference, there was a moderate correlation with flow measured in the LAD, and for all three arteries overall (see Figure 8.9). In a similar way, there was a moderate correlation between the thermodilution measurements and the vessel size-frame count index in the RCA, and overall when the cases using the RayFlow catheter are also included.

This study found that the mean absolute flow measurements from the X-ray based measurements were 1.77, 1.23 and 1.18 ml/s in the RCA, Cx and LAD respectively and from thermodilution were 2.28 and 1.61 ml/s for the same arteries (excluding the first 12 patients). Clearly the X-ray based measurements are lower than the thermodilution flow measures. The infusion of saline into the coronary artery has been shown to induce hyperaemia,[318] which may be contributory to the greater flow measured using thermodilution, as many of the comparisons in this study were performed at rest. In comparison, Xaplanteris et al.[181] reported 2.77, 2.47 and 3.15 ml/s for the RCA, Cx and LAD respectively, and Aarnoudse et al.[178] reported a mean flow of 1.6 and 2.35 ml/s pre and post intervention using thermodilution.

The vessel size-frame count reference metric is only likely to be an approximate predictor of flow. The measurement of cross sectional area from a single measurement of vessel diameter from one projection image is not likely to be either particularly precise or accurate. The assessment of TIMI frame count was also difficult due to the projection angles selected for the arteries. The RAO-caudal projection used for the LCA makes distinguishing the Cx and marginal arteries impossible in many cases, therefore making the distal landmark in the frame count method difficult to locate. This may have contributed to the poorer correlation with the X-ray flow measurements and the frame count based reference with the Cx artery. Furthermore the LAO-cranial projection for the RCA makes the posterolateral artery difficult to visualise as it can overlap with the main right coronary artery. Again this makes the artery's distal landmark difficult to discriminate in some sequences, but whilst not ideal, the

posteriolateral artery is normally only obscured for a very small number of frames.

8.5.2.1 Sources of inaccuracy X-ray flow measurements

There are several factors that, whilst steps were taken to control them, may have influenced the accuracy of the X-ray based flow measurements. Starting with the X-ray generation, the X-ray output during an acquisition locks after five frames and should be constant from that point onwards. Whilst some small variations in X-ray output can be observed in the phantom experiments under such conditions (see for example Figure 7.3 on page 131), these small variations would not affect the curve gradients over a few seconds and would be removed by the low pass filter applied to the TIC. Differences between the calibration sequence and measurement sequence may be introduced if the radiographic output used for each sequence are different; in other words if the kV, mA and ms lock at different values in the calibration and measurement sequences. This would be the case if the exact imaging geometry is not used in both sequences, there is any difference in patient positioning, or a difference in breath-hold (such as at inspiration or expiration). Any difference in kV would affect the beam energy, and a it can be seen from Figure 6.3 on page 123 the differential signal caused by a fixed amount of contrast agent varies with the kV. Nonetheless, a fairly large change in kV would be required to make much of an impact through beam energy effects. Differences in output through beam intensity changes (incurred by kV and mAs) would also impact the differential signal caused by the contrast agent, proportional to the change in X-ray output. Any difference in SID, or source-to-patient distance would also affect both the X-ray output and magnification of objects in the image leading to inaccuracies in the flow measurement. Compared to the phantom experiments, the differences in beam output are likely to be higher in the human study as differences in positioning are far more likely.

Accurate measurement using the X-ray technique also requires that both contrast injections are as per the assumptions inherent in the method. Specifically, during the calibration sequence the contrast agent must be delivered at a known rate, and all of the contrast must flow down the coronary artery. During the measurement sequences there must be complete replacement of blood with contrast agent. The injection of contrast agent for the measurement sequence used a rate that was subjectively set by the operator according to the size of the vessel being imaged. The aim of this—when combined with the maximum pressure limit

set on the pump of 200 mmHg—was to ensure that the injection of contrast could not cause harm to the patient. If the injection rate were significantly higher than the native flow, and the driving pressure not limited, then there would be the possibility of to damage the artery, and indeed adverse reaction to saline infusion when set higher than recommended with the RayFlow catheter has been reported.[319] The downside of this approach is that if there were not complete replacement of blood with contrast during the measurement sequence (in other words the injection rate was lower than the native blood flow in the coronary artery), then the measured flow would be lower than the actual flow. It can be seen that in the phantom measurements, accurate blood flow measurements were obtained when the injection rate exceeded the native flow by 1 ml/s (Figure 7.10 on page 144), but this may not directly translate into humans. The phantom used a continuous flow of blood mimicking fluid, whereas the coronary flow is pulsatile, with peak flow in diastole. This could create a situation where the contrast agent is injected at a rate above the mean coronary blood flow, but not above the peak coronary blood flow, resulting in incomplete replacement of blood with contrast. In all cases the angiograms were checked to ensure that there was clear back-flow of contrast into the aorta during the measurement injection, but it would have been impossible to ensure that this was occurring during the peak diastolic coronary flow. As such it is quite possible that this mechanism is contributory to the lower flow rates seen with the X-ray measurements compared to the thermodilution references. It would also be possible for the X-ray blood flow measurements to overestimate the actual blood flow in the case where all of the contrast injected in the calibration sequence did not enter the coronary arteries, which may be possible in the case of severe disease or poor catheter engagement. Occasionally, during the analysis, small amounts of back-flow of contrast into the aorta were seen during a calibration sequence, but were not thought to be significant.

The contrast injection itself could affect the flow of liquid down a coronary artery in a number of ways. If the injection causes an increase in arterial pressure, flow could increase. Another source of increased flow could be reactive hyperaemia that can be induced by contrast agents. On the other hand, the viscous contrast agent could reduce flow as it fills the coronary artery. A significant increase in flow and pressure has been noted if the injection of contrast is considerably distal to the proximal ostium of the artery.[185] Conversely, less than a 5% difference in flow has been noted with a contrast injection in the aortic root.[186] The injection

regime used in this study, where the contrast injection made with the catheter engaged in the artery of interest, is likely to be somewhere between the two. The size of the catheter in relation to the size of the vessel may be a factor in any effect on flow—if the catheter is small compared to vessel, any increase in pressure in the vessel is likely to be smaller than if the catheter nearly fills the vessel. In this study 6F guide catheters were used, which have an external diameter of 2 mm. Given the typical diameter of the left main coronary artery of 4.5 mm,[320] the catheter would occupy just under 20% of the cross sectional luminal area. In the RCA, the arterial diameter is more variable, ranging from 2.8 to 3.9 mm,[320] meaning the catheter would occupy between approximately 25% and 50% of the cross sectional luminal area. Given that the catheter does not tightly fit into the ostium of any of the coronary arteries, a substantial increase in arterial pressure is unlikely. The phantom experiments also did not show any increase in flow when contrast agent was injected at a rate exceeding the the native flow, and no variation in TIMI frame count has been noted despite the use of power injection.[321] The relatively short injection times would limit the effect of contrast induced reactive hyperaemia. If present, reactive hyperaemia would be present in the later parts of the sequences as the contrast agent affects the microvasculature, causing a late increase in gradient of the TIC; this effect was not seen during the analysis. The viscous effects of the contrast agent may have been seen slightly in the phantom experiments, but would not account for the 25% under estimate of the thermodilution flow from the X-ray measurements in the patient study.

The X-ray flow measures offer a relatively straight forward way to assess the flow down the whole left or right systems by drawing ROIs around the entire heart. If separate measures of flow are required for the Cx and LAD sub-regions are drawn for each artery in the measurement sequence during analysis. For this artery selective analysis to be accurate there should be separation of the arteries and their respective myocardial territories in the angiogram. This separation was best achieved in the left lateral projection, but the projection is cumbersome to achieve, with the patient's arm being prone to being in the X-ray beam when radial access is used, requiring table height adjustments to frame the heart correctly and often requiring other equipment in the catheterisation laboratory to be moved out of the way of the C-arm. For that reason the majority of cases in this study used the LAO-cranial projection for the left system. In this projection the diagonal and marginal arteries can overlap, which would

likely cause the individual measurements of flow in the two left arteries to be inaccurate.

The most common reason for a sequence to be unacceptable for analysis was due to breathing related artefact. During the sequence acquisition patient breathing would cause substantial deflections in the measured TICs, which could be far larger than the changes provoked by the contrast agent. Breathing out causes the diaphragm to rise, reducing the signal intensity in a ROI containing the diaphragm, and visa versa for inhalation. Figure 8.13 shows a series of images from a sequence where the patient has failed to breath hold at all (note the rising and falling of the diaphragm in the images), and Figure 8.14 shows an example of the sum of pixel intensities in a ROI drawn around the heart. It can be seen that the breathing artefact causes large amplitude deflections in the curve at approximately 0.25 Hz, obscuring any appreciable decrease in intensity from the injection of contrast agent.

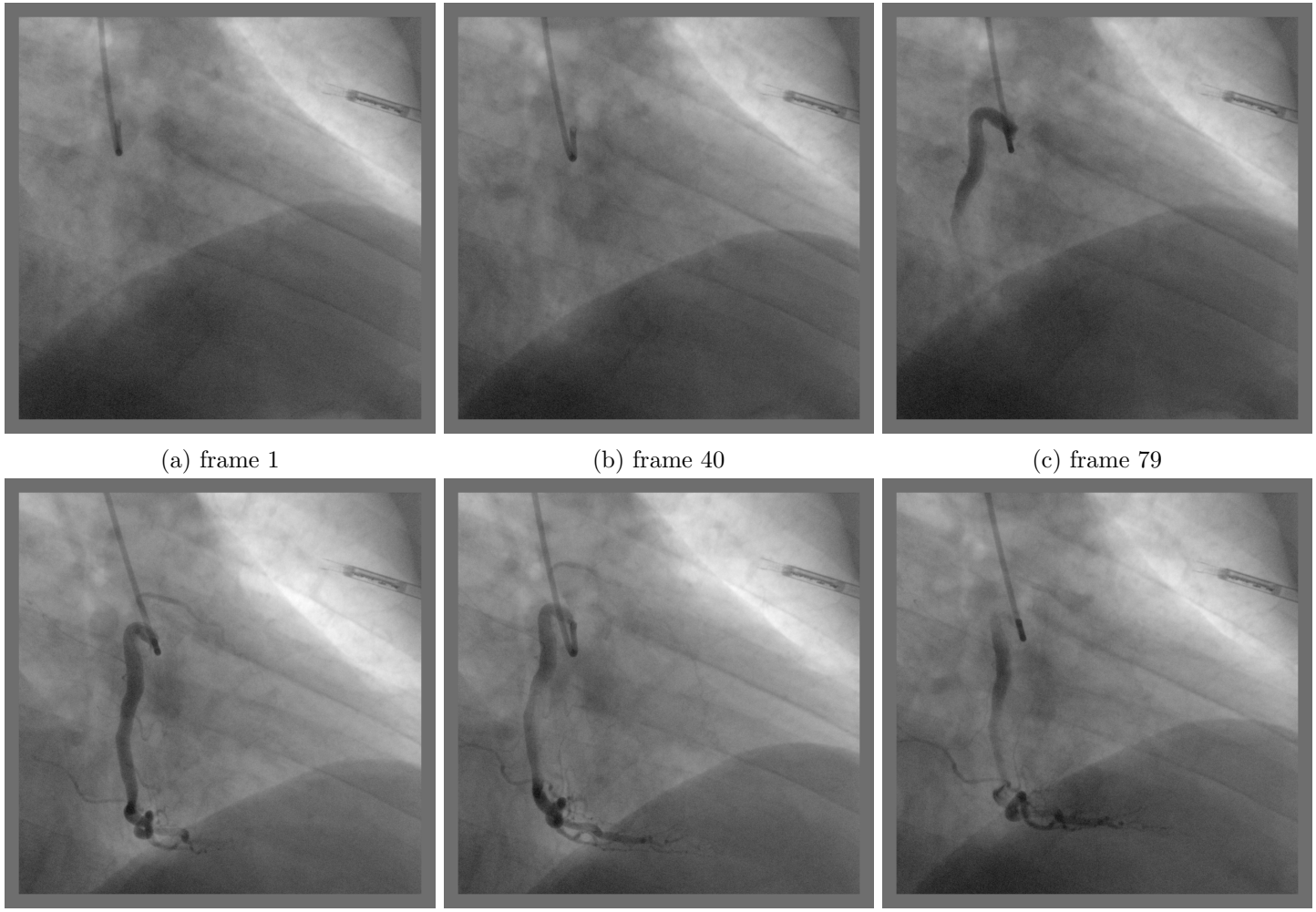

(a) frame 1 (b) frame 40 (c) frame 79

(d) frame 119 (e) frame 158 (f) frame 198

Figure 8.13: Images from an angiogram of a right coronary artery showing considerable breathing motion- note the different location of the diaphragm in the frame.

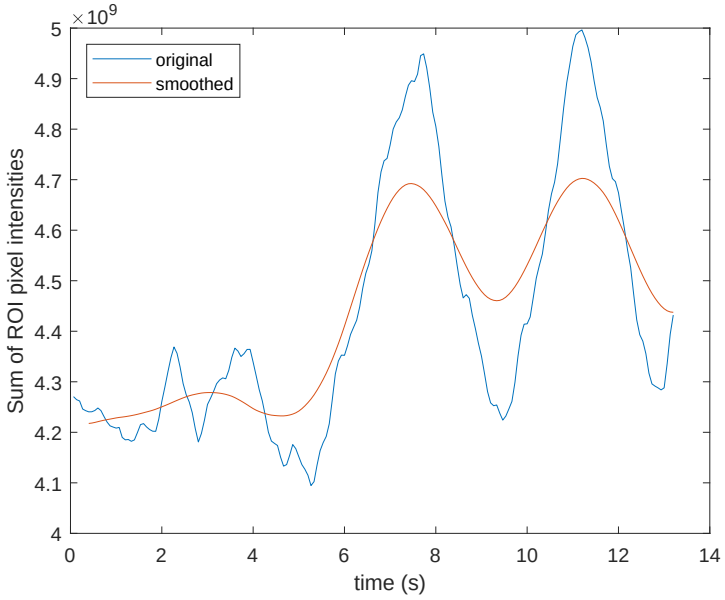

Figure 8.14: Time intensity curve from sequence shown in figure 8.13 corrupted with breathing artefact of approximately 0.25 Hz. The patient has exhaled starting at approximately 5.5 s and 9.5 s.

Whilst those sequences with the largest degrees of motion were excluded, smaller amounts of breathing would also affect the gradients of the TIC, leading to an inaccurate flow measurement. The decision as to when breathing precluded successful flow measurement was subjective, and the degree to which smaller amounts of breathing affected a flow measurement remain unknown.

The role of collateral circulation may result in cases where the actual flow of blood into a myocardial territory is greater than that measured by the X-ray based measurement (as the collateral supply is not visualised by the selective angiography). These cases are likely to be readily identified by the diagnostic angiograms, and if quantification is required coronary wedge pressure can be used to assess the extent of myocardial flow.[322] whilst it may be present in a lot of people, the physiological impact may not be too large- can see an effect below wedge pressure of 25 mm Hg.[126]

The appearance of contrast agent not flowing down the coronary artery could also cause the flow measurement to be inaccurate. This can occur in the measurement sequence with contrast that flows back into the aortic root. Whilst the aortic valve is closed contrast tends to accumulate in the aortic root, which if the aortic root is included in the ROI, will falsely increase the gradient of the processed TIC, leading an overestimate of flow. An example

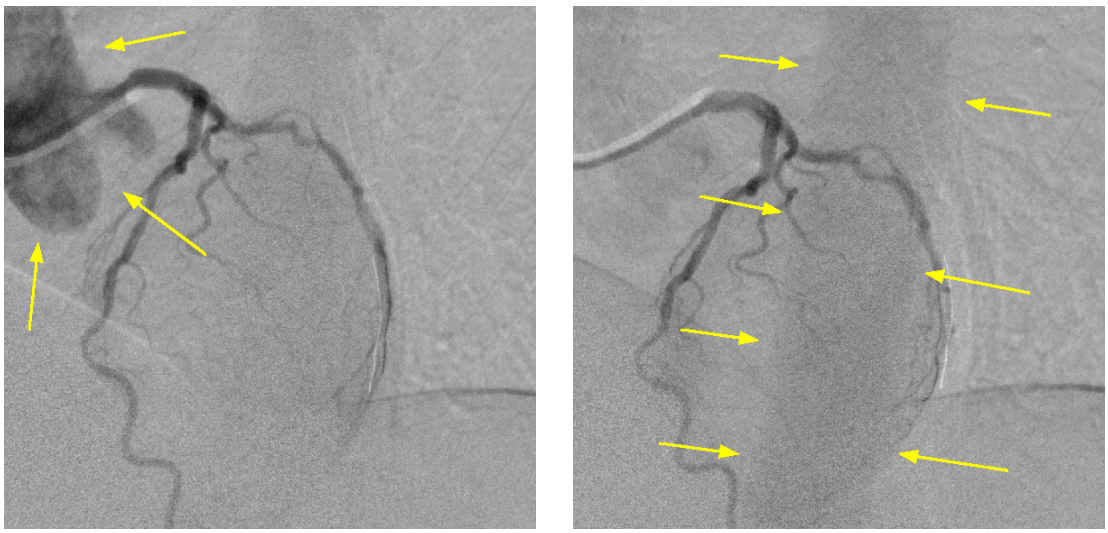

(a) (b)

Figure 8.15: Digital subtraction images from a left coronary artery in the LAO-Caudal projection, with arrows showing a) Contrast accumulating in the aortic root, and b) overlapping the circumflex artery in the image as it flows down the descending aorta. These effects could cause over-estimation of flow if the extraneous contrast is included in the analysis region of interest.

frame from a LCA angiogram is shown in Figure 8.15a. This can be avoided by adjusting the shape of the ROI to avoid the area of the aortic root. As the heart contracts, the aortic valve opens, and blood flows down the aorta along with any of the contrast accumulated in the aortic root, and that which is still flowing into the aorta, over the aortic arch and on to the descending aorta. Whilst the ascending aorta is out of measuring ROI, the descending aorta can overlap with the heart in some projections. Of those used in this study, the LAO-cranial projection used for the LCA, can place the descending aorta over the Cx and its myocardial territory. This again could lead to an overestimate of the flow in this region. Figure 8.15b shows a subtracted image where this has occurred. It is clearly not possible to adjust the ROI to avoid this area if the Cx is to be analysed. Rather the projection should be adjusted to minimise the overlap, or it may be possible to make a correction using an ROI above the heart to estimate the contrast in the descending aorta.

8.5.2.2 Variations due to the observer

There are a number of steps when performing the X-ray measurements where decisions are taken by the person performing the analysis, producing a subjective variability into the results. One example is the placement, size and shape of the ROIs. The X-ray derived flow

measurements agreed reasonably well between repeated observations from the same observer, and those between two observers performed on the RCA. There was slightly higher variability in the left system when the Cx and LAD were analysed separately compared to taking the LCA as a whole, presumably due to the fact that the decision as to where to divide the image of the heart into the Cx and LAD regions involved the observer deciding where the boundary should be, when in reality there was some overlap in the territories in most images. It is interesting that the largest difference between observations was from a case where the chosen projection had very poor delineation of the Cx and LAD (an example image from this case is shown in Figure 8.16, which should be compared to Figure 8.1). in this case the use of polygonal ROIs might help separate the territories, but a better solution would be more carefully selected angiographic projection angle. Whilst overall the difference between most measurements either between or within observers was small (less than 0.2 ml/s), some individual measurements were markedly different, with a maximum intra-observer difference of 0.84 ml/s (35%) on the whole artery, and by 0.46 ml/s (27%) between the two observers on the RCA, although such cases were uncommon. Differences between observations could be derived from different ROI size, shape and placement, as well as differences where the user has overridden the automated sections of the analysis. The latter was necessary where, for example, breathing artefact towards the end of a sequence elevated the later part of the TIC; the case could still be analysed by excluding the last frames of the sequence. A fuller analysis of variations in the analysis would require addition data, most notably more observers analysing all arteries. Such data would permit the use of a multi-level model to assess the contributions of the inter and intra observer variability, as well as variation per artery. Systematic analysis of differences in the ROIs drawn would also help investigate how much of the variation in flow measurement is due to the ROI.

8.5.3 Sources of inaccuracy in the thermodilution reference measurements

There are a number of factors that could cause the thermodilution measurements to be inaccurate. Potential sources of error using thermodilution include the loss of saline through the arterial wall, and heating of the saline between the point of infusion and temperature sensor,[178] but the largest source of error is most likely to be inadequate mixing of blood and saline. Accurate flow measurement requires that the mixture of saline and blood reaching

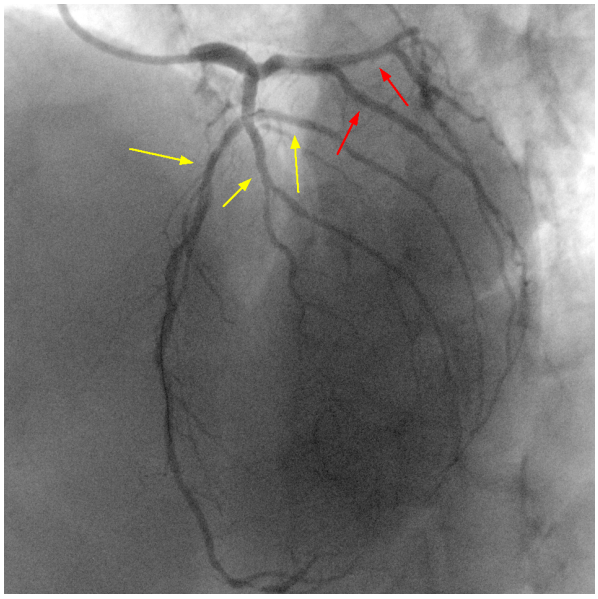

Figure 8.16: An image from a case where the chosen projection angle gave very poor separation of the circumflex (red arrows) and left anterior descending artery (yellow arrows).

the thermistor for the distal temperature measurement has a ratio of saline to blood in the ratio of the infusion rate to native blood flow. Temperature is then used to estimate the ratio of saline to blood at the thermistor. Similarly, the temperature of the infusate (or more specifically, the difference in temperature of the saline infusate to blood) must also be known accurately.

The design of the infusion catheter will have a significant effect on the degree of blood and saline mixing, and how quickly the mixing is achieved, but other factors are relevant, including the morphology of the artery and the distance between the infusion site and thermistor. The RCA has a much simpler morphology to the LCA; in particular it does not generally have a major branch for quite some distance from its proximal end. In the RCA, where a standard catheter was used in this study, it was assumed that the turbulent flow in the artery due to disease would promote good mixing of blood sand saline. Beyond a 25% stenosis turbulent flow would be expected in a coronary artery, and the degree of which would increase as the stenotic severity increases.[323,324] Fluid dynamic modelling of different catheter tip designs have shown that under turbulent flow reasonable mixing of saline and blood is achieved after approximately 5 cm even with standard catheter.[325] Conversely, mixing is very poor over a similar distance if there is only laminar flow in the artery.[325] The inclusion criteria for the study included a 30% visible stenosis in the target artery, and therefore the lack

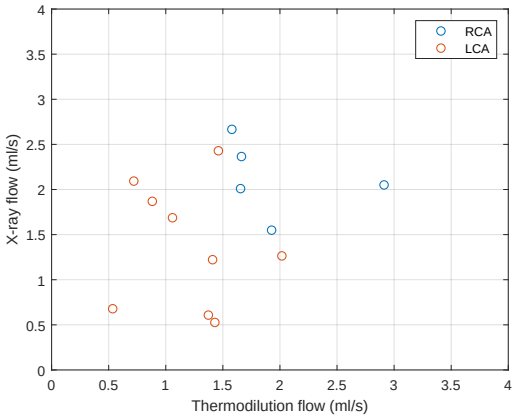

Figure 8.17: Scatter plot of thermodilution flow measurements performed with the RayFlow catheter to the X-ray based flow measurement, showing only a very modest correlation between the two measurements.

of a dedicated infusion catheter in the RCA cases, given this patient cohort may not have precluded a reasonable of flow using thermodilution, although clearly there may have been loss in accuracy and precision due to the lack of infusion catheter. Unfortunately there were too few cases performed in the RCA RayFlow catheter to draw conclusions as to the difference it may have made in this artery.

The left main artery, in contrast to the left, branches quickly into the LAD and Cx arteries, which themselves branch into a set of diagonal and marginal arteries respectively, which mean that rapid mixing of blood and saline is more important in the left system. Inadequate mixing of blood and saline prior to the bifurcation of the left main artery would explain the thermodilution results in the left system for the first patient group, where no specific thermodilution catheter was used, and unreasonably high measurements of flow were observed. Flow measurements in this artery therefore require the use of a dedicated infusion catheter. Unfortunately only 12 cases were available where there was successful measurement using both the X-ray and thermodilution measurements with the RayFlow catheter. Of these seven cases were in the LCA and five in the RCA. Comparing only the cases performed with the RayFlow catheter to the X-ray measurements overall, Figure 8.17 shows that there was a poor correlation (r=0.23), although the mean difference between the measurements was much less than that seen when the RayFlow was not used (0.17 ml/s vs 0.55 ml/s). A similar pattern is also observed with the frame count based reference (see Figure 8.11b).

8.5.3.1 The RayFlow catheter

The role of the infusion catheter is likely to be important in rapid mixing of blood and saline. A comparison of two dedicated infusion catheters has demonstrated that the catheter design is important, especially at higher blood flow rates or low infusion rates,[180] although unfortunately the two catheters used in the study were not identified. The RayFlow catheter has been shown to produce good agreement with reference flow measurement in phantoms, providing a high enough rate of saline infusion is used (0.5 ml/s), and the 95% limits on agreement compared to the actual flow of just over ±15%.[180] More recently, Xaplanteris et al. reported a slightly poorer agreement from consecutive measurements in humans (coefficient of determination of 0.71, and coefficient of variation 19.7%).[181] Unfortunately this study does not use any reference measurement of flow in the arteries. Aarnoudse et al.[178] reported excellent reproducibility of thermodilution flow measurements in humans, although their patient cohort was carefully selected, including only patients where a 3 cm segment of artery could be found between the site of infusion and the thermistor. This stringent selected was probably responsible for the unusually high number of patients with RCA investigation in the cohort (31 out of 42 patients). More recently a comparison of RayFlow based thermodilution measurements in the Cx and LAD in humans demonstrated good correlation with a non-invasive PET reference (r=0.91), although the 95% limits of agreement at ±1 ml/s (approximately 30%).[326]

Given the limited data on the RayFlow catheter, and the poor correlation with the X-ray flow measurements from this study (Figure 8.17), it was therefore decided to assess the accuracy and precision of flow measurements made using the catheter using the coronary flow phantom described in Section 7.3 on page 132. A full description of the experiment and its results is presented in Appendix A on page 215, but in summary three repeated flow measurements were made with the RayFlow catheter at each of four underlying flows in the phantom ranging from 1.24 to 2.45 ml/s. There was a mean difference between the actual flow and the flow measured by thermodilution of 0.16 ml/s. The mean relative error was 12.6%, and the average coefficient of variation for of the four conditions was 10%, in line with the previous reports. When using the RayFlow catheter, the guide wire is positioned such that the thermistor is placed some distance distal to the catheter tip to record the distal temperature. With the saline infusion continuing the wire is withdrawn bringing the thermistor into the

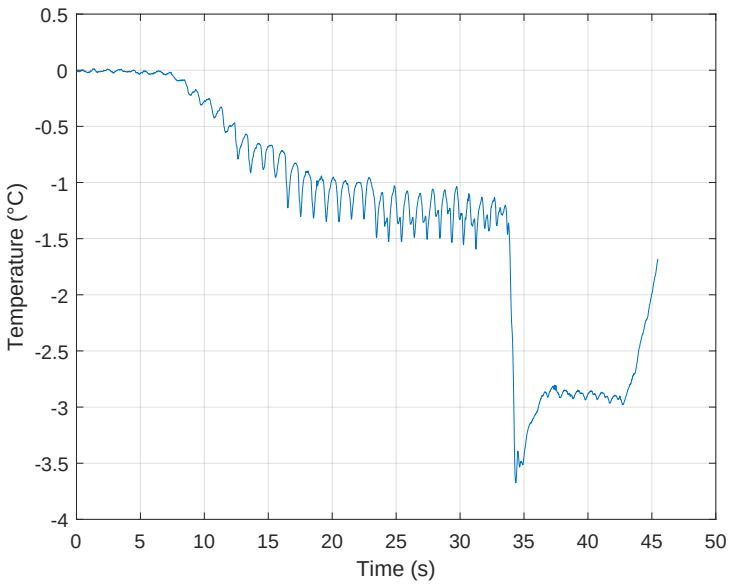

Figure 8.18: Deflections can be seen in temperature measurement from one of the clinical cases as the thermistor is pulled back to measure the infusate temperature. Pull-back was started at approximately 30 s, and the reduced temperatures between 34 and 37 s indicate that the minimum temperature (i.e. the temperature of the infusate) may not have been recorded.

catheter to measure the temperature of the infusate. It was noticed during these experiments that the infusate temperature measurement, T_i, varied considerably as small movements of the thermistor were made as it was withdrawn into the catheter to record the measurement. In other words, great care had to be taken to ensure that the thermistor was positioned such that it recorded the minimum temperature of the infused saline. This effect has been noted as point of discussion in a previous study using the catheter, but no attempt was made to quantify or demonstrate the effect.[179] Clearly inaccurate measurement of the infusate temperature would lead to an inaccurate measurement of blood flow. Discussion with the clinical team did not establish that a careful search for the minimum temperature point was performed in the clinical cases. Review of the temperature recordings, revealed that deflections in temperature as the thermistor was withdrawn into the catheter were present in the clinical cases (an example is shown in Figure A.2b), and this may have contributed to the lack of agreement seen between the X-ray and thermodilution measurements shown in Figure 8.17.

8.5.4 Limitations

There are a number of limitations to this study. Overall the number of patients, as planned, would have been perfectly reasonable for such a proof-of-concept study. However, an issue

with the thermodilution reference—the availability of an infusion catheter—has been detrimental in a number of ways. Firstly, the majority of cases in the left coronary system did not have an adequate thermodilution reference measurement. This reduced the statistical power of the study. Secondly, the majority of cases in the RCA were performed without an infusion catheter. Whilst the assumption that there was adequate mixing of the blood distal to a stenosis was not unreasonable (and supported by the results), it is likely that the thermodilution reference was less accurate than it otherwise might have been had a dedicated catheter been available. Moreover, in the RCA the thermistor was often placed a greater distance from the infusion site than may have been used with an infusion catheter, often into the distal segments of the artery. This may have led to a heating of the saline as it transited between the infusion site and thermistor, which would lead to an overestimate of the blood flow.

All of the patients with an intervention in the left system where no dedicated infusion catheter was used (seven patients) were excluded due to the unreliable measurements being obtained from the thermodilution measurements. The final seven measurements in the left system were performed using the RayFlow Catheter; in most likelihood too small a sample. Moreover, Aarnoudse et al recommended that the thermistor is placed 3–6 cm from the infusion site based on their laboratory experiments and tightly selected patients in their validation study where this was achieved.[178] This study did not impose such stringent patient selection or control of the distal temperature sensor and this may have resulted in a lack of precision in the reference flow measurements in the left system. Had the RayFlow catheter been available for use from the start, then the results from the LCA might have been more informative. Unfortunately the clinical team were not aware of the fact that very small movements of the wire affected the measured temperature when recording the infusate temperature with the RayFlow catheter and this may have led to inaccuracy in the flow measurements when this catheter was used.

The study design took flow measurements at up to four points in the procedure: pre and post intervention both at rest and at stress. Such a design has the advantage of potentially allowing measurements of CFR and ratios of flow, to ratios of FFR as performed in the relative flow experiment in Chapter 5. Unfortunately, only a relatively small number of patients went on to have intervention performed, and not all patients had the pre-intervention

stress measurements performed. The result was that too few patients had the complete set of measurements performed to make such comparisons. Given that no measurement was repeated, the design could not provide any information regarding the reproducibility of the new technique. An alternative design, incorporating a simpler test-retest protocol would have provided an assessment of reproducibility, which would be especially useful, given the issues with the reference measurements.

8.6 Conclusions

These experiments did demonstrate that the X-ray flow measurements were related to both reference measurements of flow in the RCA, however, the X-ray measurements of flow were on average 25% lower than than those made using thermodilution. It is likely that the reactive hyperaemia induced by saline infusion in the reference measurements, the lack of dedicated infusion catheter leading to sub-optimal mixing of blood and saline making the thermodilution measurements, and perhaps viscous effects of the contrast agent in the X-ray measurements may be responsible for this discrepancy. Further work is required to confirm this. In the left coronary artery no relationship was found with the X-ray and thermodilution flow measurements, although there were too few cases, and a number of methodological issues with the use of the RayFlow catheter that could have affected its accuracy to draw conclusion from these cases. There was a similar relationship between the X-ray and frame-count based reference index in the LCA as was seen in the RCA. Overall, the calibration method was shown to be viable in clinical practice, and the complete X-ray flow measurement protocol added little time the procedure. The measurements were adopted by the clinical team and safely attempted in all of the cases in this study, and once the team were familiar with the protocol approximately 75% of measurements could be successfully analysed. Further work is required to confirm the accuracy, and in particular the reproducibility of the measurements in humans.

Chapter 9

Summary, Discussion & Conclusions

9.1 Summary of Work

This aim of the work presented in this thesis was to develop methods of measuring the absolute flow of blood in the coronary arteries that could be safely and conveniently employed in clinical practice on humans. This was undertaken as a progression of work, initially developing and assessing enabling techniques, followed by the development the absolute flow measurement technique's underpinning theory, and practical testing in phantoms and ultimately humans. The key challenges that were overcome to achieve this were as follows.

Radiation dose reduction The radiation dose rate to the patient when using the acquisition mode to obtain the quantitative image sequences was reduced by introducing a spectral beam filter into the X-ray beam. This lowered the additional radiation patient received from flow measurements making them safer to perform. There was a negligible loss in image quality, undetectable by human observers in clinical images, as a result of the dose reduction.

Removal of background anatomy To analyse the contrast agent, it is necessary to be able to suppress the signals in the image from other anatomy, and to overcome cardiac motion and other patient movement during imaging, most notably from breathing. This was initially achieved using a cardiac phase matched digital subtraction (Chapter 4), and later temporal processing of the measurements taken within a ROI within the image sequence (Section 8.2.3).

Modification to the X-ray equipment settings Current X-ray systems employ closed loop feedback and feed-forward systems to control their radiographic output and computer based image processing, which is applied to images prior to display. These automated systems, under normal operation, ensure safe levels of radiation are used for the patient, and the images displayed to the clinical users are of adequate quality. They also remove the linear relationship between energy absorbed by the X-ray detector and signal intensity in the image, which would corrupt the analysis of contrast agent volume. Selectively disabling some of the these systems, and altering the behaviour of others, allowed the quantification imaging to be performed at appropriate radiation doses. This permitted quantitative comparison of blood flow between two different acquisition sequences, and it was demonstrated that this could be used to estimate the improvement in flow in an artery following angioplasty and stenting (Chapter 5).

Calibration of the X-ray signal intensity to contrast agent volume The absolute measurement of flow requires that the change in signal in an image per unit of contrast agent is known. A method, which was straight-forward to implement in clinical practice, and its underpinning theory was developed to achieve this (Chapter 6).

Phantom testing The testing of the method was performed in two phantoms in Chapter 7. In a phantom where the flow of contrast was directly controlled by a power injector, the X-ray measurements were accurate, predicting the actual contrast flow with a mean error of $\pm 9\%$, and coefficient of variation of 4%. A far more sophisticated phantom was developed, with the conditions representative of the flow in the human coronary arteries, were modelled. In this phantom the X-ray flow measurements were shown to be measure the simulated flow within 5% of the actual flow. Compared to results from similar experiments performed using a thermodilution flow measurements in the coronary circulation phantom (Appendix A), the X-ray based flow measurements were slightly more accurate and similar in terms of reproducibility.

Testing in humans The X-ray flow measurements were tested in a proof of concept study with 45 patients (Chapter 8). Once the clinical team had become familiar with the measurements, this was successfully performed in 75% of cases. The X-ray based flow measurements had a moderate correlation to reference flow measurements taken with

a continuous thermodilution technique. The X-ray flow measurements underestimated the flow measured via thermodilution, however, there were a number of issues with the thermodilution reference, which may have affected its accuracy.

Overall, the accuracy of the X-ray flow measurements in the phantom experiments was very encouraging. However, the results of the testing in humans was less conclusive. Compared to flow measured using thermodilution, the X-ray measurements underestimated flow. There are a number of possible explanations for this, and the most likely causes are the lack of a dedicated thermodilution infusion catheter for the reference measurements, a reactive hyperaemia following the injection of saline for the thermodilution, increasing flow in these cases, and the flow of contrast agent in the X-ray measurements being lower than that of blood due to the increased viscosity of the contrast agent compared to blood. It is not possible, however, to conclude that these are the cause of the difference in magnitudes of the measured flow from the existing data.

In terms of the precision of the X-ray flow measurements, the phantom results were excellent. There were limited data in the human study regarding the reproducibility of the measurements as no test-retest was performed as part of the protocol. There was an assessment of the observer variability, and overall the measurements were reasonable reproducible between observers, and for the same observer, with a standard deviation of 0.2 ml/s between measures, although on occasion difference in individual cases were larger, sometimes exceeding 0.5 ml/s. There were only two observers in the inter-observer variability assessment, and two measures of the X-ray flow by one observer in the intra-observer variability assessment, and therefore these results do not provide a complete assessment of the observer related variability.

9.2 Clinical utility of the X-ray based measurement of flow

In itself, the measurement of flow is an incomplete description of the coronary haemodynamics. A measure of coronary flow in isolation is difficult to interpret without knowing the mass of myocardium that the artery is supplying. The mass of myocardium supplied cannot be derived from planar X-ray imaging. Moreover, even if the mass of myocardium were known and it could be determined, for example, that the coronary flow was lower than normal in a given patient, this would not give an indication as to the cause of the reduction in flow. Coronary

flow (and indeed CFR) is reduced by a range of factors affecting both the coronary arteries and myocardium (such as focal CAD, diffuse CAD, myocardial bridging, syndrome X, and cardiomyopathy.[327]) Identification of the underlying cause of the reduced flow is required when making decisions about appropriate treatment for the patient. It is likely that the clear visualisation of the coronary arterial lumen in X-ray angiography has resulted in a focus on epicardial obstruction in the catheterisation laboratory, over the role of microvascular obstruction as a cause of ischaemia.[328] A more complete description of the haemodynamics of a patient therefore requires the assessment of pressure and flow, so that estimates of resistance can be obtained.

Patients referred for angiography in the catheterisation laboratory are those at high risk of CAD, as lower risk patients requiring testing are dealt with by non-invasive testing, such as cardiac-CT. Within the catheterisation laboratory, ability to proceed from angiography to angioplasty and stenting offers rapid treatment. Other treatment options are available to patients, namely medical therapy and bypass surgery. In patients where CAD is not flow limiting, patient have been shown to have better outcomes with medical therapy,[109] and for multi-vessel disease, bypass surgery results in better patient outcomes compared to PCI.[329] It is no surprise therefore that physiological measurements in the catheterisation laboratory are focussed on deciding whether to proceed to PCI or whether another form of treatment will be of greater benefit.

The current mainstay of physiological measurements are pressure based, with invasive FFR being the most common, but the pressure only measurement of FFR means that a raised (or indeed lowered) microvascular resistance will affect the ratio of hyperaemic distal to aortic pressure ratio indicative of a flow limiting stenosis (see Section 8.2.3 for a more in-depth explanation). Differences in microvascular resistance also account for the apparent discordance between FFR and CFR.[13] Combining flow with pressure can produce a measurement of resistance, and if the pressure is recorded in the aorta and distal to a stenosis then both stenotic resistance and myocardial resistance can be calculated individually. Currently IMR, HSR and HMR have been proposed to assess resistance, but they are compromised by the indexes of flow that are used, namely the reciprocal of the mean transit time ($1/T_{mn}$) for IMR and Doppler based flow-velocity for HSR and HMR. Neither $1/T_{mn}$ nor flow-velocity account for differences in vascular volume either between patients, or between arteries. Nonetheless, despite this, van

der Heof et al.[270] elegantly demonstrate how much of the apparent uncertainty in invasive FFR can be readily explained by the interplay between HSR and HMR. See Section 2.5, and in particular Figure 2.20 for further explanation.

An absolute measurement of flow as, described in this thesis, is therefore appealing to supplement intra-coronary pressure measurements to assess whether or not a stenosis would benefit from stenting. An absolute measurement of flow such as the X-ray based flow measurement, overcomes the limitations of Doppler flow-velocity and $1/T_{mn}$ and also does not require the addition of either a thermistor or Doppler sensor in the guide wire. However, to be used in clinical decisions on treatment selection understanding of the appropriate thresholds of stenotic and myocardial resistance is also required but currently unknown.

A measure of flow and pressure could also be useful following intervention to gauge the improvement of coronary blood flow. No-reflow refers to the situation where there is hypoperfusion of the myocardium despite the restoration of patent epicardial vessel lumen following intervention. No-reflow during acute MI is associated with higher rates of left ventricular dysfunction, higher creatine kinase levels, and threefold increase in mortality.[330] This can occur following intervention for acute coronary syndrome (in >20% of cases) or PCI where no ischaemia is suspected (in <2% of cases).[331] There is evidence from studies using a visual grading of myocardial blush post intervention following MI, that a deficiency of blood flow seen on X-ray imaging is associated with worse patient outcomes.[72,332–334]

Whilst no-reflow is recognisable on standard angiography from the particularly slow filling of the treated vessel, or TMBG grades of 0 or 1, in reality there will be a range of post intervention flow, and as such an assessment of post-PCI flow or myocardial resistance may be helpful in assessing the prognosis for a patient in a more graduated manner, rather than only detecting the extreme cases as at present. The high rate of no-reflow in ACS means that the clinical utility of a flow measurement post intervention is of most value in the acute setting. This is in contrast to the relative flow measurement in Chapter 5 which was performed in a non-acute patient group. Moreover, if time-to-balloon is to be minimised, then rather than a relative measurement pre and post intervention, an absolute measurement of flow alone following revascularisation would be more appropriate.

An absolute measurement of flow would also be useful in the research setting. The time after intervention following MI can be one of considerable change in the myocardium depend-

ing on the state of the myocardium when revascularisation is performed. Infarct of under than 30 minutes in duration does not affect flow once revascularisation has been achieved. Ischaemia of longer duration causes changes to the microvasculature. Gradually the smaller vessels lose the endothelium related relaxation that plays a key role in moderating flow, with this capacity lost after 120 minutes. Intra-cellular oedema and further obstruction to flow by activated leukocytes adhering to the capillarity walls further restrict flow. During PCI distal blockage can occur via atheroembolisation during the procedure.[74] Revascularisation can make matters worse—the influx of fluid and electrolytes may increase swelling in the damaged cells, reducing blood flow, and the influx of activated leukocytes and monocytes may create more vascular plugs, therefore reducing flow further. Myocardial reperfusion injury can vary in severity from myocardial stunning, no-reflow, through to lethal reperfusion injury, and is associated with poorer patient outcomes.[335] The interest in altering the reperfusion strategy within the catheterisation laboratory (for instance delaying stenting,[336,337] or performing complete rather than main lesion only revascularisation[338]) or in determining effective therapy or protective medication[74,339,340] are likely to benefit from a measurements of flow and myocardial resistance.

9.3 X-ray dose and quantitative imaging

The acquisition of flow information via the methods described in Chapter 8 requires at least two acquisition sequences, at least one of which is unlikely to be useful in the standard clinical routine. They therefore add additional radiation and contrast medium above that which is required for the standard procedure. A dose survey of PCI cases within the hospital in which this study was performed found that the average duration of cine acquisition in a similar patient cohort was 52.3 s.[16] Two additional sequences acquired for a minimum duration of 7 s (four second injections, plus the mask images) would increase the duration of angiographic acquisition by 27%. The increase in radiation for the case, given a even split between fluoroscopy dose and acquisition dose,[16] and the 40% reduced dose acquisition mode used for the quantitative image, would increase the overall procedural dose by approximately 10%. The additional dose would rise for each flow measurement performed on a patient (for example performing one at rest, and one at stress).

In absolute terms the level of radiation received for the measurement sequences is not high–a 10% increase in procedure DAP would be 380 cGy cm2 based on the data from the optimisation study from Table 3.2 on page 77. However, repeated acquisitions on the same area of skin may contribute to higher peak skin doses. It is also possible that patients receiving PCI can receive further radiation procedures, sometimes further PCI, or perhaps other modalities such as cardiac CT or radionuclide imaging). It is therefore desirable to reduce the radiation dose levels to the minimum necessary to perform the measurement, in line with the as low as reasonably achievable (ALARA) principles.

Since the study presented in Chapter 3, the use of spectral beam filters has become more widespread in cine acquisition modes, with beam filters of 0.4 mm of Cu now used. This has produced much greater despite improvements to the computer based image enhancement algorithms that were introduced, along further with reduction in patient dose.[49,64]

A substantial difficulty in deciding on appropriate dose levels for either standard coronary angiography, is that it is not known what absolute level of quality is required, nor indeed how to quantify this. Moreover for most X-ray systems the quality of images produced is not constant. A feature of the anti-isowatt, constant detector dose, ADC used on the cardiac X-ray systems in this study is that image quality is reduced as the patient size increases.[341,342] Alternative dose control systems, whereby the image quality is held constant, not the detector dose, have been described. Such systems, depending upon how high the target image quality level is set, have the potential to reduce the dose delivered to thinner patients, but could well increase the dose to larger patients.[342] Despite this, a modified dose control scheme able to monitor the image stream assessing the image, actively quantifying relevant features of the image (such as the contrast produced by the coronary arteries, or noise levels in different regions of the image[343]) could ensure that the appropriate level of image quality is delivered for an image intended for quantitative analysis.[344]

9.4 Future Work

Whilst the two phantom experiments did assess the accuracy and reproducibility of the X-ray flow measurement, there is more that could be learnt from further in vitro testing. The accuracy of the X-ray measurement in the coronary circulation phantom over a range of

underlying flows would be helpful (currently only one native flow, approximately 3 ml/s was studied). These data could also refine the injection rates used in the measurement sequences; by providing more information as to how much the native flow should be exceed by the contrast injection rate to obtain complete replacement of blood-mimicking fluid with contrast agent.

The coronary circulation phantom could also be developed further to include branching arterial segments such as those found in the LCA. These could be produced from three dimensional printed arteries,[345] , created from models from either computed tomography or rotational angiography.[346] Such a model would also be useful for investigating the accuracy of the perfusion reference measurements in a branching artery.

The question of the level of image quality, and therefore radiation dose, could be investigated using the existing image set and software that degrades an X-ray image sequence to produce a result that has the added noise contribution as if it were acquired at a lower beam intensity (lower mAs) and hence lower dose.[347] An experiment where the radiation dose is gradually reduced in both the calibration and measurement sequences until there is an impact on the measurement of flow could be performed. Given the large area ROIs used in the flow analysis, it is likely that quite substantial dose savings could be possible.

In silico testing of the effect of non-linearities between contrast volume and signal intensity could be performed. In the large ROI there are a wide range of radiographic contrasts produced by the contrast agent, for example there is considerable difference in the shadow of a large vessel (which has a high mass-thickness of contrast) compared to small vessels, or indeed myocardium. It can be seen in Figure 6.3 on page 123 that the relationship between mass thickness of iodine and signal intensity is not linear, and the non-linearity is more pronounced the softer the X-ray beam and thinner the patient. The impact of this on the flow measurement could be investigated using computer simulation, and either deterministic projection models using triangulated mesh objects (arteries, myocardium),[348] or Monte-Carlo simulation of X-ray photon interactions could provide a suitable basis for the simulation.[349–351]

The current assessment of inter and intra observer variability is limited with only one observer scoring the images twice, and only two observers scoring the images. A greater number of observers, and a greater number of repeated measurements by each observer is required to obtain a more comprehensive assessment of observer related variability.

The current clinical study was subject to a number of limitations, notably a flawed implementation of the thermodilution reference test. This meant that the majority of reference measurements were taken without the use of a dedicated thermodilution infusion catheter. Moreover, there were only had a limited number of cases (especially in the left system), and the study did not provide data to assess reproducibility. A further clinical trial should address some of these limitations. A test-retest element to the protocol should be implement to assess reproducibility. If thermodilution based reference is utilised, all measurements should be performed under hyperaemia to control for hyperaemia induced as saline is infused. The RayFlow infusion catheter (or alternative dedicated thermodilution infusion catheter) should be utilised for all cases, with the patient cohort carefully selected to include only patients with suitable arterial targets for saline infusion. If an alternative flow-index is taken, such as Doppler flow-velocity, then a measurement of vascular volume should also be obtained (perhaps via reconstruction from rotational angiograms). The effect of viscosity of the contrast agent could also be investigated by lower concentration of contrast agent in a sub-group of cases or measurement sequences.

9.4.1 Improvements to the measurement technique

There are a number of areas where improvements could be made to the techniques ultimately developed for the patient study in Chapter 8. Whilst a power injector did provide consistent and safe infusion of contrast agent, the initial part of the injection contained a mixture of contrast and blood due to contrast leakage from the catheter prior to commencing the injection. The same effect also caused contrast to continue to enter the artery following the cessation of the injection. Whilst an attempt to minimise this was made by manually flushing the catheter prior to the injection, this could be prone to error (i.e. being forgotten), or there being some time between it being performed and the injection commenced depending on the circumstances in the catheterisation laboratory. The use of a dual headed pump, as is sometimes used in CT angiography,[352,353] could deliver a pre-contrast saline flush of the catheter immediately followed by the contrast infusion, thereby giving a sharp leading edge to the contrast bolus.

Improvements are also possible in other areas of the clinical technique. The automated termination of the X-ray acquisition following the end of the contrast injection could reduce

radiation dose. Using the current X-ray system, the current angulation of the C-arm can be stored using the table side controls, and then the system can automatically set the C-arm to the same angles later in the procedure. This feature was used by the clinical team in the later stages of the clinical study. Greater consistency in the radiographic output between sequence could be achieved if, along with the C-arm angulation, the radiographic factors were also stored and used for the next measurement sequence, in a similar way that the exposure lock system works for photographic cameras. Another useful feature would be the addition of an in room automated check of the quality of the measurement and calibration sequences, assessing for example patient movement. Such a system would highlight cases where the acquisition needed repeating, which could increase the number of cases where the measurements could be successfully performed.

This study used a simple ROI shape—a rectangle. Whilst the most easily drawn, and probably subject to less inter and intra observer variation in its size and placement, a more complex ROI shape may have reduced errors from, for example, contrast accumulating in the aortic root affecting the TIC, and this should be investigated. Alternatively, automated detection of contrast in the aorta, along with a correction, could be developed. Automated quality control on subregion analysis of TICs have been shown to improve reproducibility,[193,354] and could be employed on the whole ROI or on a regional basis.

9.4.2 Overcoming breathing

The biggest reason that the X-ray measurement could not be successfully obtained was due to breathing misregistration artefacts in the measurement or calibration sequences. Whilst the clinical team did improve their success rate as the study progressed (largely due to improved communication and practice breath-holding with the patient), there were still patients that could not breath-hold. A number of strategies could be used to overcome this, as described in the following sections.

9.4.2.1 Correction of the breathing motion

A series of images could be acquired while the patient breathes, producing a set of images at a range of cardiac and respiratory phase combinations. The beam energy used should be the same in the measurement sequences. The relative change in the background intensity relating

to each combination could then be calculated as a function of both cardiac and respiratory phase. This could be used to correct the signal intensity with the ROI in the measurement or calibration sequences.

9.4.2.2 Energy subtraction

Temporal subtraction is not the only way to isolate the signal derived from the iodinated contrast agent from other materials in the image. An energy subtraction technique can also be performed, and indeed the very first DSA images in the 1970s utilised energy subtraction rather than temporal subtraction.[355] Two images are acquired with very different beam energy spectra, one lower energy beam, and one high energy beam, and the weighted subtraction of the two images can be used to create an image with only the signal from the iodine based contrast agent remaining, and the soft tissue removed. If, during cardiac imaging, rapid switching of the beam energy for alternate frames in an acquisition sequence could be implemented by switching the kV and beam filtration, this could produce a set of images where the low-energy, and high-energy pairs of images are taken with a very short period of time between them. The resultant energy subtraction would therefore be resilient to breathing, as new low and high energy image frames are acquired as the patient breathes. This technique has been demonstrated in animal experiments.[256,295,309] Unfortunately this has not been translated to human imaging, presumably due to the fact that the rapid kV-switching, beam filter-switching and modified dose control schemes, are not available on clinical cardiac X-ray systems.

9.4.2.3 Energy sensitive X-ray detectors

An alternative technique to dual-energy subtraction would be to use a standard X-ray beam energy, yet make the X-ray detector sensitive to the energy of the X-ray photons incident upon it. There are a number of approaches to achieve this, including layered detectors, detectors whose pixel matrix is divided in a mosaic pattern of pixels sensitive to different energy bands and photon counting detectors.[356] Using such a detector means that a single exposure can produce images at a range of energy sensitivities. By selecting these bands appropriately, say for instance straddling the k-absorption edge of iodine, separation of the signals from different materials can be achieved. This has been demonstrated in areas such

as CT[357] and contrast-enhanced mammography,[358] but could also be implemented in cardiac imaging, assuming that the photon fluence rates in cardiac image can be accommodated by the detectors. The advantage of such an approach would be that energy subtraction could be performed to quantify iodine mass on a per image basis, overcoming the issue of breathing without the requirement for rapid filter or kV switching required for dual energy imaging.

9.5 Towards and integrated assessment of coronary haemodynamics

Two important technologies have been developed considerably since the inception of this research. Firstly, the use of rotational angiography to produce three-dimensional models of the coronary arteries. The increased spatial resolution of planar X-ray imaging compared to cardiac-CT means that accurate outlines of the vessel lumen are possible to sub-millimetre precision.

Secondly, there are advances in computational modelling—both lumped models and CFD models of the coronary arteries. Simpler lumped models (i.e. those with no spatio-temporal considerations, considering each element in terms of a single description) can be used to make predictions regarding the overall state of a vessel and myocardial territory, when given information from imaging and physiological measurements. Indeed, one such model, proposed by Siebes et al.,[127] was used in Section 2.3.3.2 on page 41 to explore the limitations of pressure based invasive FFR. The rapid improvements in computer processing power and the increasing sophistication of software environments for modelling[359] have contributed to the developments of computer models of coronary circulation. The use of such models can provide insight into the apparent contradiction in the standard physiological measurements. Johnson et al.[360] comprehensively survey the published data where CFR and FFR measurements have been made on the same patients, Johnson's study identifies that patients with a normal FFR (>0.8) yet depressed CFR (<2.0) can be modelled by introducing increased levels of diffuse disease and with increased levels of small vessel disease. The study also noted that the threshold limits for abnormal FFR have been performed in patients with high levels of disease, as indicated by the low value of CFR found in the reference vessels from the study populations. In groups with normal CFR the cut-off level of FFR indicating ischaemia was

much lower. Coronary branch steal has been modelled, demonstrating that an atomically fixed stenosis does not have a constant function significance, but there is a dependence on other stenoses in the arterial structure.[361] CFD models take as inputs the anatomical shape of the coronary artery, physiological information (such as intracoronary pressure measurements) and population derived averages for other boundary conditions (notably myocardial resistance) and utilise computer models of fluid flow based on the Navier-Stokes equation to estimate the flow in the arteries and predict the haemodynamic significance of stenotic lesions.[251] Multi-layered models can combine different model types, for example, a three dimensional CFD model of a vessel with 1D boundary models.

The most promising use of the X-ray flow measurement would be for it to be employed in an integrated haemodynamic assessment scheme in the catheterisation laboratory which utilises physiological measurement, three-dimensional models from rotational angiography, CFD models and the X-ray flow measurement. An optimisation scheme could be implemented where the results from each component are used to refine each of the other components, updating and iterating to reach a solution best matching the data collected from the patient. The output of such a system could include the selection of the most appropriate treatment for an individual patient, an estimate as to the improvement in reperfusion given the treatment selected, and potentially prognostic information regarding the patient. The scheme is illustrated in Figure 9.1.

There are a number of ways that data from one element of the integrated assessment could help the other elements. Previous work has demonstrated how the combination of computational modelling of the coronary circulation can be informed by flow measurements from nuclear imaging, specifically PET providing regional assessment of CFR and FFR.[362] Absolute flow measurements from X-ray angiography can be used, in combination with a distal intra-coronary pressure measurement to estimate the microvascular resistance. In turn, this can be used as a patient specific boundary condition for the CFD model of flow. The CFD model could then predict the relative flow along each of the branching arteries (for example separating the overall flow in the LCA to that flowing down each of the LAD and Cx arteries) which would overcome the need to separate these on the angiographic projections. Vessel diameter, length and volume from the 3D reconstructed arterial structure could be combined with automated frame count analysis to provide further estimates of flow. Corrections for

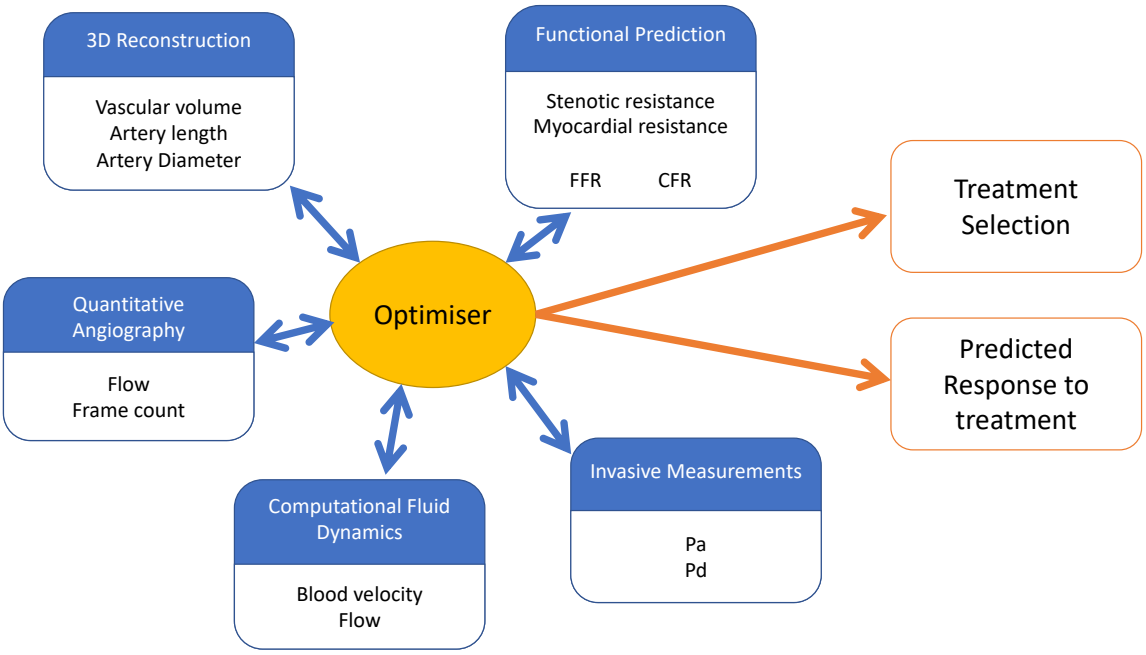

Figure 9.1: Integration of angiographic flow measurement, physiological measurement, 3D anatomical modelling and computational fluid dynamics to predict heamodynamics of the patient, optimal treatment and the outcome of the treatment.

breathing artefact in the angiographic X-ray measurements could be made by integrating an anthropomorphic model of the soft tissue, adapted to fit data acquired in the 3D rotational X-ray, to provide correction for breathing artefact (e.g. tracking of the diaphragm and calculating a soft tissue correction depending on the diaphragm location). The arterial volume from the 3D reconstruction could also be used to provide an alternative calibration for the X-ray sequence by assessing the signal intensity in the measurement sequence arising from the larger arteries alone. Such an integrated system could be used to assist in the treatment selection, which is of key importance in the catheterisation laboratory, and even predict the likely response to the treatment.

9.6 Conclusions

A measurement of flow in the coronary arteries has been developed and implemented on a clinical cardiac X-ray system and has been shown to be viable in to perform within the catheterisation laboratory. This required modifications the dose control and image processing systems, but such modifications could implemented on any modern cardiac X-ray system. The modifications to the dose control meant that appropriate radiation doses were delivered tai-

lored to individual patients. In previous work on animals, such modifications are unnecessary radiation output can be fixed as there is far less variation in size of the animals than in the human population. Spectral beam filtration was employed, reducing the radiation dose rates by 40% in the quantitative imaging modes compared to the standard angiography acquisition mode. There is potential to further reduce the radiation used during the flow measurements.

An intracoronary injection of contrast agent at a known rate using a power injector, was used to calibrate the signal intensity change observed in images to a known volume of contrast agent on a per patient basis. This approach overcame the need for external calibration phantoms that have been employed previously. External phantoms are impracticable in human imaging; they are difficult to locate in an angled X-ray beam and are also subject to error if the exact location of the heart and calibration phantom are not known, which is not the case in human imaging. Following calibration, a second injection of contrast agent, replacing all of the blood in an artery with contrast agent, was performed and used to measure flow via computer analysis of the flow and calibration image sequences. An integrated analysis application was created, which enabled the measurement of flow to be performed by clinical users. The majority of the analysis process was automated, and results could be produced quickly (in under a minute in most cases) which is similar to existing computer analysis tools available on cardiac X-ray systems.

The X-ray flow measurements proved to be reproducible and accurate in phantom experiments, producing more accurate results than reference thermodilution measurements, with similar levels of reproducibility in repeated measurements.

The clinical team found that the X-ray based flow measurements were straight forward to integrate into the clinical routine. In human testing, the X-ray measurements were completed in approximately 75% of the cases once the clinical team had gained experience with the technique. The majority of cases where the X-ray measurements could not be successfully performed were due to the patient failing to breath hold during the X-ray imaging acquisition. There was a moderate correlation between the X-ray flow measurements and a reference thermodilution based flow measurement, although the X-ray flow measurements were lower than the thermodilution measurements by an average of 25.6%. This difference may have been due to the lack of a dedicated thermodilution infusion catheter for the majority of the study, increased flow in the thermodilution measurements due to hyperaemia being induced

by the saline infusion, or the flow of contrast agent in the X-ray measurement could be lower than the flow of blood in the artery due to the viscosity of the contrast agent. Further human trials, employing a more rigorous reference measurement protocol, are required to assess the accuracy and reproducibility of the X-ray based flow measurements in humans.

Appendix A

RayFlow catheter testing

This experiment was performed following the clinical study described in Chapter 8, and used the coronary flow circulation phantom to investigate the accuracy and precision of thermodilution based flow measurements performed using the RayFlow infusion catheter (RayFlow, Hexacath, Paris, France). The motivation for this experiment was the relatively sparse data investigating the use of the catheter in humans, and the modest correlation between the thermodilution based flow measurements with the X-ray based flow measurements presented in Section 8.4.2. A full motivation, and discussion of the findings, is described in Section 8.4.2 on page 176.

A.1 Materials and methods

For this experiment the coronary flow phantom described in Section 7.3 on page 132 was used. Temperature and pressure were measured using the Radi equipment described in Section 8.2.4.1 on page 161. The phantom was filled with the same body temperature glycerol-water blood mimicking fluid used in the previous experiment. Prior to any measurements being taken the reservoir tank was stirred and the pump run for a time to ensure even mixing of the blood mimicking fluid. Clamp R1 (which controls the resistance in the distal aortic model) was adjusted so that the pressure in sections A & B (the aortic model) was approximately 100 mmHg. Clamps R2 and R3 were adjusted simulating four conditions:

1. no stenotic or myocardial resistance (R2 and R3 applying no compressions)
2. stenotic lesion in the coronary artery (R2 tightened),

3. myocardial obstruction in addition to the stenotic resistance (both R3 and R3 tightened), and

4. myocardial obstruction with no coronary stenosis (R3 tightened, R2 applying no compression).

For each condition pressure measurements were taken at locations A (simulated aortic pressure from the catheterisation laboratories monitoring system) and B (coronary distal pressure) using an intra-coronary pressure wire. Reference flow down the simulated coronary segment was measured by diverting the output from this section into a measuring cylinder and measuring the time taken for 30 ml of liquid to accumulate in the cylinder. This was repeated three times with the time averaged across the three measurements to calculate flow.

Thermodilution flow measurements were made using the RayFlow infusion catheters used in the clinical study. In the human setting, thermodilution measurements are taken with the RayFlow as follows. The guide wire is positioned in the distal artery of interest. The artery is then selectively engaged by the RayFlow catheter and thermistor position 3–6 cm distal to the catheter tip. Infusion of room temperature saline is commenced, and the distal temperature, T_d, recorded. The saline injection continues, and the wire withdrawn so that the sensor is placed within the catheter so that the temperature of the saline infusate, T_i can be recorded, after which the saline injection is stopped. In the phantom guide wire was initially positioned such that the thermistor was downstream of R2 (analogous to distal artery). Recording was initiated on the RadiAnalyser, and the saline infusion was commenced at 0.3 ml/s. Once the temperature had stabalised, the wire was pulled back so that the temperature sensor withdrawn into the infusion catheter to record the infusate temperature. The saline infusion and recording were then stopped. Three injections were performed yielding three measurements for each condition. Data from the RadiAnalyzer were transferred to a personal computer and analysed using bespoke software written in MATLAB. Temperature measurements were averaged over two seconds, and were performed at the reference, distal to the R2 clamp, and in the infusion catheter. Flow was then calculated using equation 8.2. When using the RayFlow catheter the temperature of the infusate was taken as the lowest stable measurement in the recorded temperature sequence.

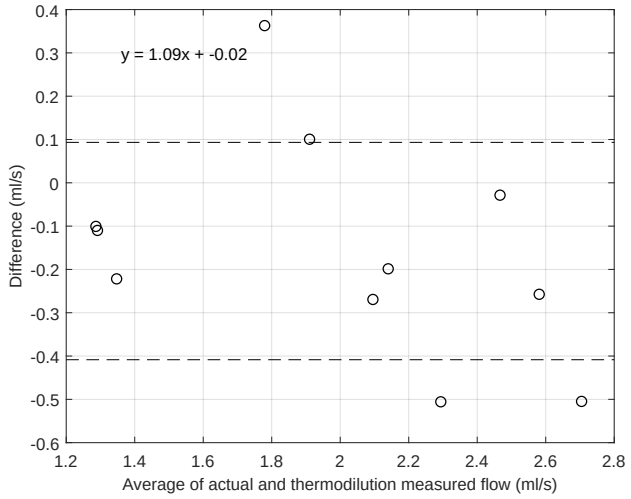

Figure A.1: Bland-Altman plot of actual flow and thermodilution measured flow with infusion from the Rayflow catheter. Dashed horizontal lines indicate mean plus and minus one standard deviation.

A.2 Results

A summary of the results are presented in Table A.1. Bland-Altman analysis showed a mean difference between the actual flow and the flow measured by thermodilution to be 0.16 ml/s with the RayFlow catheter; a Bland-Altman plot shown in Figure A.1. The mean relative error was 12.6%, and the coefficient of variation for each of the four conditions tested was 0.09, 0.17, 0.05 and 0.09 for conditions 1–4 respectively.

When using the RayFlow catheter the thermistor is initially positioned in a distal arterial to measure the temperature of the blood and saline mixture (T_d). Recording is then commenced as the wire is withdrawn, and the temperature of the infused saline (T_i) taken as the thermistor enters the catheter. During these experiments it was noticed that the T_i measurements varied with small movements of the thermistor as it was withdrawn. This effect has been reported previously as point of discussion, but not quantified.[179] The temperature traces for three of the RayFlow recordings from the phantom experiment are shown in Figure A.2. The temperature measurements and derived flow measurements in this phantom experiment were carefully extracted from the minimum infusate temperature that could be recorded.

Catheter	Condition	P_a (mmHg)	P_d (mmHg)	Time (s)			Act. Flow (ml/s)	T_b °C	T_d °C	T_i °C	Infusion (ml/s)	Thermo. Flow (ml/s)
RayFlow	(1)	98	98	12.3	12.6	11.8	2.45	0.01	-1.00	-7.66	0.3	2.48
								0.04	-1.00	-8.34		2.71
								-0.01	-0.90	-8.23		2.96
	(2)	105	80	15.2	15.4	15.3	1.96	-0.04	-1.32	-7.55		1.86
								-0.24	-1.39	-9.45		2.23
								0.05	-1.16	-5.74		1.60
	(3)	105	92	23.7	24.4	24.7	1.24	-0.03	-1.73	-7.79		1.46
								0.00	-1.85	-7.62		1.34
								0.02	-1.72	-7.17		1.35
	(4)	102	102	14.7	14.6	14.8	2.04	0.00	-1.08	-7.45		2.24
								-0.07	-1.22	*		*
								0.07	-0.99	-7.78		2.55

Table A.1: Thermodilution measurements in the coronary flow phantom with the RayFlow thermodilution infusion catheter. Measurement indicated with (*) was missing in the recorded data. the four conditions simulated were: (1) no stenotic or myocardial resistance, (2) stenotic resistance only, (3) stenotic and myocardial resistance, and (4) myocardial resistance only.

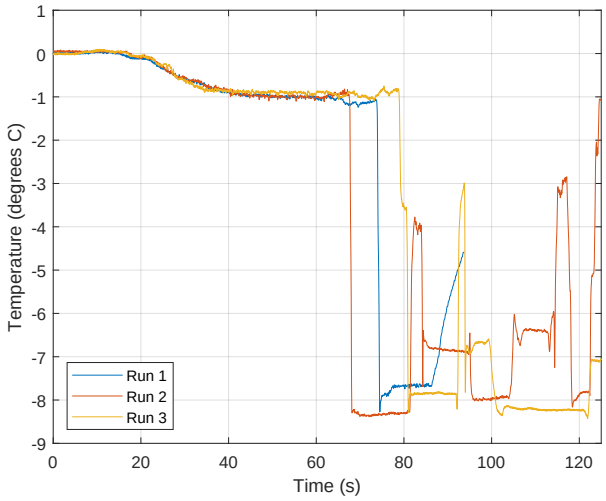

(a) Phantom measurements

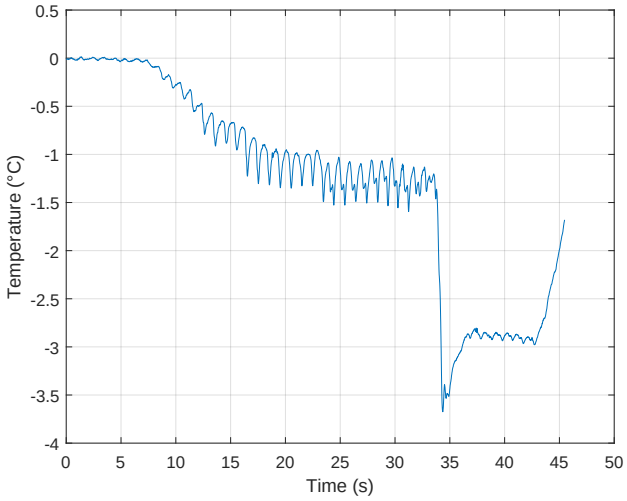

(b) Pullback from clinical case.

Figure A.2: Temperature plots during the pull-back from thermodilution measurements using the RayFlow catheter. a) is from the coronary flow phantom. Note how the reference (0–10 s) and distal temperatures (45–60 s) are in good agreement, but the measured temperature of the infusate is highly dependent on the location of the thermistor (65– s) which is being advanced and withdrawn by small amounts during this time. b) is from a clinical case from the study.

References

1. World Health Organization. Top 10 causes of death. `http://www.who.int/mediacentre/factsheets/fs310/en/`, 2014. [Online; accessed 11/11/2016].

2. Prachi Bhatnagar, Kremlin Wickramasinghe, Julianne Williams, Mike Rayner, and Nick Townsend. The epidemiology of cardiovascular disease in the UK 2014. *Heart*, 101(15):1182–1189, 2015.

3. Kate Smolina, F. Lucy Wright, Mike Rayner, and Michael J. Goldacre. Determinants of the decline in mortality from acute myocardial infarction in England between 2002 and 2010: Linked national database study. *BMJ*, 344:d8059, 2012.

4. Fabian Sanchis-Gomar, Carme Perez-Quilis, Roman Leischik, and Alejandro Lucia. Epidemiology of coronary heart disease and acute coronary syndrome. *Annals of Translational Medicine*, 4(13):256–256, 2016.

5. CW White, CB Wright, and DB Doty. Does visual interpretation of the coronary arteriogram predict the physiologic importance of a coronary stenosis? *New England Journal of Medicine*, 310:819–824, 1984.

6. Garrick Motley, Neal Dalrymple, Christine Keesling, Joseph Fischer, and William Harmon. Hounsfield unit density in the determination of urinary stone composition. *Urology*, 58(2):170–173, 2001.

7. Uwe Schneider, Eros Pedroni, and Antony Lomax. The calibration of CT Hounsfield units for radiotherapy treatment planning. *Physics in Medicine & Biology*, 41:111–124, 1996.

8. Blausen Medical Communications Inc. Coronary circulation. `https://commons.`

wikimedia.org/wiki/File:Blausen_0260_CoronaryVessels_Anterior.png, 2017. [Online; accessed 11/02/2020].

9. Henry Gewirtz. Regulating myocardial blood flow in health and disease. *Current Cardiology Reports*, 11(2):117–124, 2009.

10. Lillybeth Feliciano and Robert J. Henning. Coronary artery blood flow: Physiologic and pathophysiologic regulation. *Clinical Cardiology*, 22(12):775–786, 1999.

11. Nico Westerhof, Christa Boer, Regis R. Lamberts, and Pieter Sipkema. Cross-Talk Between Cardiac Muscle and Coronary Vasculature. *Physiological Reviews*, 86(4):1263–1308, 2006.

12. PG Camici and F Crea. Coronary microvascular dysfunction. *New England Journal of Medicine*, 356:830–840, 2007.

13. Paolo G. Camici, Giulia D'Amati, and Ornella Rimoldi. Coronary microvascular dysfunction: Mechanisms and functional assessment. *Nature Reviews Cardiology*, 12(1):48–62, 2015.

14. Ever D Grech. ABC of interventional cardiology: percutaneous coronary intervention. I: history and development. *BMJ*, 326(7398):1080–2, 2003.

15. Adam Timmis. Acute coronary syndromes. *BMJ*, 351, 2015.

16. Andrew G. Davies, Arnold R. Cowen, Stephen M. Kengyelics, Janet Moore, and Mohan U. Sivananthan. Do flat detector cardiac X-ray systems convey advantages over image-intensifier-based systems? Study comparing X-ray dose and image quality. *European Radiology*, 2007.

17. Egas Moniz. Cerebal angiography: its application in clinical practice and physiology. *The Lancet*, 222(5751):1144–1147, 1933.

18. H.W. Heiss. Profiles in Cardiology Werner Forssmann : A German Problem with the Nobel Prize. *Clinical Cardiology*, 15:547–549, 1992.

19. Thomas J. Ryan. The Coronary Angiogram and Its Seminal Contributions to Cardiovascular Medicine Over Five Decades. *Circulation*, 106:752–756, 2002.

20. William L. Proudfit, Earl K. Shirey, and F. Mason Sones. Selective Cine Coronary Arteriography. *Circulation*, 33(6):901–910, 1966.

21. Sven Ivar Seldinger. Catheter replacement of the needle in percutaneous arteriography: A new technique. *Acta Radiologica*, 39(5):368–376, 1953.

22. P Green, P Frobisher, and S Ramcharitar. Optimal angiographic views for invasive coronary angiography: a guide for trainees. *British Journal of Cardiology*, 23:110–3, 2016.

23. Charles T. Dotter and Melvin P. Judkins. Transluminal Treatment of Arteriosclerotic Obstruction. *Circulation*, 30(5):654–670, 1964.

24. Andreas Gruntzig and David A. Kumpe. Technique of percutaneous transluminal angioplasty with the Gruntzig balloon catheter. *American Journal of Roentgenology*, 132:547–552, 1979.

25. J.C. Palmaz, R.R. Sibbitt, S.R. Reuter, F.O. Tio, and W.J. Rice. Expandable intraluminal graft: a preliminary study. Work in progress. *Radiology*, 156(1):73–77, 1985.

26. Patrick W Serruys, Michael J B Kutryk, and Andrew T L Ong. Coronary-Artery Stents. *New England Journal of Medicine*, 354:483–495, 2006.

27. Alexandre Schaan De Quadros, Rogério Sarmento-Leite, Carlos A M Gottschall, Guilherme V. Silva, and Emerson C. Perin. Hyperexpansion of coronary stents and clinical outcomes. *Texas Heart Institute Journal*, 33(4):437–444, 2006.

28. Y. Friedlander, J. D. Kark, and Y. Stein. Family history of myocardial infarction as an independent risk factor for coronary heart disease. *British Heart Journal*, 53(4):382–387, 1985.

29. Pekka Jousilahti, Erkki Vartiainen, Jaakko Tuomilehto, and Pekka Puska. Sex, Age, Cardiovascular Risk Factors, and Coronary Heart Disease. *Circulation*, 99(9):1165–1172, 1999.

30. Umesh N. Khot, Monica B. Khot, Christopher T. Bajzer, Shelly K. Sapp, E. Magnus Ohman, Sorin J. Brener, Stephen G. Ellis, A. Michael Lincoff, and Eric J. Topol. Preva-

lence of Conventional Risk Factors in Patients with Coronary Heart Disease. *Journal of the American Medical Association*, 290(7):898–904, 2003.

31. NICE. Chest pain of recent onset: assessment and diagnosis. Technical Report March, National Institute for Health and Care Excellence, 2010.

32. Sigmund Silber, Per Albertsson, Francisco F Avilés, Paolo G Camici, Antonio Colombo, Christian Hamm, Erik Jørgensen, Jean Marco, Jan-Erik Nordrehaug, Witold Ruzyllo, Philip Urban, Gregg W Stone, and William Wijns. Guidelines for percutaneous coronary interventions. The Task Force for Percutaneous Coronary Interventions of the European Society of Cardiology. *European Heart Journal*, 26(8):804–47, apr 2005.

33. NICE. Clinical Guideline [CG126], Stable angina: management. Technical report, National Institute for Health and Care Excellence, 2016.

34. NICE. Clinical guidance [CG94] Unstable angina and NSTEMI: early management. Technical report, National Institute for Health and Care Excellence, 2013.

35. NICE. My Myocardial infarction with ST ocardial infarction with ST-segment -segment ele elevation: acute management vation: acute management Clinical guideline. Technical Report July, National Institute for Health and Care Excellence, 2013.

36. Peter F. Ludman. BSIS Audit Returns Adult Interventional Procedures. Technical report, British Cardiovascular Intervention Society, 2016.

37. Jens F. Lassen, Hans E. Bøtker, and Christian J. Terkelsen. Timely and optimal treatment of patients with STEMI. *Nature Reviews Cardiology*, 10(1):41–48, 2013.

38. Seema Pursnani, Frederick Korley, Ravindra Gopaul, Pushkar Kanade, Newry Chandra, Richard E. Shaw, and Sripal Bangalore. Percutaneous coronary intervention versus optimal medical therapy in stable coronary artery disease: A systematic review and meta-analysis of randomized clinical trials. *Circulation: Cardiovascular Interventions*, 5(4):476–490, 2012.

39. Jacopo Lenzi, Vera Maria Avaldi, Paola Rucci, Giulia Pieri, and Maria Pia Fantini. Burden of multimorbidity in relation to age, gender and immigrant status: A cross-sectional study based on administrative data. *BMJ Open*, 6(12):1–10, 2016.

40. Andrew Kingston, Louise Robinson, Heather Booth, Martin Knapp, Carol Jagger, Bayo Adelaja, Mauricio Avendano, Sally Marie Bamford, Sube Banerjee, Sharne Berwald, Ann Bowling, Clare Burgon, Elizabeth Bustard, Adelina Comas-Herrera, Margaret Dangoor, Josie Dixon, Nicolas Farina, Sally Greengross, Emily Grundy, Bo Hu, Derek King, Daniel Lombard, Klara Lorenz, David McDaid, A. La Park, Jitka Pikhartova, Amritpal Rehill, and Raphael Wittenberg. Projections of multi-morbidity in the older population in England to 2035: Estimates from the Population Ageing and Care Simulation (PACSim) model. *Age and Ageing*, 47(3):374–380, 2018.

41. Anthony H. Gershlick, Jamal Nasir Khan, Damian J. Kelly, John P. Greenwood, Thiagarajah Sasikaran, Nick Curzen, Daniel J. Blackman, Miles Dalby, Kathryn L. Fairbrother, Winston Banya, Duolao Wang, Marcus Flather, Simon L. Hetherington, Andrew D. Kelion, Suneel Talwar, Mark Gunning, Roger Hall, Howard Swanton, and Gerry P. McCann. Randomized trial of complete versus lesion-only revascularization in patients undergoing primary percutaneous coronary intervention for stemi and multivessel disease: The CvLPRIT trial. *Journal of the American College of Cardiology*, 65(10):963–972, 2015.

42. Hrvoje Lusic and Mark W. Grinstaff. X-ray-computed tomography contrast agents. *Chemical Reviews*, 113(3):1641–1666, 2013.

43. Lloyd W. Klein, Mark W. Sheldon, Jeffrey Brinker, Timothy A. Mixon, Kimberly Skelding, Adam O. Strunk, Carl L. Tommaso, Bonnie Weiner, Steven R. Bailey, Barry Uretsky, Morton Kern, and Warren Laskey. The use of radiographic contrast media during PCI: A focused review - A position statement of the society of cardiovascular angiography and interventions. *Catheterization and Cardiovascular Interventions*, 74(5):728–746, 2009.

44. Peter W. Rand, Eleanor Lacombe, Hamilton E. Hunt, and William H. Austin. Viscosity of normal human blood. *Journal of Applied Physiology*, 19(1):117–122, 1963.

45. Omnipaque (iohexol) perscribing information. Technical report, GE Healthcare, 2017.

46. Visipaque full perscribing information. Technical report, GE Healthcare, 2017.

47. International Commission on Radiation Units and Measurement. Report 44: Tissue Substitutes in Radiation Dosimetry and Measurement. Technical report, 1988.

48. D Sutton and K Cranley. IPEM Report 78: Catalogue of Diagnostic X-ray Spectra and Other Data, 1997.

49. Amber J. Gislason-Lee, Claire Keeble, Daniel Egleston, Josephine Bexon, Stephen M. Kengyelics, and Andrew G. Davies. Comprehensive assessment of patient image quality and radiation dose in latest generation cardiac x-ray equipment for percutaneous coronary interventions. *Journal of Medical Imaging*, 4(2), 2017.

50. AJ Wagner, GT Barnes, and X Wu. Assessing fluoroscopic contrast resolution: a practical and quantitative test tool. *Medical Physics*, 18(5):894–899, 1991.

51. Amber J Gislason-Lee, Bart Hoornaert, Arnold R. Cowen, and Andrew G. Davies. Understanding automated dose control in dynamic X-ray imaging systems. `http://dx.doi.org/10.1594/ecr2013/C-2183`, 2013.

52. Phillip Rauch, Pei-Jan Paul Lin, Stephen Balter, Atsushi Fukuda, Allen Goode, Gary Hartwell, Terry LaFrance, Edward Nickoloff, Jeff Shepard, and Keith Strauss. Functionality and operation of fluoroscopic automatic brightness control/automatic dose rate control logic in modern cardiovascular and interventional angiography systems. *Medical Physics*, 39(5):2826–8, 2012.

53. Amber J Gislason-Lee, Catherine McMillan, Arnold R Cowen, and Andrew G Davies. Dose optimization in cardiac x-ray imaging. *Medical Physics*, 40(9):091911, 2013.

54. Amber J. Gislason, Andrew G. Davies, and Arnold R. Cowen. Dose optimization in pediatric cardiac x-ray imaging. *Medical Physics*, 37(10):5258–5269, 2010.

55. Markku J Tapiovaara, Michael Sandborg, and David R Dance. A search for improved technique factors in paediatric fluoroscopy A search for improved technique factors in paediatric fluoroscopy. *Physics in Medicine and Biology*, 44:537–559, 1999.

56. R. F. Bury, A. R. Cowen, A. G. Davies, E. L. Baker, P. Hawkridge, A. J.C. Bruijns, and H. Reitsma. Technical report: Initial experiences with an experimental solid-state universal digital X-ray image detector. *Clinical Radiology*, 53(12):923–928, 1998.

57. A. R. Cowen, A. G. Davies, and M. U. Sivananthan. The design and imaging charac-

teristics of dynamic, solid-state, flat-panel x-ray image detectors for digital fluoroscopy and fluorography. *Clinical Radiology*, 63(10):1073–1085, 2008.

58. Andrew G. Davies, Arnold R. Cowen, Stephen M. Kengyelics, Robert F. Bury, and Tom J. Bruijns. Threshold contrast detail detectability measurement of the fluoroscopic image quality of a dynamic solid-state digital x-ray image detector. *Medical Physics*, 28(1):11, 2001.

59. A. R. Cowen, A. G. Davies, and M. U. Sivananthan. The design and imaging characteristics of dynamic, solid-state, flat-panel x-ray image detectors for digital fluoroscopy and fluorography. *Clinical Radiology*, 63(10):1073–1085, 2008.

60. C. Schmidgunst, D. Ritter, and E. Lang. Calibration model of a dual gain flat panel detector for 2D and 3D x-ray imaging. *Medical Physics*, 34(9):3649–3664, 2007.

61. Alexander L.C. Kwan, J. Anthony Seibert, and John M. Boone. An improved method for flat-field correction of flat panel x-ray detector. *Medical Physics*, 33(2):391–393, 2006.

62. Dong Sik Kim, Eun Kim, and Sanggyun Lee. Performance analysis of the gain correction in radiography imaging. In *2014 IEEE International Conference on Image Processing, ICIP 2014*, pages 3641–3645. IEEE, 2014.

63. Hans-Aloys Wischmann, Hans A Luijendijk, Henk J Meulenbrugge, Michael Overdick, Ralf Schmidt, and Kourosh Kiani. Correction of amplifier nonlinearity, offset, gain, temporal artifacts, and defects for flat-panel digital imaging devices. In *Proceedings Volume 4682, Medical Imaging 2002: Physics of Medical Imaging*, volume 4682, pages 4611–4682, 2002.

64. Anuja Joshi, Amber J Gislason-Lee, Claire Keeble, Uduvil M Sivananthan, and Andrew G Davies. Can image enhancement allow radiation dose to be reduced whilst maintaining the perceived diagnostic image quality required for coronary angiography ? *The British Journal of Radiology*, 90(1971):20160660, 2017.

65. L. M. Zir, S. W. Miller, R. E. Dinsmore, J. P. Gilbert, and J. W. Harthorne. Interobserver variability in coronary angiography. *Circulation*, 53(4):627–632, apr 1976.

66. Glenn J. Beauman and Robert A Vogel. Accuracy of individual and panel visual interpretations of coronary artriograms: implications for clinical decisions. *Journal of the American College of Cardiology*, 16(1):108–113, 1990.

67. Pim AL Tonino, Bernard De Bruyne, Nico H.J Pijls, Uwe Siebert, Fumiaki Ikeno, Marcel van't Veer, Volker Klauss, Ganesh Manoharan, Thomas Engstrom, Keith Oldroyd, Peter N Ver Lee, Philip A MacCarthy, and William F Fearon. Fractional flow reserve versus angiography for guiding percutaneous coronary intervention. *New England Journal of Medicine*, 360:213–224, 2009.

68. Ramón López-Palop, Pilar Carrillo, Araceli Frutos, Jesús Castillo, Alberto Cordero, Marlon Toro, and Vicente Bertomeu-Martínez. Usefulness of the Fractional Flow Reserve Derived by Intracoronary Pressure Wire for Evaluating Angiographically Intermediate Lesions in Acute Coronary Syndrome. *Revista Española de Cardiología (English Edition)*, 63(6):686–694, 2010.

69. A.W.J. van 't Hof, A. Liem, H. Suryapranata, J. C.a. Hoorntje, M.-J. de Boer, and F. Zijlstra. Angiographic Assessment of Myocardial Reperfusion in Patients Treated With Primary Angioplasty for Acute Myocardial Infarction : Myocardial Blush Grade. *Circulation*, 97(23):2302–2306, jun 1998.

70. C Michael Gibson and Albert Schömig. Coronary and myocardial angiography: angiographic assessment of both epicardial and myocardial perfusion. *Circulation*, 109(25):3096–105, jun 2004.

71. Tamás Ungi, Zsolt Zimmermann, Erika Balázs, András Lassó, Imre Ungi, Tamás Forster, András Palkó, and Attila Nemes. Vessel masking improves densitometric myocardial perfusion assessment. *The International Journal of Cardiovascular Imaging*, 25(3):229–36, mar 2009.

72. Gregg W. Stone, Michael A. Peterson, Alexandra J. Lansky, George Dangas, Roxana Mehran, and Martin B. Leon. Impact of normalized myocardial perfusion after successful angioplasty in acute myocardial infarction. *Journal of the American College of Cardiology*, 39(4):591–597, 2002.

73. Giuseppe Tarantini, Angelo Ramondo, Massimo Napodano, Claudio Bilato, Gianbattista Isabella, Renato Razzolini, and Sabino Iliceto. Myocardial perfusion grade and survival after percutaneous transluminal coronary angioplasty in patients with cardiogenic shock. *American Journal of Cardiology*, 93(9):1081–1085, 2004.

74. Shereif H. Rezkalla and Robert A. Kloner. Coronary no-reflow phenomenon: From the experimental laboratory to the cardiac catheterization laboratory. *Catheterization and Cardiovascular Interventions*, 72(7):950–957, 2008.

75. C Michael Gibson, Christopher P Cannon, William L Daley, J Theodore Dodge, Barbara Alexander, Susan J Marble, Carolyn H McCabe, Lori Raymond, Terry Fortin, W Kenneth Poole, and Eugene Braunwald. TIMI Frame Count: A Quantitative Method of Assessing Coronary Artery Flow. *Circulation*, 93(5):879–888, 1996.

76. C. M. Gibson, S. a. Murphy, M. J. Rizzo, K. a. Ryan, S. J. Marble, C. H. McCabe, C. P. Cannon, F. Van de Werf, and E. Braunwald. Relationship between TIMI frame count and clinical outcomes after thrombolytic administration. Thrombolysis In Myocardial Infarction (TIMI) Study Group. *Circulation*, 99(15):1945–1950, 1999.

77. Athanassios Manginas, Plamen Gatzov, Christos Chasikidis, Vasilis Voudris, Gregory Pavlides, and Dennis V. Cokkinos. Estimation of coronary flow reserve using the Thrombolysis In Myocardial Infarction (TIMI) frame count method. *American Journal of Cardiology*, 83(11):1562–1564, 1999.

78. Cem Barcin, Ali E. Denktas, Kirk N. Garratt, Stuart T. Higano, David R. Holmes, and Amir Lerman. Relation of Thrombolysis In Myocardial Infarction (TIMI) frame count to coronary flow parameters. *American Journal of Cardiology*, 91(4):466–469, 2003.

79. John K. French, Thomas A. Hyde, Ivan T. Straznicky, Jacqueline Andrews, Mayanna Lund, David J. Amos, Andrew Zambanini, Christopher J. Ellis, Bruce J. Webber, Stephanie C. McLaughlin, Ralph M.L. Whitlock, Samuel O.M. Manda, Hitesh Patel, and Harvey D. White. Relationship between corrected TIMI frame counts at three weeks and late survival after myocardial infarction. *Journal of the American College of Cardiology*, 35(6):1516–1524, 2000.

80. J.K. French, I.T. Straznicky, B.J. Webber, P.E. Aylward, M.J. Frey, A.A.J. Adgey, B.F. Williams, and S.C. McLaughlin. Angiographic frame counts 90 minutes after streptokinase predict left ventricular function at 48 hours following myocardial infarction. *Heart*, 81(2):128–133, 1999.

81. David J. Amos, John K. French, Jacqueline Andrews, Noel G. Ashton, Barbara F. Williams, Ralph M.L. Whitlock, Samuel O.M. Manda, and Harvey D. White. Corrected TIMI frame counts correlate with stenosis severity and infarct zone wall motion after thrombolytic therapy. *American Heart Journal*, 141(4):586–591, 2001.

82. Erkan Yildirim, Uygar Cagdas Yuksel, Murat Celik, Baris Bugan, Mutlu Gungor, Yalcin Gokoglan, Mustafa Koklu, Suat Gormel, Salim Yasar, and Cem Barcin. Evaluation of the coronary flow by the coronary clearance time in patients with cardiac syndrome X. *Journal of International Medical Research*, 46(3):1121–1129, 2018.

83. Michael C. Gibson, Kathryn A. Ryan, Sabina A. Murphy, Rebecca Mesley, Susan J. Marble, Robert P. Giugliano, Christopher P. Cannon, Elliott M. Antman, and Eugene Braunwald. Impaired coronary blood flow in nonculprit arteries in the setting of acute myocardial infarction. *Journal of the American College of Cardiology*, 34(4):974–982, 1999.

84. C. Michael Gibson, Mukesh Goel, Sabina A. Murphy, Imran Dotani, Susan J. Marble, Lawrance I. Deckelbaum, J. Theodore Dodge, and Spencer B. King III. Global impairment of coronary blood flow in the setting of acute coronary syndromes (a RESTORE substudy). *American Journal of Cardiology*, 86(12):1375–1377, 2000.

85. K. Lance Gould, Kirk Lipscomb, and Glen W. Hamilton. Physiologic basis for assessing critical coronary stenosis: Instantaneous flow response and regional distribution during coronary hyperemia as measures of coronary flow reserve. *The American journal of cardiology*, 33(1):87–94, 1974.

86. K Lance Gould and Kirk Lipscomb. Effects of Coronary Stenoses on Coronary Flow Reserve and Resistance. *Americal Journal of Cardiology*, 34(July):48–55, 1974.

87. Julien I. E. Hoffman. Maximal coronary flow and the concept of vascular reserve. *Circulation*, 70:153–159, 1984.

88. Martijn Meuwissen, Maria Siebes, Steven A J Chamuleau, Jan G P Tijssen, Jos A E Spaan, and Jan J Piek. Intracoronary pressure and flow velocity for hemodynamic evaluation of coronary stenoses. *Expert Review of Cardiovascular Therapy*, 1(3):471–479, 2003.

89. Patrick W Serruys, Carlo di Mario, Jan Piek, Erwin Schroeder, Christian Vrints, Peter Probst, Bernard de Bruyne, Claude Hanet, Eckart Fleck, Michael Haude, Edoardo Verna, Vasilis Voudris, Herbert Geschwind, Håkan Emanuelsson, V Mühlberger, Giambattista Danzi, Hans O Peels, Andrew J Ford, and Eric Boersma. Prognostic Value of Intracoronary Flow Velocity and Diameter Stenosis in Assessing the Short- and Long-term Outcomes of Coronary Balloon Angioplasty. *Circulation*, 96(10):3369–3377, 1997.

90. Ross J. McGeoch and Keith G. Oldroyd. Pharmacological options for inducing maximal hyperaemia during studies of coronary physiology. *Catheterization and Cardiovascular Interventions*, 71(2):198–204, 2008.

91. Carlo Di Mario, Robert Gil, and Patrick W. Serruys. Long-Term Reproducibility of Coronary Flow Velocity in Patients With Coronary Artery Disease. *The American Journal of Cardiology*, 75:1177–1180, 1995.

92. Martin K.C. Ng, Alan C. Yeung, and William F. Fearon. Invasive assessment of the coronary microcirculation: Superior reproducibility and less hemodynamic dependence of index of microcirculatory resistance compared with coronary flow reserve. *Circulation*, 113(17):2054–2061, 2006.

93. Gerd Heusch. Editorial: Adenosine and maximum coronary vasodilation in humans: Myth and misconceptions in the assessment of coronary reserve. *Basic Research in Cardiology*, 105(1):1–5, 2010.

94. Jennifer A. Tremmel, Yuhei Kobayashi, Peter J. Fitzgerald, Marcia Stefanick, Vedant Pargaonkar, William F. Fearon, Yasuhiro Honda, Alan C. Yeung, Shigemitsu Tanaka, and David P. Lee. Effect of Sex Differences on Invasive Measures of Coronary Microvascular Dysfunction in Patients With Angina in the Absence of Obstructive Coronary Artery Disease. *JACC: Cardiovascular Interventions*, 8(11):1433–1441, 2015.

95. J I Hoffman. Problems of coronary flow reserve. *Annals of Biomedical Bngineering*, 28(8):884–96, aug 2000.

96. Panithaya Chareonthaitawee, Philipp A. Kaufmann, Ornella Rimoldi, and Paolo G. Camici. Heterogeneity of resting and hyperemic myocardial blood flow in healthy humans. *Cardiovascular Research*, 50(1):151–161, 2001.

97. Philipp A Kaufmann and Paolo G Camici. Myocardial Blood Flow Measurement by PET : Technical Aspects and Clinical Applications. *Journal of Nuclear Medicine*, 46:75–89, 2005.

98. Michael J Lim and Morton J Kern. Coronary pathophysiology in the cardiac catheterization laboratory. *Current Problems in Cardiology*, 31(8):493–550, aug 2006.

99. Martijn Meuwissen and S.A.J. Chamuleau. Role of variability in microvascular resistance on fractional flow reserve and coronary blood flow velocity reserve in intermediate coronary lesions. *Circulation*, 103(2):184–187, 2001.

100. Nils P. Johnson, K. Lance Gould, Marcelo F. Di Carli, and Viviany R. Taqueti. Invasive FFR and Noninvasive CFR in the Evaluation of Ischemia: What is the future? *Journal of the American College of Cardiology*, 67(23):2772–2788, 2016.

101. P. L. Van Herck, C. J. Vrints, and S. G. Carlier. Coronary circulation and interventional cardiology. *Annals of Biomedical Engineering*, 33(12 SPEC. ISS.):1735–1742, 2005.

102. John E.A. Blair and Mark J. Ricciardi. Assessment of Coronary Blood Flow in the Cardiac Catheterization Laboratory. *Current Problems in Cardiology*, 39(6):159–184, 2014.

103. Morton J. Kern and Habib Samady. Current Concepts of Integrated Coronary Physiology in the Catheterization Laboratory. *Journal of the American College of Cardiology*, 55(3):173–185, 2010.

104. David V. Daniels and William F. Fearon. Fractional Flow Reserve: A Practical Update. *Current Cardiovascular Imaging Reports*, 3(4):215–221, 2010.

105. Allen Jeremias, Robert J. Whitbourn, Steven D. Filardo, Peter J. Fitzgerald, David J. Cohen, E. Murat Tuzcu, William D. Anderson, Alexandrew A. Abizaid, Gary S. Mintz,

Alan C. Yeung, Morton J. Kern, and Paul G. Yock. Intracoronary versus intravenous adenosine-induced maximal coronary hyperemia for fractional flow reserve measurements. *Americal Heart Journal*, 140:651–657, 2000.

106. Vincent Spagnoli, Nicolas Amabile, Jean Guillaume Dillinger, Aurélie Veugeois, Damien Logeart, Patrick Henry, Christophe Caussin, and Michel S. Slama. Myocardial Fractional Flow Reserve Measurement Using Contrast Media as a First-Line Assessment of Coronary Lesions in Current Practice. *Canadian Journal of Cardiology*, 32(6):739–746, 2016.

107. N H Pijls, B De Bruyne, K Peels, P H Van Der Voort, H J Bonnier, J J Bartunek J Koolen, and J J Koolen. Measurement of fractional flow reserve to assess the functional severity of coronary-artery stenoses. *The New England Journal of Medicine*, 334(26):1703–1708, 1996.

108. G. Jan Willem Bech, Bernard De Bruyne, Nico H.J. Pijls, Ebo D. De Muinck, Jan C.A. Hoorntje, Javier Escaned, Pieter R. Stella, Eric Boersma, Jozef Bartunek, Jacques J. Koolen, and William Wijns. Fractional flow reserve to determine the appropriateness of angioplasty in moderate coronary stenosis: A randomized trial. *Circulation*, 103(24):2928–2934, 2001.

109. Nico H J Pijls, Pepijn van Schaardenburgh, Ganesh Manoharan, Eric Boersma, Jan-Willem Bech, Marcel van't Veer, Frits Bär, Jan Hoorntje, Jacques Koolen, William Wijns, and Bernard de Bruyne. Percutaneous coronary intervention of functionally nonsignificant stenosis: 5-year follow-up of the DEFER Study. *Journal of the American College of Cardiology*, 49(21):2105–11, 2007.

110. Frederik M. Zimmermann, Angela Ferrara, Nils P. Johnson, Lokien X. Van Nunen, Javier Escaned, Per Albertsson, Raimund Erbel, Victor Legrand, Hyeong Cheol Gwon, Wouter S. Remkes, Pieter R. Stella, Pepijn Van Schaardenburgh, G. Jan Willem Bech, Bernard De Bruyne, and Nico H.J. Pijls. Deferral vs. performance of percutaneous coronary intervention of functionally non-significant coronary stenosis: 15-year follow-up of the DEFER trial. *European Heart Journal*, 36(45):3182–3188, 2015.

111. William F. Fearon, Pim A.L. Tonino, Bernard De Bruyne, Uwe Siebert, and Nico H.J.

Pijls. Rationale and design of the fractional flow reserve versus angiography for multivessel evaluation (FAME) study. *American Heart Journal*, 154(4):632–636, 2007.

112. Jan Willem E M Sels, Pim A L Tonino, Uwe Siebert, William F. Fearon, Marcel Van'T Veer, Bernard De Bruyne, and Nico H J Pijls. Fractional flow reserve in unstable angina and non-ST-segment elevation myocardial infarction: Experience from the FAME (Fractional flow reserve versus angiography for multivessel evaluation) study. *JACC: Cardiovascular Interventions*, 4(11):1183–1189, 2011.

113. Bernard De Bruyne, Nico H J Pijls, Bindu Kalesan, Emanuele Barbato, Pim a L Tonino, Zsolt Piroth, Nikola Jagic, Sven Möbius-Winkler, Sven Mobius-Winckler, Gilles Rioufol, Nils Witt, Petr Kala, Philip MacCarthy, Thomas Engström, Keith G. Oldroyd, Kreton Mavromatis, Ganesh Manoharan, Peter Verlee, Ole Frobert, Nick Curzen, Jane B. Johnson, Peter Jüni, and William F. Fearon. Fractional flow reserve-guided PCI versus medical therapy in stable coronary disease. *The New England Journal of Medicine*, 367(11):991–1001, 2012.

114. B De Bruyne, W F Fearon, N H Pijls, E Barbato, P Tonino, Z Piroth, N Jagic, S Mobius-Winckler, G Rioufol, N Witt, P Kala, P MacCarthy, T Engstrom, K Oldroyd, K Mavromatis, G Manoharan, P Verlee, O Frobert, N Curzen, J B Johnson, A Limacher, E Nuesch, and P Juni. Fractional flow reserve-guided PCI for stable coronary artery disease. *New England Journal of Medicine*, 371(13):1208–1217, 2014.

115. Panagiotis Xaplanteris, Stephane Fournier, Nico H J Pijls, William F Fearon, Emanuele Barbato, Pim A L Tonino, Thomas Engstrøm, Stefan Kääb, Jan-Henk Dambrink, Gilles Rioufol, Gabor G Toth, Zsolt Piroth, Nils Witt, Ole Fröbert, Petr Kala, Axel Linke, Nicola Jagic, Martin Mates, Kreton Mavromatis, Habib Samady, Anand Irimpen, Keith Oldroyd, Gianluca Campo, Martina Rothenbühler, Peter Jüni, Bernard De Bruyne, and FAME 2 Investigators. Five-Year Outcomes with PCI Guided by Fractional Flow Reserve. *The New England Journal of Medicine*, 379(3):250–259, 2018.

116. Nils P. Johnson, Gábor G. Tóth, Dejian Lai, Hongjian Zhu, Göksel Açar, Pierfrancesco Agostoni, Yolande Appelman, Fatih Arslan, Emanuele Barbato, Shao Liang Chen, Luigi Di Serafino, Antonio J. Domínguez-Franco, Patrick Dupouy, Ali M. Esen, Özlem B. Esen,

Michalis Hamilos, Kohichiro Iwasaki, Lisette O. Jensen, Manuel F. Jiménez-Navarro, Demosthenes G. Katritsis, Sinan A. Kocaman, Bon Kwon Koo, Ramón López-Palop, Jeffrey D. Lorin, Louis H. Miller, Olivier Muller, Chang Wook Nam, Niels Oud, Etienne Puymirat, Johannes Rieber, Gilles Rioufol, Josep Rodés-Cabau, Steven P. Sedlis, Yasuchika Takeishi, Pim A.L. Tonino, Eric Van Belle, Edoardo Verna, Gerald S. Werner, William F. Fearon, Nico H.J. Pijls, Bernard De Bruyne, and K. Lance Gould. Prognostic value of fractional flow reserve: Linking physiologic severity to clinical outcomes. *Journal of the American College of Cardiology*, 64(16):1641–1654, 2014.

117. Johannes Rieber, Thomas M. Schiele, Petra Erdin, Hans Ulrich Stempfle, Andreas König, Isabelle Erhard, Tobias Segmiller, Monika Baylacher, Karl Theisen, Mathias C. Haufe, Uwe Siebert, and Volker Klauss. Fractional flow reserve predicts major adverse cardiac events after coronary stent implantation. *Zeitschrift fur Kardiologie*, 91(SUPPL. 3):132–136, 2002.

118. Shiv K. Agarwal, Srikanth Kasula, Yalcin Hacioglu, Zubair Ahmed, Barry F. Uretsky, and Abdul Hakeem. Utilizing Post-Intervention Fractional Flow Reserve to Optimize Acute Results and the Relationship to Long-Term Outcomes. *JACC: Cardiovascular Interventions*, 9(10):1022–1031, 2016.

119. Thomas Engstrøm, Henning Kelbæk, Steffen Helqvist, Dan Eik Høfsten, Lene Kløvgaard, Lene Holmvang, Erik Jørgensen, Frants Pedersen, Kari Saunamäki, Peter Clemmensen, Ole De Backer, Jan Ravkilde, Hans Henrik Tilsted, Anton Boel Villadsen, Jens Aarøe, Svend Eggert Jensen, Bent Raungaard, and Lars Køber. Complete revascularisation versus treatment of the culprit lesion only in patients with ST-segment elevation myocardial infarction and multivessel disease (DANAMI-3 - PRIMULTI): An open-label, randomised controlled trial. *The Lancet*, 386(9994):665–671, 2015.

120. Jamie Layland, Keith G. Oldroyd, Nick Curzen, Arvind Sood, Kanarath Balachandran, Raj Das, Shahid Junejo, Nadeem Ahmed, Matthew M.Y. Lee, Aadil Shaukat, Anna O'Donnell, Julian Nam, Andrew Briggs, Robert Henderson, Alex McConnachie, and Colin Berry. Fractional flow reserve vs. Angiography in guiding management to optimize outcomes in non-ST-segment elevation myocardial infarction: The British Heart

Foundation FAMOUS-NSTEMI randomized trial. *European Heart Journal*, 36(2):100–111, 2015.

121. Nico H J Pijls. Fractional flow reserve after previous myocardial infarction. *European Heart Journal*, 28(19):2301–2302, 2007.

122. Bernard de Bruyne, Nico H.J. Pijls, Jozef Bartunek, Kemal Kulecki, Jan-willem Bech, Hugo De Winter, Paul Van Crombrugge, Guy R. Heyndrickx, and William Wijns. Fractional Flow Reserve in Patients With Prior Myocardial Infarction. *Circulation*, 104:157–162, 2001.

123. K. M. Marques, P. Knaapen, R. Boellaard, A. A. Lammertsma, N. Westerhof, and F. C. Visser. Microvascular Function in Viable Myocardium After Chronic Infarction Does Not Influence Fractional Flow Reserve Measurements. *Journal of Nuclear Medicine*, 48(12):1987–1992, 2007.

124. Steven A. J. Chamuleau, Maria Siebes, Martijn Meuwissen, Karel T. Koch, Jos A. E. Spaan, and Jan J. Piek. Association between coronary lesion severity and distal microvascular resistance in patients with coronary artery disease. *American Journal of Physiology - Heart and Circulatory Physiology*, 285(5):H2194–H2200, 2003.

125. Bart J. Verhoeff, Maria Siebes, Martijn Meuwissen, Bektaş Atasever, Michiel Voskuil, Robbert J. De Winter, Karel T. Koch, J. G P Tijssen, J. A E Spaan, and Jan J. Piek. Influence of percutaneous coronary intervention on coronary microvascular resistance index. *Circulation*, 111(1):76–82, 2005.

126. Tim P van de Hoef, Froukje Nolte, M Cristina Rolandi, Jan J Piek, Jeroen P H M van den Wijngaard, Jos a E Spaan, and Maria Siebes. Coronary pressure-flow relations as basis for the understanding of coronary physiology. *Journal of Molecular and Cellular Cardiology*, 52(4):786–93, 2012.

127. Maria Siebes, Steven A J Chamuleau, Martijn Meuwissen, Jan J Piek, and Jos A. E. Spaan. Influence of hemodynamic conditions on fractional flow reserve: parametric analysis of underlying model. *American Journal of Physiology - Heart and Circulatory Physiology*, 283(4):H1462–H1470, 2002.

128. D. F. Young. Fluid Mechanics of Arterial Stenoses. *Journal of Biomechanical Engineering*, 101:157–175, 1979.

129. R. E. Mates, R. L. Gupta, A. C. Bell, and F. J. Klocke. Fluid dynamics of coronary artery stenosis. *Circulation Research*, 42(1):152–162, 1978.

130. Florence Verdier-Watts, Gilles Rioufol, Nathan Mewton, Ingrid Sanchez, Lisa Green, Eric Bonnefoy-Cudraz, and Gerard Finet. Influence of arterial hypotension on fractional flow reserve measurements. *EuroIntervention*, 11(4):416–420, 2015.

131. Bernard De Bruyne, Jozef Bartunek, Stanislas U. Sys, Nico H.J. Pijls, Guy R. Heyndrickx, and William Wijns. Simultaneous coronary pressure and flow velocity measurements in humans: Feasibility, reproducibility, and hemodynamic dependence of coronary flow velocity reserve, hyperemic flow versus pressure slope index, and fractional flow reserve. *Circulation*, 94(8):1842–1849, 1996.

132. Asife Sahinarslan, Sinan Altan Kocaman, Hilal Olgun, Tolga Kunak, Emrullah Kiziltunç, Murat Ozdemir, and Timur Timurkaynak. The reliability of fractional flow reserve measurement in patients with diabetes mellitus. *Coronary Artery Disease*, 2009.

133. Annapoorna S. Kini, Michael C. Kim, Pedro R. Moreno, Prakash Krishnan, Oana C. Ivan, and Samin K. Sharma. Comparison of Coronary Flow Reserve and Fractional Flow Reserve in Patients With Versus Without Diabetes Mellitus and Having Elective Percutaneous Coronary Intervention and Abciximab Therapy (from the PREDICT Trial). *American Journal of Cardiology*, 101(6):796–800, 2008.

134. Michael S Lee and Cheng-Han Chen. Myocardial Bridging: An Up-to-Date Review. *The Journal of Invasive Cardiology*, 27(11):521–8, 2015.

135. Javier Escaned, Jorge Cortés, Alex Flores, Javier Goicolea, Fernando Alfonso, Rosana Hernández, Antonio Fernández-Ortiz, Manel Sabaté, Camino Bañuelos, and Carlos Macaya. Importance of diastolic fractional flow reserve and dobutamine challenge in physiologic assessment of myocardial bridging. *Journal of the American College of Cardiology*, 42(2):226–33, 2003.

136. Kyungil Park, Tae Jin Youn, Kyung Woo Park, Sang Hoon Na, Hae Young Lee, Hyun Jae Kang, Woo Young Chung, Bon Kwon Koo, In Ho Chae, Dong Ju Choi, Hyo Soo Kim, Byung Hee Oh, and Young Bae Park. Physiologic Evaluation of Myocardial Bridging: A New Analysis for an Old Disease. *Canadian Journal of Cardiology*, 27(5):596–600, 2011.

137. Morton J. Kern, Amir Lerman, Jan Willen Bech, Bernard De Bruyne, Eric Eeckhout, William F. Fearon, Stuart T. Higano, Michael J. Lim, Martijn Meuwissen, Jan J. Piek, Nico H.J. Pijls, Maria Siebes, and Jos A.E. Spaan. Physiological assessment of coronary artery disease in the cardiac catheterization laboratory: A scientific statement from the American Heart Association Committee on diagnostic and interventional cardiac catheterization, council on clinical cardiology. *Circulation*, 114(12):1321–1341, 2006.

138. Nico H.J. Pijls. Guidance of complex PCI by coronary pressure measurement. *Heart*, 90(9):1085–1093, 2004.

139. Colin Berry, David Corcoran, Barry Hennigan, Stuart Watkins, Jamie Layland, and Keith G. Oldroyd. Fractional flow reserve-guided management in stable coronary disease and acute myocardial infarction: Recent developments. *European Heart Journal*, 36(45):3155–3164c, 2015.

140. Matthias Götberg, Christopher M. Cook, Sayan Sen, Sukhjinder Nijjer, Javier Escaned, and Justin E. Davies. The Evolving Future of Instantaneous Wave-Free Ratio and Fractional Flow Reserve. *Journal of the American College of Cardiology*, 70(11):1379–1402, 2017.

141. Jun Yamashita, Nobuhiro Tanaka, Naohisa Shindo, Masashi Ogawa, Yo Kimura, Kunihiro Sakoda, Naotaka Murata, Yohei Hokama, Kou Hoshino, Sayo Ikeda, and Akira Yamashina. Seven-year clinical outcomes of patients with moderate coronary artery stenosis after deferral of revascularization based on gray-zone fractional flow reserve. *Cardiovascular Intervention and Therapeutics*, 30(3):209–215, 2015.

142. Do Yoon Kang, Jung Min Ahn, Cheol Hyun Lee, Pil Hyung Lee, Duk Woo Park, Soo Jin Kang, Seung Whan Lee, Young Hak Kim, Cheol Whan Lee, Seong Wook Park, and Seung Jung Park. Deferred vs. performed revascularization for coronary stenosis with

grey-zone fractional flow reserve values: Data from the IRIS-FFR registry. *European Heart Journal*, 39(18):1610–1619, 2018.

143. Ricardo Petraco, Sayan Sen, Sukhjinder Nijjer, Mauro Echavarria-Pinto, Javier Escaned, Darrel P. Francis, and Justin E. Davies. Fractional flow reserve-guided revascularization: Practical implications of a diagnostic gray zone and measurement variability on clinical decisions. *JACC: Cardiovascular Interventions*, 6(3):222–225, 2013.

144. Colin Berry, Marcel Van 'T Veer, Nils Witt, Petr Kala, Otakar Bocek, Stylianos A. Pyxaras, John D. McClure, William F. Fearon, Emanuele Barbato, Pim A L Tonino, Bernard De Bruyne, Nico H J Pijls, Keith G. Oldroyd, C Ms, William F. Fearon, Emanuele Barbato, Pim A L Tonino, Bernard De Bruyne, Nico H J Pijls, Keith G. Oldroyd, and H B Mbc. VERIFY (VERification of Instantaneous Wave-Free Ratio and Fractional Flow Reserve for the Assessment of Coronary Artery Stenosis Severity in EverydaY Practice) A Multicenter Study in Consecutive Patients. *Journal of the American College of Cardiology*, 61(13):1421–1427, 2013.

145. Nils P. Johnson, Allen Jeremias, Frederik M. Zimmermann, Julien Adjedj, Nils Witt, Barry Hennigan, Bon Kwon Koo, Akiko Maehara, Mitsuaki Matsumura, Emanuele Barbato, Giovanni Esposito, Bruno Trimarco, Gilles Rioufol, Seung Jung Park, Hyoung Mo Yang, Sérgio B. Baptista, George S. Chrysant, Antonio M. Leone, Colin Berry, Bernard De Bruyne, K. Lance Gould, Richard L. Kirkeeide, Keith G. Oldroyd, Nico H.J. Pijls, and William F. Fearon. Continuum of Vasodilator Stress from Rest to Contrast Medium to Adenosine Hyperemia for Fractional Flow Reserve Assessment. *JACC: Cardiovascular Interventions*, 9(8):757–767, 2016.

146. Sayan Sen, Javier Escaned, Iqbal S. Malik, Ghada W. Mikhail, Rodney A. Foale, Rafael Mila, Jason Tarkin, Ricardo Petraco, Christopher Broyd, Richard Jabbour, Amarjit Sethi, Christopher S. Baker, Micheal Bellamy, Mahmud Al-Bustami, David Hackett, Masood Khan, David Lefroy, Kim H. Parker, Alun D. Hughes, Darrel P. Francis, Carlo Di Mario, Jamil Mayet, and Justin E. Davies. Development and validation of a new adenosine-independent index of stenosis severity from coronary waveintensity analysis: Results of the ADVISE (ADenosine Vasodilator Independent Stenosis Evaluation) study. *Journal of the American College of Cardiology*, 59(15):1392–1402, 2012.

147. Sayan Sen, Kaleab N. Kaleb N Asrress, Sukhjinder Nijjer, Ricardo Petraco, Iqbal S. Malik, Rodney A. Foale, Ghada W. Mikhail, Nicolas Foin, Christopher Broyd, Nearchos Hadjiloizou, Amarjit Sethi, Mahmud Al-Bustami, David Hackett, Masood A. Khan, Muhammed Z. Khawaja, Christopher S. Baker, Micheal Michael Bellamy, Kim H. Parker, Alun D. Hughes, Darrel P. Francis, Jamil Mayet, Carlo Di Mario, Javier Escaned, Simon Redwood, and Justin E. Davies. Diagnostic Classification of the Instantaneous Wave-Free Ratio Is Equivalent to Fractional Flow Reserve and Is Not Improved With Adenosine Administration Results of CLARIFY (Classification Accuracy of Pressure-Only Ratios Against Indices Using Flow Study). *Journal of the American College of Cardiology*, 61(13):1409–1420, 2013.

148. Nico H.J J Pijls, Marcel Van 'T Veer, Keith G. Oldroyd, Colin Berry, William F. Fearon, Petr Kala, Otakar Bocek, Nils Witt, Bernard De Bruyne, Stylianos A Stelios Pyxaras, Marcel van't Veer, Keith G. Oldroyd, Colin Berry, William F. Fearon, Petr Kala, Otakar Bocek, Nils Witt, Bernard De Bruyne, and Stylianos A Stelios Pyxaras. Instantaneous wave-free ratio or fractional flow reserve without hyperemia: Novelty or nonsense? *Journal of the American College of Cardiology*, 59(21):1916–1917, 2012.

149. Sayan Sen, Javier Escaned, Ricardo Petraco, Sukhjinder Nijjer, Darrel P. Francis, and Justin E. Davies. Reply: Is the instantaneous wave-free ratio equivalent to fractional flow reserve? *Journal of the American College of Cardiology*, 62(10):943–945, 2013.

150. Nils P. Johnson, Richard L. Kirkeeide, Kaleab N. Asrress, William F. Fearon, Timothy Lockie, Koen M.J. Marques, Stylianos A. Pyxaras, M. Cristina Rolandi, Marcel Van 'T Veer, Bernard De Bruyne, Jan J. Piek, Nico H.J. Pijls, Simon Redwood, Maria Siebes, Jos A.E. Spaan, and K. Lance Gould. Does the instantaneous wave-free ratio approximate the fractional flow reserve? *Journal of the American College of Cardiology*, 61(13):1428–1435, 2013.

151. Allen Jeremias, Akiko Maehara, Philippe Généreux, Kaleab N. Asrress, Colin Berry, Bernard De Bruyne, Justin E. Davies, Javier Escaned, William F. Fearon, K. Lance Gould, Nils P. Johnson, Ajay J. Kirtane, Bon Kwon Koo, Koen M. Marques, Sukhjinder Nijjer, Keith G. Oldroyd, Ricardo Petraco, Jan J. Piek, Nico H. Pijls, Simon Redwood, Maria Siebes, Jos A.E. Spaan, Marcel Van'T Veer, Gary S. Mintz, and Gregg W. Stone.

Multicenter core laboratory comparison of the instantaneous wave-free ratio and resting Pd/Pa with fractional flow reserve: The RESOLVE study. *Journal of the American College of Cardiology*, 63(13):1253–1261, 2014.

152. Joo Myung Lee, Jonghanne Park, Doyeon Hwang, Chee Hae Kim, Ki Hong Choi, Tae Min Rhee, Yaliang Tong, Jin Joo Park, Eun Seok Shin, Chang Wook Nam, Joon Hyung Doh, and Bon Kwon Koo. Similarity and Difference of Resting Distal to Aortic Coronary Pressure and Instantaneous Wave-Free Ratio. *Journal of the American College of Cardiology*, 70(17):2114–2123, 2017.

153. Barry Hennigan, Keith G. Oldroyd, Colin Berry, Nils Johnson, John McClure, Peter McCartney, Margaret B. McEntegart, Hany Eteiba, Mark C. Petrie, Paul Rocchiccioli, Richard Good, Martin M. Lindsay, Stuart Hood, and Stuart Watkins. Discordance Between Resting and Hyperemic Indices of Coronary Stenosis Severity. *Circulation: Cardiovascular Interventions*, 9(11):1–9, 2016.

154. Marcel van't Veer, Nico H.J. Pijls, Barry Hennigan, Stuart Watkins, Ziad A. Ali, Bernard De Bruyne, Frederik M. Zimmermann, Lokien X. van Nunen, Emanuele Barbato, Colin Berry, and Keith G. Oldroyd. Comparison of Different Diastolic Resting Indexes to iFR: Are They All Equal? *Journal of the American College of Cardiology*, 70(25):3088–3096, 2017.

155. Justin E. Davies, Sayan Sen, Hakim-Moulay Dehbi, Rasha Al-Lamee, Ricardo Petraco, Sukhjinder S. Nijjer, Ravinay Bhindi, Sam J. Lehman, Darren Walters, James Sapontis, Luc Janssens, Christiaan J. Vrints, Ahmed Khashaba, Mika Laine, Eric Van Belle, Florian Krackhardt, Waldemar Bojara, Olaf Going, Tobias Härle, Ciro Indolfi, Giampaolo Niccoli, Flavo Ribichini, Nobuhiro Tanaka, Hiroyoshi Yokoi, Hiroaki Takashima, Yuetsu Kikuta, Andrejs Erglis, Hugo Vinhas, Pedro Canas Silva, Sérgio B. Baptista, Ali Alghamdi, Farrel Hellig, Bon-Kwon Koo, Chang-Wook Nam, Eun-Seok Shin, Joon-Hyung Doh, Salvatore Brugaletta, Eduardo Alegria-Barrero, Martijin Meuwissen, Jan J. Piek, Niels van Royen, Murat Sezer, Carlo Di Mario, Robert T. Gerber, Iqbal S. Malik, Andrew S.P. Sharp, Suneel Talwar, Kare Tang, Habib Samady, John Altman, Arnold H. Seto, Jasvindar Singh, Allen Jeremias, Hitoshi Matsuo, Rajesh K. Kharbanda, Manesh R. Patel, Patrick Serruys, and Javier Escaned. Use of the Instantaneous

Wave-free Ratio or Fractional Flow Reserve in PCI. *New England Journal of Medicine*, 376(19):1824–1834, 2017.

156. Sayan Sen, Yousif Ahmad, Hakim Moulay Dehbi, James P. Howard, Juan F. Iglesias, Rasha Al-Lamee, Ricardo Petraco, Sukhjinder Nijjer, Ravinay Bhindi, Sam Lehman, Darren Walters, James Sapontis, Luc Janssens, Christiaan J. Vrints, Ahmed Khashaba, Mika Laine, Eric Van Belle, Florian Krackhardt, Waldemar Bojara, Olaf Going, Tobias Härle, Ciro Indolfi, Giampaolo Niccoli, Flavio Ribichini, Nobuhiro Tanaka, Hiroyoshi Yokoi, Hiroaki Takashima, Yuetsu Kikuta, Andrejs Erglis, Hugo Vinhas, Pedro Canas Silva, Sérgio B. Baptista, Ali Alghamdi, Farrel Hellig, Bon Kwon Koo, Chang Wook Nam, Eun Seok Shin, Joon Hyung Doh, Salvatore Brugaletta, Eduardo Alegria-Barrero, Martijin Meuwissen, Jan J. Piek, Niels van Royen, Murat Sezer, Carlo Di Mario, Robert T. Gerber, Iqbal S. Malik, Andrew S.P. Sharp, Suneel Talwar, Kare Tang, Habib Samady, John Altman, Arnold H. Seto, Jasvindar Singh, Allen Jeremias, Hitoshi Matsuo, Rajesh K. Kharbanda, Manesh R. Patel, Patrick Serruys, Javier Escaned, and Justin E. Davies. Clinical Events After Deferral of LAD Revascularization Following Physiological Coronary Assessment. *Journal of the American College of Cardiology*, 73(4):444–453, 2019.

157. Instantaneous Wave-free Ratio versus Fractional Flow Reserve. *New England Journal of Medicine*, 377(16):1595–1599, 2017.

158. Ricardo Petraco, Tim P. van de Hoef, Sukhjinder Nijjer, Sayan Sen, Martijn A. van Lavieren, Rodney A. Foale, Martijn Meuwissen, Christopher Broyd, Mauro Echavarria-Pinto, Nicolas Foin, Iqbal S. Malik, Ghada W. Mikhail, Alun D. Hughes, Darrel P. Francis, Jamil Mayet, Carlo Di Mario, Javier Escaned, Jan J. Piek, and Justin E. Davies. Baseline Instantaneous Wave-Free Ratio as a Pressure-Only Estimation of Underlying Coronary Flow Reserve. *Circulation: Cardiovascular Interventions*, 7(4):492–502, 2014.

159. Tobias Härle, Waldemar Bojara, Sven Meyer, and Albrecht Elsässer. Comparison of instantaneous wave-free ratio (iFR) and fractional flow reserve (FFR) - First real world experience. *International Journal of Cardiology*, 199:1–7, 2015.

160. Patrick W. Serruys, Carlo Di Mario, Nicolas Meneveau, Peter de Jaegere, Sipke Strik-

werda, Pim J. de Feyter, and Håkan Emanuelsson. Intracoronary pressure and flow velocity with sensor-tip guidewires: A new methodologic approach for assessment of coronary hemodynamics before and after coronary interventions. *The American Journal of Cardiology*, 71(14):41D–53D, 1993.

161. Maria Siebes, Bart-Jan Verhoeff, Martijn Meuwissen, Robbert J de Winter, Jos a E Spaan, and Jan J Piek. Single-wire pressure and flow velocity measurement to quantify coronary stenosis hemodynamics and effects of percutaneous interventions. *Circulation*, 109(6):756–62, 2004.

162. XiongJie Jin, Myeong-Ho Yoon, Kyoung-woo Seo, Seung-jea Tahk, Hong-Seok Lim, Hyoung-Mo Yang, Byoung-Joo Choi, So-Yeon Choi, Gyo-seung Hwang, Joon-Han Shin, and Jin-Sun Park. Usefulness of Hyperemic Microvascular Resistance Index as a Predictor of Clinical Outcomes in Patients with ST-Segment Elevation Myocardial Infarction. *Korean Circulation Journal*, 45(3):194–201, 2015.

163. M. Meuwissen. Hyperemic Stenosis Resistance Index for Evaluation of Functional Coronary Lesion Severity. *Circulation*, 106(4):441–446, 2002.

164. Hironori Kitabata, Toshio Imanishi, Takashi Kubo, Shigeho Takarada, Manabu Kashiwagi, Hiroki Matsumoto, Hiroto Tsujioka, Hideyuki Ikejima, Yu Arita, Keishi Okochi, Akio Kuroi, Satoshi Ueno, Hideaki Kataiwa, Takashi Tanimoto, Takashi Yamano, Kumiko Hirata, Nobuo Nakamura, Atsushi Tanaka, Masato Mizukoshi, and Takashi Akasaka. Coronary Microvascular Resistance Index Immediately After Primary Percutaneous Coronary Intervention as a Predictor of the Transmural Extent of Infarction in Patients With ST-Segment Elevation Anterior Acute Myocardial Infarction. *JACC: Cardiovascular Imaging*, 2(3):263–272, 2009.

165. Hironori Kitabata, Takashi Kubo, Kohei Ishibashi, Kenichi Komukai, Takashi Tanimoto, Yasushi Ino, Manabu Kashiwagi, Yuichi Ozaki, Yasutsugu Shiono, Kunihiro Shimamura, Makoto Orii, Kumiko Hirata, Atsushi Tanaka, Toshio Imanishi, and Takashi Akasaka. Prognostic value of microvascular resistance index immediately after primary percutaneous coronary intervention on left ventricular remodeling in patients with reperfused

anterior acute st-segment elevation myocardial infarction. *JACC: Cardiovascular Interventions*, 6(10):1046–1054, 2013.

166. Niels A. Lassen and William Perl. *Tracer kinetic methods in medical physiology*. Raven Press, Ney york, 1979.

167. N. H.J. Pijls. Coronary Thermodilution to Assess Flow Reserve: Validation in Humans. *Circulation*, 105(21):2482–2486, 2002.

168. William F Fearon, Leora B Balsam, H M Omar Farouque, Anthony D Caffarelli, Robert C Robbins, Peter J Fitzgerald, Paul G Yock, and Alan C Yeung. Novel index for invasively assessing the coronary microcirculation. *Circulation*, 107(25):3129–32, 2003.

169. William F. Fearon, Maulik Shah, Martin Ng, Todd Brinton, Andrew Wilson, Jennifer A. Tremmel, Ingela Schnittger, David P. Lee, Randall H. Vagelos, Peter J. Fitzgerald, Paul G. Yock, and Alan C. Yeung. Predictive Value of the Index of Microcirculatory Resistance in Patients With ST-Segment Elevation Myocardial Infarction. *Journal of the American College of Cardiology*, 51(5):560–565, 2008.

170. Hong Seok Lim, Myeong Ho Yoon, Seung Jea Tahk, Hyoung Mo Yang, Byoung Joo Choi, So Yeon Choi, Seung Soo Sheen, Gyo Seung Hwang, Soo Jin Kang, and Joon Han Shin. Usefulness of the index of microcirculatory resistance for invasively assessing myocardial viability immediately after primary angioplasty for anterior myocardial infarction. *European Heart Journal*, 30(23):2854–2860, 2009.

171. Sung Gyun Ahn, Olivia Y. Hung, Jun Won Lee, Ji Hyun Lee, Young Jin Youn, Min Soo Ahn, Jang Young Kim, Byung Su Yoo, Seung Hwan Lee, Junghan Yoon, Woocheol Kwon, and Habib Samady. Combination of the Thermodilution-Derived Index of Microcirculatory Resistance and Coronary Flow Reserve Is Highly Predictive of Microvascular Obstruction on Cardiac Magnetic Resonance Imaging after ST-Segment Elevation Myocardial Infarction. *JACC: Cardiovascular Interventions*, 9(8):793–801, 2016.

172. Ross McGeoch, Stuart Watkins, Colin Berry, Tracey Steedman, Andrew Davie, John Byrne, Stewart Hillis, Mitchell Lindsay, Stephen Robb, Henry Dargie, and Keith Oldroyd. The index of microcirculatory resistance measured acutely predicts the extent

and severity of myocardial infarction in patients with ST-segment elevation myocardial infarction. *JACC: Cardiovascular Interventions*, 3(7):715–722, 2010.

173. Seung Hoon Yoo, Tae Kyung Yoo, Hong Seok Lim, Mi Young Kim, and Jong Hoon Koh. Index of microcirculatory resistance as predictor for microvascular functional recovery in patients with anterior myocardial infarction. *Journal of Korean Medical Science*, 27(9):1044–1050, 2012.

174. Jamie J. Layland, Robert J. Whitbourn, Andrew T. Burns, Jithendra Somaratne, Georg Leitl, Andrew I. MacIsaac, and Andrew Wilson. The index of microvascular resistance identifies patients with periprocedural myocardial infarction in elective percutaneous coronary intervention. *Heart*, 98(20):1492–1497, 2012.

175. Barry Hennigan, Jamie Layland, William F Fearon, and Keith G Oldroyd. Fractional flow reserve and the index of microvascular resistance in patients with acute coronary syndromes. *EuroIntervention : journal of EuroPCR in collaboration with the Working Group on Interventional Cardiology of the European Society of Cardiology*, 10 Suppl T:T55–63, 2014.

176. Joo Myung Lee, Ji Hyun Jung, Doyeon Hwang, Jonghanne Park, Yongzhen Fan, Sang Hoon Na, Joon Hyung Doh, Chang Wook Nam, Eun Seok Shin, and Bon Kwon Koo. Coronary Flow Reserve and Microcirculatory Resistance in Patients with Intermediate Coronary Stenosis. *Journal of the American College of Cardiology*, 67(10):1158–1169, 2016.

177. Andy S. Yong, Jamie Layland, William F. Fearon, Michael Ho, Maulik G. Shah, David Daniels, Robert Whitbourn, Andrew MacIsaac, Leonard Kritharides, Andrew Wilson, and Martin K. Ng. Calculation of the index of microcirculatory resistance without coronary wedge pressure measurement in the presence of epicardial stenosis. *Journal of the American College of Cardiology: Cardiovascular Interventions*, 6(1):53–58, 2013.

178. Wilbert Aarnoudse, Marcel Van't Veer, Nico H J Pijls, Joost ter Woorst, Steven Vercauteren, Pim Tonino, Maartje Geven, Marcel Rutten, Eduard van Hagen, Bernard de Bruyne, and Frans van de Vosse. Direct Volumetric Blood Flow Measurement in

Coronary Arteries by Thermodilution. *Journal of the American College of Cardiology*, 50(24):2294–2304, 2007.

179. Marcel Van't Veer, Julien Adjedj, Inge Wijnbergen, Gabor G. Tóth, Marcel C.M. Rutten, Emanuele Barbato, Lokien X. Van Nunen, Nico H.J. Pijls, and Bernard De Bruyne. Novel monorail infusion catheter for volumetric coronary blood flow measurement in humans: In vitro validation. *EuroIntervention*, 12(6):701–707, 2016.

180. Marcel van't Veer, Maartje C F Geven, Marcel C M Rutten, Arjen van der Horst, Wilbert H Aarnoudse, Nico H J Pijls, and Frans N van de Vosse. Continuous infusion thermodilution for assessment of coronary flow: theoretical background and in vitro validation. *Medical Engineering and Physics*, 31(6):688–94, 2009.

181. Panagiotis Xaplanteris, Stephane Fournier, Daniëlle C.J. Keulards, Julien Adjedj, Giovanni Ciccarelli, Anastasios Milkas, Mariano Pellicano, Marcel Van't Veer, Emanuele Barbato, Nico H.J. Pijls, and Bernard De Bruyne. Catheter-based measurements of absolute coronary blood flow and microvascular resistance feasibility, safety, and reproducibility in humans. *Circulation: Cardiovascular Interventions*, 11(3), 2018.

182. Simon D. Shpilfoygel, Robert A. Close, Daniel J. Valentino, and Gary R. Duckwiler. X-ray videodensitometric methods for blood flow and velocity measurement: A critical review of literature. *Medical Physics*, 27(9):2008–2023, 2000.

183. W. Rutishauser, H. Simon, J. P. Stucky, N. Schad, G. Noseda, and J. Wellauer. Evaluation of Roentgen cinedensitometry for flow measurement in models and in the intact circulation. *Circulation*, 36(6):951–963, 1967.

184. Wilhelm Rutishauser, Wulf-Dirk Bussmann, Giorgio Noseda, Willy Meijer, and Josef Wellauer. Blood flow measurement through single coronary arteries by Roentgen densitometry. Part I. A comparison of flow measured by radiologic technique applicable in the intact organism and by electromagnetic flowmeter. *American Journal of Roentgenology*, 109(1):12–20, 1970.

185. Wilhelm Rutishauser, Giorgio Noseda, Wulf-Dirk Bussmann, and Bruno Preter. Blood flow measurement through single coronary arteries by roentgen densitometry: Part

II right coronary artery flow in conscious man. *American Journal of Roentgenology*, 109(1):21–24, 1970.

186. HC Smith, RE Sturm, and EH Wood. Videodensitometric System for Measurement of Vessel Blood Flow, Particularly in the Coronary Arteries in Man. *The American Journal of Cardiology*, 32:144–150, 1973.

187. M. L. Marcus, R. F. Wilson, and C. W. White. Methods of measurement of myocardial blood flow in patients: A critical review. *Circulation*, 76(2):245–253, 1987.

188. R Vogel, M LeFree, E Bates, W O'Neill, R Foster, P Kirlin, D Smith, and B Pitt. Application of digital techniques to selective coronary arteriography: use of myocardial contrast appearance time to measure coronary flow reserve. *American Heart Journal*, 107(1):153–64, 1984.

189. N. H. Pijls, G. J. Uijen, a. Hoevelaken, T. Arts, W. R. Aengevaeren, H. S. Bos, J. H. Fast, K. L. van Leeuwen, and T. van der Werf. Mean transit time for the assessment of myocardial perfusion by videodensitometry. *Circulation*, 81(4):1331–1340, apr 1990.

190. NL L Eigler, H Schühlen, JS S Whiting, JM M Pfaff, A Zeiher, and S Gu. Digital angiographic impulse response analysis of regional myocardial perfusion. Estimation of coronary flow, flow reserve and distribution volume by compartmental transit time measurement in a canine model. *Circulation Research*, 68:870–880, 1991.

191. W R Aengevaeren, G J Uijen, and T van der Werf. Comparison of coronary flow velocity and regional myocardial perfusion for functional evaluation of coronary artery disease in the setting of angioplasty. *Catheterization and Cardiovascular Diagnosis*, 45(1):16–24, 1998.

192. NH Pijls, WR Aengevaeren, and GJ Uijen. Concept of maximal flow ratio for immediate evaluation of percutaneous transluminal coronary angioplasty result by videodensitometry. *Circulation*, 83:854–865, 1991.

193. M Haude, G Caspari, D Baumgart, T Ehring, R Schulz, T Roth, L Koch, R Erbel, P Spiller, and G Heusch. X-ray densitometry for the measurement of regional myocardial perfusion. *Basic Research in Cardiology*, 95(3):261–70, 2000.

194. C Vassanelli, G Menegatti, J Molinari, G Zanotto, L Zanolla, I Loschiavo, and P Zardini. Maximal myocardial perfusion by videodensitometry in the assessment of the early and late results of coronary angioplasty: relationship with coronary artery measurements and left ventricular function at rest. *Catheterization and Cardiovascular Diagnosis*, 34(4):301–10; discussion 311–2, 1995.

195. H. Schuhlen, N. L. Eigler, a. M. Zeiher, M. M. Rombach, and J. S. Whiting. Digital angiographic assessment of the physiological changes to the regional microcirculation induced by successful coronary angioplasty. *Circulation*, 90(1):163–171, 1994.

196. Tamás Ungi, Imre Ungi, Zsuzsanna Jónás, Viktor Sasi, András Lassó, Zsolt Zimmermann, Tamás Forster, András Palkó, and Attila Nemes. Myocardium selective densitometric perfusion assessment after acute myocardial infarction. *Cardiovascular Revascularization Medicine : including Molecular Interventions*, 10(1):49–54, 2009.

197. N H Pijls, G J Uijen, A Hoevelaken, T Pijnenburg, K L van Leeuwen, J H Fast, H S Bos, W R Aengevaeren, and T van der Werf. Mean transit time for videodensitometric assessment of myocardial perfusion and the concept of maximal flow ratio: a validation study in the intact dog and a pilot study in man. *International Journal of Cardiac Imaging*, 5(2-3):191–202, 1990.

198. J. M. Foerster, D. P. Link, B. M.T. Lantz, G. Lee, J. W. Holcroft, and D. T. Mason. Measurement of coronary reactive hyperemia during clinical angiography by video dilution technique. *Acta Radiologica - Series Diagnosis*, 22(3 A):209–216, 1981.

199. J. M. Foerster, B. M.T. Lantz, J. W. Holcroft, D. P. Link, and D. T. Mason. Angiographic measurement of coronary blood flow. *Acta Radiologcia*, 22(2):121–127, 1981.

200. J M Hodgson, V LeGrand, E R Bates, G B Mancini, F M Aueron, W W O'Neill, S B Simon, G J Beauman, M T LeFree, and R a Vogel. Validation in dogs of a rapid digital angiographic technique to measure relative coronary blood flow during routine cardiac catheterization. *The American Journal of Cardiology*, 55(1):188–93, 1985.

201. P W Serruys, F Zijlstra, G J Laarman, H H Reiber, K Beatt, and J Roelandt. A comparison of two methods to measure coronary flow reserve in the setting of coronary

angioplasty: intracoronary blood flow velocity measurements with a Doppler catheter, and digital subtraction cineangiography. *European Heart Journal*, 10(8):725–36, 1989.

202. J. T. Cusma, E. J. Toggart, J. D. Folts, W. W. Peppler, N. J. Hangiandreou, C. S. Lee, and C. a. Mistretta. Digital subtraction angiographic imaging of coronary flow reserve. *Circulation*, 75(2):461–472, 1987.

203. OM Hess, MJ McGillem, SF DeBoe, IM Pinto, Gallagher KP, and GB Mancini. Determination of coronary flow reserve by parametric imaging. *Circulation*, 82:1438–1448, 1990.

204. M Haude, R Brennecke, R Erbel, M Lang, H P Deutsch, U Renneisen, and J Meyer. Parametric assessment of myocardial perfusion during interventional cardiac catheterization by means of X-ray densitometry-short-and long-term results. *International Journal of Cardiac Imaging*, 5(2-3):183–90, 1990.

205. J. S. Whiting, J. K. Drury, J. M. Pfaff, B. L. Chang, N. L. Eigler, S. Meerbaum, E. Corday, T. Nivatpumin, J. S. Forrester, and H. J. Swan. Digital angiographic measurement of radiographic contrast material kinetics for estimation of myocardial perfusion. *Circulation*, 73(4):789–798, 1986.

206. M. Haude, R. Brennecke, R. Erbel, U. Renneisen, M. Lang, H.P. Deutsch, and J Meyer. Computerized estimation of quality standards for the X-ray densitometric assessment of myocardial perfusion. In *Computers in Cardiology 1989, Proceedings*, pages 317–320. IEEE, 1989.

207. M J Geldof, M J Schalij, V Manger Cats, P M van der Zwet, P Steendijk, E T van der Velde, E M Nagtegaal, J H Reiber, and a V Bruschke. Comparison between regional myocardial perfusion reserve and coronary flow reserve in the canine heart. *European Heart Journal*, 16(12):1860–71, 1995.

208. K Murata, V Bhargava, F Ricou, S Ono, M Kambayashi, B H Oh, and K L Peterson. The influence of coronary collateral flow on the assessment of myocardial perfusion by videodensitometry. *Cardiovascular Research*, 33(2):359–69, 1997.

209. Mathijs Vogelzang, Pieter J Vlaar, Tone Svilaas, Diny Amo, Maarten W N Nijsten, and Felix Zijlstra. Computer-assisted myocardial blush quantification after percutaneous coronary angioplasty for acute myocardial infarction: a substudy from the TAPAS trial. *European Heart Journal*, 30(5):594–9, 2009.

210. Grigorios Korosoglou, Andreas Haars, Gick Michael, Markus Erbacher, Stefan Hardt, Evangelos Giannitsis, Kerstin Kurz, Neumann Franz-Josef, Helmut Dickhaus, Hugo a Katus, and Helmut Kuecherer. Quantitative evaluation of myocardial blush to assess tissue level reperfusion in patients with acute ST-elevation myocardial infarction: incremental prognostic value compared with visual assessment. *American Heart Journal*, 153(4):612–20, 2007.

211. Grigorios Korosoglou, Nina Riedle, Markus Erbacher, Thomas J Dengler, Christian Zugck, Wolfgang Rottbauer, Stefan Hardt, Raffi Bekeredjian, Arnt Kristen, Evangelos Giannitsis, Neal F Osman, Hartmut Dickhaus, and Hugo a Katus. Quantitative myocardial blush grade for the detection of cardiac allograft vasculopathy. *American Heart Journal*, 159(4):643–651.e2, 2010.

212. Christian Hamilton-Craig, Italo Porto, Giovanni Luigi De Maria, Luigi Natale, and Filippo Crea. Quantitative blush evaluator (QuBE) accurately quantifies microvascular dysfunction in patients with ST-Elevation Myocardial Infarction; comparison with Cardiovascular Magnetic Resonance. *Journal of Cardiovascular Magnetic Resonance*, 13(S1):O53, 2011.

213. Italo Porto, Christian Hamilton-Craig, Giovanni Luigi De Maria, Rocco Vergallo, Giorgio Cautilli, Leonarda Galiuto, Francesco Burzotta, Antonio Maria Leone, Giampaolo Niccoli, Luigi Natale, Lorenzo Bonomo, and Filippo Crea. Quantitative Blush Evaluator accurately quantifies microvascular dysfunction in patients with ST-elevation myocardial infarction: Comparison with cardiovascular magnetic resonance. *American Heart Journal*, 162(2):372–381.e2, 2011.

214. Tomasz Florianczyk, Malgorzata Golabek-Dylewska, Beata Kucinska, and Bozena Werner. Evaluation of left ventricular function in overweight children and teenagers

with arterial hypertension and white coat hypertension. *Cardiology Journal*, (X):1–11, 2013.

215. Joost D.E. Haeck, Youlan L Gu, Mathijs Vogelzang, Luc Bilodeau, Mitchell W Krucoff, Jan G.P. Tijssen, Robbert J. De Winter, Felix Zijlstra, and Karel T Koch. Feasibility and applicability of computer-assisted myocardial blush quantification after primary percutaneous coronary intervention for ST-segment elevation myocardial infarction. *Catheterization and Cardiovascular Interventions*, 75(5):701–706, 2010.

216. Haryadi Prasetya, Marcel A M Beijk, Praneeta R Konduri, Thabiso Epema, Alexander Hirsch, Pim Van Der, Ed Van Bavel, Bas A J M De Mol, and Henk A Marquering. Limitations of Quantitative Blush Evaluator (QuBE) as myocardial perfusion assessment method on digital coronary angiograms. *Journal of Clinical and Translational Research*, 3(S2):394–400, 2018.

217. GitHub. Git repository for the QuBE (Quantitative Blush Evaluator) project. `https://github.com/mathijs81/qube`, 2015. [Online; accessed 6/6/2019].

218. James T Maddux, Onno Wink, John C Messenger, Bertron M Groves, Robert Liao, Jodi Strzelczyk, Shiuh-Yung Chen, and John D Carroll. Randomized study of the safety and clinical utility of rotational angiography versus standard angiography in the diagnosis of coronary artery disease. *Catheterization and Cardiovascular Interventions*, 62(2):167–74, 2004.

219. Klaus Empen, Eberhard Kuon, Astrid Hummel, Chris Gebauer, Marcus Dorr, Raik Konemann, Wolfgang Hoffman, Alexander Staudt, Kerstin Weitmann, Thorsten Reffelmann, and Stephen B Felix. Comparison of rotational with conventional coronary angiography. *American Heart Journal*, 160:552–563, 2010.

220. N. Guggenheim, P. A. Doriot, P. A. Dorsaz, P. Descouts, and W. Rutishauser. Spatial reconstruction of coronary arteries from angiographic images. *Physics in Medicine and Biology*, 36(1):99–110, 1991.

221. Shiuh Yung James Chen and Charles E. Metz. Improved determination of biplane imaging geometry from two projection images and its application to three-dimensional reconstruction of coronary arterial trees. *Medical Physics*, 24(5):633–654, 1997.

222. John C. Messenger, S. Y.James Chen, John D. Carroll, J. E.B. Burchenal, Kathy Kioussopoulos, and Bertron M. Groves. 3D coronary reconstruction from routine single-plane coronary angiograms: Clinical validation and quantitative analysis of the right coronary artery in 100 patients. *International Journal of Cardiac Imaging*, 16(6):413–427, 2000.

223. S. James Chen and John D. Carroll. 3-D reconstruction of coronary arterial tree to optimize angiographic visualization. *IEEE Transactions on Medical Imaging*, 19pp(4):318–336, 2000.

224. Nathan E Green, S-Y James S.-Y. James Chen, Adam R Hansgen, John C Messenger, Bertron M Groves, and John D Carroll. Angiographic Views Used for Percutaneous Coronary Interventions : A Three-Dimensional Analysis of Physician-Determined vs. Computer-Generated Views. *Catheterization and Cardiovascular Interventions*, 459:451–459, 2005.

225. Anne M. Neubauer, Joel A. Garcia, John C. Messenger, Eberhard Hansis, Michael S. Kim, Andrew J.P. Klein, Gert A.F. Schoonenberg, Michael Grass, and John D. Carroll. Clinical feasibility of a fully automated 3D reconstruction of rotational coronary x-ray angiograms. *Circulation: Cardiovascular Interventions*, 3(1):71–79, 2010.

226. Shengxian Tu, Liang Xu, Jurgen Ligthart, Bo Xu, Karen Witberg, Zhongwei Sun, Gerhard Koning, Johan H C Reiber, and Evelyn Regar. In vivo comparison of arterial lumen dimensions assessed by co-registered three-dimensional (3D) quantitative coronary angiography, intravascular ultrasound and optical coherence tomography. *International Journal of Cardiovascular Imaging*, 28(6):1315–1327, 2012.

227. Andy S C Yong, Austin C C Ng, David Brieger, Harry C. Lowe, Martin K C Ng, and Leonard Kritharides. Three-dimensional and two-dimensional quantitative coronary angiography, and their prediction of reduced fractional flow reserve. *European Heart Journal*, 32(3):345–353, 2011.

228. G. A. ten Brinke, C. H. Slump, and M. G. Stoel. Automated TIMI frame counting using 3-d modeling. *Computerized Medical Imaging and Graphics*, 36(7):580–588, 2012.

229. Łukasz Kołtowski, Martyna Zaleska, Jakub Maksym, Mariusz Tomaniak, Mateusz Soliński, Dominika Puchta, Niels R. Holm, Grzegorz Opolski, and Janusz Kochman.

Quantitative flow ratio derived from diagnostic coronary angiography in assessment of patients with intermediate coronary stenosis: a wire-free fractional flow reserve study. *Clinical Research in Cardiology*, 107(9):858–867, 2018.

230. Kyoichiro Yazaki, Masato Otsuka, Shohei Kataoka, Mitsuru Kahata, Asako Kumagai, Koji Inoue, Hiroshi Koganei, Kenji Enta, and Yasuhiro Ishii. Applicability of 3-Dimensional Quantitative Coronary Angiography-Derived Computed Fractional Flow Reserve for Intermediate Coronary Stenosis. *Circulation Journal*, 81(7):988–992, 2017.

231. Shengxian Tu, Emanuele Barbato, Zsolt Köszegi, Junqing Yang, Zhonghua Sun, Niels R. Holm, Balázs Tar, Yingguang Li, Dan Rusinaru, William Wijns, and Johan H.C. Reiber. Fractional flow reserve calculation from 3-dimensional quantitative coronary angiography and TIMI frame count: A fast computer model to quantify the functional significance of moderately obstructed coronary arteries. *JACC: Cardiovascular Interventions*, 7(7):768–777, 2014.

232. Tu Shengxian, Reiber Johan, and Li Yingguang. Method And Device For Determining Deviation In Pressure In a Blood Vessel. US 9891044 B2, 2018.

233. Shengxian Tu, Jelmer Westra, Junqing Yang, Clemens von Birgelen, Angela Ferrara, Mariano Pellicano, Holger Nef, Matteo Tebaldi, Yoshinobu Murasato, Alexandra Lansky, Emanuele Barbato, Liefke C. van der Heijden, Johan H.C. Reiber, Niels R. Holm, and William Wijns. Diagnostic Accuracy of Fast Computational Approaches to Derive Fractional Flow Reserve From Diagnostic Coronary Angiography: The International Multicenter FAVOR Pilot Study. *JACC: Cardiovascular Interventions*, 9(19):2024–2035, 2016.

234. Bo Xu, Shengxian Tu, Shubin Qiao, Xinkai Qu, Yundai Chen, Junqing Yang, Lijun Guo, Zhongwei Sun, Zehang Li, Feng Tian, Weiyi Fang, Jiyan Chen, Wei Li, Changdong Guan, Niels R. Holm, William Wijns, and Shengshou Hu. Diagnostic Accuracy of Angiography-Based Quantitative Flow Ratio Measurements for Online Assessment of Coronary Stenosis. *Journal of the American College of Cardiology*, 70(25):3077–3087, 2017.

235. Jelmer Westra, Birgitte Krogsgaard Andersen, Gianluca Campo, Hitoshi Matsuo, Lukasz

Koltowski, Ashkan Eftekhari, Tommy Liu, Luigi Di Serafino, Domenico Di Girolamo, Javier Escaned, Holger Nef, Christoph Naber, Marco Barbierato, Shengxian Tu, Omeed Neghabat, Morten Madsen, Matteo Tebaldi, Toru Tanigaki, Janusz Kochman, Samer Somi, Giovanni Esposito, Giuseppe Mercone, Hernan Mejia-Renteria, Federico Ronco, Hans Erik Bøtker, William Wijns, Evald Høj Christiansen, and Niels Ramsing Holm. Diagnostic performance of in-procedure angiography-derived quantitative flow reserve compared to pressure-derived fractional flow reserve: The FAVOR II Europe-Japan study. *Journal of the American Heart Association*, 7(14), 2018.

236. Barbara E. Stähli, Aslihan Erbay, Julia Steiner, Jens Klotsche, Hans Christian Mochmann, Carsten Skurk, Alexander Lauten, Ulf Landmesser, and David M. Leistner. Comparison of resting distal to aortic coronary pressure with angiography-based quantitative flow ratio. *International Journal of Cardiology*, 279:12–17, 2019.

237. Shengxian Tu, Niels R. Holm, Gerhard Koning, Michael Maeng, and Johan H.C. Reiber. The impact of acquisition angle differences on three-dimensional quantitative coronary angiography. *Catheterization and Cardiovascular Interventions*, 78(2):214–222, 2011.

238. Shengxian Tu, Zheng Huang, Gerhard Koning, Kai Cui, and Johan H.C. Reiber. A novel three-dimensional quantitative coronary angiography system: In-vivo comparison with intravascular ultrasound for assessing arterial segment length. *Catheterization and Cardiovascular Interventions*, 76(2):291–298, 2010.

239. Jelmer Westra, Shengxian Tu, Simon Winther, Louise Nissen, Mai Britt Vestergaard, Birgitte Krogsgaard Andersen, Emil Nielsen Holck, Camilla Fox Maule, Jane Kirk Johansen, Lene Nyhus Andreasen, Jo Krogsgaard Simonsen, Yimin Zhang, Steen Dalby Kristensen, Michael Maeng, Anne Kaltoft, Christian Juhl Terkelsen, Lars Romer Krusell, Lars Jakobsen, Johan H.C. Reiber, Jens Flensted Lassen, Morten Bøttcher, Hans Erik Bøtker, Evald Høj Christiansen, and Niels Ramsing Holm. Evaluation of Coronary Artery Stenosis by Quantitative Flow Ratio during Invasive Coronary Angiography: The WIFI II Study (Wire-Free Functional Imaging II). *Circulation: Cardiovascular Imaging*, 11(3):1–8, 2018.

240. Monique Tröbs, Stephan Achenbach, Jens Röther, Thomas Redel, Michael Scheuer-

ing, David Winneberger, Klaus Klingenbeck, Lucian Itu, Tiziano Passerini, Ali Kamen, Puneet Sharma, Dorin Comaniciu, and Christian Schlundt. Comparison of Fractional Flow Reserve Based on Computational Fluid Dynamics Modeling Using Coronary Angiographic Vessel Morphology Versus Invasively Measured Fractional Flow Reserve. *American Journal of Cardiology*, 117(1):29–35, 2016.

241. Michail I. Papafaklis, Takashi Muramatsu, Yuki Ishibashi, Christos V. Bourantas, Dimitrios I. Fotiadis, Emmanouil S. Brilakis, Héctor M. Garcia-Garcia, Javier Escaned, Patrick W. Serruys, and Lampros K. Michalis. Virtual Resting Pd/Pa From Coronary Angiography and Blood Flow Modelling: Diagnostic Performance Against Fractional Flow Reserve. *Heart Lung and Circulation*, 27(3):377–380, 2018.

242. Mariano Pellicano, Ifat Lavi, Bernard De Bruyne, Hana Vaknin-Assa, Abid Assali, Orna Valtzer, Yonit Lotringer, Giora Weisz, Yaron Almagor, Panagiotis Xaplanteris, Ajay J. Kirtane, Pablo Codner, Martin B. Leon, and Ran Kornowski. Validation study of image-based fractional flow reserve during coronary angiography. *Circulation: Cardiovascular Interventions*, 10(8):1–8, 2017.

243. Paul D. Morris, Andrew Narracott, Hendrik Von Tengg-Kobligk, Daniel Alejandro Silva Soto, Sarah Hsiao, Angela Lungu, Paul Evans, Neil W. Bressloff, Patricia V. Lawford, D. Rodney Hose, and Julian P. Gunn. Computational fluid dynamics modelling in cardiovascular medicine. *Heart*, 102(1):18–28, 2016.

244. Anastasios Kopanidis, Ioannis Pantos, Andreas Theodorakakos, Efthalia Tzanalaidou, and Demosthenes Katritsis. Fractional flow reserve derived from conventional coronary angiograms and computational fluid dynamics. *International Journal of Cardiology*, 190:187–189, 2015.

245. Paul D. Morris, Desmond Ryan, Allison C. Morton, Richard Lycett, Patricia V. Lawford, D. Rodney Hose, and Julian P. Gunn. Virtual fractional flow reserve from coronary angiography: Modeling the significance of coronary lesions. Results from the VIRTU-1 (VIRTUal fractional flow reserve from coronary angiography) study. *JACC: Cardiovascular Interventions*, 6(2):149–157, 2013.

246. Rebecca C. Gosling, Paul D. Morris, Daniel A. Silva Soto, Patricia V. Lawford, D. Rod-

ney Hose, and Julian P. Gunn. Virtual Coronary Intervention: A Treatment Planning Tool Based Upon the Angiogram. *JACC: Cardiovascular Imaging*, 12(5):865–872, 2019.

247. H. Omori, G. Witberg, Y. Kawase, T. Tanigaki, S. Okamoto, T. Hirata, Y. Sobue, H. Ota, H. Kamiya, M. Okubo, O. Valzer, R. Kornowski, and H. Matsuo. Angiogram based fractional flow reserve in patients with dual/triple vessel coronary artery disease. *International Journal of Cardiology*, 283:17–22, 2019.

248. Carlos Collet, Yoshinobu Onuma, Jeroen Sonck, Taku Asano, Bert Vandeloo, Ran Kornowski, Shengxian Tu, Jelmer Westra, Niels R. Holm, Bo Xu, Robbert J. De Winter, Jan G. Tijssen, Yosuke Miyazaki, Yuki Katagiri, Erhan Tenekecioglu, Rodrigo Modolo, Ply Chichareon, Bernard Cosyns, Daniel Schoors, Bram Roosens, Stijn Lochy, Jean Francois Argacha, Alexandre Van Rosendael, Jeroen Bax, Johan H.C. Reiber, Javier Escaned, Bernard De Bruyne, William Wijns, and Patrick W. Serruys. Diagnostic performance of angiography-derived fractional flow reserve: A systematic review and Bayesian meta-analysis. *European Heart Journal*, 39(35):3314–3321, 2018.

249. P. J. Blanco, C. A. Bulant, L. O. Müller, G. D.Maso Talou, C. Guedes Bezerra, P. L. Lemos, and R. A. Feijóo. Comparison of 1D and 3D Models for the Estimation of Fractional Flow Reserve. *Scientific Reports*, 8(1):1–12, 2018.

250. Jacob Sturdy, Johannes Kløve Kjernlie, Hallvard Moian Nydal, Vinzenz G. Eck, and Leif R. Hellevik. Uncertainty quantification of computational coronary stenosis assessment and model based mitigation of image resolution limitations. *Journal of Computational Science*, 31:137–150, 2019.

251. Paul D. Morris, Daniel Alejandro Silva Soto, Jeroen F.A. Feher, Dan Rafiroiu, Angela Lungu, Susheel Varma, Patricia V. Lawford, D. Rodney Hose, and Julian P. Gunn. Fast Virtual Fractional Flow Reserve Based Upon Steady-State Computational Fluid Dynamics Analysis: Results From the VIRTU-Fast Study. *JACC: Basic to Translational Science*, 2(4):434–446, 2017.

252. Don P. Giddens. Computing Fractional Flow Reserve During Coronary Angiography: How Good Is Good Enough? *JACC: Cardiovascular Interventions*, 9(19):2036–2038, 2016.

253. Baiyan Zhuang, Shuli Wang, Shihua Zhao, and Minjie Lu. Computed tomography angiography-derived fractional flow reserve (CT-FFR) for the detection of myocardial ischemia with invasive fractional flow reserve as reference: systematic review and meta-analysis. *European Radiology*, 30(2):712–725, 2020.

254. CJ Kotre and RM Harrison. An approach to iodine quantification in digital fluorography. *Physics in Medicine and Biology*, 34(12):1795–1808, 1989.

255. Sabee Molloi, Greg Bednarz, Jerry Tang, Yifang Zhou, and Tarun Mathur. Absolute volumetric coronary blood flow measurement with digital subtraction angiography. *International Journal of Cardiac Imaging*, 14(3):137–145, 1998.

256. Sabee Molloi, Atila Ersahin, James Hicks, and James Wallis. In-vivo validation of video-densitometric coronary cross-sectional area measurement using dual-energy digital subtraction angiography. *International Journal of Cardiac Imaging*, 11:223–231, 1995.

257. Jerry T. Wong, Farzad Kamyar, and Sabee Molloi. Quantitative coronary angiography using image recovery techniques for background estimation in unsubtracted images. *Medical Physics*, 34(10):4003, 2007.

258. S. Molloi, G.S. Kassab, and Y. Zhou. Quantification of coronary artery lumen volume by digital angiography. *Circulation*, 104(19):2351–2357, 2001.

259. Sabee Molloi, Yifang Zhou, and Ghassan S Kassab. Regional volumetric coronary blood flow measurement by digital angiography: in vivo validation. *Academic Radiology*, 11(7):757–66, 2004.

260. Jerry T Wong, Justin L Ducote, Tong Xu, Mohamed T Hassanein, and Sabee Molloi. Automated technique for angiographic determination of coronary blood flow and lumen volume. *Academic Radiology*, 13(2):186–94, 2006.

261. Sabee Molloi and Jerry T Wong. Regional blood flow analysis and its relationship with arterial branch lengths and lumen volume in the coronary arterial tree. *Physics in Medicine and Biology*, 52(5):1495–503, 2007.

262. Jerry T Wong and Sabee Molloi. Determination of fractional flow reserve (FFR) based

on scaling laws: a simulation study. *Physics in Medicine and Biology*, 53(14):3995–4011, 2008.

263. Sabee Molloi, David Chalyan, Huy Le, and JT Wong. Estimation of coronary artery hyperemic blood flow based on arterial lumen volume using angiographic images. *The International Journal of Cardiovascular Imaging*, 28(1):1–11, 2012.

264. Marieke L. Fokkema, Stefan K. James, Per Albertsson, Axel Akerblom, Fredrik Calais, Peter Eriksson, Jens Jensen, Tage Nilsson, Bart J. De Smet, Iwar Sjögren, Björn Thorvinger, and Bo Lagerqvist. Population trends in percutaneous coronary intervention: 20-Year Results: From the SCAAR (Swedish Coronary Angiography and Angioplasty Registry). *Journal of the American College of Cardiology*, 61(12):1222–1230, 2013.

265. S. Jennings, K. Bennett, E. Shelley, P. Kearney, K. Daly, and W. Fennell. Trends in percutaneous coronary intervention and angiography in Ireland, 2004-2011: Implications for Ireland and Europe. *IJC Heart and Vessels*, 4(1):35–39, 2014.

266. Giuseppe De Luca, Harry Suryapranata, Felix Zijlstra, Arnoud W.J. Van't Hof, Jan C.A. Hoorntje, A. T.Marcel Gosselink, Jan Henk Dambrink, and Menko Jan De Boer. Symptom-onset-to-balloon time and mortality in patients with acute myocardial infarction treated by primary angioplasty. *Journal of the American College of Cardiology*, 42(6):991–997, 2003.

267. William M Wilson, Anoop S.V. Shah, Duncan Birse, Emma Harley, David B Northridge, and Neal G Uren. The relationship between the basal coronary translesional pressure ratio and fractional flow reserve. *Catheterization and Cardiovascular Interventions*, 90(5):745–753, 2017.

268. Tim P. Van De Hoef, Martijn A. Van Lavieren, Peter Damman, Ronak Delewi, Martijn A. Piek, Steven A.J. Chamuleau, Michiel Voskuil, José P.S. Henriques, Karel T. Koch, Robbert J. De Winter, Jos A.E. Spaan, Maria Siebes, Jan G.P. Tijssen, Martijn Meuwissen, and Jan J. Piek. Physiological basis and long-term clinical outcome of discordance between fractional flow reserve and coronary flow velocity reserve in coronary stenoses of intermediate severity. *Circulation: Cardiovascular Interventions*, 7(3):301–311, 2014.

269. Martijn Meuwissen, Maria Siebes, Jos A E Spaan, and Jan J. Piek. Rationale of combined intracoronary pressure and flow velocity measurements. *Zeitschrift fur Kardiologie*, 91(SUPPL. 3):108–112, 2002.

270. Tim P. Van De Hoef, Froukje Nolte, Mauro Echavarría-Pinto, Martijn A. Van Lavieren, Peter Damman, Steven A.J. Chamuleau, Michiel Voskuil, Hein J. Verberne, José P.S. Henriques, Berthe L.F. Van Eck-Smit, Karel T. Koch, Robbert J. De Winter, Jos A.E. Spaan, Maria Siebes, Jan G.P. Tijssen, Martijn Meuwissen, and Jan J. Piek. Impact of hyperaemic microvascular resistance on fractional flow reserve measurements in patients with stable coronary artery disease: Insights from combined stenosis and microvascular resistance assessment. *Heart*, 100(12):951–959, 2014.

271. Tim P. Van De Hoef, Martijn Meuwissen, Javier Escaned, Sayan Sen, Ricardo Petraco, Martijn A. Van Lavieren, Mauro Echavarria-Pinto, Froukje Nolte, Sukhjinder Nijjer, Steven A.J. Chamuleau, Michiel Voskuil, Berthe L.F. Van Eck-Smit, Hein J. Verberne, José P.S. Henriques, Karel T. Koch, Robbert J. De Winter, Jos A.E. Spaan, Maria Siebes, Jan G.P. Tijssen, Justin E. Davies, and Jan J. Piek. Head-to-head comparison of basal stenosis resistance index, instantaneous wave-free ratio, and fractional flow reserve: Diagnostic accuracy for stenosis-specific myocardial ischaemia. *EuroIntervention*, 2015.

272. Zhang Zhang, Shigeho Takarada, and Sabee Molloi. Quantification of coronary microvascular resistance using angiographic images for volumetric blood flow measurement: in vivo validation. *American Journal of Physiology - Heart and Circulatory Physiology*, 300(6):H2096–104, 2011.

273. UNSCEAR. Sources and Effects of Ionizing Radiation. United Nations Scientific Committee on the Effects of Atomic Radiation Annex B Exposures of the public and workers from various sources of radiation. Technical report, United Nations Scientific Committee on the Effects of Atomic Radiation, 2008.

274. Titus R Koenig, Fred A Mettler, and Louis K Wagner. Skin Injuries from Fluoroscopically Guided Recommendations for Minimizing Dose Delivered to Patient. *American Journal of Roentgenology*, 177(1):13–20, 2001.

275. Stephen Balter, John W Hopewell, Donald L Miller, Louis K Wagner, and Michael J

Zelefsky. Fluoroscopically Guided Interventional Procedures: A Review of Radiation Effects on Patients' Skin and Hair. *Radiology*, 254(2):326–341, 2010.

276. Maria Grazia Andreassi, Lamia Ait-Ali, Nicoletta Botto, Samantha Manfredi, Gaetano Mottola, and Eugenio Picano. Cardiac catheterization and long-term chromosomal damage in children with congenital heart disease. *European heart journal*, 27(22):2703–8, nov 2006.

277. D G W Onnasch. Optimization of radiographic parameters for paediatric cardiac angiography. *British Journal of Radiology*, 77(918):479–487, 2004.

278. R Nicholson, F Tuffee, and M C Uthappa. Skin sparing in interventional radiology: the effect of copper filtration. *The British journal of radiology*, 73(865):36–42, jan 2000.

279. F H Wittkampf, E F Wever, K Vos, J Geleijns, M J Schalij, J van der Tol, and E O Robles de Medina. Reduction of radiation exposure in the cardiac electrophysiology laboratory. *Pacing and clinical electrophysiology : PACE*, 23(11 Pt 1):1638–44, 2000.

280. Andrew G Davies, Arnold R Cowen, Stephen M Kengyelics, Janet Moore, Chris Pepper, Campbell Cowan, and Mohan U Sivanathan. X-ray dose reduction in fluoroscopically guided electrophysiology procedures. *Pacing and Clinical Electrophysiology : PACE*, 29(3):262–71, 2006.

281. A M Norbash, D Busick, and M P Marks. Techniques for reducing interventional neuroradiologic skin dose: tube position rotation and supplemental beam filtration. *American jJurnal of Neuroradiology*, 17(1):41–9, 1996.

282. HD Nagel. Comparison of performance characteristics of conventional and K-edge filters in general diagnostic radiology. *Physics in Medicine and Biology*, 34:1269, 1989.

283. R.M. Gagne, PW Quinn, and RJ Jennings. Comparison of beam-hardening and K-edge filters for imaging barium and iodine during fluoroscopy. *Medical Physics*, 21(1):107–121, 1994.

284. Pier Luca Rossi, Matteo Mariselli, Ivan Corazza, David Bianchini, Mauro Biffi, Cristian Martignani, Romano Zannoli, and Giuseppe Boriani. Decrease in patient radiation ex-

posure by a tantalum filter during electrophysiological procedures. *Pacing and Clinical Electrophysiology : PACE*, 32:S109–12, 2009.

285. Phillip Rauch, Pei Jan Paul Lin, Stephen Balter, Atsushi Fukuda, Allen Goode, Gary Hartwell, Terry Lafrance, Edward Nickoloff, Jeff Shepard, and Keith Strauss. Functionality and operation of fluoroscopic automatic brightness control/automatic dose rate control logic in modern cardiovascular and interventional angiography systems: A Report of Task Group 125 Radiography/Fluoroscopy Subcommittee, Imaging Physics Co. Technical report, AAPM, 2012.

286. E Bogaert, K Bacher, K Lemmens, M Carlier, W Desmet, X De Wagter, D Djian, C Hanet, G Heyndrickx, V Legrand, Y Taeymans, and H Thierens. A large-scale multicentre study of patient skin doses in interventional cardiology: dose-area product action levels and dose reference levels. *The British Journal of Radiology*, 82(976):303–12, 2009.

287. CJ Martin, DG Sutton, A Workman, AJ Shaw, and D Temperton. Protocol for measurement of patient entrance surface dose rates for fluoroscopic X-ray equipment. *British Journal of Radiology*, 71:1283–1287, 1998.

288. E Bogaert, K Bacher, and H Thierens. Interventional cardiovascular procedures in Belgium: effective dose and conversion factors. *Radiation protection dosimetry*, 129(1-3):77–82, jan 2008.

289. K. Van Der Marel, S. Vedantham, I. M.J. Van Der Bom, M. Howk, T. Narain, K. Ty, A. Karellas, M. J. Gounis, A. S. Puri, and A. K. Wakhloo. Reduced patient radiation exposure during neurodiagnostic and interventional X-ray angiography with a new imaging platform. *American Journal of Neuroradiology*, 38(3):442–449, 2017.

290. Philips Healthcare. AlluraClarity with ClarityIQ technology. `https://www.philips.co.uk/healthcare/product/HCNOCTN163/alluraclarity-with-clarityiq-technology`, 2019. [Online; accessed 25/9/2019].

291. A. Fouras, M. J. Kitchen, S. Dubsky, R. a. Lewis, S. B. Hooper, and K. Hourigan. The past, present, and future of x-ray technology for in vivo imaging of function and form. *Journal of Applied Physics*, 105(10):102009, 2009.

292. William H Barry. Digital Subtraction Angiography- A Cardiologist's View. *Cardiovascular and interventional radiology*, 6:263–264, 1983.

293. R Simon, G Herrmann, and I Amende. Comparison of three different principles in the assessment of coronary flow reserve from digital angiograms. *International Journal of Cardiac Imaging*, 5(2-3):203–12, 1990.

294. Thomas P Fuerst and Michael S Van Lysel. Measurement of absolute blood iodine concentration during digital subtraction angiography. *Medical Physics*, 20(3):795–803, 1993.

295. Sabee Molloi, Atila Ersahin, Jerry Tang, James Hicks, and Cyril Y Leung. Quantification of Volumetric Coronary Blood Flow With Dual-Energy Digital Subtraction Angiography. *Circulation*, 93:1919–1927, 1996.

296. MingDe Lin, Craig T. Marshall, Yi Qi, Samuel M. Johnston, Cristian T. Badea, Claude a. Piantadosi, and G. Allan Johnson. Quantitative blood flow measurements in the small animal cardiopulmonary system using digital subtraction angiography. *Medical Physics*, 36(11):5347, 2009.

297. L Van Tran and J Sklansky. Flexible mask subtraction for digital angiography. *IEEE Transactions on Medical Imaging*, 11(3):407–15, 1992.

298. Yu Deuerling-Zheng, Michael Lell, Adam Galant, and Joachim Hornegger. Motion compensation in digital subtraction angiography using graphics hardware. *Computerized Medical Imaging and Graphics*, 30(5):279–289, 2006.

299. Andrew J Boyle, Karl H Schuleri, Jean Lienard, Regis Vaillant, Michael Y Chan, Jeffrey M Zimmet, Ramesh Mazhari, Marco Centola, Gary Feigenbaum, Joud Dib, Navin K Kapur, Joshua M Hare, and Jon R Resar. Quantitative automated assessment of myocardial perfusion at cardiac catheterization. *The American Journal of Cardiology*, 102(8):980–7, 2008.

300. Ying Zhu, Simone Prummer, Peng Wang, Terrence Chen, Dorin Comaniciu, and Martin Ostermeier. Dynamic layer separation for coronary DSA and enhancement in fluoroscopic

sequences. *Medical image computing and computer-assisted intervention : MICCAI International Conference on Medical Image Computing and Computer-Assisted Intervention*, 12(Pt 2):877–84, 2009.

301. Mansour Nejati, Saeid Sadri, and Rassoul Amirfattahi. Nonrigid image registration in digital subtraction angiography using multilevel B-spline. *BioMed Research International*, 2013.

302. Vincent Auvray, Patrick Bouthemy, and Jean Liénard. Joint Motion Estimation and Layer Segmentation in Transparent Image SequencesApplication to Noise Reduction in X-Ray Image Sequences. *Eurasip Journal on Advances in Signal Processing*, 2009.

303. Caroline A. Schneider, Wayne S. Rasband, and Kevin W. Eliceiri. NIH Image to ImageJ: 25 years of image analysis. *Nature Methods*, 9(7):671–675, 2012.

304. J Pinheiro, D Bates, S DebRoy, D Sarkar, and R Core Team. nlme: Linear and Nonlinear Mixed Effects Models. R package version 3.1-118, 2014.

305. S Yamamoto, Y Koyama, M Suzuki, H Nagasawa, R Kakinuma, and N Moriyama. Optimized Control of X-ray Exposure and Image Noise Using a Particular Multislice CT Scanner. *Nihon Hoshasen Gijutsu Gakkai Zasshi*, 64(8):955–959, 2008.

306. Wei Zhang, Haibin Ling, Simone Prummer, Kevin Shaohua Zhou, Martin Ostermeier, and Dorin Comaniciu. Coronary tree extraction using motion layer separation. *Medical image computing and computer-assisted intervention : MICCAI International Conference on Medical Image Computing and Computer-Assisted Intervention*, 12(Pt 1):116–23, 2009.

307. Marius Staring, Stefan Klein, and Josien P.W. Pluim. Nonrigid registration with tissue-dependent filtering of the deformation field. *Physics in Medicine and Biology*, 52(23):6879–6892, 2007.

308. Megumi Yamamoto, Yasuhiko Okura, Masaharu Ishihara, Masayuki Kagemoto, Kengo Harada, and Takayuki Ishida. Development of digital subtraction angiography for coronary artery. *Journal of Digital Imaging*, 22(3):319–25, 2009.

309. Sabee Y. Molloi and Charles A. Mistretta. Quantification techniques for dual-energy cardiac imaging. *Medical Physics*, 16(2):209–217, 1989.

310. H. K. Thompson, C. F. Starmer, R. E. Whalen, and H. D. Mcintosh. Indicator Transit Time Considered as a Gamma Variate. *Circulation Research*, 14(6):502–515, 1964.

311. Austin, Gabriel S Aldea, Dwain L Coggins, Arthur E Flynn, and Julien I E Hoffman. Profound Spatial Heterogeneity of Coronary Reserve Myocardial Blood Flow. *Circulation research*, 67:319–331, 1990.

312. Baruch B. Lieber, Chander Sadasivan, Qing Hao, Jaehoon Seong, and Liliana Cesar. The mixability of angiographic contrast with arterial blood. *Medical Physics*, 36(11):5064–5078, 2009.

313. Hanna Goszczyńska and Marek Rewicki. Coronary flow evaluation by densitometric analysis of sequences of coronarographic images. *Medical and Biological Engineering and Computing*, 46(2):199–204, 2008.

314. D Gil, O Rodriguez-Leor, P Radeva, and J Mauri. Myocardial perfusion characterization from contrast angiography spectral distribution. *IEEE Transactions on Medical Imaging*, 27(5):641–9, 2008.

315. G. A. Gardiner, M. F. Meyerovitz, L. M. Boxt, D. P. Harrington, R. H. Taus, K. Kandarpa, P. Ganz, and A. P. Selwyn. Selective coronary angiography using a power injector. *American Journal of Roentgenology*, 146(4):831–833, 1986.

316. Michael Sanders, Jacob Shani, George Saviano, and Marcos Rivera. Distal coronary power injection during percutaneous transluminal coronary angioplasty. *Catheterization and Cardiovascular Diagnosis*, 10(6):603–605, 1984.

317. Yuichi Ozaki, Hironori Kitabata, Hiroto Tsujioka, Seiki Hosokawa, Manabu Kashiwagi, Kohei Ishibashi, Kenichi Komukai, Takashi Tanimoto, Yasushi Ino, Shigeho Takarada, Takashi Kubo, Keizo Kimura, Atsushi Tanaka, Kumiko Hirata, Masato Mizukoshi, Toshio Imanishi, and Takashi Akasaka. Comparison of contrast media and low-molecular-weight dextran for frequency-domain optical coherence tomography. *Circulation Journal*, 76(4):922–927, 2012.

318. Bernard De Bruyne, Julien Adjedj, Panagiotis Xaplanteris, Angela Ferrara, Yujing Mo, Martin Penicka, Vincent Floré, Mariano Pellicano, Gabor Toth, Emanuele Barbato, Dirk J. Duncker, and Nico H.J. Pijls. Saline-Induced Coronary Hyperemia. *Circulation: Cardiovascular Interventions*, 10(4):1–8, 2017.

319. Marcos Garcia-Guimaraes, Fernando Rivero, Javier Cuesta, and Fernando Alfonso. Iatrogenic coronary artery dissection induced during invasive absolute coronary blood flow measurement: Optical coherence tomography findings. *EuroIntervention*, 13(3):364–365, 2017.

320. J T Dodge, B G Brown, E L Bolson, and H T Dodge. Lumen diameter of normal human coronary arteries. Influence of age, sex, anatomic variation, and left ventricular hypertrophy or dilation. *Circulation*, 86(1):232–46, 1992.

321. J. Theodore Dodge, Micheal Rizzo, Martha Nykiel, Jane Altmann, Kathy Hobkirk, Mary Brennan, and C. Michael Gibson. Impact of injection rate on the Thrombolysis In Myocardial Infarction (TIMI) trial frame count. *American Journal of Cardiology*, 81(10):1268–1270, 1998.

322. Philip Urvan, Bernhard Meier, Leo Finci, Bernard de Bruyne, Giuseppe Steffenino, and Wilheim Rutishauser. Coronary wedge pressure: A predictor of restenosis after coronary balloon angioplasty. *Journal of the American College of Cardiology*, 10(3):504–509, 1987.

323. AMA Khalifa and DP Giddens. Characterization and evolution of poststenotic flow disturbances. *Journal of Biomechanics*, 14(5):279–296, 1981.

324. Fang Bao Tian, Luoding Zhu, Pak Wing Fok, and Xi Yun Lu. Simulation of a pulsatile non-Newtonian flow past a stenosed 2D artery with atherosclerosis. *Computers in Biology and Medicine*, 43(9):1098–1113, 2013.

325. Kiyya Ararsa and Ralph C Aldredge. Computational Analysis of Catheter-Tip Geometries for Optimizing Drug Infusion in Arterial Blood Flow. *American Journal of Biomedical Engineering*, 2013(4):91–98, 2013.

326. Henk Everaars, Guus A de Waard, Stefan P Schumacher, Frederik M Zimmermann, Michiel J Bom, Peter M van de Ven, Pieter G Raijmakers, Adriaan A Lammertsma,

Marco J Götte, Albert C van Rossum, Akira Kurata, Koen M J Marques, Nico H J Pijls, Niels van Royen, and Paul Knaapen. Continuous thermodilution to assess absolute flow and microvascular resistance: validation in humans using [15O]H2O positron emission tomography. *European Heart Journal*, 40(28):2350–2359, 2019.

327. K. Lance Gould, Nils P. Johnson, Timothy M. Bateman, Rob S. Beanlands, Frank M. Bengel, Robert Bober, Paolo G. Camici, Manuel D. Cerqueira, Benjamin J.W. Chow, Marcelo F. Di Carli, Sharmila Dorbala, Henry Gewirtz, Robert J. Gropler, Philipp A. Kaufmann, Paul Knaapen, Juhani Knuuti, Michael E. Merhige, K. Peter Rentrop, Terrence D. Ruddy, Heinrich R. Schelbert, Thomas H. Schindler, Markus Schwaiger, Stefano Sdringola, John Vitarello, Kim A. Williams, Donald Gordon, Vasken Dilsizian, and Jagat Narula. Anatomic versus physiologic assessment of coronary artery disease: Role of coronary flow reserve, fractional flow reserve, and positron emission tomography imaging in revascularization decision-making. *Journal of the American College of Cardiology*, 62(18):1639–1653, 2013.

328. Joerg Herrmann, Juan Carlos Kaski, and Amir Lerman. Coronary microvascular dysfunction in the clinical setting: From mystery to reality. *European Heart Journal*, 33(22):2771–2781, 2012.

329. Cristiano Spadaccio and Umberto Benedetto. Coronary artery bypass grafting (CABG) vs. percutaneous coronary intervention (PCI) in the treatment of multivessel coronary disease: Quo vadis? -A review of the evidences on coronary artery disease. *Annals of Cardiothoracic Surgery*, 7(4):506–515, 2018.

330. David Brosh, Abid R. Assali, Aviv Mager, Avital Porter, David Hasdai, Igal Teplitsky, Eldad Rechavia, Shmuel Fuchs, Alexander Battler, and Ran Kornowski. Effect of No-Reflow During Primary Percutaneous Coronary Intervention for Acute Myocardial Infarction on Six-Month Mortality. *American Journal of Cardiology*, 99(4):442–445, 2007.

331. Ronen Jaffe, Thierry Charron, Geoffrey Puley, Alexander Dick, and Bradley H. Strauss. Microvascular Obstruction and the No-Reflow Phenomenon After Percutaneous Coronary Intervention. *Circulation*, 117(24):3152–3156, 2008.

332. Marthe A. Kampinga, Maarten W.N. Nijsten, Youlan L. Gu, W. Arnold Dijk, Bart J.G.L. De Smet, Ad F.M. Van Den Heuvel, Eng Shiong Tan, and Felix Zijlstra. Is the myocardial blush grade scored by the operator during primary percutaneous coronary intervention of prognostic value in patients with ST-elevation myocardial infarction in routine clinical practice? *Circulation: Cardiovascular Interventions*, 3(3):216–223, 2010.

333. Jaroslaw Zalewski, Krzysztof Nycz, Tadeusz Przewlocki, Monika Durak, Michal Cul, Wojciech Zajdel, and Krzysztof Zmudka. Evolution of myocardial perfusion during primary angioplasty in spontaneously reperfused infarct-related artery: Impact on long-term clinical outcomes and left ventricular function recovery. *International Journal of Cardiology*, 147(1):25–31, 2011.

334. Katsuomi Iwakura, Hiroshi Ito, Shigeo Kawano, Yasunori Shintani, Koichi Yamamoto, Akinobu Kato, Masashi Ikushima, Koji Tanaka, Masashi Kitakaze, Masatsugu Hori, Yorihiko Higashino, and Kenshi Fujii. Predictive factors for development of the no-reflow phenomenon in patients with reperfused anterior wall acute myocardial infarction. *Journal of the American College of Cardiology*, 38(2):472–477, 2001.

335. Derek M. Yellon and Derek J. Hausenloy. Myocardial Reperfusion Injury. *New England Journal of Medicine*, 357:1121–1135, 2007.

336. Henning Kelbæk, Dan Eik Høfsten, Lars Køber, Steffen Helqvist, Lene Kløvgaard, Lene Holmvang, Erik Jørgensen, Frants Pedersen, Kari Saunamäki, Ole De Backer, Lia E. Bang, Klaus F. Kofoed, Jacob Lønborg, Kiril Ahtarovski, Niels Vejlstrup, Hans E. Bøtker, Christian J. Terkelsen, Evald H. Christiansen, Jan Ravkilde, Hans Henrik Tilsted, Anton B. Villadsen, Jens Aarøe, Svend E. Jensen, Bent Raungaard, Lisette O. Jensen, Peter Clemmensen, Peer Grande, Jan K. Madsen, Christian Torp-Pedersen, and Thomas Engstrøm. Deferred versus conventional stent implantation in patients with ST-segment elevation myocardial infarction (DANAMI 3-DEFER): An open-label, randomised controlled trial. *The Lancet*, 387(10034):2199–2206, 2016.

337. Je Sang Kim, Hyun Jong Lee, Cheol Woong Yu, Yang Min Kim, Soon Jun Hong, Jae Hyung Park, Rak Kyeong Choi, Young Jin Choi, Jin Sik Park, Tae Hoon Kim, Ho Jun Jang, Hyung Joon Joo, Sang A. Cho, Young Moo Ro, and Do Sun Lim. INNOVATION

study (Impact of Immediate Stent Implantation Versus Deferred Stent Implantation on Infarct Size and Microvascular Perfusion in Patients With ST-Segment-Elevation Myocardial Infarction). *Circulation: Cardiovascular Interventions*, 9(12):1–9, 2016.

338. Santiago Garcia, Yader Sandoval, Henri Roukoz, Selcuk Adabag, Mariana Canoniero, Demetris Yannopoulos, and Emmanouil S. Brilakis. Outcomes after complete versus incomplete revascularization of patients with multivessel coronary artery disease: A meta-analysis of 89,883 patients enrolled in randomized clinical trials and observational studies. *Journal of the American College of Cardiology*, 62(16):1421–1431, 2013.

339. Ronak Delewi, Anouk Andriessen, Jan G P Tijssen, Felix Zijlstra, Jan J. Piek, and Alexander Hirsch. Impact of intracoronary cell therapy on left ventricular function in the setting of acute myocardial infarction: A meta-analysis of randomised controlled clinical trials. *Heart*, 99(4):225–232, 2013.

340. Derek J. Hausenloy, Hans Erik Botker, Thomas Engstrom, David Erlinge, Gerd Heusch, Borja Ibanez, Robert A. Kloner, Michel Ovize, Derek M. Yellon, and David Garcia-Dorado. Targeting reperfusion injury in patients with ST-segment elevation myocardial infarction: Trials and tribulations. *European Heart Journal*, 38(13):935–941d, 2017.

341. N W Marshall, C J Kotre, K J Robson, and a R Lecomber. Receptor dose in digital fluorography: a comparison between theory and practice. *Physics in medicine and biology*, 46(4):1283–96, apr 2001.

342. Andrew G Davies, Stephen M Kengyelics, and Amber J Gislason-Lee. Image quality based x-ray dose control in cardiac imaging. In Karen O Egiazarian, Sos S Agaian, and Atanas P Gotchev, editors, *Image Processing: Algorithms and Systems XIII*, volume 9399, pages 81–88. International Society for Optics and Photonics, SPIE, 2015.

343. Stephen M. Kengyelics, Amber J. Gislason-Lee, Claire Keeble, Derek R. Magee, and Andrew G. Davies. Noise estimation in cardiac x-ray imaging: A machine vision approach. *Biomedical Physics and Engineering Express*, 2(6), 2016.

344. Stephen M Kengyelics, Amber J Gislason-Lee, Claire Keeble, Derek R Magee, and Andrew G Davies. Context sensitive cardiac x-ray imaging: a machine vision approach to x-ray dose control. *Journal of Electronic Imaging*, 24(5):1–9, 2015.

345. Marija Vukicevic, Bobak Mosadegh, James K Min, and Stephen H Little. Cardiac 3D Printing and Its Future Directions. *JACC: Cardiovascular Imaging*, 10(2):171–184, 2017.

346. Joel A Garcia, Chen James, Adam Hangsen, Onno Wink, Babak Movassaghi, and John C Messenger. Rotational angiography (RA) and three-dimensional imaging (3-DRA): an available clinical tool. *International Journal of Cardiac Imaging*, 23:9–13, 2007.

347. Amber J Gislason-Lee, Asli Kumcu, Stephen M Kengyelics, David S Brettle, Laura A Treadgold, Mohan Sivananthan, and Andrew G Davies. How much image noise can be added in cardiac x-ray imaging without loss in perceived image quality? *Journal of Electronic Imaging*, 24(5):1–14, 2015.

348. Stephen M Kengyelics, Laura A Treadgold, and Andrew G Davies. X-ray system simulation software tools for radiology and radiography education. *Computers in Biology and Medicine*, 93:175–183, feb 2018.

349. Julien Bert, Hector Perez-Ponce, Ziad El Bitar, Sébastien Jan, Yannick Boursier, Damien Vintache, Alain Bonissent, Christian Morel, David Brasse, and Dimitris Visvikis. Geant4-based Monte Carlo simulations on GPU for medical applications. *Physics in Medicine and Biology*, 58(16):5593–5611, 2013.

350. J. Allison, K. Amako, J. Apostolakis, H. Araujo, P. Arce Dubois, M. Asai, G. Barrand, R. Capra, S. Chauvie, R. Chytracek, G. A.P. Cirrone, G. Cooperman, G. Cosmo, G. Cuttone, G. G. Daquino, M. Donszelmann, M. Dressel, G. Folger, F. Foppiano, J. Generowicz, V. Grichine, S. Guatelli, P. Gumplinger, A. Heikkinen, I. Hrivnacova, A. Howard, S. Incerti, V. Ivanchenko, T. Johnson, F. Jones, T. Koi, R. Kokoulin, M. Kossov, H. Kurashige, V. Lara, S. Larsson, F. Lei, F. Longo, M. Maire, A. Mantero, B. Mascialino, I. McLaren, P. Mendez Lorenzo, K. Minamimoto, K. Murakami, P. Nieminen, L. Pandola, S. Parlati, L. Peralta, J. Perl, A. Pfeiffer, M. G. Pia, A. Ribon, P. Rodrigues, G. Russo, S. Sadilov, G. Santin, T. Sasaki, D. Smith, N. Starkov, S. Tanaka, E. Tcherniaev, B. Tomé, A. Trindade, P. Truscott, L. Urban, M. Verderi, A. Walkden, J. P. Wellisch, D. C. Williams, D. Wright, H. Yoshida, and M. Peirgentili. Geant4 developments and applications. *IEEE Transactions on Nuclear Science*, 53(1):270–278, 2006.

351. Andreu Badal and Aldo Badano. Monte Carlo simulation of x-ray imaging using a graphics processing unit. *IEEE Nuclear Science Symposium Conference Record*, (3):4081–4084, 2009.

352. Karen E. Thomas, E. H. Mann, N. Padfield, L. Greco, G. BenDavid, and A. Alzahrani. Dual bolus intravenous contrast injection technique for multiregion paediatric body CT. *European Radiology*, 25(4):1014–1022, 2015.

353. Suhny Abbara, Philipp Blanke, Christopher D. Maroules, Michael Cheezum, Andrew D. Choi, B. Kelly Han, Mohamed Marwan, Chris Naoum, Bjarne L. Norgaard, Ronen Rubinshtein, Paul Schoenhagen, Todd Villines, and Jonathon Leipsic. SCCT guidelines for the performance and acquisition of coronary computed tomographic angiography: A report of the society of Cardiovascular Computed Tomography Guidelines Committee: Endorsed by the North American Society for Cardiovascular Imaging (NASCI). *Journal of Cardiovascular Computed Tomography*, 10(6):435–449, 2016.

354. M Lang, R Brennecke, M Haude, U Renneisen, R Erbel, and J Meyer. Improving the applicability of myocardial densitometry and parametric imaging by extended automated densogram analysis. *International Journal of Cardiac Imaging*, 11(2):105–15, 1995.

355. Andrew B. Crummy, Charles M. Strother, and Charles A. Mistretta. The History of Digital Subtraction Angiography. *Journal of Vascular and Interventional Radiology*, 29(8):1138–1141, 2018.

356. Katsuyuki Taguchi and Jan S. Iwanczyk. Vision 20/20: Single photon counting x-ray detectors in medical imaging. *Medical Physics*, 40(10):100901, 2013.

357. Cynthia H. McCollough, Leng Shuai, Lifeng Yu, and Joel G. Fletcher. Dual- and Multi-Energy CT: Principles, Technical Approaches, and Clinical Applications. *Radiology*, 276(3):637–653, 2015.

358. Silvia Pani, Sarene C. Saifuddin, Filipa I.M. Ferreira, Nicholas Henthorn, Paul Seller, Paul J. Sellin, Philipp Stratmann, Matthew C. Veale, Matthew D. Wilson, and Robert J. Cernik. High energy resolution hyperspectral x-ray imaging for low-dose contrast-enhanced digital mammography. *IEEE Transactions on Medical Imaging*, 36(9):1784–1795, 2017.

359. J. Fernandez de Canete, P. del Saz-Orozco, D. Moreno-Boza, and E. Duran-Venegas. Object-oriented modeling and simulation of the closed loop cardiovascular system by using SIMSCAPE. *Computers in Biology and Medicine*, 43(4):323–333, 2013.

360. Nils P. Johnson, Richard L. Kirkeeide, and K. Lance Gould. Is discordance of coronary flow reserve and fractional flow reserve due to methodology or clinically relevant coronary pathophysiology? *JACC: Cardiovascular Imaging*, 5(2):193–202, 2012.

361. K. Lance Gould, Richard Kirkeeide, and Nils P. Johnson. Coronary Branch Steal. *Circulation: Cardiovascular Imaging*, 3(6):701–709, 2010.

362. Nils P. Johnson and K. Lance Gould. Integrating noninvasive absolute flow, coronary flow reserve, and ischemic thresholds into a comprehensive map of physiological severity. *JACC: Cardiovascular Imaging*, 5(4):430–440, 2012.